University of Kentucky
UKnowledge

University of Kentucky Doctoral Dissertations | Graduate School

2008

PRECISION MEASUREMENTS OF THE NEUTRON ELECTRIC FORM FACTOR AT HIGH MOMENTUM TRANSFERS

Ameya Suresh Kolarkar
University of Kentucky, roolarkar@bu.edu

Right click to open a feedback form in a new tab to let us know how this document benefits you.

Recommended Citation

Kolarkar, Ameya Suresh, "PRECISION MEASUREMENTS OF THE NEUTRON ELECTRIC FORM FACTOR AT HIGH MOMENTUM TRANSFERS" (2008). *University of Kentucky Doctoral Dissertations*. 612.
https://uknowledge.uky.edu/gradschool_diss/612

This Dissertation is brought to you for free and open access by the Graduate School at UKnowledge. It has been accepted for inclusion in University of Kentucky Doctoral Dissertations by an authorized administrator of UKnowledge. For more information, please contact UKnowledge@lsv.uky.edu.

ABSTRACT OF DISSERTATION

Ameya Suresh Kolarkar

The Graduate School

University of Kentucky

2008

PRECISION MEASUREMENTS OF THE NEUTRON ELECTRIC FORM FACTOR AT HIGH MOMENTUM TRANSFERS

ABSTRACT OF DISSERTATION

A dissertation submitted in partial fulfillment of the
requirements for the degree of Doctor of Philosophy
at the University of Kentucky

By

Ameya Suresh Kolarkar

Lexington, Kentucky

Director: Dr. Wolfgang Korsch, Professor of Physics and Astronomy

Lexington, Kentucky

2008

Copyright © Ameya Suresh Kolarkar 2008

ABSTRACT OF DISSERTATION

PRECISION MEASUREMENTS OF THE NEUTRON ELECTRIC FORM FACTOR AT HIGH MOMENTUM TRANSFERS

The neutron, although electrically neutral, is composed of elementary *charged* particles and as a result, possesses a charge distribution within. The charge distribution can be studied by measuring a quantity called the neutron electric form factor, G_E^n.

Experiment E02-013 at Jefferson Lab's Hall A measured G_E^n at high four-momentum transfer values of $Q^2 = 1.2, 1.7, 2.5$ and 3.4 $(\mathrm{GeV}/c)^2$ in double polarized semi-exclusive $^3\overrightarrow{\mathrm{He}}(\vec{e}, e'n)$ scattering in quasi-elestic kinematics by measuring the transverse asymmetry A_T of the cross section.

The neutron electric form factor is essential to know for a variety of reasons. Results from the recent Jefferson Lab experiment on the proton revealed interesting features at these momentum transfers, whereas no accurate data for the neutron is available. Also the recent development in Generalized Parton Distributions (GPDs) necessitates the need for precise values for G_E^n in Q^2 range between 1 and 10 $(\mathrm{GeV}/c)^2$; they appear as limiting conditions for certain GPD functions, for example, to constrain spin-flip GPDs.

The experiment used the polarized ^{3}He target and the polarized CEBAF electron beam at energies of about 1.52, 2.08, 2.64 and 3.29 GeV. The electrons were detected in the BigBite spectrometer and the neutrons in a large array of scintillators in coincidence with the electrons.

In this dissertation, we report a preliminary result, $G_E^n = 0.03457 \pm 0.007239$ at $Q^2 = 1.7$ $(\mathrm{GeV}/c)^2$.

Ameya Suresh Kolarkar

April 29, 2008

PRECISION MEASUREMENTS OF THE NEUTRON ELECTRIC FORM FACTOR AT HIGH MOMENTUM TRANSFERS

By

Ameya Suresh Kolarkar

Dr. Wolfgang Korsch
(Director of Dissertation)

Dr. Joseph W. Brill
(Director of Graduate Studies)

April 29, 2008
(Date)

RULES FOR THE USE OF DISSERTATIONS

Unpublished theses submitted for the Doctor's degree and deposited in the University of Kentucky Library are as a rule open for inspection, but are to be used only with due regard to the rights of the authors. Bibliographical references may be noted, but quotations or summaries of parts may be published only with the permission of the author, and with the usual scholarly acknowledgements.

Extensive copying or publication of the thesis in whole or in part requires also the consent of the Dean of the Graduate School of the University of Kentucky.

A library which borrows this thesis for use by its patrons is expected to secure the signature of each user.

Name and Address	Date

DISSERTATION

Ameya Suresh Kolarkar

The Graduate School

University of Kentucky

2008

PRECISION MEASUREMENTS OF THE NEUTRON ELECTRIC FORM FACTOR AT HIGH MOMENTUM TRANSFERS

DISSERTATION

A dissertation submitted in partial fulfillment of the
requirements for the degree of Doctor of Philosophy
at The University of Kentucky

By

Ameya Suresh Kolarkar

Lexington, Kentucky

Director: Dr. Wolfgang Korsch, Professor of Physics and Astronomy

Lexington, Kentucky

2008

Copyright © Ameya Suresh Kolarkar 2008

To my parents

Hemlata and Suresh Kolarkar

ACKNOWLEDGEMENTS

First and foremost, I would like to thank my advisor Wolfgang Korsch for his support and trust towards me, without which this work would not have been possible. I will always cherish all the great moments with him, be it at lunch in Kentucky or in the experimental Hall during the experiment. He gave me the freedom every student would ask for - including the freedom to make mistakes - to develop skills and critical thinking to work independently and excellent guidance when needed; all of which have helped me become a better physicist. His excellent troubleshooting techniques have helped me throughout my time at Jefferson lab - over the phone or in person, regarding complex electronics or simple C++ routines! And his always jovial nature made even the most challenging tasks enjoyable.

I'd like to thank Jian-Ping Chen, my target supervisor at Jefferson Lab under whom I learnt all about the polarized ^{3}He target apart from other physics. JP's ability to sit with a student and explain and/or discuss with him/her all possible topics in physics made him fun to talk to. I acknowledge all his help and advice during my entire stay at Jefferson Lab, in particular, during the installation period with all-night laser alignment shifts! I also thank him for supporting me and giving credit where it was due. Being in charge of laser safety was fun too.

I would like to thank Bogdan Wojtsekhowski, my Jefferson Lab sponsor and experiment spokesperson. There is seldom a time where you talk to him and not learn something. It was indeed a pleasure working with him; his insistence on perfection - be it an *xfig* design or experimental technique - has helped me become a better researcher. Who can forget his laptop presentation on form factors at the G_E^n picnic by the lakeside? His emphasis on the physics aspect of everything I did in the lab, as well as testing things himself with attention to even the smallest detail will always be an inspiration.

In a huge endeavor like this one, a lot of people are involved and I am indebted to so many of them for a wonderful Jefferson Lab experience during my graduate years. My sincere acknowledgements to the following:

Gordon Cates for lending his expertise in the wee hours of the night during target installation, and his inspirational words towards becoming a better scientist.

Nilanga Liyanage for his knack for clearly explaining things during the experiment; and useful discussions during data analysis.

Bob Michaels for giving me the chance to work on the DAQ electronics and software,

and the experiment homepage. The skills I learnt from him have helped me greatly.

Robert Feuerbach, the analysis wizard, for being available anytime to explain anything, from the most trivial of things to the complex; and his very valuable role in the data analysis.

Alexandre Camsonne, Shigeyuki Tajima and Brad Sawatzky for their relentless work and fun shifts during the installation and data-taking.

The experiment's graduate student team. It was fun to work with Aidan Kelleher on various aspects of the target, and learning American words for much of the equipment. Discussing analysis with Seamus Riordan, Brandon Craver and Tim Ngo over meals was always enlightening. I enjoyed the late night discussions with Jonathan Miller on various topics including vegetarianism and religion. I learnt a lot from Sergey Abrahamyan about the history of Armenia.

(I would like to mention here how much fun I had being part of an amazing night analysis team with Nerses, Jonathan and Alexandre. It is not easy to man 75 night shifts in a row and I cannot think of a better team.)

Samvel Mayilyan for teaching me how to build - and rotate - scintillators in Armenian; Albert Shahinyan for teaching me the basics of data acquisition and fun conversations about Indian music. Nerses Gevorgyan for showing me a lot of software tricks. *shnorhakalutyun*!

Xiaofeng Zhu for being such a sport and helping me out in the nights with laser alignment and other target matters. It was wonderful working with him - in the laboratory and in the experimental Hall.

Vladimir Nelyubin, Alex Lukhanin, Hakob Voskanyan and Igor Rachek for all their help and suggestions on optics, hardware and electronics. Dmitri Nikolenko for his work on the G_E^n compass and the exclusive half-verbal half-sign language we invented to communicate. Arie Beck for all the physics discussions we had and for all his help with the compass measurements. Daniela Rohe for useful discussions on various magnetic field direction measuring techniques.

Vahe Mamyan for being a good friend. Tanja Horn for lots of evening discussions and thoughts on various topics in physics and life. Sarah Phillips for all the concerts and the hunts for vegetarian food together; her cheerful and bubbly nature always put me in good spirits. Lisa Kaufman for all the tea-times and great conversations about all things in life. The others of the (forward angle) G^0 team who became good friends over time: Jianglai

Liu, Kazutaka Nakahara, Julie Roche, Paul King; The Kentucky PrimEx team: Aram Teymurazyan, Marianna Gabrielyan, Itaru Nakagawa, and my office-mate Dan Dale (also for his help on physics aspects and discussions in the office).

Vincent Sulkosky for showing me the workings of the target system at JLab and patiently answering all my questions and troubleshooting. Thanks to Jaideep Singh for making any aspect of the target seem easy. I appreciate all his help before and during the experiment. Patricia Solvignon for her super laser alignment training sessions and very patient and expert help on various target matters. Tim Holmstrom for being a wonderful person and for all his support.

Fatiha Benmokhtar for being a wonderful friend throughout my stay at Jefferson Lab. Without her and the *weekend gang* - Agus Ananda, Clarisse Tur, Jörn Langheinrich, Pawel Nadal-Turonski and on occasions Yordanka Ilieva and Rakhsha Nasseripour - enduring the stress of extreme hard work would have been very difficult.

Sirish Nanda for all his wonderful ideas that helped me in the designing and measuring aspects for my projects and otherwise. I am very much impressed by his vast experience and active experimenting with the newest technology. Also thanks to him for letting me use his lab and equipment therein for my studies. Deepa for her very positive and energetic outlook towards life and lab work. It was fun to work with her in the lab and to know about some engineering aspects of the green Compton upgrade.

Sabine Fuchs and Klaus Grimm for their wonderful friendship (and trusting my cooking skills). Thanks to Sabine for creating a very workable environment wherever she went, and Klaus for physics discussions.

I acknowledge all the help and company given to me by the next generation of experimenters - Kalyan Allada, Chiranjib Dutta and Gretchen Phelps of Kentucky and Xin Qian, Huan Yao and Xiaohui Zhan at Jefferson Lab - and wish them the best for their Ph.D.'s.

Bodo Reitz for getting me started on the basics of the analyzer and answering umpteen questions about scattering experiments. Kathy McCormick for teaching me some EPICS; and her and Lingyan Zhu for being great labmates for a while. Xiaodong Jiang for his lively discussions and suggestions on various topics.

Mark Taylor, the fast electronics expert and a good friend. As the laser-safety in-charge, I relied almost exclusively on him for almost all aspects of safety electronics. All his hard work at anytime of the day or week - in a very good natured way - is very much appreciated.

Also thanks for teaching me how to solder fine wires and circuit boards, and helping me out with his truck in non-work issues. Thanks also to Chris Cuevas, who in his very jovial and playful manner, made every electronic item or design work.

The machinists, Casey and Dave, for realizing in physical space all my drawings on paper and in the air! Also to Casey for playfully solving all my design troubles and always being helpful when I wanted extra aluminum pieces.

The Hall A technicians, Ed Folts, Scot Spiegel and others for doing a marvellous job at installation and offering suggestions at every point during the target installation.

The accelerator guys, Joe Grames and Tim Southern for making me understand the various accelerator aspects. Thanks to Tim for showing me things about the accelerator that I probably would never have otherwise seen. Also to Tim and Ya Li for being great landlords and friends.

Alan Gavalya for so many discussions on the designs of all things target and the world. I appreciate all the time I spent with Al trying to make things work in the design. His expertise and experience have always impressed me. It was great fun to work with Al, and the other members of the design team, Joyce Miller and Susan Esp. Thanks to Susan for working closely with me on the optics design.

The Alignment/Survey group, especially Chris Curtis, for listening to my ideas and giving suggestions to make my design work.

Back in Kentucky, I'd like to thank Susan Gardner for a superb course in Statistical Mechanics and particle physics. Her insights and way of thinking have proven valuable to me over time; Tom Troland and Joseph Brill for being great Directors of Graduate Studies; Terry Yun for being a wonderful friend in all the times we shared over all the years; members of the SPS group for entertaining discussions of homework problems; Shelly Lesher (and Eric vanOsdol), Elizabeth Mayo and Nick Abel for great times during homework and outside, and while organizing the department picnics; Seema Dhamija for trying to troubleshoot problems at Jefferson Lab based on work at U.K.; Bill Fuqua, the electronics engineer for designing and building all fancy electronic equipment for my use in the experiment. Mridupawan Deka, Rupak Dutta and Nilmani Mathur for various discussions on QCD and QFT.

I appreciate the support and great advice of Charlene Leach of the Office of International Affairs in all international issues at every step, and Niti Gupta, the F-1 advisor. Yancy

Ackerman for taking time off her busy schedule to solve my complicated tax issues. All the office staff at U.K. and at JLab for their prompt actions with all the paperwork. Peace of mind in all these areas is important to keep focus on research.

Finally I would like to thank my parents, who have suffered the most during my period away from home and not visiting them for years, for their extreme patience and understanding! Also my sister, for whom I wasn't there when she needed me. And lastly, my wife Shalinee for being most patient and loving during all the hardships in life. There was a time when I did not see her for six months. I deeply appreciate all her love and keeping me motivated at all times. Also thanks to her for reading my thesis and attending all my talks, and her suggestions.

TABLE OF CONTENTS

Acknowledgements . . . iii

List of Tables . . . xii

List of Figures . . . xiii

CHAPTER 1: INTRODUCTION AND THEORY . . . 1
1.1 Introduction . . . 1
1.1.1 Neutrons . . . 1
1.1.2 Electron Scattering . . . 1
1.2 Nucleon Structure . . . 2
1.2.1 Theoretical description . . . 2
1.2.2 Nucleon Form Factors . . . 2
1.2.3 Quasi-elastic Scattering . . . 7
1.2.4 World data so far . . . 9
1.3 Theory Models . . . 10
1.3.1 Perturbative QCD . . . 10
1.3.2 Vector Meson Dominance . . . 12
1.3.3 Constituent Quark Models and Pion Cloud Models . . . 14
1.3.4 Generalized Parton Distributions . . . 15
1.3.5 The Galster Parametrization . . . 20
1.3.6 Shapes of the nucleons and their distributions . . . 20
1.4 Summary of Motivations for G_E^n at high Q^2 . . . 22

CHAPTER 2: THE EXPERIMENT . . . 23
2.1 CEBAF Accelerator Overview . . . 23
2.2 Beam Polarization . . . 28
2.2.1 Spin Dance . . . 28
2.2.2 Compton Polarimetry . . . 29
2.2.3 Møller Polarimetry . . . 31
2.3 The Hall A Beamline . . . 34
2.3.1 Beam Position Monitors . . . 34
2.3.2 Beam Current Monitors . . . 35
2.3.3 Raster . . . 36
2.4 G_E^n Experimental Setup in Hall A . . . 36
2.5 Experimental methods . . . 37
2.5.1 The Double Polarized Cross Section and Asymmetries . . . 39
2.5.2 Two Photon Exchange . . . 40
2.6 Corrections . . . 42
2.6.1 Final State Interactions . . . 42
2.6.2 Meson Exchange Currents . . . 43

2.6.3 Isobar Configurations . . . 44
2.6.4 Radiative Corrections . . . 44

CHAPTER 3: THE POLARIZED ^{3}HE TARGET . . . 45
3.1 Polarized ^{3}He . . . 46
3.2 The Polarized ^{3}He Target . . . 48
3.3 Methods of Polarization of the ^{3}He Target . . . 48
3.4 The Target . . . 49
3.4.1 Construction of the Magnet Box . . . 49
3.4.2 Producing the Holding Field . . . 51
3.4.3 Target Ladder Positions . . . 52
3.4.4 Hybrid Target Cells . . . 53
3.4.5 Making of the Target Cells . . . 54
3.4.6 Heating of the Gas . . . 55
3.4.7 Optical Pumping Method . . . 55
3.4.8 Spin Exchange . . . 56
3.4.9 Lasers and Optical Fibers . . . 59
3.4.10 Polarizing Optics . . . 60
3.4.11 Monitoring the Target during the Experiment . . . 65
3.5 Measuring Polarization . . . 66
3.6 NMR Polarimetry . . . 67
3.6.1 Hardware and Setup . . . 68
3.7 EPR Polarimetry . . . 70
3.7.1 Hardware and Setup . . . 70
3.7.2 Procedure . . . 72
3.8 Polarization Analysis and Results . . . 76
3.8.1 NMR-EPR Calibration . . . 76
3.8.2 Temperature of the Pumping Chamber . . . 76
3.9 Holding Field Direction Measurements . . . 78
3.9.1 Testing and Systematics . . . 78
3.9.2 Compass Measurements . . . 80
3.9.3 Friction Torque . . . 83
3.9.4 Self Effects . . . 86
3.9.5 Direction Measurement Results . . . 86
3.10 Nitrogen in the Target Cell . . . 86

CHAPTER 4: DETECTORS AND ELECTRONICS . . . 89
4.1 The Neutron Detector . . . 89
4.1.1 Construction . . . 89
4.1.2 Planes of the Neutron Arm . . . 90
4.1.3 Neutron Arm Position . . . 92
4.1.4 ND performance . . . 93
4.2 The BigBite detector . . . 93
4.2.1 Construction . . . 93
4.2.2 BB performance . . . 97
4.3 Pulsed Beam Analysis . . . 99

4.4 Data Acquisition System . . . 100
4.5 Helicity . . . 101
4.6 Scalers . . . 103
4.7 Beam Position and Raster Calibration . . . 105

CHAPTER 5: ANALYSIS AND RESULTS . . . 107
5.1 Detector Calibrations . . . 107
5.1.1 BigBite Scintillator Calibration . . . 107
5.1.2 Neutron Detector Scintillator Calibration . . . 111
5.1.3 Neutron Detection Analysis . . . 111
5.2 RF Analysis . . . 114
5.3 Dilution Factors . . . 115
5.3.1 Nitrogen Dilution . . . 115
5.3.2 Proton-to-Neutron Conversion . . . 117
5.4 ND Acceptance Studies with Monte Carlo . . . 118
5.4.1 A brief introduction to MCEEP . . . 119
5.4.2 Results and Future Prospects . . . 119
5.5 Radiative Effects and Corrections . . . 121
5.5.1 Internal Effects . . . 123
5.5.2 External Effects . . . 124
5.5.3 Simulation and Results . . . 124
5.6 Asymmetries and G_E^n . . . 126
5.6.1 Quasielastic Events Selection . . . 126
5.6.2 Asymmetries . . . 127
5.6.3 Extracting G_E^n . . . 128
5.6.4 Errors: Statistical . . . 128
5.6.5 Errors: Systematic . . . 129

CHAPTER 6: CONCLUSION AND OUTLOOK . . . 131
6.1 Conclusions . . . 131
6.2 Future . . . 132

APPENDIX A: FERMI GAS MODEL . . . 133
A.1 The Fermi Gas Model . . . 133

APPENDIX B: FREQUENCY SWEEP NMR . . . 135
B.1 Frequency Sweep Fundamentals . . . 135
B.2 The Adiabatic Condition . . . 136

APPENDIX C: EPR INSTRUMENT DETAILS . . . 139

APPENDIX D: SCALER MAP . . . 141

APPENDIX E: MASCARAD DETAILS 144
E.1 MASCARAD Input File 144
E.2 Run Options 144
E.3 Output File 145

APPENDIX F: MCEEP INPUT AND OPTIONS 146
F.1 Input File and Parameters 146
F.2 ND Pointing Coordinates 147
F.3 Running MCEEP 147

Bibliography 149

Vita 156

LIST OF TABLES

2.1 The electron beam polarization as measured by Møller polarimetry. The systematic error can be taken equal to ±0.3% (absolute). The sign depends on the electron helicity. (The only way to know for sure the beam polarization sign in a Hall is to measure it in the Hall using Møller/Compton polarimeters or some other spin-sensitive process.) 34
2.2 The kinematical settings for the experiment. Subscripts e and n denote the electron and neutron respectively. E denotes the energy and θ, the angle of scattering. The scattering angles correspond to the nominal angle for the detector positioning. 38

3.1 The target cells used during the G_E^n kinematics 53
3.2 Cells characteristics. V stands for the volume with subscripts indicating total (tot), pumping chamber (pc), transfer tube (tt) and target chamber (tc), and P stands for pressure. The alkali ratio is the K to Rb ratio at 235°C. The volumes are in cubic centimeters, the pressures in atmospheres and the density in amagats. [UVa, 2006] 54
3.3 Laser power on the pumping chamber after fibers and optical elements . . . 60
3.4 Circular polarization measurement of the incident laser light done the crude way. $P_c^2 = 1 - A^2$, $A = \frac{P_{\max} - P_{\min}}{P_{\max} + P_{\min}}$. The two sets indicate two separate measurements for the same quantities. 65

4.1 The Neutron Arm Position and Angles at all the kinematics. 93
4.2 BigBite configuration during the experiment for all the kinematic points. Table taken from [Riordan, 2007] 95

5.1 Radiative corrections Δ_i (internal) to the transverse asymmetry from MASCARAD for polarized scattering (transverse asymmetry). 125
5.2 Energy loss from other than target material from MCEEP for kinematic 4. 125
5.3 Systematic errors for $Q^2 = 1.7$ (GeV/c)^2 data. The *Nuclear Effects* include FSI and other effects due to the neutron being in a nuclear medium (Section 2.6.1). Total systematic error is about 6% - 9%. 130

LIST OF FIGURES

1.1 Feynman diagram for the scattering of an electron with 4-momentum $p \equiv (E_e, \vec{p})$ off a nucleon of mass M_N and 4-momentum P. The diagram depicts a single photon exchange, whose 4-momentum is $q = p - p' \equiv (\omega, \vec{q})$. The primes represent scattered particles. 3
1.2 The scattering diagram in the lab frame for a one-photon exchange reaction. θ_e is the electron scattering angle and q^2 is the 4-momentum transferred to the nucleon. 4
1.3 Ratio of proton form factors [Arrington *et al.*, 2006]. 6
1.4 Schematic representation of the Breit frame 6
1.5 A cartoon representation of the scattered energy spectrum from various processes in electron-nucleon scattering. The positions on the energy axis and the widths of the peaks are approximate. The height of the elastic peak is largely reduced. 8
1.6 Quasi-elastic scattering in the PWIA. 8
1.7 The various form factors of nucleons. These are normalized to the dipole form factor. 10
1.8 World data for double polarized experiments for G_E^n. 11
1.9 World data for double polarized experiments for G_E^n/G_d. 12
1.10 pQCD picture for the nucleon EMFFs. The highly virtual photon sees the three-quark states of the nucleon. The large momentum is transferred between the quarks through two successive gluon exchanges. 12
1.11 Systematic depiction of the production and decay of a resonance (in this case, a ρ^0 meson; see text for more). 13
1.12 Schematic representation of deeply virtual exclusive processes, Compton Scattering and Meson Production (the *handbag* diagram) 17
1.13 Representation of a GPD in impact parameter space. The upper diagram is for the region $x \in [\xi, 1]$, and the lower is for the region $x \in [-\xi, \xi]$. [Diehl, 2003] 19
1.14 Transverse region probed at different x. 20
1.15 Different "phase-space" regions accessed by the GPD formalism. See subsubsection 1.3.4 21
1.16 Parametrization fits by [Kelly, 2004] 21
1.17 The neutron showing negative charge distribution at its center. This recent analysis is by [Miller, 2007]. See text for explanation. 22

2.1 (color) CEBAF Layout 24
2.2 (color) Laser schematic for Halls A, B and C. 26
2.3 (color) The Master Slit to "clean up" the electron bunches to reduce leakage currents into other Halls. 27
2.4 (color) Superconducting Cavities 27
2.5 (color) The Wien filter. η_{Wien} is the Wien angle. During the spin dance, the beam polarization is measured as a function of the Wien angle. 29
2.6 The Wien angle scan during the experiment. The polarization was measured with the Hall A Compton polarimetry. The Wien angle which gave us a beam polarization of about 85% was 92.49°. 29

2.7 (color) Schematic of the Compton polarimetry setup. The electron beam is deflected into the Compton *chicane* by dipoles D_1 and D_2 and restored to its original path by dipoles D_3 and D_4. The beam interacts with polarized photons in the cavity. 30
2.8 (color) The Møller optics schematic. 32
2.9 The beam position monitor beampipe 35
2.10 (color) Raster: Before and after calibration [Craver, 2007b] 36
2.11 (color)The experimental setup for the E02-013 experiment in Hall A. The electron beam comes in from the left. 37
2.12 (color)The scattering diagram. For E02-013, ideally, $\theta^* = 90°$, $\phi^* = 0°$, that is, the target spins lie in the electron scattering plane. 38
2.13 The two-photon-exchange Feynman diagrams. 41
2.14 Proton form factor ratios with the Rosenbluth data uncorrected (above) and corrected (below) for two-photon exchange reactions [Arrington *et al.*, 2007]. 42
2.15 Corrections to the PWIA: FSI, MEC, IC 43
2.16 Schematic representation of the 2-body and 3-body breakup (2bbu and 3bbu, respectively) of ^{3}He. 44

3.1 Schematic description of S- and S'-states in ^{3}He (left two) and ^{3}H (rightmost) [Friar, 1991]. The shaded and unshaded circles are the protons and neutrons, respectively. 47
3.2 (color) The target magnet box. Shown are the direction of holding field and elements of EPR, Spectrum Analyzer and NMR. 50
3.3 (color) The target setup within the box. The figure is not to scale. The polarizing optics are shown offset to the right of their actual position (which is above the coils on the right in the figure) for clarity. The numbers correspond to various target positions: 1. the Polarized ^{3}He target position; 2. the empty target position; 3. the carbon foils (optics target) position and 4. the reference cell position. The target ladder and other support systems are not shown. The beam enters the box at 30° to the side of the box (see Figure 3.2). 51
3.4 Cell geometry and dimensions. 54
3.5 (color) Subfigure (a) shows how Rb is optically pumped (in this case into the $m_F = +3$ state) and subfigure (b) shows the 2-step process of spin-exchange first from rubidium to potassium and then from potassium to ^{3}He. 56
3.6 (color) The sense of circular polarization of laser light and selection rules. . 57
3.7 (color) The spin-up curves for target cell Edna. The two plots correspond to the up and down sweeps of NMR polarimetry method (See section 3.6). . . 58
3.8 5-1 Combiner 60
3.9 The laser beam Gaussian parameters. Laser light went through a 75 m long optical fiber. w_0 is the beam waist, $z_0 = \frac{\pi w_0^2}{\lambda}$ is the Rayleigh range, θ is the beam divergence, $\Theta = 2\theta$ is the total beam spread from the waist position and $b = 2z_0$ is the confocal parameter. (Figure from Wikipedia.) 61
3.10 Data from setup to determine Gaussian beam parameters for a set of optical components. 62
3.11 The polarizing optics setup. 63
3.12 Degree of circular polarization for the laser light. 64
3.13 Spectrum Analyzer output seen on the main target monitor. 65
3.14 The NMR setup. 68

3.15 A typical NMR resonance fitted to the square root of a Lorentzian. This plot is for the up sweep (see text for explanation). 69
3.16 The EPR setup. The RF coils, photodiode with D_2 filters and the EPR RF amplifier were in the Hall; the rest were in the Counting House. 72
3.17 The EPR PI feedback circuit diagram. [Romalis, 1997] 73
3.18 (a) The EPR *error signal* and (b) various states during an EPR flip. See text for explanation. 74
3.19 (color) EPR spectrum during G_E^n. Region I is before the ^{3}He spin flip, Region II, after and Region III brings the system back to its original configuration. 75
3.20 ^{3}He polarization measured with EPR in the pumping chamber. This plot shows select EPR numbers over a period of a month from mid-March to mid-April. EPR was done about once a day during this period. (The three values between days 8 and 9 indicate three EPRs were done on that day.) 76
3.21 A cartoon representation of the NMR-EPR calibration procedure. 77
3.22 (color) Polarization results for target cell Edna. The drops in polarization indicate periods of change in kinematics during which target tests were done. 77
3.23 (color) The G_E^n compass. The guiding bar and spacer are not shown in a). . 79
3.24 Construction of the G_E^n compass. (Sectional view through center.) 80
3.25 (color) The determination of angle between the magnetic axis and mirror. The ellipse is a result of the 360°scan of the cylinder (as shown on the right). 81
3.26 The absolute measurement setting. Note that for reflection off the compass mirror, the reference mirror bar was removed. The compass position along the beamline in this figure corresponds to hole #7 shown in Figure 3.27. . . 82
3.27 The positions of the compass and the corresponding laser spots during scanning. See text for explanation. The 4″ spacer position corresponded to the beamline. 84
3.28 The target region scanned by the compass. The result of the scan as shown in Figure 3.29 corresponds to the middle point in the lower figure. Figure from [Beck *et al.*, 2007]. 85
3.29 The compass results indicating the deviation of the target holding field along the length of the target. The angle at 0 is relative to the beam direction. The fit is performed only over the range of the target length. The scans at other positions (in both the horizontal and vertical planes as seen in Figure 3.28) had the same structure and the readings were within 1 mrad of these values. The deviation of the field in the same direction on both sides of the target center is explained in Figure 3.30. 87
3.30 The angle the target cell made with the holding field causes the angle to change in the same direction on either side of the target center. 88

4.1 The Neutron Detector. (Figure is to scale and does not show the lead or iron shielding.) The neutrons come in from the left in the figure. (Figure taken from the collaboration's technical drawings.) 91
4.2 BigBite spectrometer stack. 94
4.3 The three coordinate systems used in the experiment. Figures from [Craver, 2007b]. 94
4.4 Pre-shower detector separating out pions and electrons. [Riordan, 2007] . 97
4.5 Pulsed beam scattering off a hydrogen target: Matching of the BigBite scintillator timing to the pulsed beam phase. 100

4.6 Pulsed beam scattering off a hydrogen target: Matching of the Neutron Detector plane N1 timing to the pulsed beam phase. 101
4.7 Pulsed beam scattering off a nitrogen target: Matching of the BigBite scintillator timing to the pulsed beam phase. 102
4.8 Oscilloscope view of the G^0 helicity structure used during the G_E^n experiment. MPS is the master pulse which acts as the gate and, with a 2 μs delay, as the LNE signal. The LNE loads data into the helicity scaler. QRT is the quartet signal which denotes the beginning of the HEL (= helicity) signal. The first state of the helicity quartet signal is chosen pseudo-randomly using software. [Michaels, 2006] 103
4.9 Scaler circuit diagram and channels. (1) and (2) are two example signals fed into the scalers. NORM is the normalization scaler and TIR is the Trigger Interrupt Register. The scaler counts are displayed in real-time and can be converted into rates using the 105kHz clock on board the scaler modules. . 104
4.10 BPM calibration. For the lower plots, the $x-$ and $y-$axes represent corresponding raster sizes. The upper plots show the projections on the respective axes separately. 106

5.1 Schematic representation of a particle traversing two consecutive scintillator paddles. 108
5.2 Time-walk effect and correction. The scintillator left time differences in the lower plot are linear (constant) after the correction. 109
5.3 The average-time alignment for two consecutive BB scintillator paddles. . . 110
5.4 Resolution for comparison of timing of two adjacent paddles. Note that this resolution is for two paddles; the resolutions for single paddles are better than seen in the figure by a factor of $\sqrt{2}$. 110
5.5 The Neutron Detector showing a neutron event. The blue "hits" show the path of a neutron cluster through the detector scintillators. 113
5.6 BigBite scintillator correlation with the beam RF phase for all planes. (This plot is for production run 4364.) 115
5.7 The number of tracks discarded by the BigBite tracking algorithm. There were upto six tracks present for some events. 116
5.8 MCEEP: An "infinite" ND is considered (much larger than the real ND dimensions). The top left plot has no perpendicular missing momentum cuts whereas the one on the top right has $P_{mperp} < 150$ MeV/c. The black outline is the position and size of the real Neutron Detector. The lower two plots show the horizontal and vertical angular spread of the neutrons. All variables are defined within the laboratory coordinate system. 120
5.9 MCEEP: Number of events with different ND sizes - horizontal and vertical independently - with $P_{mperp} < 150$ MeV/c cut. 121
5.10 MCEEP: Number of neutrons accepted as a function of the horizontal and vertical size of the ND. The vertical line in both plots indicates the size (along the corresponding axis) of the real ND. These plots show that the real ND accepts about 87% of neutrons scattered from the target. 122
5.11 MCEEP: Comparing nitrogen reference cell data with oxygen $1s_{\frac{1}{2}}$ from MCEEP. This was mainly to check the efficiencies and spatial acceptances as a function of perpendicular missing momentum (phase space). 123

5.12 Internal radiative correction plots by MCEEP. The plot show the angle between the outgoing hadron and $\vec{q}$. 126
5.13 W vs. perpendicular missing momentum for kinematic #4. 127
5.14 G_E^n at $Q^2 = 1.7$ (GeV/c)^2. $G_E^n = 0.03457 \pm 0.007239\%$. (Preliminary result.) 128
5.15 The variation of the raw asymmetry as a function of the perpendicular missing momentum cut, P_{mperp}. We see that, within errors, the asymmetry does not change, implying that the electrons at these momenta do indeed scatter off the neutrons. This plot is for one run only. 129

F.1 The distance upstream where the normal to the front face of the ND was pointing during kinematic #4. 147

CHAPTER 1: INTRODUCTION AND THEORY

1.1 Introduction

1.1.1 Neutrons

Neutrons were first discovered by Bothe and Becker in 1930 and were explained and identified in 1932 by Chadwick which earned him the Nobel prize. Although the neutron has been extensively studied since its discovery, a lot about it remains unknown, examples being the electric charge distribution within and the electric dipole moment. The proton, on the other hand, has been better studied than the neutron. The difficulty - and hence the fascination - with studying the neutron is that it is a neutral composite particle which is unstable outside the nuclear medium. Advances in technology now enable us to use methods previously unavailable to unlock the mysteries that the neutron holds. The neutron experiences all four fundamental forces in strengths accessible via today's experimental methods and thus is a fascinating object to either study itself or to use as a probe to study other materials.

In this document, we delve into the study of the neutron's electric charge distribution via electron scattering.

1.1.2 Electron Scattering

High energy electron scattering is a valuable probe for studying structures of objects however small. Electrons are elementary (*structureless, pointlike*) particles implying there are no complicated structures of the *probe* to worry about. They penetrate dense systems and reach their interior without significant absorption thus enabling to accurately measure the spatial charge and current densities. They are very light and charged and thus are easily accelerated to high energies for resolving structure to smaller length scales, and it is easy to deflect them by electric and magnetic fields. Electron scattering thus can be viewed as a high resolution microscope for nucleon and nuclear structure.

1.2 Nucleon Structure

1.2.1 Theoretical description

The non-relativistic Rutherford cross-section for an electron of kinetic energy E scattering off an atomic nucleus of charge Ze is given by

$$\left(\frac{\mathrm{d}\sigma}{\mathrm{d}\Omega}\right)_{\text{Rutherford}} = \frac{(Ze^2)^2}{(4\pi\epsilon_0)^2 \cdot (4E)^2 \sin^4 \frac{\theta_e}{2}}, \tag{1.1}$$

where θ_e is the electron scattering angle. This formula is obtained by neglecting the spatial distribution of the target particle. When we include relativistic effects, the above scattering formula becomes (in terms of the fine structure constant α)

$$\left(\frac{\mathrm{d}\sigma}{\mathrm{d}\Omega}\right)_{\text{Rutherford}} = \frac{Z^2\alpha^2(\hbar c)^2}{4E^2 \sin^4 \frac{\theta_e}{2}}\,. \tag{1.2}$$

Here, $\hbar$ and c are the Planck's constant and speed of light, respectively. At relativistic energies, however, the Rutherford cross-section is modified by spin effects. Once the effects due to the electron spin are included, we get the *Mott cross-section*

$$\left(\frac{\mathrm{d}\sigma}{\mathrm{d}\Omega}\right)^*_{\text{Mott}} = \left(\frac{\mathrm{d}\sigma}{\mathrm{d}\Omega}\right)_{\text{Rutherford}} \cdot \left(1 - \beta^2 \sin^2 \frac{\theta_e}{2}\right), \tag{1.3}$$

where $\beta = \frac{v}{c}$. The asterisk indicates that the recoil of the nucleus has been neglected (infinite mass).

1.2.2 Nucleon Form Factors

Equation 1.3 above is derived for an infinite mass target and no spatial electric or magnetic distribution. But in reality, the energies used to probe these nuclei are comparable to their masses making recoil effects important. The Mott cross-section then becomes

$$\sigma_{\text{M}} \equiv \left(\frac{\mathrm{d}\sigma}{\mathrm{d}\Omega}\right)_{\text{Mott}} = \left(\frac{\mathrm{d}\sigma}{\mathrm{d}\Omega}\right)^*_{\text{Mott}} \cdot \frac{E'}{E}, \tag{1.4}$$

where E and E' are the electron energies before and after the collision. Also, in the infinite mass target case, three-momentum transfer could be used in the formulae since there was no energy loss of the electron in the scattering process. In this case, however, since recoil effects are significant, four-momentum transfer needs to be used.

$$q^2 = (p - p')^2 = 2m_e^2 - 2\left(EE' - |\vec{p}||\vec{p'}|\cos\theta_e\right) \tag{1.5}$$

$$\approx -4EE' \sin^2 \frac{\theta_e}{2} \tag{1.6}$$

The four-momentum squared is a Lorentz-invariant quantity. In order to work with positive quantities, we define $Q^2 := -q^2$. Furthermore, the interaction of the electron current with the nucleon's magnetic moment needs to be taken into account as well. For a spin-$\frac{1}{2}$ point particle (a *Dirac particle*), the magnetic moment is given by

$$\mu = g \cdot \frac{e}{2M} \cdot \frac{\hbar}{2} \tag{1.7}$$

where M is the mass of the particle. For a point (Dirac) particle, $g = 2$ as predicted from the Dirac equation (relativistic quantum mechanics). The cross-section now reads

$$\left(\frac{\mathrm{d}\sigma}{\mathrm{d}\Omega}\right)_{\text{point, spin}\frac{1}{2}} = \left(\frac{\mathrm{d}\sigma}{\mathrm{d}\Omega}\right)_{\text{Mott}} \cdot \left[1 + 2\tau \tan^2 \frac{\theta_e}{2}\right] \tag{1.8}$$

where[1] $\tau = \frac{Q^2}{4M^2}$. However, the nucleons are not Dirac particles but have an internal structure ($g \neq 2$).

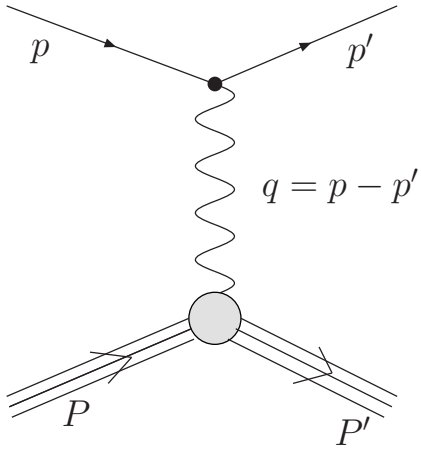

Figure 1.1: Feynman diagram for the scattering of an electron with 4-momentum $p \equiv (E_e, \vec{p})$ off a nucleon of mass M_N and 4-momentum P. The diagram depicts a single photon exchange, whose 4-momentum is $q = p - p' \equiv (\omega, \vec{q})$. The primes represent scattered particles.

Figure 1.2 shows the scattering of electrons off nucleons in the one photon exchange or Born approximation. The amplitude for elastic scattering can be written as the product of the leptonic current, ℓ_μ and hadronic current, $\mathcal{J}_\mu$ as

$$i\mathcal{M} = \frac{-ig_{\mu\nu}}{q^2} \left[ie\overline{u}(k')\gamma^\nu(k)\right] \left[ie\overline{N}(p')\Gamma^\mu(p)\right] = \frac{-i}{q^2}\ell_\mu \mathcal{J}^\mu \,, \tag{1.9}$$

[1]Henceforth, we will use *natural* units in which $\hbar = c = 1$.

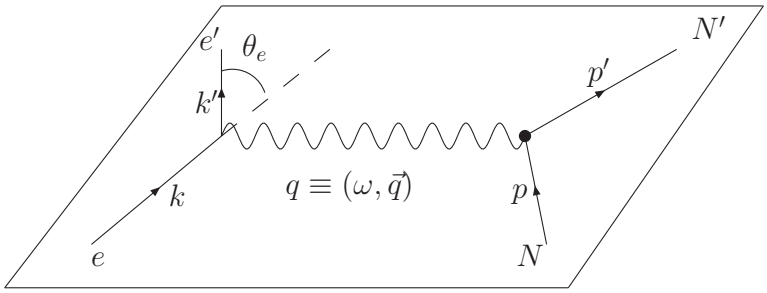

Figure 1.2: The scattering diagram in the lab frame for a one-photon exchange reaction. θ_e is the electron scattering angle and q^2 is the 4-momentum transferred to the nucleon.

where Γ^μ contains all information about the nucleon structure, u and N are the electron and nucleon spinors, respectively, $g_{\mu\nu}$ is the metric tensor[2] and k, k', p and p' are the initial and final 4-momenta of the electron and nucleon, respectively. The electromagnetic current at the nucleon vertex, $\mathcal{J}_\mu$ reads

$$\mathcal{J}_\mu(p', s'; p, s) = \bar{N}(p', s')\Lambda_\mu(q, p)N(p, s) \tag{1.10}$$

$$= \bar{N}(p', s')\left(\gamma_\mu F_1(q^2) + \frac{1}{2M} i\sigma_{\mu\nu}q^\nu F_2(q^2)\right) N(p, s)\,. \tag{1.11}$$

This is a vector current since the photon is a spin one (vector) particle[3]. Here, the spin-dependent structure function F_2 is called the Pauli form factor and is an indicator of deviation from a pointlike Dirac particle nature. The cross section for scattering off such a particle is

$$\frac{\mathrm{d}\sigma}{\mathrm{d}\Omega} = \frac{\overline{|\mathcal{M}|}^2}{64\pi^2}\left(\frac{E'}{E}\right)^2 \frac{1}{M} \tag{1.12}$$

$$= \sigma_M\left(F_1^2(Q^2) + \tau F_2^2(Q^2) + 2\tau[F_1(Q^2) + F_2(Q^2)]^2 \tan^2(\theta_e/2)\right) \tag{1.13}$$

where $\overline{|\mathcal{M}|}^2 = \frac{1}{Q^2}\overline{|\ell \cdot \mathcal{J}|}^2$, $\tau = Q^2/4M^2$, $\sigma_M \equiv (\frac{\alpha\cos(\theta_e/2)}{2E_e \sin^2(\theta_e/2)})\frac{E'}{E}$ is the Mott cross-section as in Equation 1.4. We now define G_E and G_M, the electric and magnetic form factors,

[2]We shall always use the metric tensor

$$g_{\mu\nu} = \begin{pmatrix} 1 & 0 & 0 & 0 \\ 0 & -1 & 0 & 0 \\ 0 & 0 & -1 & 0 \\ 0 & 0 & 0 & -1 \end{pmatrix}$$

[3]This intermediate photon has to be a virtual photon. It cannot correspond to a real photon since a free particle cannot absorb or emit such a photon and $q^2 = (p' - p)^2 < 0$.

respectively, as

$$G_E(Q^2) = F_1(Q^2) - \tau F_2(Q^2); \qquad G_E^p(0) = 1; \quad G_E^n(0) = 0; \tag{1.14}$$

$$G_M(Q^2) = F_1(Q^2) + F_2(Q^2); \qquad G_M^p(0) = \mu_p; \quad G_M^n(0) = \mu_n; \tag{1.15}$$

These are known as the *Sachs* form factors [Sachs, 1962]. Using these definitions, we can re-write Equation 1.12 as the so-called Rosenbluth formula:

$$\frac{\mathrm{d}\sigma}{\mathrm{d}\Omega} = \sigma_M \left[\frac{(G_E)^2 + \tau (G_M)^2}{1+\tau} + 2\tau (G_m)^2 \tan^2\left(\tfrac{\theta_e}{2}\right) \right] \tag{1.16}$$

$$= \frac{\sigma_M}{\epsilon(1+\tau)} \left[\tau G_M^2(Q^2) + \epsilon G_E^2(Q^2) \right] \tag{1.17}$$

where $\epsilon = 1/[1 + 2(1+\tau)\tan^2(\theta_e/2)]$ is the virtual photon polarization parameter. G_E and G_M are the electric and magnetic form factors respectively. This equation shows that G_E and G_M can be determined separately by measuring cross sections at fixed Q^2 as a function of ϵ over a range of (θ_e, E) combinations (Rosenbluth Separation method).

Form factors are an important gauge of a hadron's structure. They are measurable and a physical manifestation of the nature of the hadron's constituents and the dynamics that binds them together. An virtual photon of 3-momentum $\vec{q}$ resolves the hadron structure on a length scale $d \sim 1/|\vec{q}|$ [Arrington *et al.*, 2006]. For *heavy* targets ($|\vec{q}| \ll M$), where recoil effects are small, form factors can be interpreted as charge and current distributions within the nucleon (see Section 1.2.2), the radii[4] given by

$$\langle r_{E,M}^2 \rangle = \frac{-6}{G_{E,M}(0)} \left[\frac{\mathrm{d}}{\mathrm{d}Q^2} G_{E,M}(Q^2) \right]_{Q^2=0} . \tag{1.18}$$

We see that the radii equal the slopes of the corresponding form factors at $Q = 0$. For the proton, in the neighborhood of $Q^2 = 0$,

$$\mu_p \frac{G_E^p(Q^2)}{G_M^p(Q^2)} = 1 - \frac{Q^2}{6} \left[(r_p)^2 - (r_p^\mu)^2 \right] \tag{1.19}$$

where r_p and r_p^μ are the electric and magnetic radii of the proton, respectively. We see that, experimentally, $r_p \approx r_p^\mu$ which explains the data near 1 in the range $Q^2 \in (0, 0.6)$ $(\mathrm{GeV}/c)^2$ (Figure 1.3). This region is affected by the proton's pion cloud, that is, at lower Q^2, the *cloud* of quark-antiquark pairs (the *pions*) that spontaneously appear and disappear in the region surrounding the "core" of the proton. Ignoring the pions, one finds $r_p > r_p^\mu$, and

[4] If $G(0) = 0$, the normalizing factor is omitted [Sachs, 1962, Ernst *et al.*, 1960, Dombey, 1969]

thus the ratio above falls[5] with increasing Q^2. In the case of the neutron,

$$\mu_n \frac{G_E^n(Q^2)}{G_M^n(Q^2)} = -\frac{r_n^2}{6} Q^2, \tag{1.20}$$

where r_n is the neutron's electric charge radius. [Bhagwat *et al.*, 2006] shows this to be a good approximation for $r_n^2 Q_n^2 \lesssim 1$. Data from [Madey *et al.*, 2003] are consistent with Equation 1.20 suggesting that, at small Q^2, the ratio's behavior is affected by the neutron's pion cloud. [Bhagwat *et al.*, 2006] also predicted that this ratio will continue to increase steadily until $Q^2 \simeq 8\ (\mathrm{GeV}/c)^2$. Discussion with respect to data from the current experiment appears in Chapter 6.

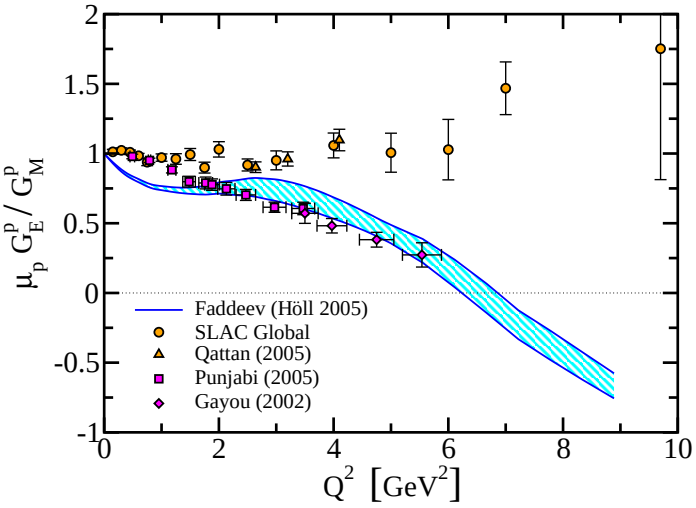

Figure 1.3: Ratio of proton form factors [Arrington *et al.*, 2006].

Physical Interpretation of Form Factors

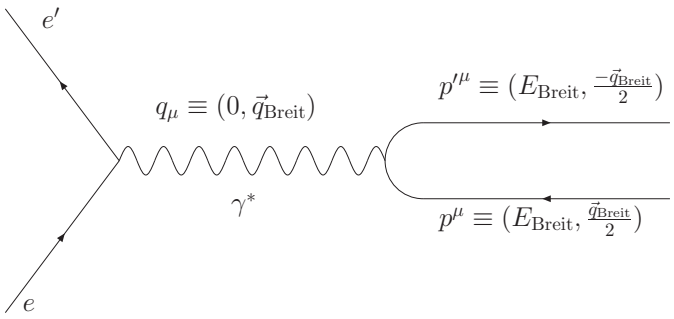

Figure 1.4: Schematic representation of the Breit frame

[5] At higher Q^2, a deeper region within the nucleon is probed, thus resolving valence quark structure.

So far, we have only used form factors in momentum space, which is sufficient to describe observed phenomena. However, a somewhat useful and more intuitive physical interpretation can be given by regarding them as Fourier transforms of certain functions of the space coordinates. To this end, we take a frame of reference in which $\vec{P} = \vec{p} + \vec{p'} = 0$ where $P \equiv (P^0, \vec{P})$. This is called the *Breit frame*. Referring to Figure 1.4, $p \equiv (E_1, \frac{\vec{q}_{\text{Breit}}}{2})$, $p' \equiv (E_2, -\frac{\vec{q}_{\text{Breit}}}{2})$, $E_1 = E_2 = E_{\text{Breit}}$, so that $P^0 = 2E_{\text{Breit}}$, and the components of the 4-vector $q \equiv (0, \vec{q}_{\text{Breit}})$. Thus, only momentum is transferred to the nucleon but not energy. From this we can see that the form factor $F(-q^2)$ can be interpreted as the Fourier transform of a static distribution of electric charge and magnetization densities, respectively,

$$\rho_{ch}(\vec{r}) = \frac{1}{(2\pi)^3} \int G_E(-q^2) e^{i\vec{q}\cdot\vec{r}} \mathrm{d}^3 q \tag{1.21}$$

$$\mu\rho_{mag}(\vec{r}) = \frac{1}{(2\pi)^3} \int G_M(-q^2) e^{i\vec{q}\cdot\vec{r}} \mathrm{d}^3 q \tag{1.22}$$

A Breit frame always exists[6] since $P^2 > 4M^2 > 0$. An interpretation of the form factors in terms of a pion cloud and constituent quarks is given by Friedrich and Walcher [Friedrich and Walcher, 2003] with plots for densities in coordinate space (in the Breit frame) for various models (see Section 1.3.3).

1.2.3 Quasi-elastic Scattering

For elastic scattering off free nucleons at rest, for a given beam energy E and a fixed electron scattering angle θ_e, the scattered electrons always have a definite energy E' given by

$$E' = \frac{E}{1 + \frac{E}{M}(1 + \cos\theta_e)}\,, \tag{1.23}$$

where M is the nucleon mass. But when we scatter off nucleons in a nucleus (with more than one nucleon), we observe a more complicated energy spectrum. The energy peak in this case is shifted along the E' axis and is widened. In Figure 1.5, this peak is clearly identified. This process is called *quasi-elastic scattering*.

Both the shift and broadening of the quasi-elastic energy spectrum contain information about the internal structure of the atomic nucleus. In Plane Wave Impulse Approximation

[6] In the Breit frame, $p_{\text{Breit}} \equiv (E_{\text{Breit}}, \pm\vec{q}_{\text{Breit}}/2)$, for the initial and final nucleon 4-momenta respectively, thus $q_{\text{Breit}} \equiv (0, \vec{q}_{\text{Breit}})$. In the lab frame, initial 4-momentum $p \equiv (M, \vec{0})$ and 4-momentum transferred $q \equiv (\omega, \vec{q})$ giving a final 4-momentum $p \equiv (M + \omega, \vec{q})$. Lorentz invariance of Q^2 then implies $Q^2 = \vec{q}^{\,2}_{\text{Breit}} = \vec{q} - \omega^2 = 2M\omega$. Thus,

$$Q^2 = \vec{q}^{\,2}_{\text{Breit}} = \frac{\vec{q}^{\,2}}{1 + \tau}\,.$$

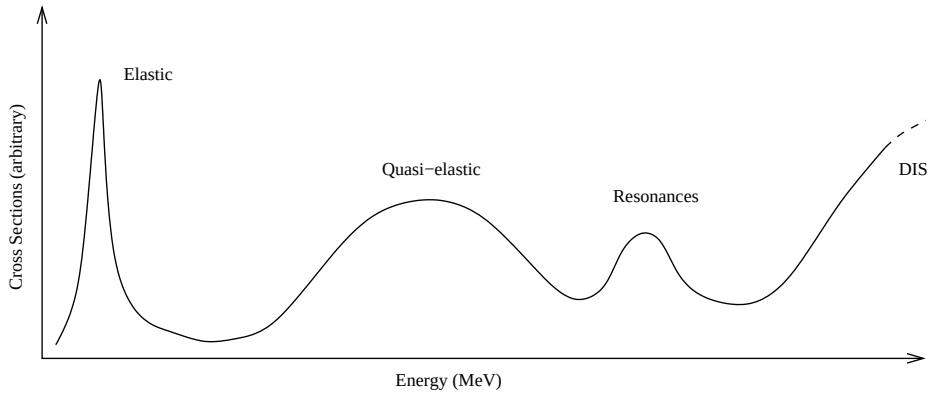

Figure 1.5: A cartoon representation of the scattered energy spectrum from various processes in electron-nucleon scattering. The positions on the energy axis and the widths of the peaks are approximate. The height of the elastic peak is largely reduced.

(PWIA) we assume that the virtual photon interacts with only the nucleon and the rest of the nucleus is only a spectator. The shift of the maxima in the energy towards lower energies is due to the energy required by the struck nucleon to be removed from the nucleus - its binding energy. The broadening is caused due to the fact that the various nucleons within the nucleus are not stationary but moving around "quasi-freely" within the nucleus, with (Fermi-) momenta[7] of up to 250 MeV/c. This motion brings about a change in the kinematics as compared to the free, stationary nucleon case.

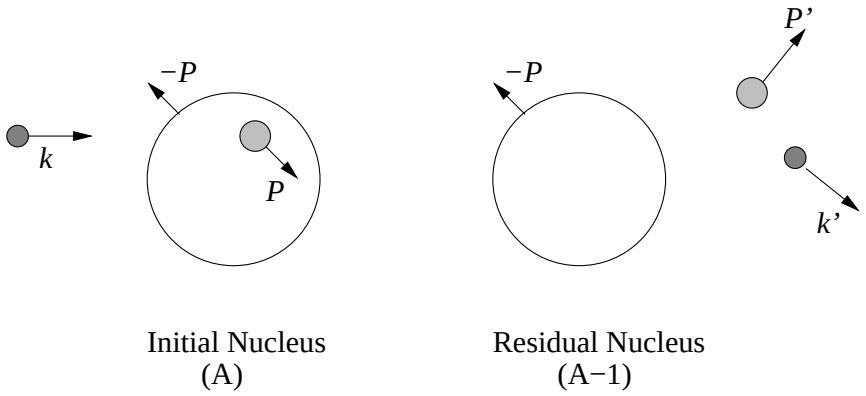

Figure 1.6: Quasi-elastic scattering in the PWIA.

Consider a bound nucleon moving with momenutm $\vec{P}$ (Figure 1.6) in an effective nuclear potential of strength S. This nucleon's binding energy is $S-|\vec{P}|/2M$ after neglecting residual interactions with other nucleons. When an electron of initial momentum $\vec{k}$ scatters off this

[7]Fermi momenta, $p_F \approx 250$ MeV for nuclei of high atomic numbers. See Appendix A.

nucleon, we have

$$k + P = k' + P' \tag{1.24}$$

$$\vec{P'} = \vec{q} + \vec{P}\,, \tag{1.25}$$

where the first equation states the 4-momentum conservation for the $e - N$ system and the second one states the momentum conservation for the $\gamma - p$ system, $\vec{q}$ is the momentum transfer 3-vector and the primed variables represent scattered particles. The energy transfer ν from the electron to the nucleon (for $E, E' \gg m_e$ and $|\vec{P}|, |\vec{P}| \ll M$) is given by

$$\nu = E - E' = \left(M + \frac{|\vec{P'}|^2}{2M}\right) - \left(M + \frac{|\vec{P}|^2}{2M} - S\right) \tag{1.26}$$

$$= \frac{(\vec{P} + \vec{q})^2}{2M} - \frac{|\vec{P}|^2}{2M} + S \tag{1.27}$$

$$= \frac{|\vec{q}|^2}{2M} + S + \frac{2|\vec{q}||\vec{P}|\cos\alpha}{2M}\,, \tag{1.28}$$

where α is the angle between $\vec{q}$ and $\vec{P}$. Now, assuming an isotropic (spherically symmetric) distribution of nucleon motion leads to a symmetric distribution for ν about an average value

$$\nu_0 = \frac{|\vec{q}|^2}{2M} + S \tag{1.29}$$

with a width

$$\sigma_\nu = \sqrt{\langle(\nu - \nu_0)^2\rangle} = \frac{|\vec{q}|}{M}\sqrt{\langle|\vec{P}|^2\cos^2\alpha\rangle} = \frac{|\vec{q}|}{M}\sqrt{\frac{1}{3}\langle|\vec{P}|^2\rangle}\,. \tag{1.30}$$

1.2.4 World data so far

Figures 1.7(a), 1.7(b), 1.7(c) show the world data for G_E^p, G_M^p, and G_M^n, respectively. All data are normalized to the dipole form factor

$$G_D = \frac{1}{(1 + \frac{Q^2}{\Lambda^2})} \tag{1.31}$$

with $\Lambda = 0.84$ (GeV/c)^2 and Q is in GeV. This dipole parametrization corresponds to two poles with opposite sign close to each other in the time-like regime. In coordinate space, G_D corresponds to exponentially decreasing radial densities for charge and magnetization (but with a non-physical discontinuity at the origin). The existing world data for G_E^n from polarized experiments are shown in Figures 1.8 and 1.9.

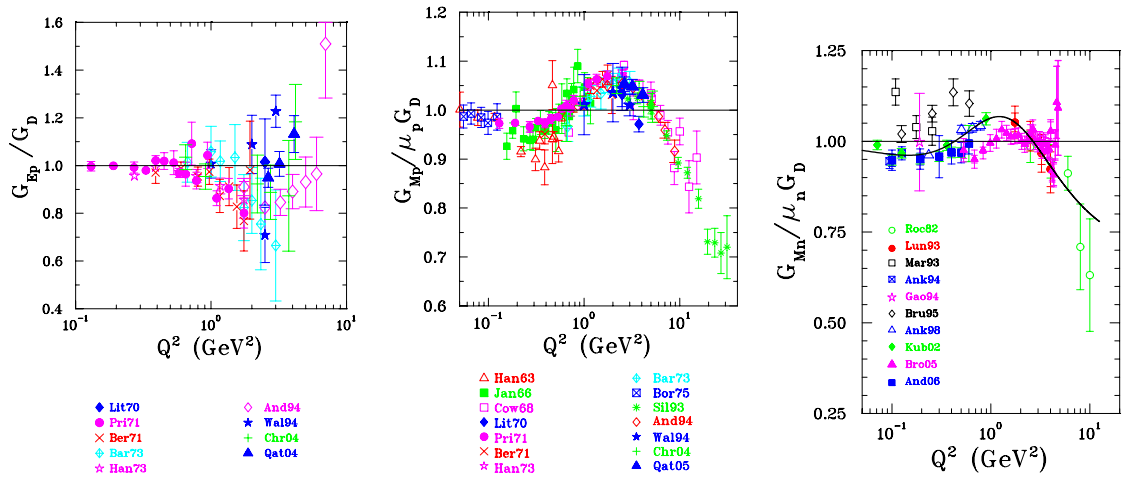

(a) The proton magnetic form factor.

(b) The proton magnetic form factor.

(c) The neutron magnetic form factor. The solid curve is a fit by J. J. Kelly.

Figure 1.7: The various form factors of nucleons. These are normalized to the dipole form factor.

1.3 Theory Models

1.3.1 Perturbative QCD

At very high Q^2 - a few GeV and higher (or equivalently, at very small distances - smaller than a nucleon), the strong coupling constant, $\alpha_s \rightarrow 0$ i.e. the quarks are essentially "free" thus permitting the use of perturbative QCD techniques as the theory becomes asymptotically free. The nucleon electromagnetic form factors provide a good test for pQCD.

At sufficiently high Q^2, a virtual photon will see a nucleon consisting of three massless quarks moving collinearly with the nucleon. For elastic scattering, the final state again consists of three massless quarks moving collinearly with the nucleon, which is an unlikely process at these momentum transfers. In order for this to happen, the large momentum of the virtual photon has to be transferred to the three quarks through two hard gluon exchanges (Figure 1.10). This hard scattering mechanism is generated by valence quark configurations with small transverse size and finite momentum fraction carried by each valence quark. The amplitude for the hard scattering process can be factorized as a product of a perturbatively calculable hard scattering amplitude and two distribution amplitudes describing the way the large longitudinal momentum of the initial and final nucleons is shared between their constituents. Each gluon in such a hard scattering process carries a

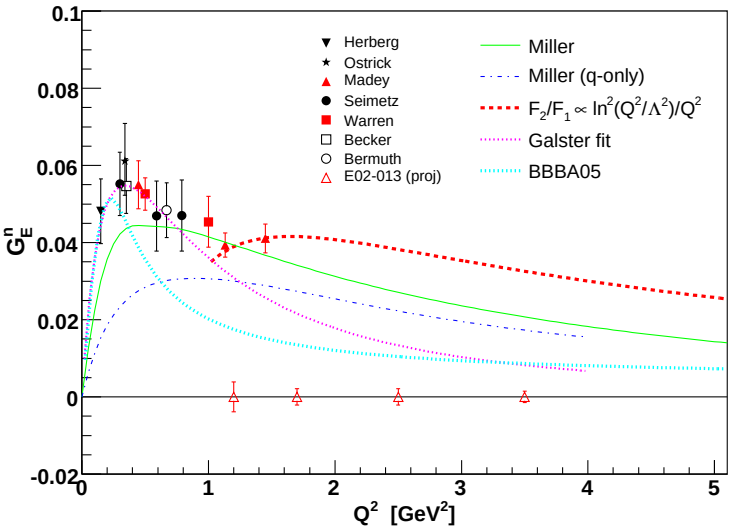

Figure 1.8: World data for double polarized experiments for G_E^n.

virtuality proportional to Q^2. This leads to the prediction [Brodsky and Farrar, 1975] for the helicity conserving Dirac form factor in elastic electron-hadron scattering that

$$F_1 \sim (Q^2)^{1-n_h} \tag{1.32}$$

where n_h denotes the number of quark fields in the hadron. Thus, in the quark model, $F_1 \sim 1/Q^2$ for mesons and $F_1 \sim 1/Q^4$ for baryons. The Pauli form factor, F_2, on the other hand, involves a helicity flip between the initial and final nucleons. It thus requires a helicity flip at the quark level, which is suppressed at large Q^2. Therefore, for quarks moving collinearly with the final nucleon, pQCD predicts a $1/Q^6$ fall-off for F_2 at high Q^2.

The experimental results, however, did not follow these predictions (unlike the Rosenbluth data). Instead it was found that QF_2/F_1, and not Q^2F_2/F_1 as predicted by pQCD, is constant at high Q^2. The $1/Q$ prediction by Miller [Miller and Frank, 2002] was in excellent agreement at intermediate Q^2 range. He observed that imposing Poincaré invariance removes the pQCD condition that the transverse momentum should be zero and introduces a quark orbital angular momentum in the proton wave function. It was observed that the Q^2 behavior in the polarized data implies significant contribution from the quark orbital angular momentum [Hyde-Wright and de Jager, 2004]. Among recent developments in this domain [Brodsky *et al.*, 2004, Belitsky *et al.*, 2003], Belitsky *et al.* have

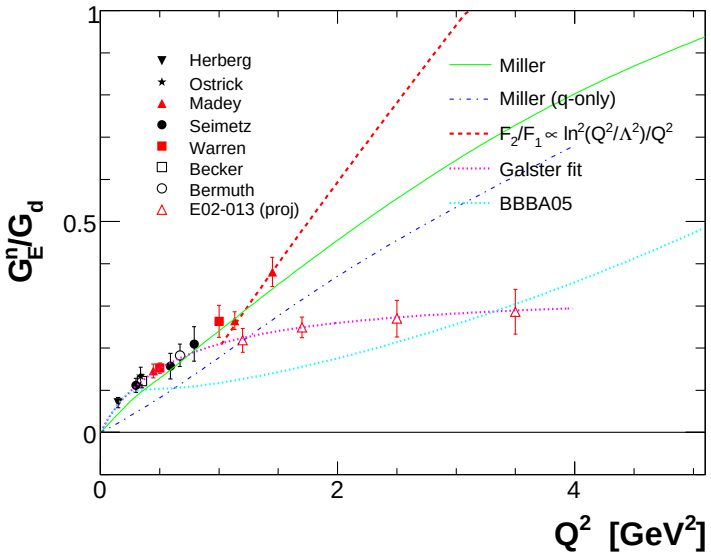

Figure 1.9: World data for double polarized experiments for G_E^n/G_d.

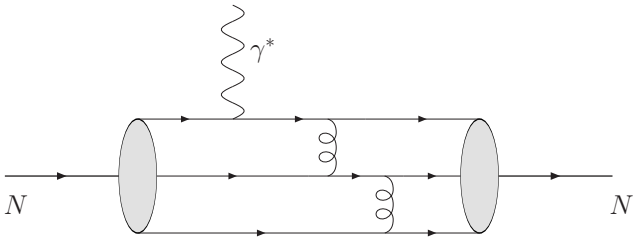

Figure 1.10: pQCD picture for the nucleon EMFFs. The highly virtual photon sees the three-quark states of the nucleon. The large momentum is transferred between the quarks through two successive gluon exchanges.

the following large Q^2-behavior [Belitsky *et al.*, 2003]:

$$\frac{F_2}{F_1} \propto \frac{\ln^2 Q^2/\Lambda^2}{Q^2} \tag{1.33}$$

where Λ is a soft scale related to the size of the nucleon. Belitsky *et al.* warn that this could be precocious since pQCD is not expected to be valid at such low Q^2. Brodsky *et al.* [Brodsky *et al.*, 2004] argue that a non-zero orbital angular momentum wavefunction should contribute to both F_1 and F_2 and thus Q^2F_2/F_1 should still be asymptotically constant.

1.3.2 Vector Meson Dominance

Vector mesons that correspond to masses comparable to the nucleon masses are the ρ, ω and ϕ resonances. These have lifetimes from about 10^{-22} s to 10^{-24} s, which are typical of the

strong interaction [Povh *et al.*, 1999]. These quark-antiquark states must have the same quantum numbers as the virtual photon, that is, total angular momentum $J = 1$ and negative parity. One therefore expects that in the elastic electron scattering process on the nucleon, the nucleon EMFFs at low space-like momentum transfers will be dominated by these lowest lying singularities from the time-like region. A large class of models of F_1 and F_2 are based on this vector meson dominance (VMD) hypothesis. Figure 1.11 shows one

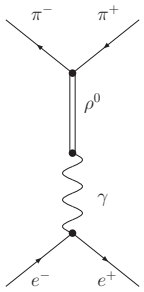

Figure 1.11: Systematic depiction of the production and decay of a resonance (in this case, a ρ^0 meson; see text for more).

of the resonances, the ρ^0 meson with a mass of 770 MeV/c^2. Two other mesons are the ω meson ($m_\omega = 782$ MeV/c^2) and the ϕ meson ($m_\phi = 1019$ MeV/c^2). The lighter two are mixed states of $u\bar{u}$ and $d\bar{d}$, whereas the heaviest of the three is an $s\bar{s}$ state.

In quantum field theory a meson (quark-antiquark bound state) appears as a pole in a four-point quark-antiquark Green's function, the residue of which is proportional to the Bethe-Salpeter amplitude determined by a homogeneous Bethe-Salpeter equation [Arrington *et al.*, 2006]. Analogously, a nucleon (three quark bound state) must appear as a pole in a six-point quark Green's function. Within such VMD models, the approximate dipole behavior of the nucleon EMFFs can be understood as being due to the contribution of two nearby vector meson poles of opposite residua. Consider two such poles as in Figure 1.11 with masses m_{V_1} and m_{V_1} and residua a and $-a$ respectively. We get [Perdrisat *et al.*, 2006]

$$F_{1,2}(q^2) \sim \frac{a}{q^2 - m_{V_1}^2} + \frac{(-a)}{q^2 - m_{V_1}^2} \tag{1.34}$$

$$= \frac{a(m_{V_1}^2 - m_{V_2}^2)}{(q^2 - m_{V_1}^2)(q^2 - m_{V_2}^2)} \tag{1.35}$$

An early VMD fit performed by Iachello *et al.* [Iachello *et al.*, 1973] predicted a linear decrease of the proton G_E^p/G_M^p ratio which is in agreement with the result from the polariza-

tion transfer experiments. These models have been extended by [Gari and Krümpelmann, 1985] to include pQCD scaling relations for the nucleon EMFFs (See Section 1.3.1).

More recently, good parametrization of all nucleon EMFFs have been obtained by using extended VMD fits. Lomon's fit uses $\rho(770)$, $\omega(782)$, $\phi(1020)$ and $\rho'(1450)$ mesons and contains 11 parameters. Another parametrization by [Bijker and Iachello, 2004] including only ρ, ω and ϕ mesons achieved a good fit by adding a phenomenological contribution attributed to a quark-like intrinsic qqq structure besides the vector-meson exchange terms. The pQCD scaling relations mentioned earlier are built into this fit which has six free parameters fit to data. In contrast to the earlier fit ([Iachello *et al.*, 1973]), this new fit ([Bijker and Iachello, 2004]) gives a very good description of the neutron data at the expense of a slightly worse fit for the proton data. We shall see from the results of this experiment if these VMD fits work well with the neutron EMFFs at higher $Q^2$and test its "prediction" that both F_1 and F_2 tend toward the same value for the proton and neutron.

1.3.3 Constituent Quark Models and Pion Cloud Models

Non-relativistic Constituent Quark Models (CQMs) describe nucleons as a ground state of a three-quark quantum mechanical system in a confining potential. Here the ground state baryons (consisting of up, down and strange quarks) are described by $SU(6)$ spin-flavor wavefunctions plus an antisymmetric color wavefunction.

Despite their relative success in describing the spectrum and structure of low-lying baryons, models based on constituent quarks alone suffer from evident shortcomings as they do not satisfy all symmetry properties of the QCD Lagrangian. In nature, the up and down (current) quarks are nearly massless. In the exact massless limit, the QCD Lagrangian is invariant under $\mathrm{SU}(2)_L \times \mathrm{SU}(2)_R$ rotations of left (L) and right (R) handed quarks in flavor space. This chiral symmetry is spontaneously broken in nature leading to the appearance of massless Goldstone modes. For two flavors, there are three Goldstone bosons pions, which acquire a mass due to the explicit breaking of chiral symmetry by the current quark masses.

Since pions are the lightest hadrons, they dominate the long-distance behavior of hadron wave functions and yield characteristic signatures in the low-momentum transfer behavior of hadronic form factors. Therefore, a natural way to qualitatively improve on the above-mentioned CQMs is to include the pionic degrees of freedom.

An early quark model with chiral symmetry is the chiral (or *cloudy*) bag model. This model improves the early MIT bag model by introducing an elementary, perturbative pion which couples to quarks in the bag in such a way that chiral symmetry is restored [Thomas, 1984]. Within the cloudy bag model, [Lu *et al.*, 1999] performed a calculation of the nucleon EMFFs improving upon previous calculations by applying a correction for the center-of-mass motion of the bag. This calculation also implemented Lorentz covariance in an approximate way by using a prescription for the Lorentz contraction of the internal structure of the nucleon. Using a bag radius R $\approx$ 1 fm, this model provides a good description of the nucleon EMFFs in the range $Q^2 < 1$ (GeV/c)^2.

To extend such a calculation to larger Q^2, Miller performed a light-front cloudy bag model calculation [Miller, 2002]. Starting from a model in terms of constituent quarks [Miller and Frank, 2002], described by the light-front wavefunction of Schlumpf, the effects of the pion cloud were calculated through one-loop diagrams, including relativistic πNN vertex form factors. The model gives a relatively good gobal account of the data both at low Q^2 and larger Q^2, though tends to show too much structure around the dipole form for the magnetic form factors at low Q^2.

[Miller, 2003] has defined spin-dependent quark densities as matrix elements of density operators in proton states of definite spin-polarization. Within a constituent quark picture, the spin-dependent density operator for a quark in the proton to be found at position $\vec{r}$ and with spin-direction $\hat{n}$ is given by

$$\hat{\rho}(\vec{r},\hat{n}) = \sum_i \frac{e_i}{e}\delta(\vec{r}-\vec{r_i})\frac{1}{2}(1+\sigma_i\cdot\hat{n}) \ , \tag{1.36}$$

where the sum runs over the three constituent quarks i with fractional charge e_i/e. Relative to the spin-direction $\hat{s}$ of the proton, Miller then studied the distribution of quarks for different quark spin orientations $\hat{n}$. The densities defined thus may become non-spherical as shown in [Miller, 2003]. Averaging over quark spin $\hat{n}$ or over nucleon spin $\hat{s}$ yields a spherical distribution.

1.3.4 Generalized Parton Distributions

The physical interpretation of EMFFs, as we have seen in (1.22) of subsection 1.2.2, is that their Fourier transforms give the static charge and magnetization densities within the nucleon in the Breit frame. But the initial and final nucleons have different momenta and

therefore, different wave functions because the relativistic boost operator that transforms a nucleon at rest into a moving one changes the wave function of the nucleon [Miller, 2007]. This change depends on the momentum of the nucleon. The presence of different wave functions of the initial and final nucleons renders the probability or density interpretation invalid. A proper determination of, e.g. a charge density requires that the quantity be related to the square of a wave function or a field operator. The technical solution to the problem of determining the relevant density operator has been known for a long time and has been explained recently in terms of Generalized Parton Distributions (GPDs).

Some Notation

The GPD formalism is understood best and intuitively in the *light-cone* coordinates. We define the system and our notation here [Diehl, 2003]. For any four-vector $v \equiv (v^0, v^1, v^2, v^3)$,

$$v^{\pm} = \frac{1}{\sqrt{2}}(v^0 \pm v^3), \qquad v_{\perp} = (v^1, v^2) \tag{1.37}$$

where the $\perp$ subscript will indicate two-dimensional transverse vectors.

Parton distributions have the simplest interpretation in the infinite momentum frame as the densities of the partons in the longitudinal momentum x. The light cone momentum p^+ becomes proportional to the momentum or energy of a particle in the infinite momentum frame where $p^3 \to +\infty$, but can be used to calculate in any convenient reference frame (e.g. the hadron rest frame). For GPDs we will use

$$P = \frac{p + p'}{2}, \quad \Delta = p' - p, \quad t = \Delta^2, \tag{1.38}$$

where p and p' are the incoming and outgoing hadron momenta. For $\gamma^* p$ collisions we will use

$$Q^2 \equiv -q^2, \quad W^2 = (p+q)^2, \quad x_B = \frac{Q^2}{2p \cdot q}, \tag{1.39}$$

where W is the invariant mass on the hadron side and x_B is the Bjorken x variable.

Basic concepts of GPDs

Hard reactions such as Deeply Virtual Compton Scattering (DVCS), qualitatively, allow us to remove in a controlled way a quark of one spin and flavor from a nucleon and implant another quark of in general, a different flavor and spin in the final nucleon. The DVCS process in the GPD language is illustrated in Figure 1.12. The shaded region, representing

the non-perturbative stage of such hard exclusive electroproduction processes is described by the GPDs ([Ji, 2004] and references therein). Refering to Figure 1.12, x is momentum-

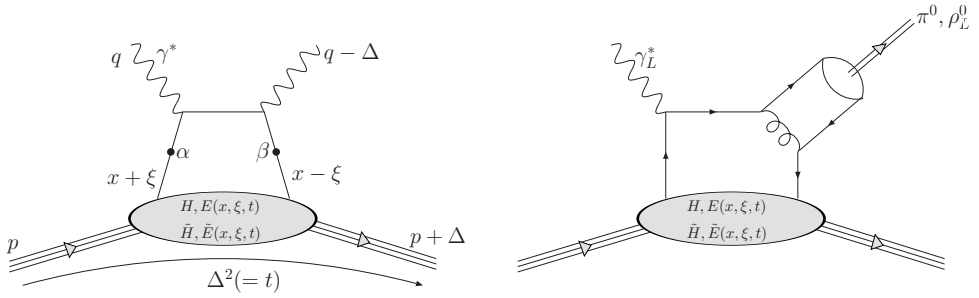

Figure 1.12: Schematic representation of deeply virtual exclusive processes, Compton Scattering and Meson Production (the *handbag* diagram)

fraction carried away by the quark, ξ is the skewness parameter and z is the direction of motion of the nucleon.

We define generalized quark distributions as

$$\begin{aligned} F_q &= \frac{1}{2}\int \frac{\mathrm{d}z^-}{2\pi}\, e^{ixP^+z^-} \langle p'|\bar{q}(-\frac{1}{2}z)\gamma^+ q(\frac{1}{2}z)|p\rangle\Big|_{z^+=0,z_\perp=0} \\ &= \frac{1}{2P^+}\left[H^q(x,\xi,t)\bar{u}(p')\gamma^+u(p) + E^q(x,\xi,t)\bar{u}(p')\frac{i\sigma^{+\alpha}\Delta_\alpha}{2M}u(p)\right], \qquad (1.40) \\ \tilde{F}_q &= \frac{1}{2}\int \frac{\mathrm{d}z^-}{2\pi}\, e^{ixP^+z^-} \langle p'|\bar{q}(-\frac{1}{2}z)\gamma^+\gamma_5 q(\frac{1}{2}z)|p\rangle\Big|_{z^+=0,z_\perp=0} \\ &= \frac{1}{2P^+}\left[\tilde{H}^q(x,\xi,t)\bar{u}(p')\gamma^+\gamma_5u(p) + \tilde{E}^q(x,\xi,t)\bar{u}(p')\frac{\gamma_5\Delta^+}{2M}u(p)\right], \qquad (1.41) \end{aligned}$$

where M is the hadron mass and q indicates quark flavor. The polarization dependence of the hadron states and spinors has not been displayed in the above equations. Due to Lorentz invariance, the GPDs $H^q, E^q, \tilde{H}^q$ and $\tilde{E}^q$ depend only on the kinematical variables x, ξ and t. This is the case where the partons do not transfer helicity[8].

Basic Properties of GPDs and Sum Rules

For $p = p'$ and equal helicities of the initial and final state hadrons, we obtain *reduction formulae* which define the ordinary spin independent density $q(x)$ and the spin dependent

[8]There are eight GPDs per quark flavor ($q = u, d, s$). Here we stick to only the helicity-conserving processes for quarks. GPDs for gluons also will not be discussed here. For a complete set of GPDs, see and of the References [Ji, 2004, Diehl, 2003, ?]

density $\Delta q(x)$ for the quarks

$$H^q(x,0,0) = \begin{cases} q(x) & \text{for } x > 0, \\ -\bar{q}(-x) & \text{for } x < 0 \end{cases} \tag{1.42}$$

$$\tilde{H}^q(x,0,0) = \begin{cases} \Delta q(x) & \text{for } x > 0, \\ \Delta\bar{q}(-x) & \text{for } x < 0. \end{cases} \tag{1.43}$$

The first moments of GPDs are constrained by the form factors of the electromagnetic and axial currents. On integrating over x, we have [Ji, 2004]

$$\int_{-1}^{1} \mathrm{d}x\, H_q(x,\xi,t) = F_1^q(t), \qquad \int_{-1}^{1} \mathrm{d}x\, E_q(x,\xi,t) = F_2^q(t), \tag{1.44}$$

$$\int_{-1}^{1} \mathrm{d}x\, \tilde{H}_q(x,\xi,t) = G_A^q(t), \qquad \int_{-1}^{1} \mathrm{d}x\, \tilde{E}_q(x,\xi,t) = G_P^q(t), \tag{1.45}$$

where F_1, F_2, G_A and G_P are the Dirac, Pauli, axial and pseudoscalar elastic form factors, respectively. H and E are sometimes called *unpolarized* GPDs and $\tilde{H}$ and $\tilde{E}$, the *polarized* GPDs.

Impact Parameter Space Interpretation of GPDs

Taking the Fourier Transform for the function F_q above

$$f_q(\vec{r},x) = \int \frac{\mathrm{d}^3\vec{q}}{(2\pi)^3}\, e^{-i\vec{q}\cdot\vec{r}} F_q(x,\xi,t). \tag{1.46}$$

Here x is the fraction of the nucleon momentum carried away by the struck quark (xp^+, where $p^+ = E_q/\sqrt{2}$ and $E_q = \sqrt{M^2 + \vec{q}^2/4}$). Integrating over the $z-$coordinate in the above equation, we get

$$f_q(\vec{b},x) = \int_{-\infty}^{\infty} \mathrm{d}z\, f_q(\vec{b} = \vec{r}_\perp, z, x) = \int \frac{\mathrm{d}^2\vec{q}_\perp}{(2\pi)^2} F_q(x,0,-\vec{q}_\perp^{\,2}), \tag{1.47}$$

where $\vec{b}$ is the impact parameter perpendicular to the $z-$direction [Burkardt, 2004] i.e. *localized in the transverse plane* [Diehl, 2003]. From two-dimensional non-relativistic mechanics, the conserved quantity following from Galilean invariance is the center-of-mass coordinate $\vec{r} = \sum m_i\vec{r}_i / \sum m_i$ of a many body system. By analogy, the conserved quantity following from the invariance under transverse boosts is the *center of plus-momentum* or *transverse center of momentum* $\vec{b} = \sum p_i^+\vec{b}_i / \sum p_i^+$ of the partons in the nucleon state.

$f_q(\vec{b},x)$ is the expectation value of a number operator and in that sense, is a real density. Its interpretation does not suffer from relativistic effects. Also, there is no quantum mechanical uncertainty principle constraint since the variables $\vec{b}$ and x live in different dimensions.

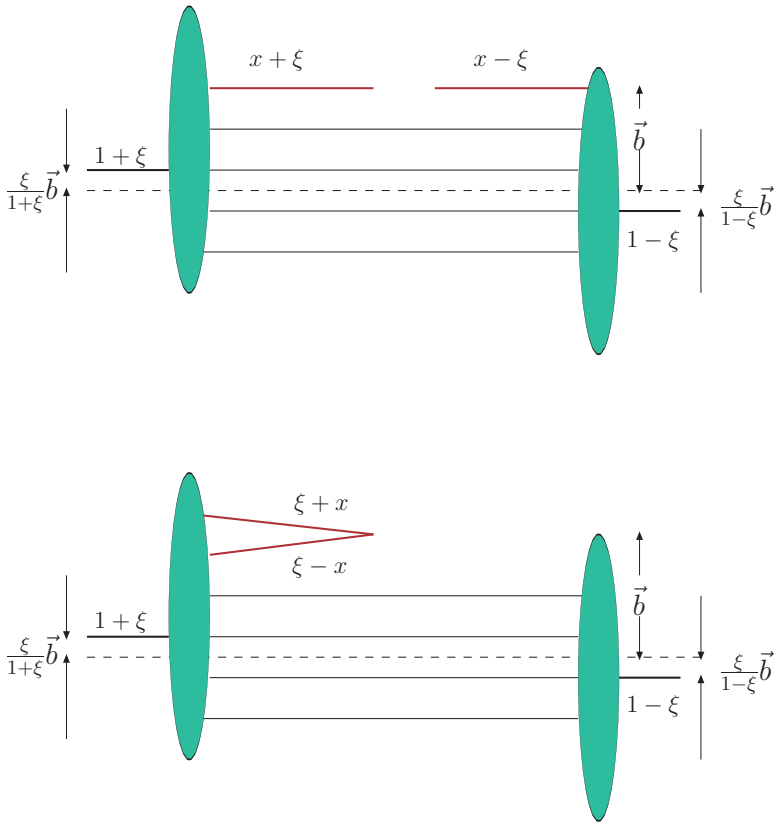

Figure 1.13: Representation of a GPD in impact parameter space. The upper diagram is for the region $x \in [\xi, 1]$, and the lower is for the region $x \in [-\xi, \xi]$. [Diehl, 2003]

$f_q(\vec{b}, x)$ is a *spatial-and-momentum-density hybrid* [Ji, 2004] in that it represents a spatial density in the transverse directions and momentum density in the longitudinal direction. It is also invariant under boost along the $z-$direction. if the nucleon has infinite momentum, its effective mass is also infinite. Therefore, its spatial structure in the transverse directions can be obtained directly from the Fourier transformation of the form factors without the relativistic recoil effects.

From Section 1.3.4 we have for the phase-space charge density

$$\rho_+(\vec{r}, x) = \int \frac{\mathrm{d}^3\vec{q}}{(2\pi)^3}\, e^{-i\vec{q}\cdot\vec{r}}\, [H(x,\xi,t) - \tau E(x,\xi,t)]\,, \tag{1.48}$$

where $\tau = \vec{q}^2/4M_N^2$. This is independent of the nucleon spin.

1.3.5 The Galster Parametrization

[Galster, 1971] proposed a parametric fit to the then existing G_E^n data (at low Q^2 values), known as the Galster Parametrization:

$$G_E^n(Q^2) = \frac{A_\tau}{1 + B_\tau} G_D(Q^2) \ , \tag{1.49}$$

where G_D is the dipole form factor as mentioned earlier (Equation 1.31). It was found that for $A_\tau = \mu_n \tau$ and $B_\tau = 5.6\tau$, the Galster parametrization fitted the existing (low-Q^2) data very well. The conclusions from this experiment and its implications on the Galster fit will be discussed in Chapter 6.

1.3.6 Shapes of the nucleons and their distributions

Based mostly on GPDs (section 1.3.4), theorists like Ji and Burkardt have come up with *pictures* of the nucleons to help visualize the charge and magnetic distributions within. This is known as *Nucleon Tomography*.

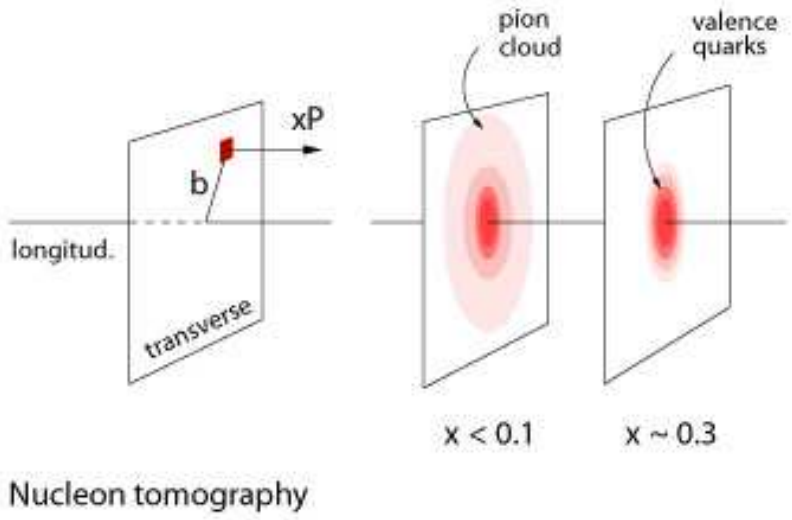

Figure 1.14: Transverse region probed at different x.

Kelly in 2004 proposed a parametrization with which he could fit data for G_M^n, G_E^p and G_M^p nicely [Kelly, 2004]:

$$G(Q^2) \propto \frac{\sum_{k=0}^{n} a_k \tau^k}{1 + \sum_{k=1}^{n+2} b_k \tau^k} \ , \tag{1.50}$$

where both numerator and denominator are polynomials in $\tau = Q^2/4m_p^2$. However, for G_E^n, due to limited data, he used the Galster parametrization. G_E^n data at higher Q^2 - this

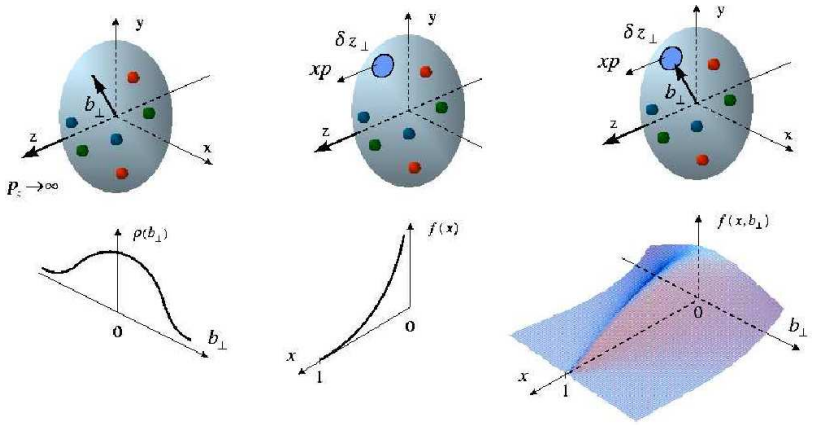

Figure 1.15: Different "phase-space" regions accessed by the GPD formalism. See subsubsection 1.3.4

experiment - would test the Galster fit and allow us to extend Kelly's parametrization to G_E^n as well (as well as the BBBA fits [Bradford *et al.*, 2006]).

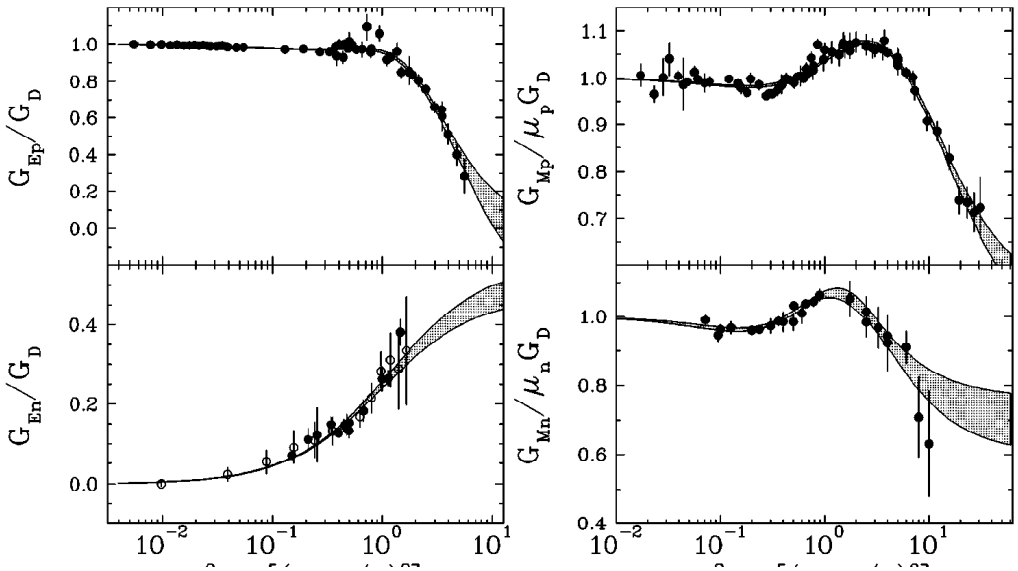

Figure 1.16: Parametrization fits by [Kelly, 2004]

Very recently, Miller presented a model-independent analysis of the infinite-momentum-frame charge density of partons in the transverse plane in the light-cone coordinate system [Miller, 2007]. He found that the parton charge density for the neutron is negative at the center. This implies that the square of the transverse charge radius ((1.20)) is positive, in contrast with expectations. Other quantities from the analysis suggest, for the proton, a larger central d quark density than that of the u quark by about 30%. Also, it is seen that the

neutron (proton) charge density has a long range negatively (positively) charged component. The analysis, however, considered only the F_1 form factor in the Fourier transform.

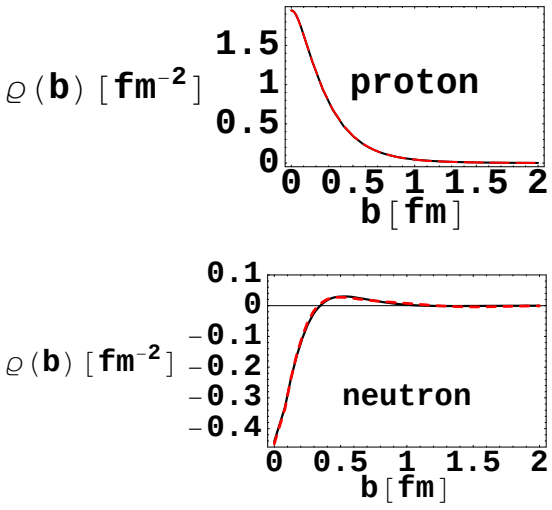

Figure 1.17: The neutron showing negative charge distribution at its center. This recent analysis is by [Miller, 2007]. See text for explanation.

1.4 Summary of Motivations for G_E^n at high Q^2

We have seen that there is enough motivation to know G_E^n precisely at high Q^2. Let us summarize the reasons below:

1. It is currently the least well known EMFF; this experiment puts it at par with the rest of its siblings. It will enable us to better understand the structure of the neutron and other quantities that dependent on it (like the strange form factors and GPDs).
2. It will help us test the pQCD prediction and look for surprises like in the proton case.
3. We can finally pick out a theory model as *the* model for the neutron; it will be a good test for the Galster parametrization which has so far fit G_E^n data at low Q^2 quite well.
4. It will help put stricter bounds on certain GPDs enabling more insight into the dynamic characteristics of the nucleons.

Copyright © Ameya Suresh Kolarkar 2008

CHAPTER 2: THE EXPERIMENT

The experiment was performed in Hall A of the Thomas Jefferson National Accelerator Facility in Newport News, Virginia. The polarized electron beam scattered off the polarized ^{3}He target and the outgoing particles - electrons and neutrons - were detected in the BigBite Spectrometer and the Neutron Detector, respectively. The standard Hall A detector equipment - the High Resolution Spectrometers - were not used for this experiment. The beamline components (beam current/position monitors, etc.) and beam polarimetry instruments (Compton, Möller), were part of the standard Hall A equipment.

The BigBite spectrometer was used for its large momentum acceptance (whence its name) instead of the HRSs. The solid-angle acceptance of BigBite was about 76 msr averaged over the extended (40 cm) target[1]. The Neutron Detector (ND) was built to match the BigBite in terms of solid-angle acceptance. The ND was positioned at about 8 m from the target to achieve better timing resolution of the detected events (neutron). As a result, the ND was a huge detector - the largest in the world at the time of the experiment.

Following sections detail the working of the accelerator and the detectors. We follow the path of the electrons from the source till they are detected along with the neutrons.

2.1 CEBAF Accelerator Overview

The Continuous Electron Beam Accelerator Facility (CEBAF) is an electron accelerator with 100% duty-cycle and a maximum energy now approaching 6 GeV. Three electron beams with a maximum total current of 200 μA can be used for simultaneous experiments in the three experimental areas, Halls A, B, and C.

The accelerator design is based on two parallel linear accelerators joined by magnetic recirculation arcs. The accelerating structures are 338 five-cell superconducting niobium cavities operating at a temperature of 2 K. The cavities are tuned to a resonant frequency of 1497 MHz. Following Figure 2.1, the principle of operation of the accelerator is outlined below:

- At the gun, electrons are emitted from a photocathode that is hit by laser light. Using three independent pulsed lasers each producing short light pulses with 499 MHz

[1]The maximum possible acceptance is 95 msr for a point target.

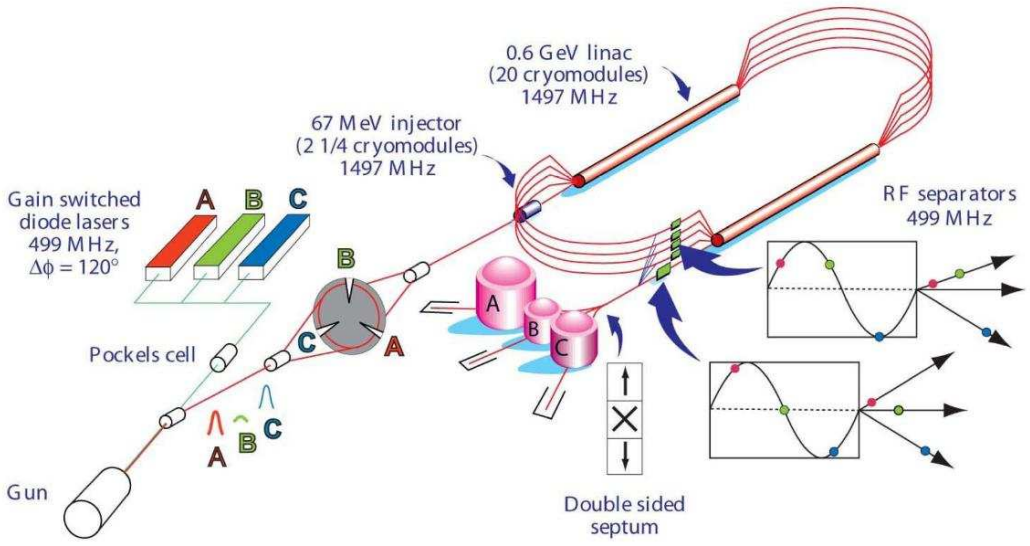

Figure 2.1: (color) CEBAF Layout

repetition frequency (1/3 of the accelerating frequency) creates three bunch trains; the bunch trains are offset in phase (by one 1497 MHz RF period or 120° in Figure 2.1) to form a single 1497 MHz bunch train. The charge of every third bunch is the same; it can be varied by varying the intensity of the corresponding laser. These bunches are further cleaned up by an adjustable three-slit system. This minimizes the interference between the bunches and thus, between the Halls.

- Polarized electrons are emitted by shining circularly polarized light on the photocathode. The lasers produce linearly polarized light which is circularly polarized in a Pockels cell. Inverting the high voltage on the Pockels cell changes the helicity of the circular polarization and thus the helicity of the emitted electrons.

- The electron beam (the 1497 MHz bunch train) now gets accelerated in the injector (up to 67 MeV for a maximum output energy of 6 GeV) and then enters the North Linac where it gains an additional 600 MeV (for 6 GeV).

- At the other end of the north linac, a vertically deflecting magnet system (*spreader*) guides the beam up to the highest orbit of the five 180° east arcs. After traversing the arc, a symmetric magnet system (*recombiner*) brings the beam back down to the axis of the South Linac.

- The beam gains an additional 600 MeV(for 6 GeV) in the South Linac. Again, at

the other end of the south linac, a spreader magnet system lifts the beam up to the highest orbit of the four 180° west arcs. After traversing the arc, another recombiner magnet system brings the beam back to the axis of the North Linac where its bunches now sit on top of newly injected bunches. After the beam passes through the North Linac for the second time, the spreader guides the beam up to the second highest orbit of the east arcs.

- The beam can thus be recirculated up to five times through the linacs. After each of the first four passes, transverse radio frequency separators located in the energy-separated beam lines can be activated to extract every third bunch, and to deliver an electron beam with an energy of $E, 2E, 3E$ or $4E$ to one of the three experimental areas, where E is the combined linac energy per pass. At the end of the fifth pass, a last separator can split the beam up to three ways; this allows the highest energy beam to be sent to all three halls.

The light from the three lasers needs to be combined into a single beam that will then pass through the same location of the subsequent optical elements. The two high-intensity lasers for Halls A and C are combined in a loss-free way by using the birefringent crystal PBSC ('polarizing beam splitter cube') and orienting the linear polarization planes perpendicular to each other. The Hall B laser is added to the Hall C laser in the semi-transparent mirror DM (accepting some losses in the Hall B laser intensity). Therefore, the Hall B helicity is the same as the Hall C helicity[2] (Figure 2.2) .

The pulsed lasers are not perfect: the pulses ride on a small background of DC light (typical pulse/background ratio is 1,000/1 to 10,000/1. This leads to an undesirable coupling between the halls: beam caused by the Hall X laser to leak into Hall Y, an effect called *bleedthrough*. In fact, leakage from a high-current hall can be enough to satisfy the Hall B current needs (leaving Hall B with no control of its current or polarization). Note that the wavelength of the leakage light can be different from the main pulsed component. This can cause the charge asymmetry and the magnitude of the polarization to be different from the main beam.

Fortunately, the leakage caused by the DC component of the laser light can be reduced further by using the bunching system. This system consists of two orthogonal transverse

[2]The helicity structure used in this experiment was the G^0 helicity structure which is described in Section 4.5.

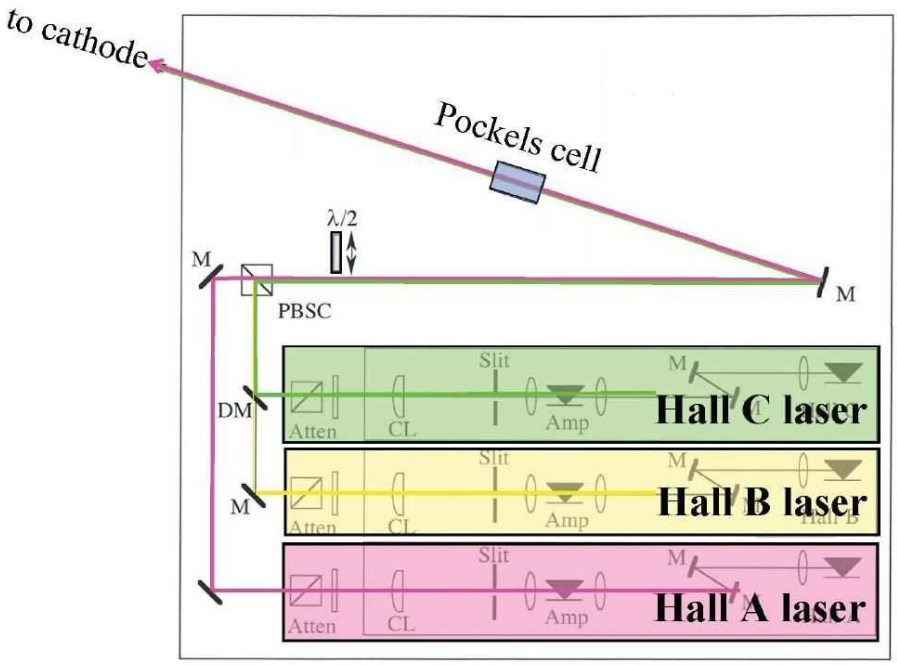

Figure 2.2: (color) Laser schematic for Halls A, B and C.

499 MHz cavities (with 90 degrees phase difference) that move the beam around a circle on the Master Slit (see Figure 2.3). Three adjustable slits located symmetrically around the circle are used to create a 1497 MHz bunch train and to set the intensities for the three halls. Behind the slit system, two additional transverse cavities undo the circular deflection and put the beam back onto the straight-ahead beam line. Typically, the Hall A and C slits are wide open while the Hall B slit has a small opening to reduce the beam current from a few μA created by the Hall B laser to the desired few nA.

Another effect to consider is the "charge asymmetry" of the electron beam, that is, a change in the beam intensity with helicity. Ideally, there are no changes in the electron beam as one changes its helicity. In reality, there are subtle changes in the beam properties. These changes are mainly caused by a remnant linear polarization in the circularly polarized light which then couples to polarization-dependent transmission in the optical elements and the properties of the photocathode. Changes in beam properties are of grave concern for parity violation experiments since they can easily mask the parity violating asymmetry. A few systems are in place to minimize these effects: a feedback system that modulates the intensity of the Hall X laser to keep the average current in Hall X independent of the

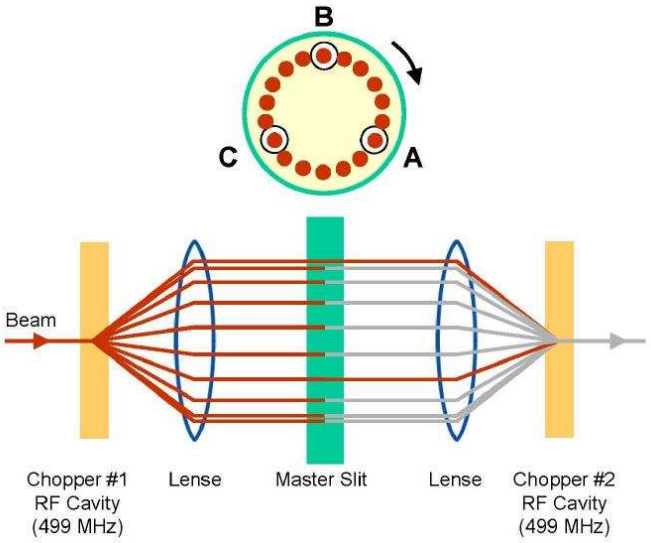

Figure 2.3: (color) The Master Slit to "clean up" the electron bunches to reduce leakage currents into other Halls.

helicity[3]; and another feedback system that keeps the position, angle, and energy of the beam independent of the helicity. We did not worry too much about the charge asymmetry but did keep an eye on it to prevent it from being too high.

The electron beam gets accelerated by superconducting cavities made out of niobium (Nb). Each cavity has 5 individual coupled cells. The following sketch shows a cross section of a 5-cell cavity and the distribution of magnetic and electric fields at a given point in time. In the instantaneous picture shown in Fig. 2.4, the direction of the electric field changes

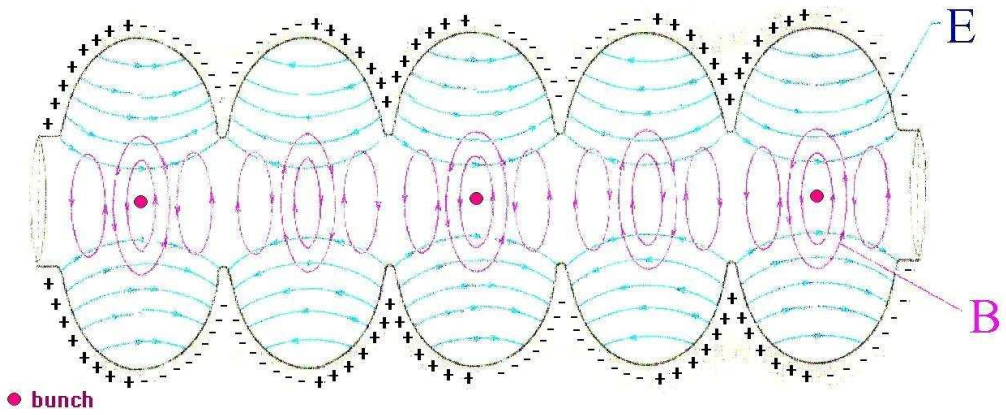

Figure 2.4: (color) Superconducting Cavities

in subsequent cells, so electron bunches (shown as red dots) get accelerated only in every

[3]This system acts on the Hall X laser only. One may still have to worry about the charge asymmetry in the leakage from other halls .

second cell. Since the cell spacing is 10 cm the bunch separation is 20 cm, which - combined with the velocity of light - leads to a bunch frequency of about 1500 MHz. One RF period (667 ps) later, the bunch will have proceeded to the center of the next cell where the electric field has now also changed direction, thus continuing to accelerate the bunch.

2.2 Beam Polarization

The polarization of the beam electrons is measured in a number of different ways - the spin-dependent Mott asymmetry at the injector, and the Compton and Möller polarimetry measurements in the Hall[4].

2.2.1 Spin Dance

Since the electron beam is "steered" along its way to the Halls by magnetic fields in the spreader, recirculation arcs, recombiner and transport arcs, the spins of the electrons precess in proportion to the beam's energy, E_{beam}, and bend angle θ_{bend}

$$\phi_{\text{spin}} = \frac{(g-2)}{2m_e} \cdot E_{\text{beam}} \cdot \theta_{\text{bend}} \tag{2.1}$$

g and m_e being the $g-$factor and mass of the electron, respectively. The *Wien filter* is the only dedicated spin manipulator in the accelerator used to compensate the beam's precession. The beam polarization measured in the Hall is a function of the Wien angle. The measured polarization varied sinusoidally with the Wien angle. Compton polarimetry was used to measure the polarization in the Hall while the Wien angle was scanned over a range to determine the value that corresponds to a good beam polarization in the Hall. Since our experiment ran with the higher priority G^0 experiment in Hall C (a parity experiment), the Wien angle was optimized to get maximum beam polarization in Hall C. We, thus, had a little less than maximum polarization as discussed in the next subsections.

A Wien filter is a region of crossed electric and magnetic fields a few meters after the source. The fields are adjusted such that the Lorentz force on the electrons disappears. The resulting rotation of the electron spins, shown in Figure 2.5, is termed the *Wien angle*, η_{Wien}. The polarization is measured using spin-dependent Mott asymmetry method at the injector, and Compton and Möller polarimetries in the Hall. The variation in measured

[4]Here we only talk about Hall A measurements.

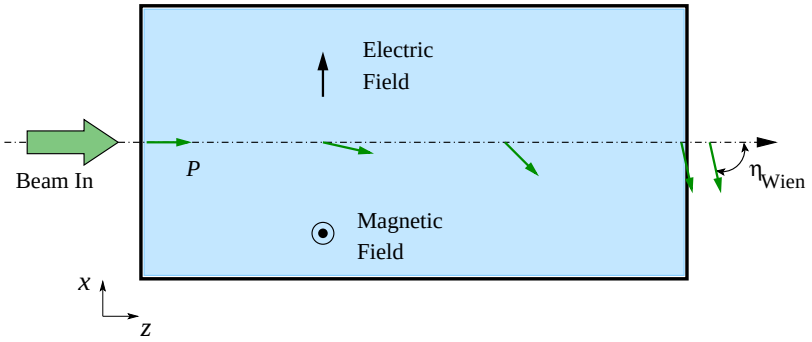

Figure 2.5: (color) The Wien filter. η_{Wien} is the Wien angle. During the spin dance, the beam polarization is measured as a function of the Wien angle.

polarization as the Wien angle was scanned as shown in Figure 2.6. The final value chosen was $\eta_{\text{Wien}} = 92.49°$ (during kin3)[5].

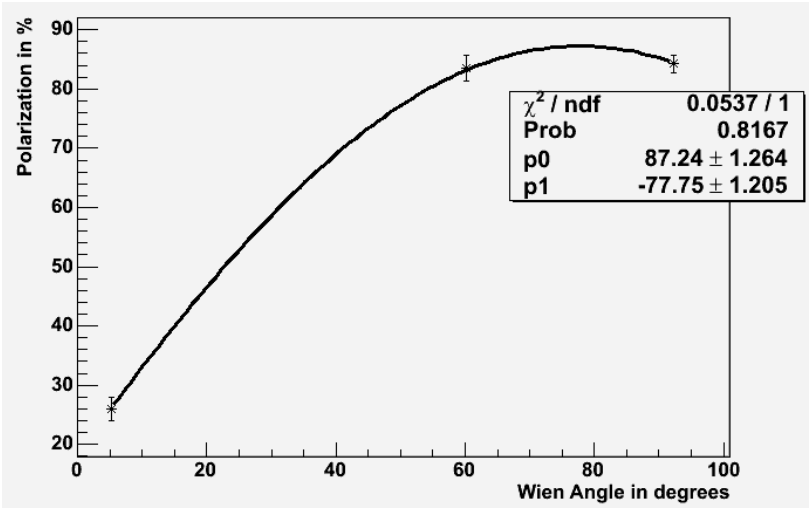

Figure 2.6: The Wien angle scan during the experiment. The polarization was measured with the Hall A Compton polarimetry. The Wien angle which gave us a beam polarization of about 85% was 92.49°.

2.2.2 Compton Polarimetry

In order to measure the longitudinal polarization of the 3-6 GeV high intensity TJNAF electron beam, a Compton Polarimeter was built by Saclay, Clermont and Jefferson Lab in 1999-2000.

The Compton effect, light scattering off electrons, discovered by Arthur Holly Compton (1892-1962), Nobel prize in Physics, 1927, is one of the cornerstones of the wave-particle

[5] $\eta_{\text{Wien}} = 76.4°$ should provide a polarization of about 0.953 of the maximum value.

duality. Compton scattering is a basic process of Quantum Electrodynamics (QED), the theory of electromagnetic (EM) interactions. This is a well established theory, and is thus natural to use the EM interaction, such as Compton scattering, to measure the polarization of an electron beam. Many of the Hall A experiments at Jefferson Laboratory using a polarized electrons beam require a measurement of this polarization as fast and accurate as possible. Unfortunately the standard polarimeters, like Møller, require the installation of a target in the beam. Therefore, the polarization measurement can not be performed at the same time as the data-taking because the beam after the interaction with the target is misdefined in terms of polarization, momentum and position. Compton Polarimetry permits a non-invasive polarization measurement of the beam.

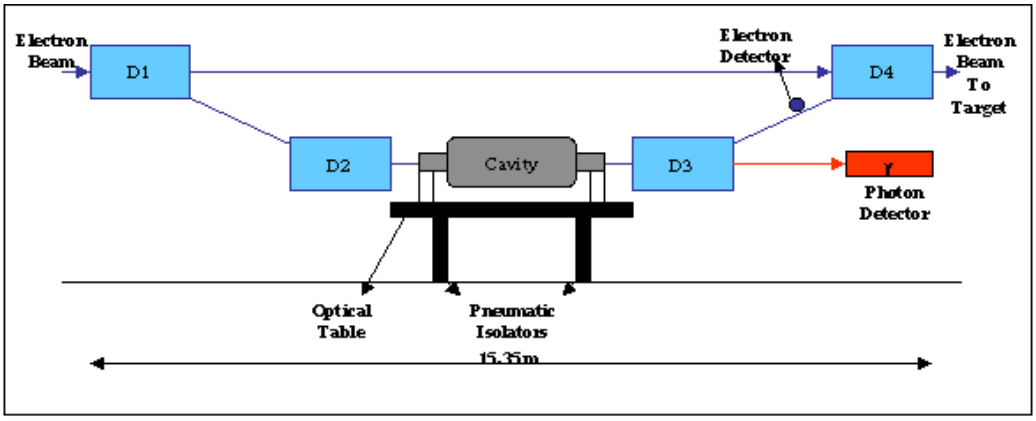

Figure 2.7: (color) Schematic of the Compton polarimetry setup. The electron beam is deflected into the Compton *chicane* by dipoles D_1 and D_2 and restored to its original path by dipoles D_3 and D_4. The beam interacts with polarized photons in the cavity.

The Jefferson Lab electron beam interacts with a laser beam of known circular polarization. This physical process is described by Quantum Electrodynamics which allows us to calculate the cross sections of the polarized electrons scattering off polarized photons as a function of their energies and scattering angle. The asymmetry in the counting rates is

directly proportional to the laser and electrons beam polarizations and cross sections.

The main constraints are to preserve the positions, the orientations and the physical characterictics of the beam at the exit of the polarimeter. The backward scattering angle of the Compton photons being very small, the first priority is to separate these particles from the beam using a magnetic chicane (see Figure 2.7). The energy of the backward photons is measured by an electromagnetic calorimeter. The third dipole of the chicane, coupled to the electron detector, is used as a spectrometer in order to measure the scattered electron momentum. To perform a quick polarization measurement, the photon flux has to be as high as possible. A Fabry-Pérot cavity made of two multi-layers concave mirrors of very high reflectivity amplifies this flux to a factor greater than 7000.

Compton polarimetry was used during the entire run of the experiment and electron beam polarizations between 82 and 86° were typically obtained. See Table 2.1 for polarization numbers from Møller polarimetry.

2.2.3 Møller Polarimetry

The Møller polarimeter along the Hall A beamline measures the polarization of the electron beam delivered to the Hall. It was built jointly by the University of Kentucky and the Kharkov Institute. The Møller polarimeter consists of:

- a magnetized ferromagnetic foil used as a polarized electron target, placed 17.5 m upstream of the central pivot point of the Hall A High Resolution Spectrometers;
- a spectrometer consisting of three quadrupole magnets and a dipole magnet, used to deflect the electrons scattered in a certain kinematic range towards the Møller detector;
- a detector and its associated shielding house;
- a stand alone data acquisition system;
- off-line analysis software which helps to extract the beam polarization from the data immediately after the data are taken.

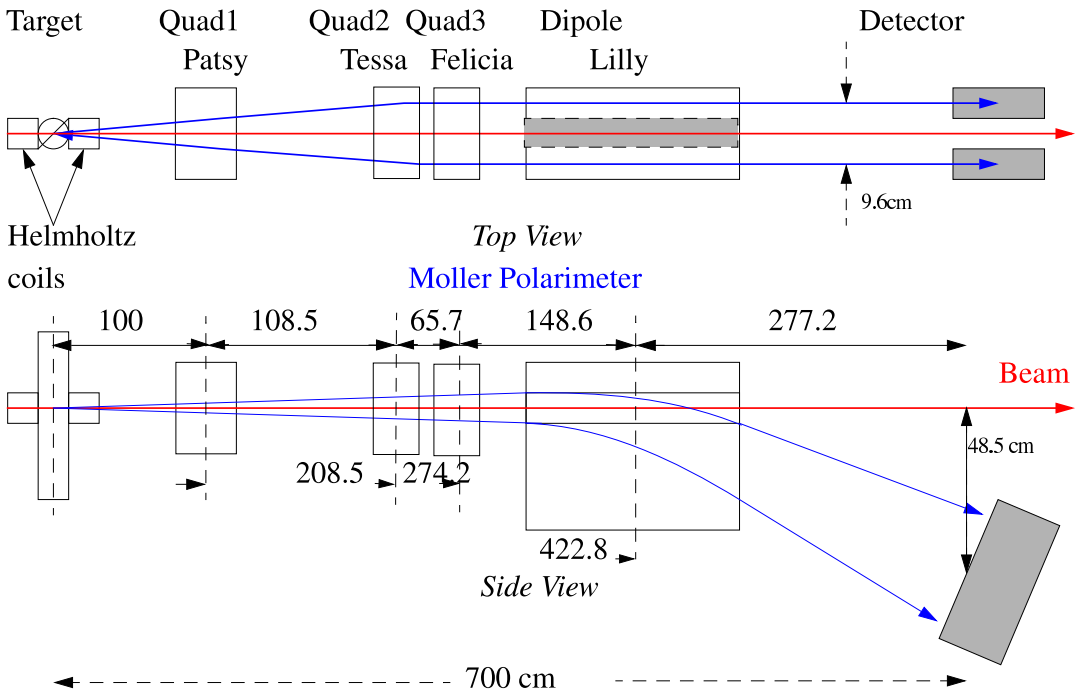

Figure 2.8: (color) The Møller optics schematic.

The cross-section of the Mller scattering $\vec{e^-} + \vec{e^-} \rightarrow e^- + e^-$ depends on the beam and target polarizations $\mathcal{P}_{beam}$ and $\mathcal{P}_{target}$ as:

$$\sigma \propto (1 + \sum_{i=X,Y,Z} (A_{ii} \cdot \mathcal{P}_{targ\ i} \cdot \mathcal{P}_{beam\ i})), \tag{2.2}$$

where $i = X, Y, Z$ defines the projections of the polarizations. The analyzing power A_{ii} depends on the scattering angle in the CM frame θ_{CM}. Assuming that the beam direction is along the Z-axis and that the scattering happens in the ZX plane:

$$A_{ZZ} = -\frac{\sin^2\theta_{CM} \cdot (7 + \cos^2\theta_{CM})}{(3 + \cos^2\theta_{CM})^2}, A_{YY} = -A_{XX} \tag{2.3}$$

The analyzing power does not depend on the beam energy. At $\theta_{CM} = 90^o$ the analyzing power has its maximum $A_{ZZ\ max} = 7/9$. A transverse polarization also leads to an asym-

metry, though the analyzing power is lower: $A_{XX\ max} = A_{ZZ}/7$. The main purpose of the polarimeter is to measure the longitudinal component of the beam polarization.

The Møller polarimeter of Hall A detects pairs of scattered electrons in a range of $75^\circ < \theta_{CM} < 105^\circ$. The average analyzing power is about $< A_{ZZ} >= 0.76$.

The target consists of a thin magnetically saturated ferromagnetic foil. In such a material about 2 electrons per atom can be polarized. An average electron polarization of about 8% can be obtained. In Hall A Møller polarimeter the foil is magnetized along its plane and can be tilted at angles $20 - 160^\circ$ to the beam. The effective target polarization is $\mathcal{P}_{target} = \mathcal{P}_{foil} \cdot \cos\theta_{target}$.

The secondary electron pairs pass through a magnetic spectrometer which selects particles in a certain kinematic region. Two electrons are detected with a two-arm detector and the coincidence counting rate of the two arms is measured. The beam longitudinal polarization is measured as:

$$\mathcal{P}_{beam\ Z} = \frac{N_+ - N_-}{N_+ + N_-} \cdot \mathcal{P}_{foil} \cdot \cos\theta_{target} \cdot < A_{ZZ} > , \tag{2.4}$$

where N_+ and N_- are the measured counting rates with two opposite mutual orientation of the beam and target polarizations, while $< A_{ZZ} >$ is obtained using Monte-Carlo calculation of the Møller spectrometer acceptance, $\mathcal{P}_{foil}$ is derived from special magnetization measurements of the foil samples and θ_{target} is measured using a scale, engraved on the target holder and seen with a TV camera, and also using the counting rates measured at different target angles.

The target is rotated in the horizontal plane. The beam polarization may have a horizontal transverse component, which would interact with the horizontal transverse component of the target polarization. The way to cancel the influence of the transverse component is to take an average of the asymmetries measured at two supplementary target angles[6].

Different targets were used to measure the polarizations thus providing a cross-check between polarization values. Table 2.1 summarizes the electron beam polarizations during various stages of this experiment.

[6]Two angles are *supplementary* when their sum is 180°.

Table 2.1: The electron beam polarization as measured by Møller polarimetry. The systematic error can be taken equal to ±0.3% (absolute). The sign depends on the electron helicity. (The only way to know for sure the beam polarization sign in a Hall is to measure it in the Hall using Møller/Compton polarimeters or some other spin-sensitive process.)

Day	**Target**	**Beam Pol.**	**Pol. Error**
Feb 28	SM	88.8	±0.2
	Fe	86.8	±0.2
Mar 04	SM	+88.2	±0.14
Mar 09	SM	-86.5	±0.15
Mar 25	SM	-82.2	±0.3
May 10	SM	∼ 85%	-

2.3 The Hall A Beamline

The electron beam entering Hall A was first passed through the Compton Polarimeter. It then went through a series of beam current and position monitors, a fast raster system and the Møller Polarimetry setup before finally entering the target region. The unscattered electrons go through to the beam dump outside the Hall. The Compton and Møller polarimeters were described in the previous sections. Here we describe the other beamline components.

2.3.1 Beam Position Monitors

Beam position monitors, or BPMs, determine the position of the electron beam. Hall A has two BPMs about 7.5 m and 1.3 m upstream of the target. Each BPM consists of four wire antennae parallel to the beam direction tuned to the fundamental RF frequency of 1.497 GHz of the beam and positioned at ±45° relative to the (Hall) horizontal and vertical directions as shown in Figure 2.9. The beam induces a signal in the antennae that is inversely proportional to their distance from the beam. The standard difference-over-sum technique[7] is then used to determine the relative position of the beam to within 100 microns for currents above 1 μA (Equation 2.5). The absolute position of the BPMs can be calibrated with respect to the scanners (superharps) which are located adjacent to each of the BPMs [J. H. Mitchell, 2000]. The BPMs provide a non-invasive measurement when beam is present in the hall. By looking at the difference in reading from the two BPMs, the direction of the beam could also be determined.

[7]This method eliminates the current dependence of the signals in the antennae.

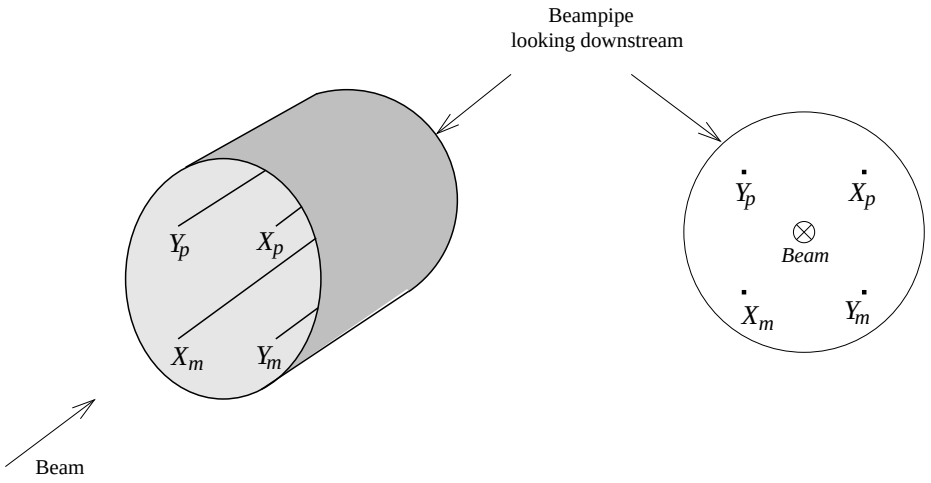

Figure 2.9: The beam position monitor beampipe

$$x_p = k\frac{X_p - X_m}{X_p + X_m} \tag{2.5}$$

$$y_p = k\frac{Y_p - Y_m}{Y_p + Y_m} \tag{2.6}$$

where $k \approx 18.87$ mm is a constant obtained after calibrating the BPMs. The (pedestal-subtracted) signals $X_{p,m}$ and $Y_{p,m}$ are proportional to the product of the beam current and distance of the antennae from the beam.

2.3.2 Beam Current Monitors

Two types of beam current monitors were used in this experiment[8] - the resonant cavity type and the Unser monitor (a parametric DC current transformer [Unser, 1981]). The Unser monitor was used to calibrate the cavity BCMs.

The output of the cavity BCM's stainless steel cylindrical waveguides tuned to the beam's frequency (1447 MHz) is proportional to the beam current. This is calibrated with the Unser monitor which measures absolute currents and has a very stable and well measured gain. However, the Unser monitor suffers from low signal-to-noise ratio and large drifts in its offsets thus making it unsuitable for regular monitoring of the current. Once calibrated, the cavity BCMs serve as our beam current monitors. These have a good signal-to-noise ratio and stable gain and offsets. Since we measured asymmetries instead of cross-sections, a precise measurement of beam current was not required.

[8]These are part of the standard Hall A beamline equipment.

2.3.3 Raster

The experiment used high pressure target cells with thin glass walls and end-caps. To prevent overheating caused by the high intensity beam (about 100 μm in diameter), the beam was rastered into a square of side 2-3 mm. A triangular waveform of frequency 25 kHz was used for the raster in both $x-$ and $y-$directions. This distributed the energy deposition more uniformly on the target cell end-caps.

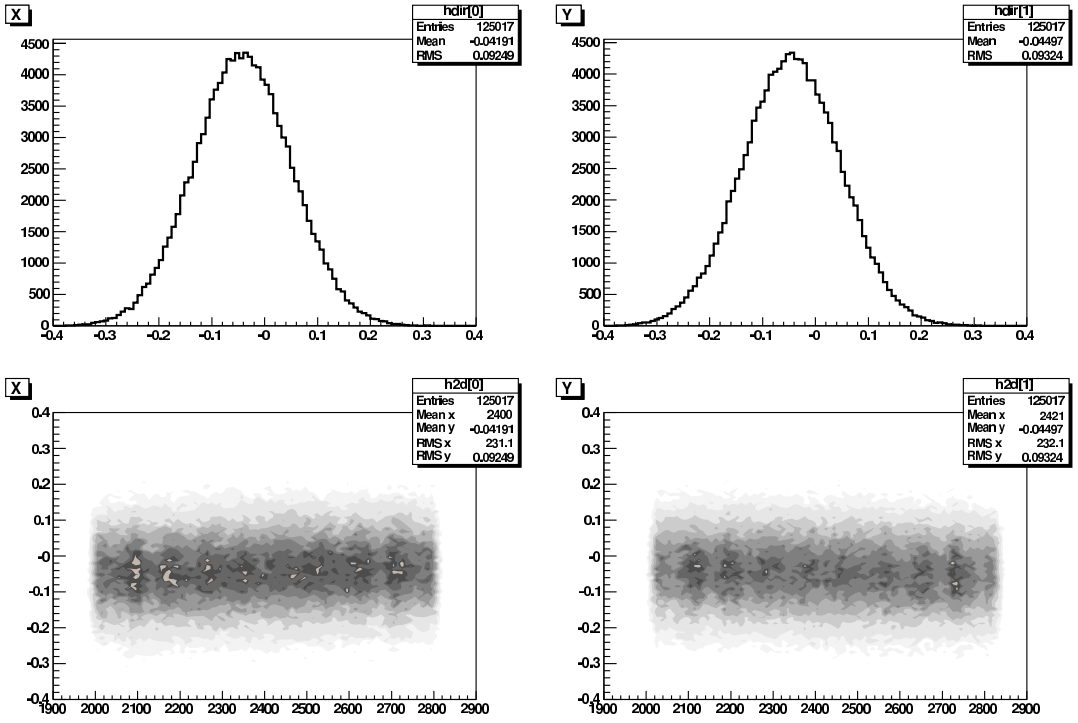

Figure 2.10: (color) Raster: Before and after calibration [Craver, 2007b]

2.4 G_E^n Experimental Setup in Hall A

Looking downstream in Hall A, the target region was at the center of the Hall with the two standard Hall A High Resolution Spectrometers positioned at 90° to the beamline on either side of it. These were not used in the experiment. The scattered electrons were detected in the BigBite (BB) Spectrometer which was placed on the right of the target region at about 56° to the beamline and at a distance of about 1 m from it. An iron shield was placed between the target box and the BB magnet to minimize the effects of the BB magnet fringe fields on the target.

The Neutron Detector (ND) was towards the left of the beamline at a distance of about 8 m from the target center. Various positions and angles that were kinematics-dependent are detailed in Table 4.1. Figure 2.11 shows the experimental setup and Figure 2.12 is the scattering diagram for the experiment. The polarized ^{3}He target is described in Chapter 3 and the detectors and electronics in Chapter 4.

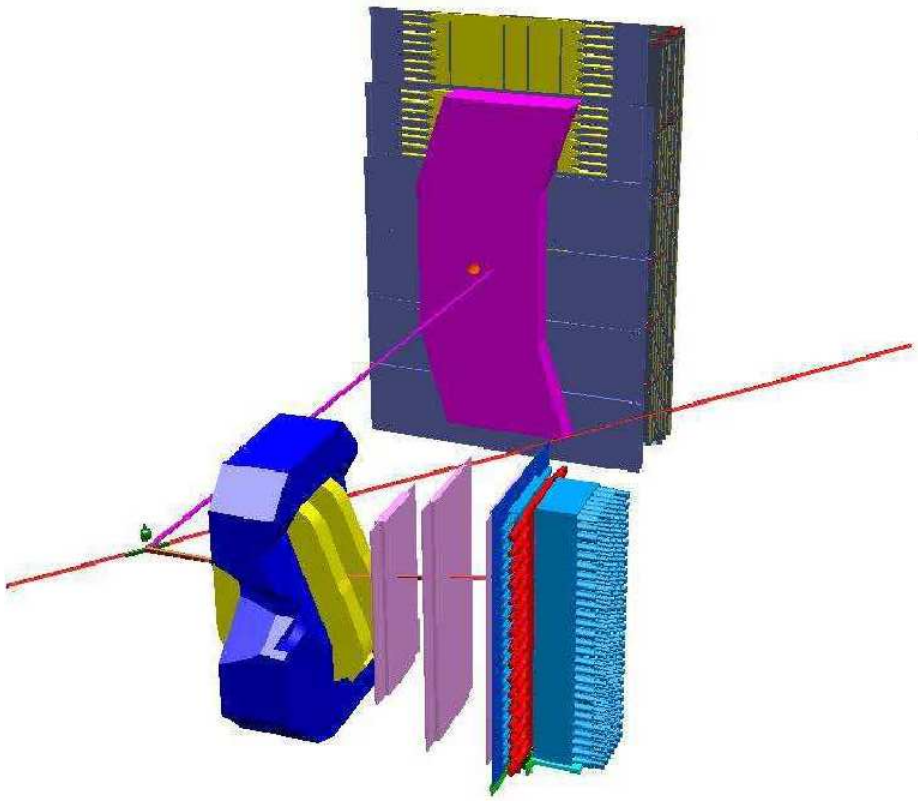

Figure 2.11: (color)The experimental setup for the E02-013 experiment in Hall A. The electron beam comes in from the left.

2.5 Experimental methods

Scattering experiments until the 1990s used the Rosenbluth Separation method described in Section 1.2.2. Almost 50 years ago [Akhiezer and Rekalo, 1968] and later, [Arnold *et al.*, 1981] showed that the accuracy of nucleon electric form factor measurements could be increased significantly by using the double polarization method (now also known as the Super-Rosenbluth method). This meant scattering polarized electrons off a polarized target or equivalently by measuring the polarization of the recoiling nucleon. Also, this provides a better way to measure G_E^n than the Rosenbluth Separation method, where the relative con-

Table 2.2: The kinematical settings for the experiment. Subscripts e and n denote the electron and neutron respectively. E denotes the energy and θ, the angle of scattering. The scattering angles correspond to the nominal angle for the detector positioning.

Q^2 $(\mathrm{GeV}/c)^2$	E GeV	θ_e deg.	p_e GeV/c	θ_n deg.	p_n GeV/c	T_n GeV
1.2	1.52	56	0.89	35.7	1.26	0.63
1.7	2.08	52	1.12	32.5	1.65	0.96
2.5	2.64	52	1.27	28.2	2.12	1.38
3.4	3.29	52	1.40	24.5	2.67	1.89

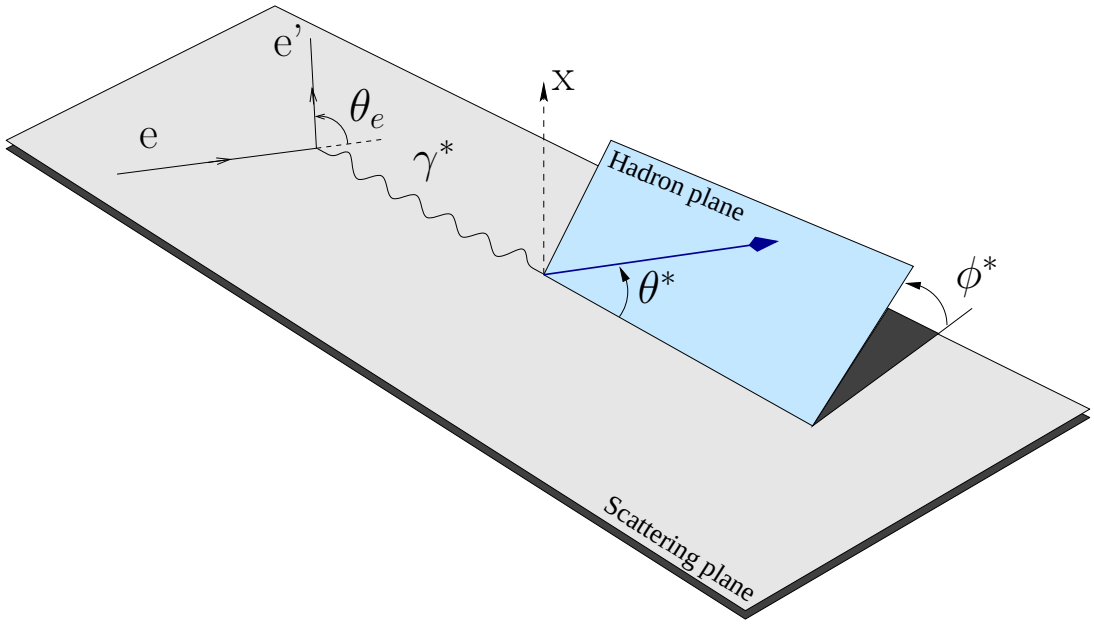

Figure 2.12: (color)The scattering diagram. For E02-013, ideally, $\theta^* = 90°$, $\phi^* = 0°$, that is, the target spins lie in the electron scattering plane.

tribution of G_E^n is suppressed as $(G_E^n/G_M^n)^2$. Technological advances in the past 15 years or so have enabled experimenters to utilise this method to measure the nucleon electric form factors. In the case of the proton, a standard magnetic spectrometer for proton detection can be coupled to a large acceptance non-magnetic detector to detect the scattered electrons. In the case of the neutron, however, one needs a magnetic spectrometer to detect the scattered electron in order to cleanly identify the reaction channel. Thus, the figure of merit of a polarized ^{3}He target is comparable to that of a neutron polarimeter.

A clean detection of coincident (e,e$'$N) events requires electron beams of a relatively high duty factor in order to supress contributions from accidental coincidences. CEBAF has a duty cycle of almost 100%, whence the phrase *Continuous* Electron Beam.

2.5.1 The Double Polarized Cross Section and Asymmetries

In the Born approximation, the elastic electron nucleon scattering $(e-N)$ cross section can be written as a sum of two parts: Σ, which corresponds to the unpolarized elastic cross section $\frac{\mathrm{d}\sigma}{\mathrm{d}\Omega_e}$, and a polarized part Δ, which is non-zero only if the electron is longitudinally polarized (helicity h= $\pm$1) [Donnelly and Raskin, 1986, Raskin and Donnelly, 1989]

$$\sigma_h = \Sigma + h\Delta \tag{2.7}$$

The asymmetry for the $e-N$ scattering cross section is defined by

$$A_N := \frac{\sigma_+ - \sigma_-}{\sigma_+ + \sigma_-} = \frac{\Delta}{\Sigma}\,, \tag{2.8}$$

where the subscripts + and - indicate electron spin parallel and anti-parallel to the electron momentum. The unpolarized eN cross section Σ for elastic scattering off a free nucleon at rest is given (in the Born approximation) by (1.17). The polarized cross section Δ is given by

$$\Delta = -2\sigma_{\mathrm{M}}\sqrt{\frac{\tau}{1+\tau}}\tan(\tfrac{\theta}{2})\left[\sqrt{\tau(1+(1+\tau)\tan^2(\tfrac{\theta}{2}))}\cos\theta^* G_M^2 + \sin\theta^*\cos\phi^* G_E G_M\right] \tag{2.9}$$

where θ^* is the polar angle and ϕ^* is the azimuthal angle of the target polarization in the laboratory frame with respect to the axis of the momentum transfer (see Figure 2.12).

The measured experimental asymmetry for the $^3\overrightarrow{\mathrm{He}}(\vec{e},e'n)$ reaction is reduced compared to the ideal $\vec{n}(\vec{e},e'n)$ reaction because of the finite polarization of the electron beam P_e , the finite polarization of the neutrons P_n in the ^{3}He target, the dilution D of atoms other than ^{3}He in the target, and the dilution $V = (1 + N/S)$ of events originating from random coincidences and reactions other than quasi-elastic scattering. N/S is the noise-to-signal ratio. Our beam polarization was $P_e \approx 0.85$ (Section 2.2.1) and the polarized ^{3}He target attained stable polarizations of $P_{\mathrm{He}} \approx 0.50$ (Section 3.8) during the experiment. The polarization of the neutron within the ^{3}He nucleus is $P_n \approx 86\%$ of ^{3}He polarization. Also, the presence of nitrogen in the target cell gave $D = 0.95$ (Section 5.3.1) and background events lead to $V = 0.91$.

The measured asymmetry from the neutron can now be expressed as follows:

$$A_{\text{phys}} = -\frac{2\sqrt{\tau(\tau+1)}\tan(\frac{\theta}{2})G_E^n G_M^n \sin\theta^* \cos\phi^*}{(G_E^n)^2 + (G_M^n)^2(\tau + 2\tau(1+\tau)\tan^2(\frac{\theta}{2}))} - \frac{2\tau\sqrt{1+\tau+(1+\tau)^2\tan^2(\frac{\theta}{2})}\tan(\frac{\theta}{2})(G_M^n)^2\cos\theta^*}{(G_E^n)^2 + (G_M^n)^2(\tau + 2\tau(1+\tau)\tan^2(\frac{\theta}{2}))} . \quad (2.10)$$

By aligning the target spins perpendicular to the momentum transfer direction and in the electron scattering plane, that is, $\theta^* = 90^\circ$ and $\phi^* = 0^\circ$, we get the perpendicular or *transverse* asymmetry

$$A_\perp \equiv A_{\text{perp}} = -\frac{G_E^n}{G_M^n} \cdot \frac{2\sqrt{\tau(\tau+1)}\tan(\frac{\theta}{2})}{\left(\frac{G_E^n}{G_M^n}\right)^2 + (\tau + 2\tau(1+\tau)\tan^2(\frac{\theta}{2}))} . \quad (2.11)$$

Since $(G_E^n/G_M^n)^2$ is small compared to the second term of the denominator in our kinematics, G_E^n is nearly proportional to A_{perp} . To extract G_E^n from this ratio, knowledge of G_M^n is necessary. Experiment E94-017 in Hall B measured G_M^n up to $Q^2 = 4.8$ (GeV/c)^2 which will provide us with very accurate G_M^n data. Due to the large acceptance of the BigBite spectrometer and the neutron detector array, the perpendicular spin alignment can only be made for part of the acceptance, and longitudinal contributions to the asymmetry had to be taken into account:

$$A_\parallel \equiv A_{\text{long}} = -\frac{2\tau\sqrt{1+\tau+(1+\tau)^2\tan^2(\frac{\theta}{2})}\tan(\frac{\theta}{2})}{\left(\frac{G_E^n}{G_M^n}\right)^2 + (\tau + 2\tau(1+\tau)\tan^2(\frac{\theta}{2}))} . \quad (2.12)$$

These contributions are small, and, to first order, depend only on the kinematics and not on the value of G_E^n itself. The analysis for one kinematic data point is presented in Chapter 5.

2.5.2 Two Photon Exchange

In order to resolve the discrepancy between the results from the two experimental techniques - Rosenbluth and Double Polarized, an ϵ-dependent[9] modification of the cross-section is necessary [Hyde-Wright and de Jager, 2004]. In two or more photon exchanges (TPE), the first virtual photon is exchanged, which can lead to an intermediate excited state of the nucleon, and then a second one (or more) is exchanged finally leading the nucleon back in its ground state (Figure 2.13). These TPE contributions have been investigated both

[9] ϵ is defined on page 5.

experimentally and theoretically for the past 50 years. The contributions fall under radiative corrections in the so-called box diagrams (Section 5.5). Almost all analyses with the Rosenbluth technique have used the radiative corrections derived by [Mo and Tsai, 1969] which only include the infrared divergent parts of the box diagrams in which one of the photons exchanged is soft.

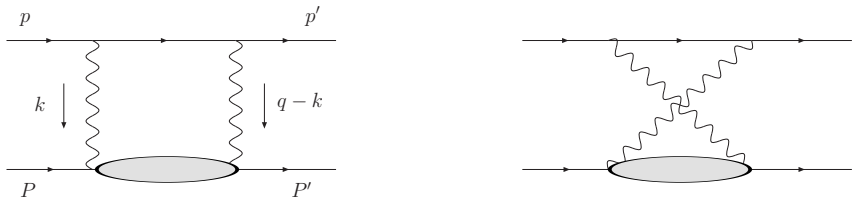

Figure 2.13: The two-photon-exchange Feynman diagrams.

Several studies have provided estimates of the size of the ϵ-dependent corrections necessary to resolve the discrepancy. [Guichon and Vanderhaeghen, 2003] introduced a general form of the TPE contribution from the box diagram in radiative corrections into the amplitude for elastic electron-proton scattering. The modified Rosenbluth expression now reads

$$\mathrm{d}\sigma \propto \tau + \epsilon\frac{\tilde{G}_E^2}{\tilde{G}_m^2} + 2\epsilon\left(\tau + \frac{\tilde{G}_E}{\tilde{G}_m}\right) Y_{2\gamma} \ , \tag{2.13}$$

where $Y_{2\gamma} = \mathcal{R}\frac{\nu\tilde{F}^3}{M^2\tilde{G}_M}$ and $\tilde{G}_M$, $\tilde{F}_2$, and $\tilde{F}_3$ are equal to G_M, F_2, and 0, respectively, in the Born approximation. $Y_{2\gamma}$ and the *two-photon* form factors $\tilde{G}_E$ and $\tilde{G}_M$ were fitted to the Rosenbluth and polarization-transfer data sets resulting in a value of ~ 0.03 for $Y_{2\gamma}$ with very little ϵ- or Q^2-dependence. For further discussion, refer to [Arrington *et al.*, 2006].

Very recently, [Arrington *et al.*, 2007] performed a global analysis of elastic electron-proton scattering data using calculations of two-photon exchange effects to extract corrected values of the protons electric and magnetic form factors over the entire existing Q^2 range of the data. The analysis combined the corrected Rosenbluth cross section and polarization transfer data. This is the first extraction of G_E and G_M including explicit two-photon exchange corrections and their associated uncertainties. Figure 2.14 shows the pre- and post- corrected plots.

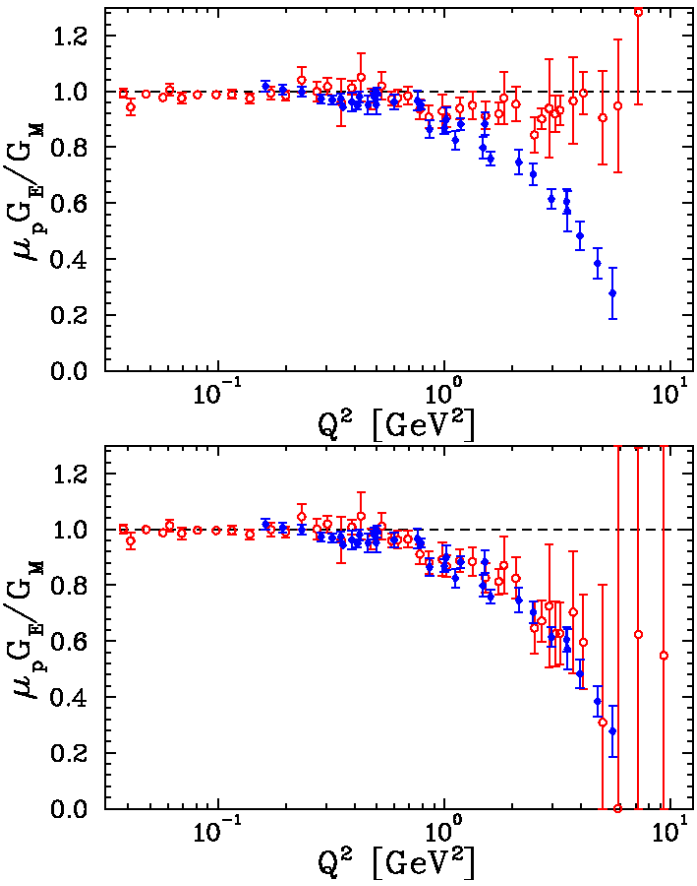

Figure 2.14: Proton form factor ratios with the Rosenbluth data uncorrected (above) and corrected (below) for two-photon exchange reactions [ARRINGTON *et al.*, 2007].

2.6 Corrections

If we were doing elastic scattering, that is, if our target were not a part of a bigger system, we would not have to worry about effects that arise from being in a nuclear medium. But in reality, this is seldom the case (the only exception being the hydrogen atom) and there are nuclear medium and other effects to consider. These effects include Final State Interactions (FSI), Meson Exchange Currents (MEC) and Isobar Configurations (IC).

2.6.1 Final State Interactions

The physical motivation for the PWIA comes from the fact that the electron probes a region of a length scale of $\sim 1/|\vec{q}|$ of the nuclear target. For large enough momentum transfers, we can assume that the scattering process involves only one nucleon with the residual $(A-1)-$particle system acting only as a spectator. This assumption leads to

two simplifications in the structure of the nucleon tensor (Equation 1.10): (i) the nuclear current operator can be written as the sum of the one-body nucleon currents; and (ii) the final nuclear state reduces to the product of a one-particle state describing the free propagation of the struck nucleon and an $(A-1)-$particle state of the spectator system. Thus the dynamics of the nuclear target is decoupled from the electromagnetic vertex and the relativistic description of the motion of ths struck nucleon reduces to a purely kinematic problem that can be treated exactly.

This, however, occurs at high Q^2 ($Q^2 > M_N^2$) and for momentum transfers of the order of the nucleon mass, the interaction between the struck nucleon and the residual system needs to be taken into account (Figure 2.15).

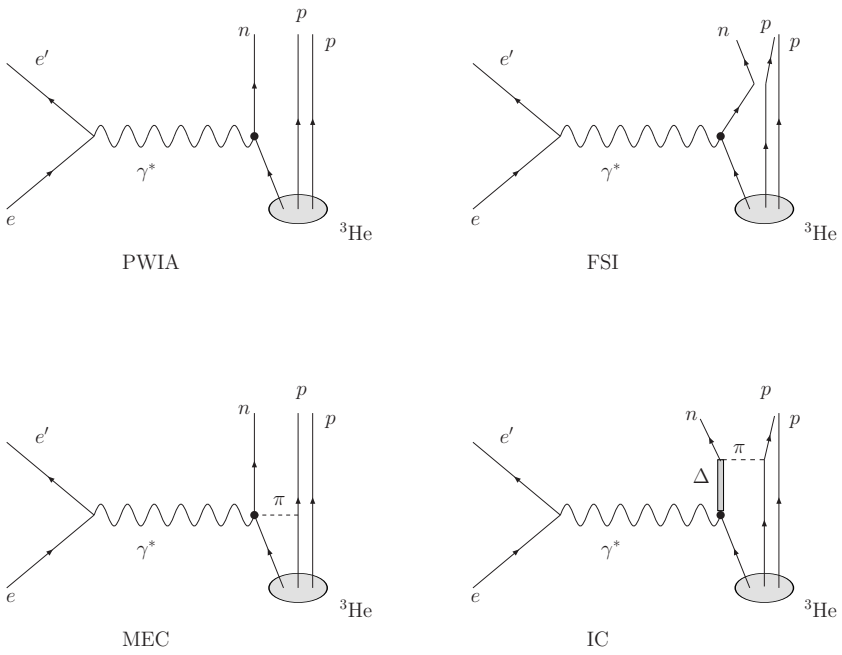

Figure 2.15: Corrections to the PWIA: FSI, MEC, IC

2.6.2 Meson Exchange Currents

Protons and neutrons in a nuclear medium are bound by forces arising due to the exchange of charged mesons between the nucleons giving rise to meson exchange currents. It is likely during the scattering process that the virtual photon hits an exchange meson instead of a nucleon (Figure 2.15).

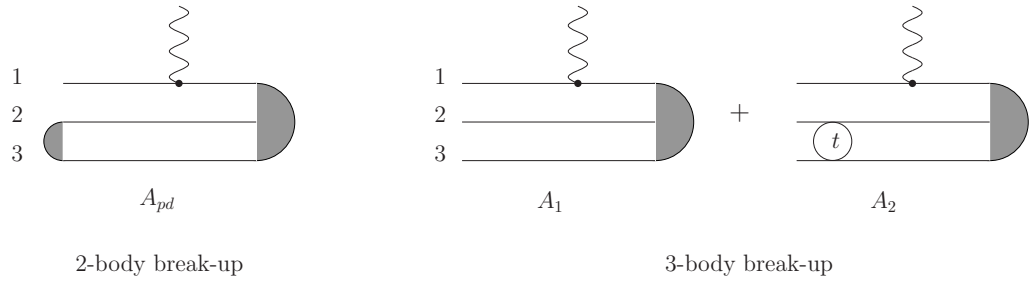

Figure 2.16: Schematic representation of the 2-body and 3-body breakup (2bbu and 3bbu, respectively) of ^{3}He.

2.6.3 Isobar Configurations

Sometimes the virtual photon might scatter off an excited state or resonant state of a nucleon, e.g. the $\Delta(1232)$ resonance instead of the ground state configuration. The nucleon can be in many such excited state configurations (known as Isobar Configurations). This effect can be reduced, even almost eliminated by placing cuts on the invariant mass W since the masses of these resonances are significantly larger than the ground state nucleon (e.g. a nucleon in the $\Delta(1232)$ state mentioned above has a mass of 1232 MeV and is the lightest of the Isobar Configurations) (Figure 2.15).

2.6.4 Radiative Corrections

Apart from the effects mentioned above, there are other corrections that need to be applied to the asymmetry because of radiative effects. Radiative effects are essentially the loss of energy of particles due to various processes like *bremstrahlung* (internal) and energy loss while passing through the glass wall of the target cell (external). These processes and corrections are discussed in Section 5.5.

Copyright © Ameya Suresh Kolarkar 2008

CHAPTER 3: THE POLARIZED ^{3}He TARGET

Outside the nucleus, free neutrons are unstable and have a mean lifetime of 885.7 ± 0.8 seconds (about 15 minutes), decaying by emission of an electron and an anti-neutrino into a proton: $n \rightarrow p + e^- + \overline{\nu}_e$. This decay mode, known as beta decay, can also occur in neutrons within unstable nuclei.

Inside of a bound nucleus, protons can also transform via beta decay into neutrons. In this case, the transformation may occur by emission of a positron and neutrino: $p \rightarrow n + e^+ + \nu_e$. The transformation of a proton to a neutron inside of a nucleus is also possible through electron capture: $p + e^- \rightarrow n + \nu_e$. Positron capture by neutrons in nuclei that contain an excess of neutrons would also be possible, but is hindered due to the fact that positrons are repelled by the nucleus, and furthermore, quickly disappear through annihilation when they encounter electrons.

When bound inside of a nucleus, the instability of a single neutron to beta decay is balanced against the instability that would be acquired by the nucleus as a whole if the resulting proton were to participate in repulsive interactions with the other protons that are already also present in the nucleus. As such, although free neutrons are unstable, bound neutrons are not necessarily so. The same reasoning explains why protons, which are stable in empty space, may transform into neutrons when bound inside of a nucleus. The requirement of having a high density neutron target for extended periods of time necessitates the use of "effective" neutron targets, like the nuclei of deuterium or ^{3}He. ^{3}He has been successfully used as a polarized neutron target in many experiments as explained in the next section.

^{3}He is a primordial substance in the Earth's mantle, considered to have become entrapped within the Earth during planetary formation. ^{3}He is present within the mantle, in the ratio of 200-300 parts of ^{3}He to a million parts of ^{4}He. ^{3}He is also present in the Earth's atmosphere. The natural abundance of ^{3}He in naturally occurring helium gas is 1.38×10^{-6}. Since the mass of the Earth's atmosphere is about 5,000 trillion metric tons, there are about 35,000 metric tons of ^{3}He in the atmosphere.

^{3}He is produced on Earth from three sources: lithium spallation, cosmic rays, and decay of tritium (^{3}H). The total amount of ^{3}He in the mantle may be in the range of 100 thousand to a million tonnes. However, this mantle helium is not directly accessible. It is believed

that the Moon's surface has large amounts of helium-3 in the lunar regolith [Wikipedia].

3.1 Polarized ^{3}He

In nuclear physics, the force between nucleons is strongly dependent on their spin orientations. Also, the protons and neutrons are treated as identical particles which differ only in their isospin projections making the nuclear force strongly dependent on isospin too. Thus each nucleon has 4 spin-isospin components reflecting its spin 1/2 and isospin 1/2 [Friar, 1991].

The spin-isospin states are classified according to their asymmetries with respect to the interchange of any two particles. The types of symmetries possible are: symmetric, antisymmetric and mixed-symmetric. The mixed-symmetry states are neither symmetric nor anti-symmetric. The states constructed for the three nucleons in a trinucleon system should be antisymmetric with respect to interchange of *all* the coordinates of any pair of nucleons: space, spin and isospin. This is the statement of the Generalized Pauli Principle. Therefore, the antisymmetric spin-isospin wave-functions must couple with symmetric spatial wave functions while mixed-symmetry wavefunctions must couple with mixed-symmetry spatial wave functions.

The significance of this lies in the kinetic energy of the system. Spatially symmetric states will have the least kinetic energy because they have the least structure. Spatially mixed-symmetry states have more kinetic energy than the spatially symmetric states and spatially antisymmetric states have the most. For a trinucleon ground states this implies that the most probable wave function component is the one with the least kinetic energy, that is, the spatially symmetric state. This is indeed observered as roughly 90% of the trinucleon wave-function is the spatially symmetric s-wave component denoted as the S-state, whereas the mixed-symmetric s-wave component (the S'-state) only has a few percent probability (e.g. $\sim$ 1.5% for ^{3}He). There also exists a spatially antisymmetric s-wave component (the S''-state) which has a tiny probability of about 10^{-5}.

Of the possible ($4^3 =$) 64 possible spin (S) and isospin (I) components, 32 have $I = 3/2$ and 32 have $I = 1/2$; only the latter are important for the trinucleon ground states. Half of those refer to $I_z = +1/2$ (^{3}He) and the other half to $I_z = +1/2$ (^{3}H). Thus, 16 spin-isospin states are required to specify the most general ^{3}He wave-function. Of all possible spin projections of these states, only six are $I = 1/2$ basis wave functions: four doublet

($S = 1/2$) and two quartet ($S = 3/2$). Since the total spin of ^{3}He is $J = 1/2$, the maximum possible total orbital angular momentum is $L = 2$ and the minimum possible is $L = 0$. The $L = 1$ (P) states are very tiny and can be ignored for most purposes.

However, the D-states cannot be ignored if there is a tensor force in the nuclear Hamiltonian arising from a component of the force that mixes orbital angular momenta. Since the tensor force is very strong, the D-state in ^{3}He is quite large ($\sim 8 - 9\%$). The small but important S'-state component arises from the spin dependence of the nucleon-nucleon potential. This leads to effective neutron and proton polarizations of $P_n = 86.5\%$ and $P_p = -2.7\%$ [Friar *et al.*, 1990].

Figure 3.1 depicts two trinucleon systems, ^{3}He and ^{3}H. The shaded and unshaded circles are the protons and neutrons respectively. The center of mass (CM) of the three nucleons is shown by a cross and x and y are the Jacobi coordinates The equilateral configuration shown in Figure 3.1(a) is a semiclassical depiction of the S-state. Here r is the distance of the nucleons from the CM. The other two figures are the depiction of the actual ^{3}He and ^{3}H nuclei as seen in nature. The force between two like nucleons ($p - p$ or $n - n$) is weaker than the neutron-proton ($n - p$) force since only the $n - p$ system has a bound state. The neutron in ^{3}He is consequently drawn closer to the CM and the protons move out further ($\theta > 60°$). This asymmetry with respect to the more symmetric (leftmost figure) state is due to the space-isospin (or spin) correlations of the S'-state of the ^{3}He produced by the state dependence of the nucleon-nucleon force. A physical consequence of this is that the charge radius (R in the figures) as measured by electron scattering will be smaller for the triton (since the proton is closer to the CM) than for the helion[1] (since the protons are further away from the CM) [Friar, 1991].

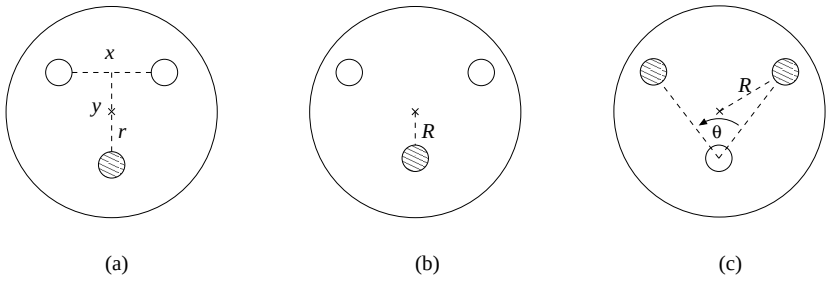

Figure 3.1: Schematic description of S- and S'-states in ^{3}He (left two) and ^{3}H (rightmost) [Friar, 1991]. The shaded and unshaded circles are the protons and neutrons, respectively.

[1] *triton* is the ^{3}H nucleus and *helion* is the ^{3}He nucleus.

3.2 The Polarized ^{3}He Target

The length of an experiment and the quality of data (high statistics) depends on the Figure-of-Merit (FOM) of various components of the experiment. For a polarized target, the FOM is proportional to the product of the luminosity and the target polarization:

$$\text{F.O.M.} \propto \mathcal{L} P_t^2 \tag{3.1}$$

where $\mathcal{L} = I\rho\ell$ is the luminosity, P_t is the target polarization, ρ is the target gas density, I is the electron beam current and ℓ is the length of the target cell. Thus, doubling the density reduces experiment run time (for production data) by a factor of two, and doubling the target polarization reduces it by a factor of four, a big advantage in terms of time and money. In this experiment, a total luminosity[2] of $\mathcal{L}_T \sim 5 \times 10^{36}$ cm^{-2}s^{-1} and an electron-neutron luminosity of $\mathcal{L}_{en} \sim 0.45 \times 10^{36}$ cm^{-2}s^{-1} was achieved.

Deuterium is a good choice as a neutron source mainly for unpolarized experiments on account of smaller dilution from the single proton in the nucleus (compared to two in ^{3}He). Running polarized experiments with deuterium as a neutron source (along with ^{3}He) is also beneficial to isolate nuclear effects since the deuteron is the simplest nuclear system to study nucleon-nucleon interaction. These effects inadvertently come into play as the neutrons are bound within the nucleus in both these cases.

3.3 Methods of Polarization of the ^{3}He Target

There are at least two ways of polarizing a ^{3}He target that have been and are being used in electron scattering experiments: spin-exchange optical pumping (SEOP) and metastability-exchange optical pumping (MEOP) [Happer, 1972].

For ^{3}He polarization by spin exchange, the high density of ^{3}He gas and the presence of N_2 lead to homogeneous broadening of the Rb absorption line[3] of 18 GHz/amagat for ^{3}He and 14 GHz/amagat for N_2, which greatly exceeds the natural (5.7 MHz) and Doppler (250 MHz at 200°C) widths. Under these conditions, broad-band laser light is effective for optical pumping. For metastability-exchange polarization of ^{3}He and spin-exchange polarization of H and D, the densities are hundreds of times less and Doppler broadening is dominant.

[2] *Total* here implies all particles encountered by the electrons including protons, nucleons from other gases present in the target, etc.

[3] As N_2 density was much less than the ^{3}He density (about 1.5%), nitrogen contribution to the broadening was small.

Effective optical absorption by all of the atoms requires careful matching the laser frequency distribution to the Doppler distribution.

The target region at the center of the Hall consisted of an iron target magnet box with the target cell with all required components for polarization and polarimetry within. The various aspects of the target are described in the sections below.

3.4 The Target

The target region consisted of the target magnet box placed at the center of the Hall with its longest sides rotated by about 30° to the electron beam direction. To its right (looking downstream) was the BigBite detector and the Neutron Detector to its left. The two Hall A HRS's (High Resolution Spectrometers) were positioned at about 90° to the beamline on either side. The arrangement of the Hall during the experiment is shown schematically in Figure 2.11.

The target holding field was generated by the magnet box which acted as a big electromagnet, unlike the earlier experiments in which Helmholtz coils were used. The main reason for this box was to shield the fringe fields of the powerful BigBite detector (dipole) magnet. It allowed us to place the detector very close to the target - at about 1 m - resulting in a high acceptance of 76 msr averaged over the target length (40 cm).

3.4.1 Construction of the Magnet Box

The box was made of $1/4''$ thick iron and was about $2 \times 2 \times 1$ m^3 in dimensions (see Figure 3.2). The current carrying coils produced the magnetic field within the box as demonstrated in the figure. The box had two windows on its longest sides, one for the scattered electrons to leave the box to be detected by the BigBite detector, and the other for access to the target region; and another smaller window along the shorter downstream side. The big windows affected the uniformity of the holding field; this will be discussed in section 3.9.

In order to make the target region "light-tight" as part of the safety protocol, the magnet box access windows were covered by quarter inch thick G10 plastic sheets. These were interlocked to the lasers. Since G10 was not entirely opaque to infrared light at 795 nm, aluminum tape was applied to the G10 plastic window covers. The window on the

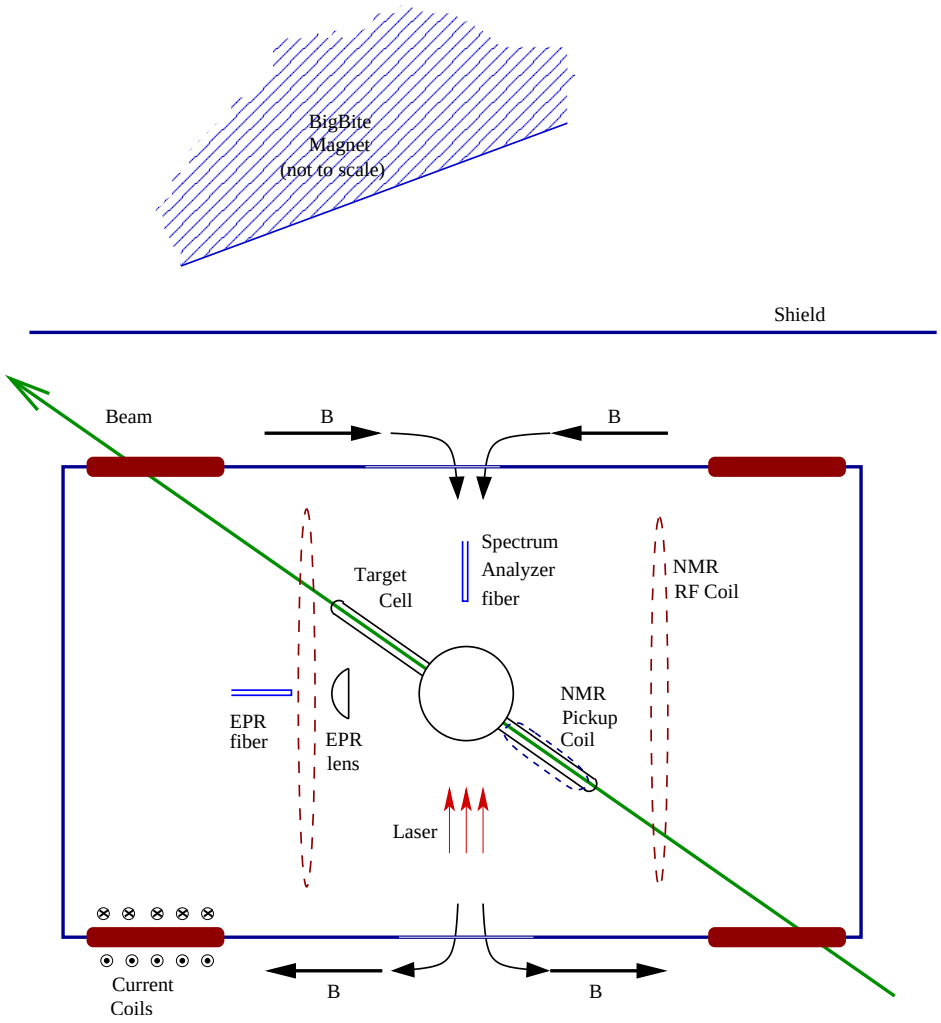

Figure 3.2: (color) The target magnet box. Shown are the direction of holding field and elements of EPR, Spectrum Analyzer and NMR.

BigBite side was covered by two layers of 5 mil thick *tedlar*[4] film. The tedlar film was thin enough for the scattered electrons to go through. The main reason for this cover was to prevent glass particles from leaving the box and getting into the BigBite magnet in case of a target cell explosion. Tedlar was opaque to the infrared laser light and was able to withstand high radiation within the target region. Due to safety concerns, the air inside the box was vented out from the top.

[4]From DuPont. http://www.dupont.com

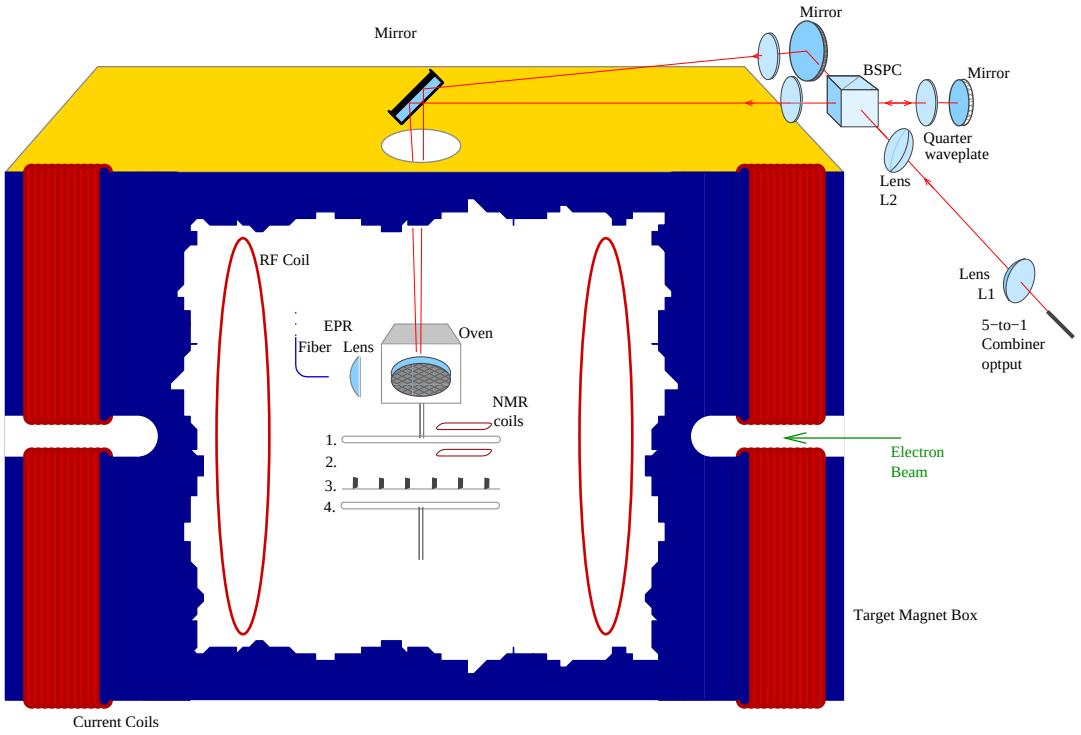

Figure 3.3: (color) The target setup within the box. The figure is not to scale. The polarizing optics are shown offset to the right of their actual position (which is above the coils on the right in the figure) for clarity. The numbers correspond to various target positions: 1. the Polarized ^{3}He target position; 2. the empty target position; 3. the carbon foils (optics target) position and 4. the reference cell position. The target ladder and other support systems are not shown. The beam enters the box at 30° to the side of the box (see Figure 3.2).

3.4.2 Producing the Holding Field

The magnet coils were connected to Agilent 6673A power supply. This power supply was remotely controlled by a DC voltage from a function generator. Ramping the voltage changes the current going through the coils thus effecting a sweep of the magnetic holding field. This method was implemented rather than controlling the power supply directly by computer since this method guaranteed completion of a sweep[5] in the event of a computer glitch or communication error. Stopping a sweep midway can be disastrous since it tends to destroy the polarization rather quickly.

[5]See sections 3.6 and 3.7 on polarimetry.

3.4.3 Target Ladder Positions

Figure 3.3 shows the G_E^n target setup within the target magnet box. The target ladder was mounted onto the box from the roof and consisted of the following elements:

- polarized ^{3}He target cell (our production target cell);
- empty target (for beam tuning and some background studies);
- carbon foils (the *optics* target for detector optics studies and beam tuning)
- reference cell (to study dilutions and background; also elastics, detector studies, etc.)

Any of the above targets could be positioned in the electron beam path within a millimeter by moving the target ladder vertically. This motion was controlled remotely via EPICS[6] from the counting house.

The Polarized ^{3}He target position

This was the topmost component of the target ladder. The target oven and other polarization and polarimetry optics were connected to the ladder so that they moved along with the ladder. These will be discussed later in this chapter. The cell was mounted by the transfer tube on a plate which is attached to the oven from below. RTV held the cell in place. The target cell pumping chamber was positioned at the center of the oven.

The empty target position

The empty target position had *no target*. This position was mostly used for beam tuning and during Møller measurements (section 2.2.3).

The optics target position: (carbon foils)

The optics target consisted of six carbon (^{12}C) foils, each with thickness[7] of about 47.79 mg/cm^2. This position was used for beam tuning, checking the raster size (section 2.3.3) and most importantly, for the optics studies of the BigBite spectrometer (section 4.2). A beryllium oxide (BeO) foil was placed at the center of the optics target to make the beam

[6] Experimental Physics and Industrial Control System
[7] Densities of ^{12}C and BeO are 2.2 and 3.01 g/cm^3, respectively.

spot visible to the naked eye due to florescence and thus ensure a well rastered beam and correct beam position. This foil was about 150.1 mg/cm^2 thick.

The reference cell position

The reference cell was very useful to determine backgrounds and for elastics studies for detector calibration and resolution. Depending on the nature of the study, the reference cell was filled with either hydrogen, nitrogen or helium-3 for elastic scattering, dilution and background studies or was evacuated to study background from glass.

3.4.4 Hybrid Target Cells

A new "hybrid" technology was used for the target cells. These contained a mixture of potassium (K) and rubidium (Rb) alkali metals in the pumping chamber. This new "hybrid" pumping technology was reported by [Babcock *et al.*, 2003] and [Chann *et al.*, 2002]. It was observed that while about 50 photons were required to polarize a single polarized ^{3}He nucleus for pure rubidium pumping, only four photons were required in the case of hybrid pumping [Babcock *et al.*, 2003]. This results in faster spin-ups and lower polarization losses during polarimetry. Also, because of the faster polarization rates, the competing relaxation rates are further subdued, resulting in higher overall polarizations [Newbury *et al.*, 1993]. Table 3.1 shows the target cells used for various kinematics during the experiment.

Table 3.1: The target cells used during the G_E^n kinematics

Kinematic $(\mathrm{GeV}/c)^2$	**Designation**	**Period of run**	**Target cell used**
1.3	kin1	Mar01 - Mar 09	Barbara
2.5	kin2a	Mar 09 - Mar 22	Dolly
3.4	kin3a	Mar 22 - Apr 14	Edna
2.5	kin2b	Apr 14 - Apr 18	Edna
3.4	kin3b	Apr 20 - Apr 30	Edna
1.8	kin4	May 01 - May 10	Edna

3.4.5 Making of the Target Cells

The cells used in the experiment were blown at Princeton by Mike Souza and filled at the University of Virginia[8]. The G_E^n geometry cells were conventionally decided to be given female names in the Roman alphabetical order. The cells used were Barbara for kinematic 1 (1.3 $(\mathrm{GeV}/c)^2$), Dolly for kinematic 2a (2.5 $(\mathrm{GeV}/c)^2$) and Edna for kinematics 2b, 3 and 4 (2.5, 3.5 and 1.7 $(\mathrm{GeV}/c)^2$, respectively[9]). The characteristics of the cells are summarized in Table 3.2.

Cell	V_{tot}	V_{pc}	V_{tt}	V_{tc}	density	P_{tc} (at 255°C)	K/Rb ratio
Barbara	393.49	306.81	3.49	83.19	7.56	13.2	20
Dolly	378.22	293.54	3.37	81.30	7.39	12.5	18.6
Edna	374.85	290.30	3.40	81.15	7.40	12.5	5.1

Table 3.2: Cells characteristics. V stands for the volume with subscripts indicating total (tot), pumping chamber (pc), transfer tube (tt) and target chamber (tc), and P stands for pressure. The alkali ratio is the K to Rb ratio at 235°C. The volumes are in cubic centimeters, the pressures in atmospheres and the density in amagats. [UVa, 2006]

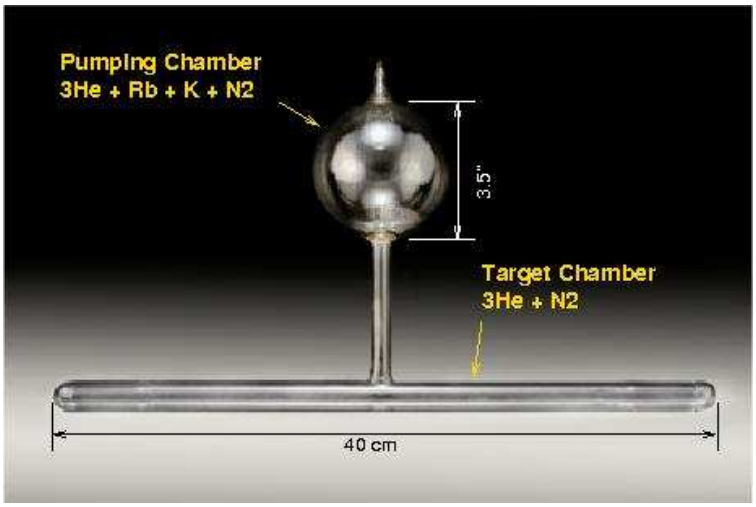

Figure 3.4: Cell geometry and dimensions.

The geometry of the target cells was a little different than in the previous polarized ^{3}He experiments [Kramer, 2003, Solvignon, 2006, Sulkosky, 2007]. The dimensions of the target cell are as shown in Figure 3.4.

[8]The details of cell filling are given in many theses, e.g. [Romalis, 1997, Kramer, 2003].
[9]Data for kinematic 2b was taken for a few days in the middle of the kinematic 3 period.

3.4.6 Heating of the Gas

The oven which enclosed the pumping chamber of the target cell was connected to a source of compressed air. The air passed through two heaters - one controlled by a variac and the other by PID feedback electronic control chassis[10] - and was heated to temperatures of about 245°C. Resistive Temperature Devices (RTDs) placed in the oven measured the temperature within the oven. Thus, the gases and alkali metals inside the pumping chamber were heated up to 245°C, too. The air pipes entered and exited the target area and the oven through a larger ceramic pipe attached to the top of the magnet box and also supported the oven.

3.4.7 Optical Pumping Method

Alkali metal rubidium with a $5\,^2S_{1/2}$ ground state and a $5\,^2P_{1/2}$ excited state is illuminated by 794.7 nm circularly polarized light that corresponds to the frequency difference between the two states and which propagates along or against the magnetic holding field direction [Wagshul and Chupp, 1994]. Rubidium has an nuclear spin $I = \frac{5}{2}$ making $F = I \oplus J$ for the hyperfine splitting, where $J = L \oplus S$, thus making $F = 2, 3$ for the system. Furthermore, the presence of the magnetic field Zeeman splits the F levels into further sub-levels with magnetic quantum number $m_F = -F, -F+1, \ldots, F-1, F$. For right (left) circularly polarized light, $\sigma_+(\sigma_-)$, the selection rules transform as $\Delta m_F = +1(-1)$ and thus, only atoms in the $-\frac{1}{2}(+\frac{1}{2})$ sub-level can absorb the photons and get promoted to the $m_F = +\frac{1}{2}(-\frac{1}{2})$ sublevel of the $^2P_{1/2}$ state. These atoms decay quickly ($\sim 10^{-8}$ s) back to the ground state sub-level $m_F = -\frac{1}{2}(+\frac{1}{2})$ and $m_F = +\frac{1}{2}(-\frac{1}{2})$ with probability 2/3 and 1/3, respectively. As this process continues, the atoms are eventually "pumped" to the $m_F = +\frac{1}{2}(-\frac{1}{2})$ sub-level, thus leading to the polarization of the rubidium. These rubidium atoms then transfer their spins to potassium which in turn transfer it to the ^{3}He nucleus via hyperfine-like interaction[11]. The alignment of the spins parallel or anti-parallel to the holding field[12] is schematically shown in Figure 3.6.

^{3}He S-P transitions lie in the far ultraviolet region making it difficult to polarize the

[10] The heater control chassis was homemade.

[11] Hyperfine-*like* because the interaction is between electrons and nucleus of different atoms. ^{3}He electrons are in a spin singlet state and do not contribute to any interactions (whence the *inert gas* character for helium).

[12] During the experiment, we flipped the sense of circular polarization of the laser light between right and left thus switching the direction of the ^{3}He spins with respect to the holding field.

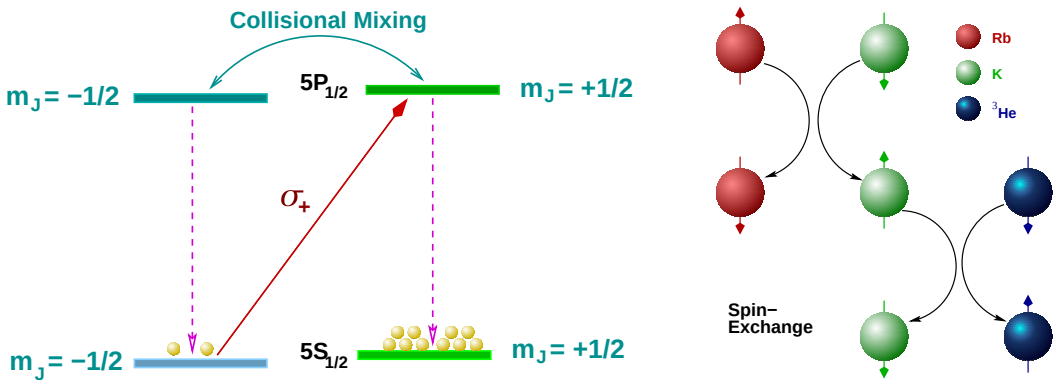

(a) Optical pumping (b) Two-step spin-exchange

Figure 3.5: (color) Subfigure (a) shows how Rb is optically pumped (in this case into the $m_F = +3$ state) and subfigure (b) shows the 2-step process of spin-exchange first from rubidium to potassium and then from potassium to ^{3}He.

target using MEOP. Instead a three-step process was used in the G_E^n experiment[13]. First, rubidium is optically pumped by circularly polarized laser light corresponding to the $^5S_{1/2}$–$^5P_{1/2}$ (D_1) transition, the polarization is then transferred to potassium via (electronic) spin-exchange and then finally to ^{3}He by spin-exchange via hyperfine interaction.

Since the magnetic moment of ^{3}He is negative ($\mu_{^3\mathrm{He}} = -2.12\mu_B$), the ^{3}He spins being parallel to the magnetic holding field reduces the Zeeman splitting whereas the spins being anti-parallel increases the Zeeman splitting.

3.4.8 Spin Exchange

Hybrid SEOP (Spin Exchange Optical Pumping) relies on rapid spin transfer from the Rb to the K atoms. The K-Rb spin-exchange cross section is extremely large, about 200 Å [Babcock *et al.*, 2003]. At typical densities of 10^{14} cm^{-3} or more, the K-Rb spin-exchange rate exceeds 10^5/s which is much greater than the typical alkali spin-relaxation rates (~ 500/s). Thus, the K and Rb atoms are in spin-temperature equilibrium and have equal electron spin polarizations P_A. The ^{3}He gains polarization P_{He} by collisions with both polarized K and polarized Rb atoms, and loses it in other processes at a rate γ_{He} [Babcock *et al.*, 2003]:

$$\frac{\mathrm{d}P_{^3\mathrm{He}}}{\mathrm{d}t} = \gamma_{\mathrm{SE}}(P_A - P_{^3\mathrm{He}}) - \gamma_{^3\mathrm{He}}P_{^3\mathrm{He}}, \tag{3.2}$$

[13] In previous experiments, a two-step process was used since the cells had only one alkali metal, viz. rubidium.

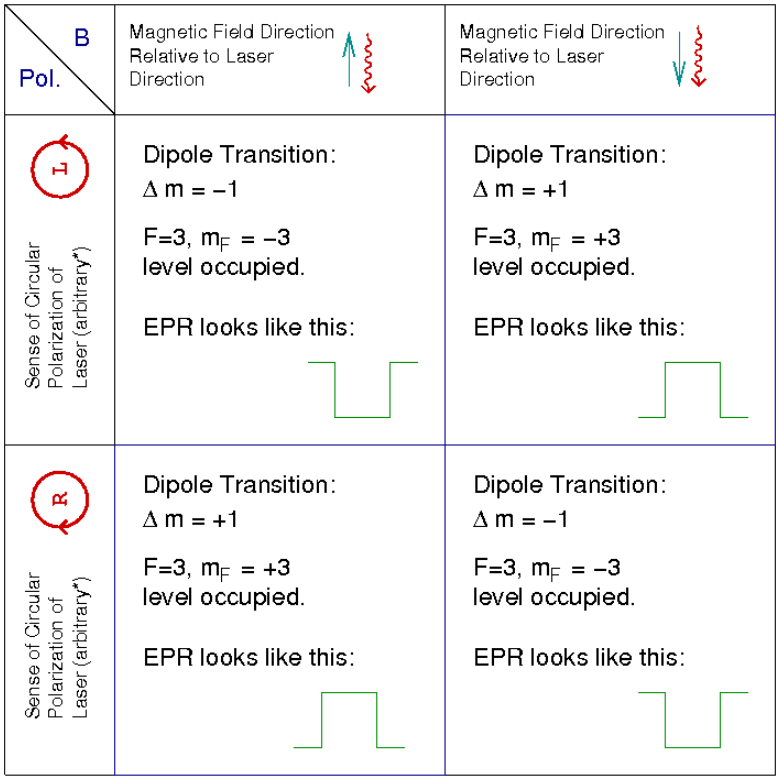

Figure 3.6: (color) The sense of circular polarization of laser light and selection rules.

where $\gamma_{\rm SE} = k_K[\rm K] + k_{\rm Rb}[\rm Rb]$ is the spin-exchange rate, $k_{\rm K}$ and $k_{\rm Rb}$ are the spin-exchange rate coefficients, and [K] and [Rb] are the potassium and rubidium densities, respectively. The SE rate coefficients are velocity averaged to account for the Maxwell-Boltzmann distribution of the atoms in the cell; $k_{\rm K} = \langle \sigma_{\rm SE} v \rangle_{\rm K}$, $k_{\rm Rb} = \langle \sigma_{\rm SE} v \rangle_{\rm Rb}$

The K atoms lose angular momentum by spin exchange to ^{3}He and by spin relaxation mainly in K-K, K-Rb and K-^{3}He collisions. The effective spin relaxation rate for Rb in this case increases from its rate in the absence of K to

$$\Gamma'_{\rm Rb} = \Gamma_{\rm Rb} + \mathcal{D}\Gamma_{\rm K} + q_{KR}[\rm K], \tag{3.3}$$

where $\mathcal{D} = [\rm K]/[\rm Rb]$ and Γ_K is the total K relaxation rate. The K-Rb collisional loss rate $q_{KR}[\rm K]$ is small under most conditions of interest.

The spin exchange efficiency for hybrid pumping is

$$\eta_{\rm SE} = \frac{\gamma_{\rm SE}[^3\rm He]}{[\rm Rb]\Gamma'_{\rm Rb}} = \frac{(k_{\rm Rb} + \mathcal{D}k_{\rm K})[^3\rm He]}{\Gamma_{\rm Rb} + \mathcal{D}\Gamma_{\rm K} + q_{KR}[\rm K]}. \tag{3.4}$$

For large $\mathcal{D}$, the K-Rb SE efficiency is equal to the K-^{3}He SE efficiency $k_{\mathrm{K}}[^3\mathrm{He}]/\Gamma_{\mathrm{K}}$, though $\mathcal{D} \sim 1$ already promises substantial improvements over Rb only cells. The hybrid target cells used in this experiments had $\mathcal{D} \sim 20$ in the gaseous phase at operating temperatures for Barbara and Dolly and about 5 for Edna.

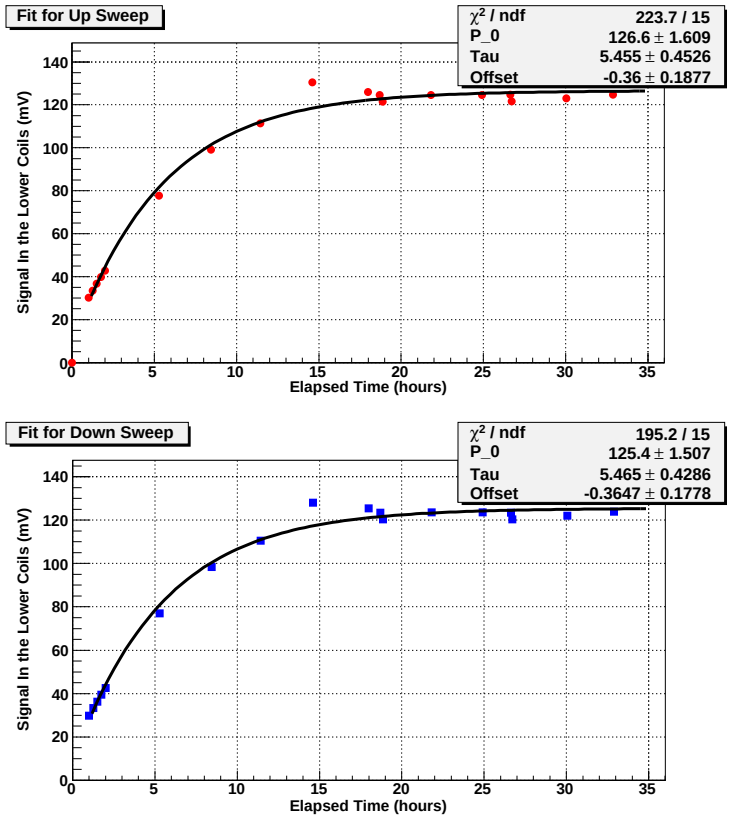

Figure 3.7: (color) The spin-up curves for target cell Edna. The two plots correspond to the up and down sweeps of NMR polarimetry method (See section 3.6).

Polarization of ^{3}He in the target cell is obtained by transfer of polarized atoms from the optical pumping cell with polarization P_p. For a given rate of polarization transfer to the target cell per ^{3}He or, in other words, the diffusion rate, G, the time dependence of the target-cell polarization (P_t) can be represented

$$\frac{\mathrm{d}P_t}{\mathrm{d}t} = G(P_p - P_t) - \Gamma_t P_t \tag{3.5}$$

where Γ_t is the total ^{3}He spin-relaxation rate in the target cell. The equilibrium ^{3}He polarization is therefore

$$P_t = P_p \frac{G}{G + \Gamma_t} \tag{3.6}$$

For a spin-exchange target, the polarization rate in the pumping chamber is much less than the transfer rate to the target chamber, and G is effectively equal to the spin-exchange rate γ^{SE}. For our target geometry [Kelleher *et al.*, 2007],

$$G = \frac{A_{tr}}{V_p L} D_t K, \tag{3.7}$$

$$D_t = D(T_0) \frac{n_0}{n_t} \left(\frac{T_t}{T_0} \right)^{m-1} \tag{3.8}$$

where A_{tr} and L are the cross-sectional area and length of the transfer tube, V_p is the volume of the pumping chamber, D_t is the diffusion constant at the target chamber, $n_0 = 7.4$ amg[14], n_t is the ^{3}He number densities at temperature T_t, $m = 1.7$ and $D(T_0) = 2.76$ cm^2/s at 80°C and K is a constant that depends on the target chamber and pumping chamber temperatures ratio given by

$$K = \frac{(m-2)(T_T - T_P)T_T}{(T_T/T_P)^m T_P^2 - T_T^2} \tag{3.9}$$

3.4.9 Lasers and Optical Fibers

For G_E^n, we used three single FAP system diode lasers from Coherent, and one DuoFAP system, which was a newly developed technology by Coherent. The DuoFAP consisted on two diode lasers in one physical unit, although in our case, both these diodes were used as individual lasers. These lasers were located in the *laser lab* behind the Hall A counting house. Light from these lasers was transported into the Hall via 75 m long optical fibers. These fibers were connected to a five *legs* of the five-to-one combiner in the Hall via SMA-SMA adapters. The output of the combiner was then incident on the first lens of the polarizing optics elements. The switch from 75 m fibers to the combiner input legs took place in an enclosed box. This box was interlocked to the lasers. Cool air circulating through the box kept the fiber and adapters temperature well below the damage threshold of 40°C, as stated by the manufacturing company. As a further safety precaution, we had set the limit to 35°C. A temperature interlock box was built to shut off the lasers in case the temperatures exceeded the set limits[15], but we mostly relied on the shift crew to keep an eye on the fiber temperatures. The fiber temperatures did not cause any trouble throughout the experiment.

[14] 1 amg (amagat) is the density of a gas at standard pressure and 0°C.

[15] This box was located in the laser lab, near the lasers. The temperatures were read off by RTDs attached to the fibers in the Hall and fed into the interlock box and displayed on the main target computer via VNC (Virtual Network Computing).

Table 3.3: Power hitting the pumping chamber after the fibers and the polarizing optics elements. Single-pass and double-pass beams refer to light going through the beam-splitter-polarizing cube once and twice respectively. The vertical placement of the powermeter head was not optimal during the measurement (because of positioning difficulties), so the actual powers are about 5% higher than those in this table.

Laser	Single-pass beam (W)	Double-pass beam (W)
Laser # 1	7.11	6.18
Laser # 2	9.8	8.48
Laser # 3	10.2	10.0
Duo # 1	10.8	10.2
Duo # 2	9.2	8.46

3.4.10 Polarizing Optics

We faced a new challenge in circularly polarizing the laser light since we were using the combiner. The combiner output had five beams at the vertices of a regular pentagon as shown in Figure 3.8. Thus, even though the individual beams themselves converge after passing through the first lens (Figure 3.11), the five beams diverge from each other. To overcome this problem, a second lens of a much larger effective focal length was placed between the first lens and the beam-splitter-polarizing cube (BSPC). This two-lens system converged the five beams onto the target. [Singh, 2007]

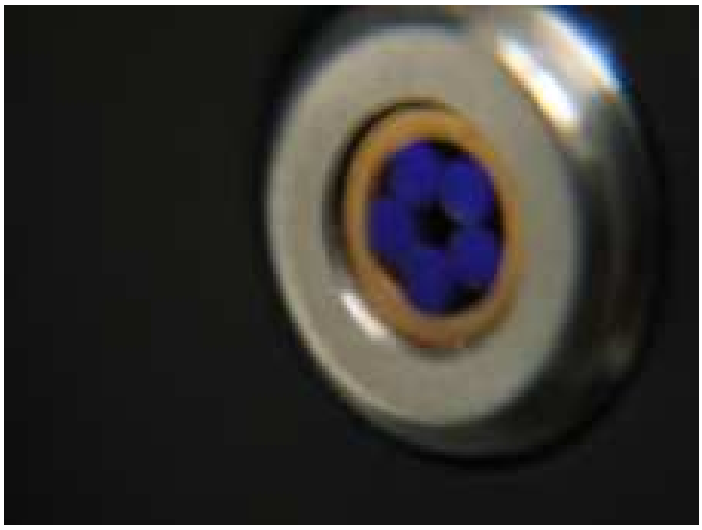

Figure 3.8: The outlet of the five-to-one combiner.

To begin, the Gaussian parameters of the laser beam from a given laser-fiber combination were determined: the beam waist, the waist position and beam divergence. The laser

beam was captured in the powermeter head after being passed through a lens of effective focal length (efl) of 38.1 mm and diameter of 2″ as shown in Figure 3.9. An iris was placed between the lens and the powermeter head and moved between the two with the iris diameter adjusted such that the power measured by the powermeter was I_0/e^2, where I_0 is the maximum power measured with no iris. Iris radius versus distance from lens was plotted and fitted to the Gaussian beam form

$$w(z) = w_0 \left[1 + \left(\frac{\lambda z}{\pi w_0^2}\right)^2\right]^{\frac{1}{2}} \tag{3.10}$$

and the beam parameters were extracted. Here, w is the beam diameter (corresponding to e^{-2} of the maximum intensity), λ is the wavelength of the propagating light beam along the $z-$direction. Using ray transfer matrix method (or ABCD matrix method), the Gaussian beam was propagated backwards to the fiber and the position and size of the beam waist and the divergence of the beam were determined at the output of the fiber. The transfer matrix for this system is given by

$$\mathbf{S} = \begin{pmatrix} 1 + \frac{t}{R_1}\frac{n-n'}{n'} & \frac{t}{n'} \\ \frac{n-n'}{R_1 R_2}\left[R_2 - R_1 - \frac{t(n-n')}{n'}\right] & 1 - \frac{t}{R_2}\frac{n-n'}{n'} \end{pmatrix} \tag{3.11}$$

where R_1, R_2 are the radii of curvature of the front and back surfaces of the lens, t is the lens thickness at the thickest region and n, n' are the indices of refraction of the two media the light travels from and into.

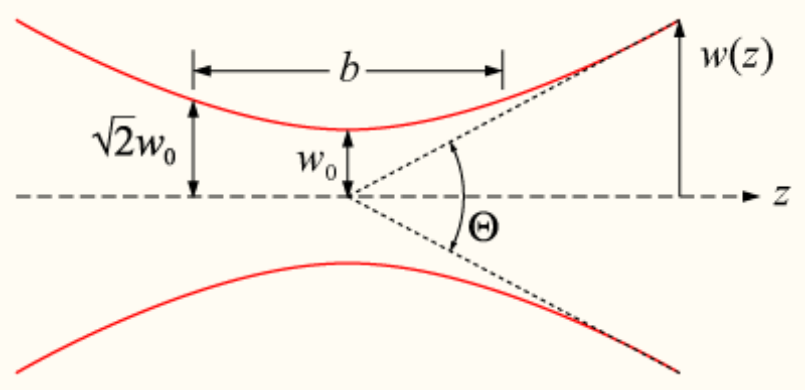

Figure 3.9: The laser beam Gaussian parameters. Laser light went through a 75 m long optical fiber. w_0 is the beam waist, $z_0 = \frac{\pi w_0^2}{\lambda}$ is the Rayleigh range, θ is the beam divergence, $\Theta = 2\theta$ is the total beam spread from the waist position and $b = 2z_0$ is the confocal parameter. (Figure from Wikipedia.)

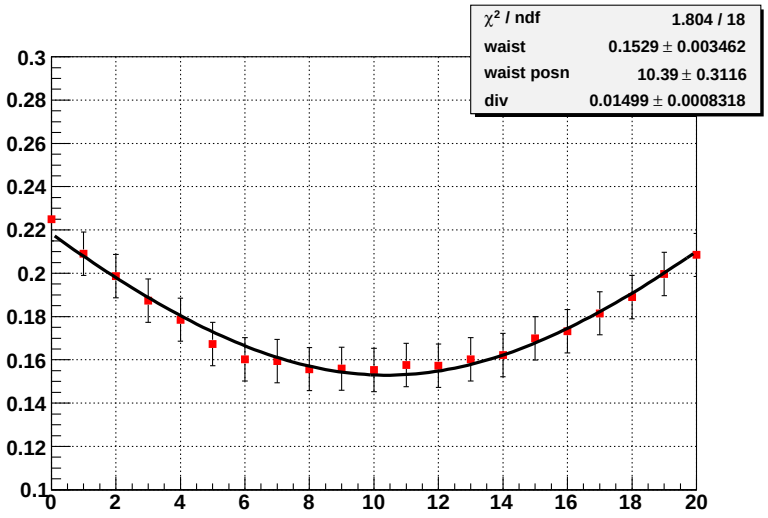

Figure 3.10: Data from setup to determine Gaussian beam parameters for a set of optical components.

These parameters were then fed into two simulation programs to determine the final optics parameters like distances and focal lengths. One simulation program was written in FORTRAN to be used with PAW++ on a Linux machine and the other was based on the LabVIEW software from National Instruments running on a Windows machine. The PAW++ simulation had lens thicknesses built-in whereas the LabVIEW simulation used the thin lens approximation[16]. The numbers obtained from the simulations served as a first starting point for the optics setup. Once the first rough setup was in place, further fine tuning had to be done for optimum results. These fine tunings were required because real characteristics of the beams (Gaussian parameters) varied between the five lasers and optical fibers, and the simulations were not done for all the permutations possible between lasers and fibers. Furthermore, the bending of the fibers along with coupling between the 75 m fibers and the combiner caused the beam characteristics to change along the way.

Figure 3.11 shows the optics setup. Laser light from combiner output passes through the first lens L1 where the five beams start to diverge from each other. The second lens, L2, at a distance of about 120 cm converged the five beams at the pumping chamber[17]. Note that the five beams converged towards the central axis, the individual beam sizes

[16]Thin lens approximation can be used when the effective focal length of the lens is much greater than its thickness.

[17]This distance was for a 3.5″ diameter pumping chamber and a distance of about 4 m between the first lens and the pumping chamber (this experiment). The distance between L1 and L2 for a pumping chamber diameter of 2.5″ was about 135 cm.

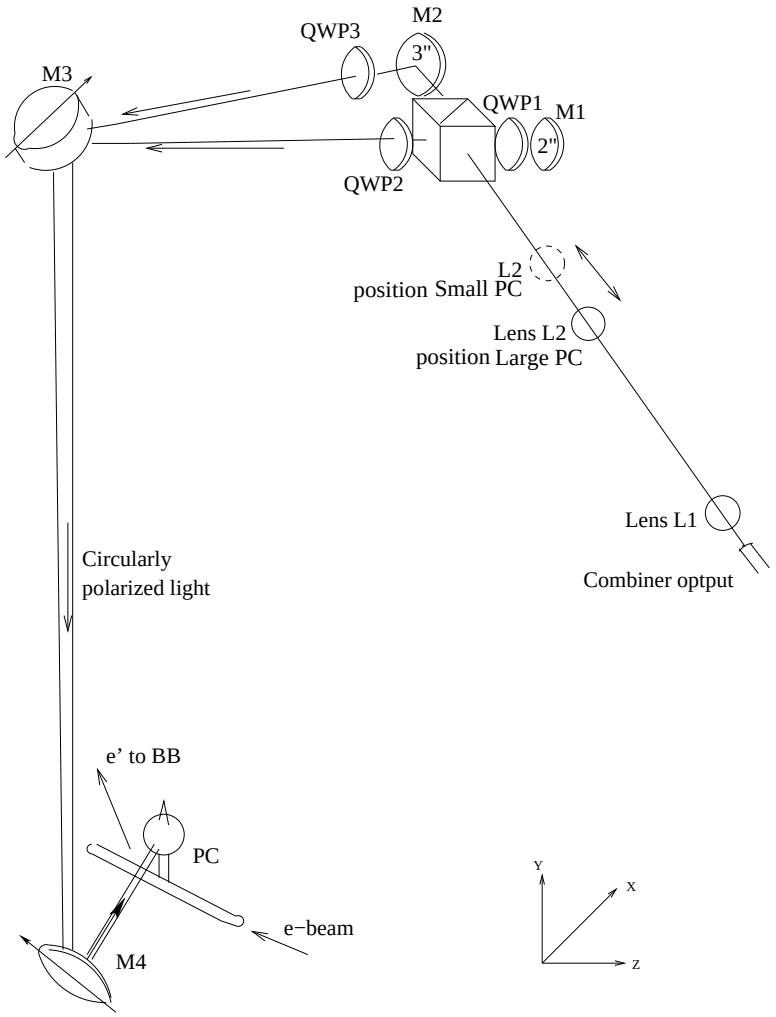

Figure 3.11: The polarizing optics setup.

grew according to their Gaussian beam characteristics. On the way to the cell, the beams have to pass, after the lens L2, through a set of polarizing optics which give us circularly polarized light required to optically pump the rubidium. The first element is the Beam Splitting Polarizing Cube or BSPC. It splits the beam into two components - the S wave, perpendicular to the plane of reflection[18] and the P wave, parallel to the plane of reflection. The S-wave is reflected while the P-wave is transmitted. This P-wave then simply reflects from a $3''$ mirror and onto the cell via a quarter waveplate and two $6''$ mirrors. The S-wave on the other hand goes through a quarter waveplate and attains a certain circular polarization. This wave is then reflected back by a mirror which reverses the helicity of the

[18]From the German words *senkrecht* meaning perpendicular, and *parallel* meaning parallel.

circular polarization which on passing through the quarter waveplate once again, rotates the plane of the linear polarization by 90° to the original plane, or, the S wave now becomes a P-wave and passes through the BSPC. This beam then goes through another quarter waveplate to attain circular polarization and hits the cell via the two 6″ mirrors. Whether the $m_F = +3$ or $m_F = -3$ state of the rubidium gets occupied depends on the angles of the final two quarter waveplate with respect to the linear laser polarizations incident on them.

The degree of circular polarization of the laser light was measured about half a dozen times. All but one measurements were done in the *short cut* (or coarse) way to save time during data taking[19]. A detailed measurement was done after the experiment the result of which is shown in Figure 3.12. The data in the figure was fit to the formula

$$I(\theta) = \frac{I_0}{2}\left[1 + A\cos(2\theta - \phi)\right] + \text{ a linear term.} \tag{3.12}$$

where $I_0/2$ is the mean power reading, A is the asymmetry and θ is the angle of the polarizer that was varied over 360°. Note that had the laser polarization been perfectly circular, then $A = 0$ and the plot would be a straight line at $I_0/2$ (ignoring linear drifts). The *circularity* is then calculated using $P_c^2 + A^2 = 1$, where P_c is the degree of circular polarization of the laser light. Table 3.4 shows results of a typical crude measurement.

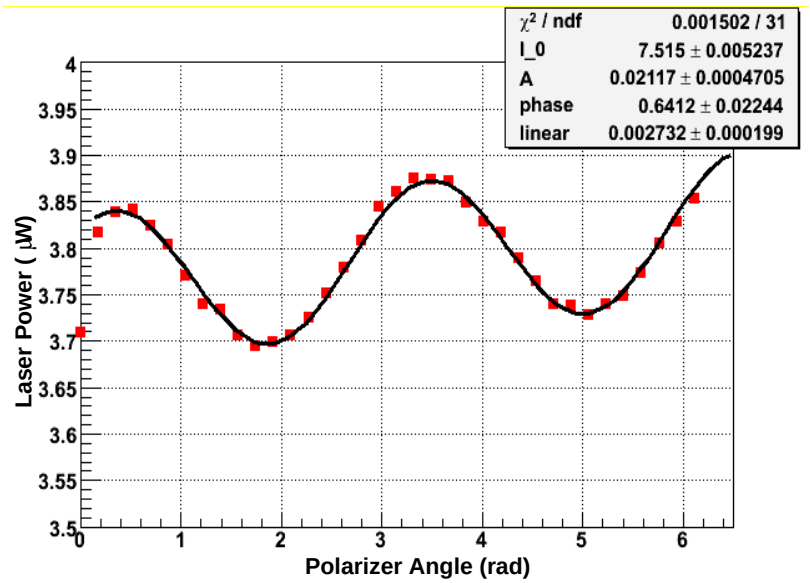

Figure 3.12: Degree of circular polarization for the laser light.

[19] All laser related work had to be done by putting the Hall in Laser Controlled Access due to safety reasons and hence no one else could be present in the Hall during the measurements (except other laser trained personnel).

Table 3.4: Circular polarization measurement of the incident laser light done the crude way. $P_c^2 = 1 - A^2$, $A = \frac{P_{\max} - P_{\min}}{P_{\max} + P_{\min}}$. The two sets indicate two separate measurements for the same quantities.

	Double-pass beam		Single-pass beam	
	Set 1	Set 2	Set 1	Set 2
Max. Power, $P_{\max}$ (μW)	5.355	5.329	10.820	10.709
Min. Power, $P_{\min}$ (μW)	5.149	5.129	8.976	8.907
P_c	99.98%	99.98%	99.565%	99.577%
Average P_c	**99.98%**		**99.57%**	

3.4.11 Monitoring the Target during the Experiment

The taret system was monitored in real time from the counting house by various temperature sensors (RTDs) attached to most components of the target. One important instrument for monitoring the target cell was the Spectrum Analyzer. The laser light that passed through the target pumping chamber was captured onto an optical fiber and fed into the Spectrum Analyzer. When the Rb atoms absorbed the laser light corresponding to the D_1 transition, the laser light spectrum showed a dip at that wavelength, as seen in Figure 3.13. This dip was an indication that the target was being pumped. If the dip disappeared, it meant that either the oven was cold or that the target pumping chamber had exploded. In the earlier case, the dip would disappear slowly as the target gradually cooled down. In the case of an explosion, the dip would disappear instantly.

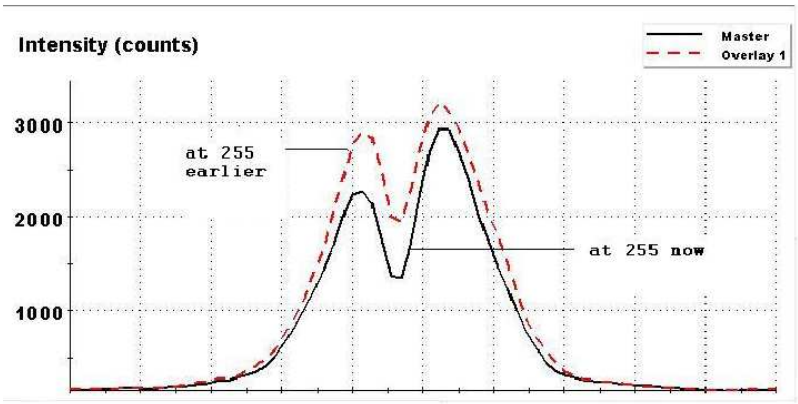

Figure 3.13: Spectrum Analyzer output seen on the main target monitor.

The spectrum and the dip were also indicative of the wavelength at which the lasers were putting light out. If the dip was off-center, the laser wavelength was not optimal (794.7 nm)

and we were not utilizing all of the output laser power for polarization. The wavelength of the diode lasers was dependent on the temperature of the diodes[20] and by adjusting this temperature, the laser wavelength could be shifted so that the spectrum dip is at the center of the lineshape of the laser light.

3.5 Measuring Polarization

Polarimetry methods employed during the experiment - Nuclear Magnetic Resonance and Electron Paramagnetic Resonance - used the Adiabatic Fast Passage (AFP) technique to measure the polarization of the ^{3}He gas. The passage of the spins through resonance must be fast enough compared to the spin relaxation times (the Fast condition) or else we lose spins due to relaxation, and slow enough compared to their Larmor precession (the Adiabatic condition) or else the spins cannot follow the sweep. AFP can be performed in two ways that are mutually symmetric in concept. One can sweep the magnetic holding field while keeping the frequency constant (Field Sweep method) or alternatively, sweep the frequency while keeping the holding field constant (Frequency Sweep method). The AFP signal is symmetric with respect to the two parameters[21]. The AFP condition for Frequency Sweep (FS) is worked out in Appendix B; the Field Sweep condition is derived in [Abragam, 1996] and reads:

$$\frac{H_1}{T_2} \ll |\dot{H}_0| \ll \gamma H_1^2. \tag{3.13}$$

where H_1 is the RF field, T_2 is the spin relaxation time, H_0 is the target magnetic holding field and γ is the gyromagnetic ratio (3.24 kHz/G for ^{3}He). The dot represents derivative with respect to time. We see that the rate depends on the RF field, H_1. A good starting number to choose for the rate is the geometric mean of the two extremities, e.g. for $H_1 = 90$ mG and $T_2 \approx 3$s, $\dot{H}_0 \approx 0.9$ G/s.

The AFP condition for frequency sweep is derived in Appendix B. Though FS-NMR was not used for G_E^n, it will be extensively used by future JLab experiments.

[20] $\Delta\lambda/\Delta T = 0.28$ nm/(C°); $\Delta P/\Delta T = -1\%/(\text{C}^\circ)$. It also depends on the ambient temperature, so if the surrounding temperature changed drastically, the diode temperature to achieve a particular wavelength changed, too. The diode temperatures were adjusted for all the lasers used to achieve the optimal wavelength of 794.7 nm.

[21] There is one major difference in that the electrical components - including electronic devices - have frequency dependent response which brings about the difference in the two methods.

3.6 NMR Polarimetry

The AFP method described above essentially comprises NMR or Nuclear Magnetic Resonance. NMR was used to monitor the polarization of the target during the experiment. It was performed using the field sweep method. There were a few concerns about the linearity of the field sweep due to observed hysteresis effect in the iron target magnet box. Studying this effect revealed that the up sweep was very linear over a large range (20 -40 Gauss), whereas the down sweep was slightly more non-linear towards the extremities of this range [Kelleher *et al.*, 2007]. The overall results, though, were not affected much by this non-linearity.

NMR by itself does not give the absolute polarization of the ^{3}He nuclei. It needs to be calibrated against a method which gives the absolute polarization. We traditionally used two such means: water NMR and Electron Paramagnetic Resonance[22]. The thermal polarization of water is a very well known quantity and calibrating the ^{3}He NMR against water NMR gives a very good calibration for ^{3}He NMR. Unfortunately, water NMR could not be successfully performed primarily due to the magnet box and its hysteresis and non-linearity effects. Therefore, only EPR was used to calibrate the NMR. EPR is explained in much detail in the following section (3.7).

Since water NMR was not performed, calibration due to EPR could not be cross-checked by another independent method. This prompted development of new techniques to get a better understanding of the systematic uncertainties. One such real-time technique involved mounting a second pick-up coil at the pumping chamber. This allowed us to evaluate the polarization gradients from the pumping chamber to the target chamber due to diffusion of the ^{3}He gas. The transfer tube in this case was narrower and longer than in the earlier cases. Also, this allowed us to better correct the EPR calibration constant since the EPR measures polarization in the pumping chamber whereas NMR measures it in the target chamber.

NMR measurements were made on both chambers (pumping and target chambers) roughly once every four hours throughout the run of the experiment. EPR was done about once a day and the calibration constant was monitored as a measure of stability of the target system.

[22] Another method, the elastic scattering from the target coupled with electron detection in the HRS, was planned but not implemented.

3.6.1 Hardware and Setup

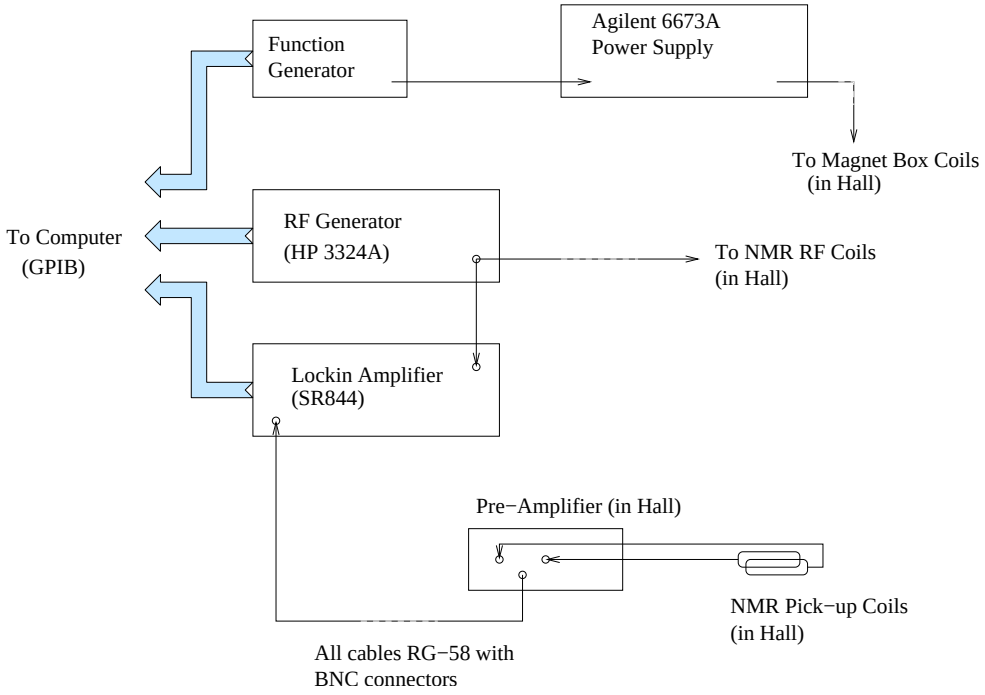

Figure 3.14: The NMR setup.

The essential NMR hardware consisted of radio frequency (RF) generating coils and a pair of pick-up coils. The setup is shown in Figure 3.14. An RF generator (HP 3324A) produced an RF field at a frequency of 91 kHz in the target region in a direction perpendicular to the holding field direction. This frequency corresponds to a ^{3}He resonance at about 28.1 G[23]. The holding field was then swept from about 25 G (the nominal value of the field) to 32 G and back at about 0.9 G/s as determined by Equation 3.13. During the sweep, the ^{3}He spins flip from being parallel to the holding field to being anti-parallel (*up sweep*) and back (*down sweep*). Each time, as the spins pass through resonance, the flux through each of the pick-up coils changes. This change in flux induces an electromotive force (EMF) through the coils and the currents produced are fed into a pre-amplifier (channels A and B of SR620 instrument). The coils are connected such that when the two input signals are subtracted (A-B), the real signals add and noise subtracts. The pickup coils are placed as close to the cell as possible and perpendicular to the RF field so as to minimize direct pickup from the applied RF field. This signal from the pre-amplifier (set to a gain of 10) is sent to a lock-in amplifier which is locked to an external 91 kHz signal (from the RF

[23] $H_{res} = \frac{\omega}{\gamma}$, where $\gamma \approx 3.24$ kHz/G for ^{3}He.

generator HP 3324A). This signal is read out by a computer via a GPIB interface. The signal produced, S is proportional to the target polarization and is fitted to the square root of a Lorentzian[24].

$$S \propto \frac{\omega_1}{\sqrt{(\omega - \omega_0)^2 + \omega_1^2}} \tag{3.14}$$

where ω_0 is the precession frequency of the spins in the holding field and ω, that due to the applied RF field. ω_1 is related to the width of the peak, and gives the magnitude of the magnetic field due to the applied RF.

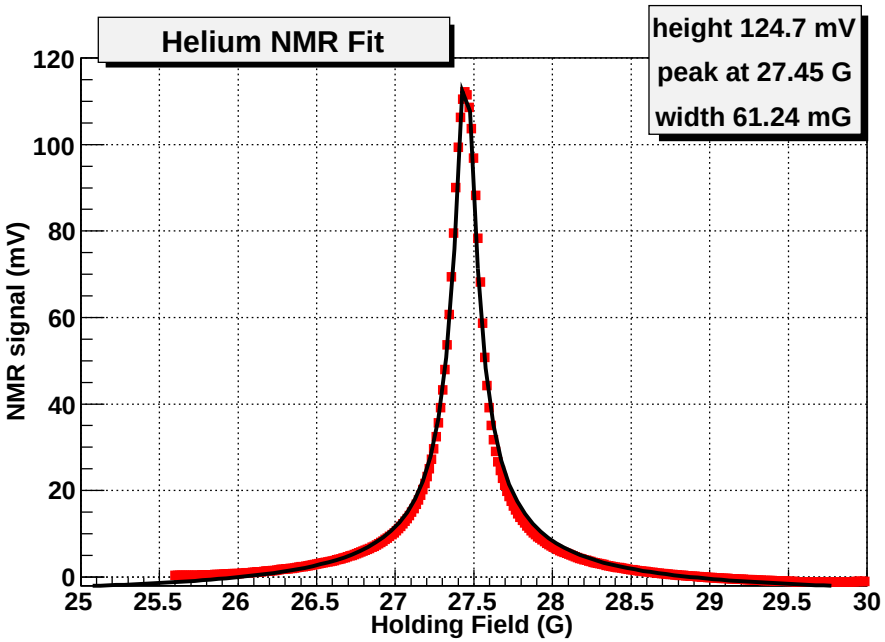

Figure 3.15: A typical NMR resonance fitted to the square root of a Lorentzian. This plot is for the up sweep (see text for explanation).

Figure 3.15 shows a typical NMR measurement with the fit. The width of the peak (FWHM or full-width at half-maximum) gives the magnitude of the applied RF field. The height of the peak is proportional to the ^{3}He polarization which, after calibration, gives the absolute polarization of the ^{3}He gas. In our case, the calibration was done against EPR as described in the next section.

[24]This is an approximation to the solution to the Bloch equations as explained in [Abragam, 1996] or Appendix B.

3.7 EPR Polarimetry

EPR, or Electron Paramagnetic Resonance, was used as the method to calibrate the NMR and get the absolute polarization of the target. EPR measures the splitting of energy levels in the presence of an external magnetic field via the Zeeman effect: $\nu_{\mathrm{EPR}} = |(\nu_0 + \Delta\nu_{B'}) - (\nu_0 - \Delta\nu_{B'})|$. In the pumping chamber, the rubidium and potassium energy levels are split due to the magnetic holding field. This splitting corresponds to a frequency $\nu_0 = k_z B_0$ with $k_z = 0.466\mathrm{MHz/G}$ for rubidium. A shift in this frequency, $\Delta\nu_{B'}$, comes about because of small effective magnetic fields created by Rb-K and K-^{3}He spin exchange interactions, B_{SE}, and by the polarized ^{3}He, $B_{^3\mathrm{He}}$,

$$B_{\mathrm{SE}} = \frac{2\hbar K_{\mathrm{SE}}[^3\mathrm{He}]\Gamma_{\mathrm{SE}}}{g_e\mu_B}P \tag{3.15}$$

$$B_{^3\mathrm{He}} = C\mu_{^3\mathrm{He}}[^3\mathrm{He}]P \tag{3.16}$$

Flipping the direction of the ^{3}He spins enables us to isolate the effect due to the polarized ^{3}He. This change in the EPR frequency is of the order of a few tens of kilohertz and is easily measurable. It is actually twice the frequency change due to the ^{3}He as shown in Figure 3.19. This change in the base EPR frequency due to the extra fields can be expressed as

$$\Delta\nu_{B'} = \frac{\mathrm{d}\nu_{B'}(F,M)}{\mathrm{d}B}(B_{\mathrm{SE}} + B_{^3\mathrm{He}}) \tag{3.17}$$

$$= \frac{8\pi}{3}\frac{\mu_0}{4\pi}\frac{\mathrm{d}\nu_{B'}(F,M)}{\mathrm{d}B}\kappa_0\mu_{^3\mathrm{He}}[^3\mathrm{He}]P \tag{3.18}$$

where $\kappa_0 \equiv \kappa_0(T) = \kappa_{00}(T_{\mathrm{ref}}) + \kappa_{0T}(T - T_{\mathrm{ref}})(^\circ C)$ is a dimensionless constant for K-^{3}He interaction that depends on the geometry of the cell. For a geometric cell, a measurement of κ_0 has been recently reported by [Babcock *et al.*, 2005] with $\kappa_{00}(200^\circ = 5.99 \pm 0.11)$ and $\kappa_{0T} = 0.0086 \pm 0.0020$. Thus, the error on κ_{0T} is significantly larger than κ_{00} at our running temperatures of about 260°C. This is also the source of the biggest error in the target polarization measurements.

3.7.1 Hardware and Setup

The EPR setup consisted of the following:

- EPR RF coil with a RF function generator (HP/Agilent E4400B) and RF amplifier,
- Photodiode and Rb D_2 filters,

- A counter, a frequency generator (modulator, SR620), a PI (Proportional-Integral) feedback box and a lock-in amplifier (EG&G 745).

This setup is outlined in Figure 3.16. The RF coil broadcasts a signal that matches the energy difference between the $m_F = -3$ to $m_F = -2$ levels (12.2 MHz for rubidium-85 and 20.2 MHz for potassium-39 for about a 25.6 G field)[25] and de-excites the respective alkali metal. These electrons in the $F = 3, m_F = -2$ state can now absorb photons from the circularly polarized laser light and get excited to the ^5P state. During this transition, there's an increase in the photons dropping from the ^5P to the ^5S state as these excited electrons decay. This resonance is indicated most strongly by the D_1 transition. Due to thermal mixing between the energy levels corresponding to D_1 and D_2 transitions, electrons can jump to the latter energy level thus also giving off D_2 light in the process of relaxation. The energy gap between $5\,^2P_{1/2}$ state and $5\,^2P_{3/2}$ state is about 0.0294 eV. The kinetic energy of the gas at the operating temperature of the target chamber ($\sim 260°$) is $\frac{3}{2}kT \approx 0.069$ eV and thus the two states become thermally mixed [Slifer, 2004]. The D_1 light (795 nm) is washed out by the huge intensity of the laser light, hence we detect the D_2 light at 780.2 nm.

Potassium EPR works as follows: The potassium is depolarized by exciting the K EPR transition (20.2 MHz for ^{39}K or 16.0 MHz for ^{41}K). The K then quickly gets repolarized by K-Rb spin exchange thus depolarizing Rb. The process then continues exactly as if the rubidium was depolarized using RF as above. Thus, in this case also, the Rb D_2 light is observed and the EPR frequency is measured.

The D_2 signal from the pumping chamber was focused by a lens onto a 1 mm diameter, 10 m long optical fiber which carried it to a photodiode. Since the intensity of this light is very small compared to D_1 light, two D_2 filters were mounted on the photodiode to minimize the D_1 light[26,27]. Even after using the filters, the D_1 light dominates, so the applied RF is modulated at about 200 Hz consequently modulating the D_2 light which is then fed into a lock-in amplifier. The lock-in amplifier locks on to the 200 Hz D_2 light giving us a clean signal. The photodiode was placed in the small lead brick housing to protect it from radiation damage.

[25] In case the $m_F = +3$ state is occupied, these numbers are 11.72 MHz and 16.00 MHz respectively.

[26] Two filters had to be used since the photodiode saturated at 200 mV and the signal with one filter and three lasers was more than 200 mV. For the experiment, we used at least four lasers.

[27] Note that if T_1 and T_2 are the transmittivities of the two filters, the combined trasmittivity is not $T_1 \times T_2$, but a little more than that because of multiple reflections between the two filters and the photodiode.

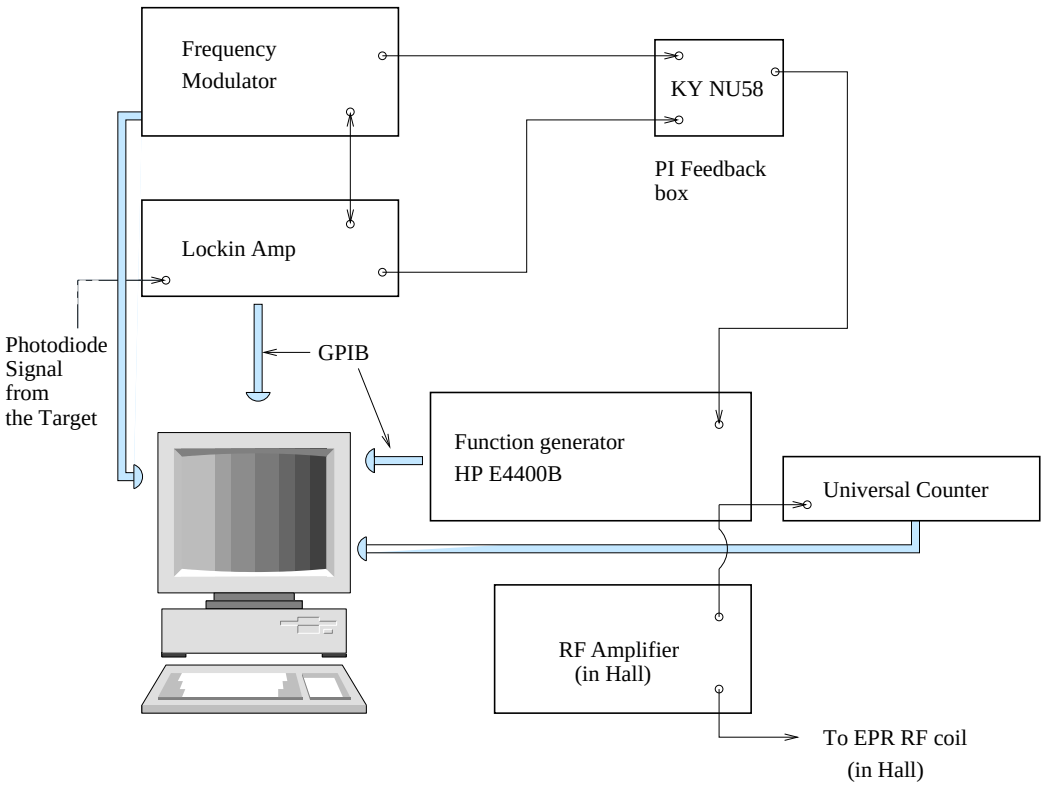

Figure 3.16: The EPR setup. The RF coils, photodiode with D_2 filters and the EPR RF amplifier were in the Hall; the rest were in the Counting House.

The list of instruments and their settings appears in Appendix C.

3.7.2 Procedure

Before we started doing EPR, we decided to calibrate the Kentucky PI feedback box. The total gain is given by

$$G_{tot} = m_F \left(\frac{10mV}{S_l} (G_{abs})(2G_{MP} \frac{\Delta\nu_{depth}}{1V_{pp}}) \right) \tag{3.19}$$

where G_{tot} is the total gain for the proportional branch of the PI box, m_{FM} is the feedback slope of the FM sweep (as shown in Figure 3.18(a), sometimes called the *error curve*), S_l is the sensitivity of the lock-in amplifier, G_{abs} is the gain of the absolute potentiometer (Figure 3.17), $\Delta\nu_{depth}$ is the change in frequency of the RF generator (HP E4400B) per volt of input. G_{MP} is the gain of the RF generator determined by measuring its output with varying input. This number obtained by a fit to the data was 0.9886. The $\Delta\nu_{depth}$ could be chosen and was set to 20 kHz for the experiment[28]. Also, it was found that the maximum

[28]This was determined by trial and error as the best value for our settings. This is different than earlier EPRs in the way that a Wavetek 80 used earlier had a fixed value and was some percentage of the output

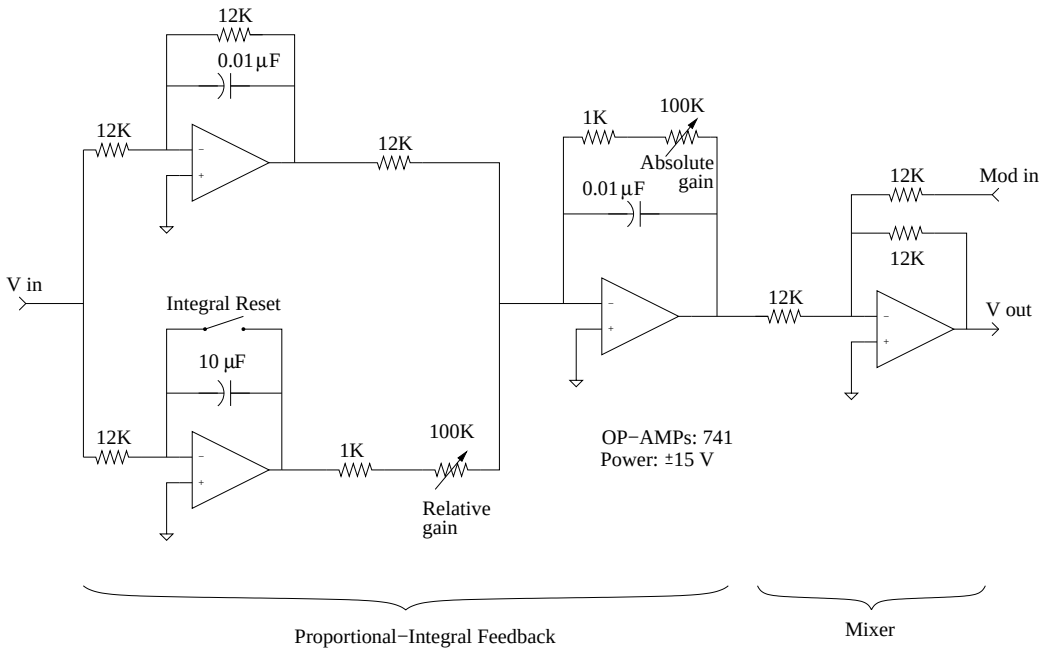

Figure 3.17: The EPR PI feedback circuit diagram. [Romalis, 1997]

total input that would give reliable output for the RF generator was 0.6volts. The above equation now reads

$$G_{tot} = m_F(\frac{\Delta\nu_{depth}}{S_l})G'_{abs} \tag{3.20}$$

For a feedback circuit, the G_{tot} lies between -1 and 0, so a safe value of -0.5 was chosen. The quantities m_{FM}, $\Delta\nu_{depth}$ and S_l are in μV/kHz, kHz and μV, respectively.

The total gain of the EPR feedback circuit depends on the absolute gain of the PI box, G'_{abs}, and the sensitivity S_l of the lock-in amplifier as we have seen in Equation 3.20. G'_{abs} depends on the number of turns of the potentiometer. Hence, a relationship between the absolute gain and number of turns on the absolute potentiometer was desired. For this purpose, a modulated signal was simulated from one of the function generators. This signal was set to mimic the Rb D_2 signal from the target cell. The signal was fed into the PI box input and its output was measured by a multimeter. For every half a turn of the absolute gain, the voltage reading on the multimeter was noted. The data was fit to a straight line and an equation was obtained[29] For the Ky PI box NU-112, the equation for absolute gain

frequency (about 20%). This necessitated the use of an attenuator since the frequency jump was too large compared to the change brought on by flipping the ^{3}He spins. In this case, no such attenuator was needed since we could control this value.

[29]The potentiometer knobs on the PI feedback box were not graduated and so there was no way of telling the number of turns (and whence the gains) on both the relative and absolute potentiometers. Hence, to set G'_{abs} to a particular value, i.e. to set the absolute gain potentiometer to a given number of turns, a

was:

$$G'_{abs} = -(5.12n + 1.17) \tag{3.21}$$

where n is the number of turns of the absolute gain knob. For the KY NU-112 box, the potentiometer had about 15 turns and the ground for the input Operational Amplifier (OP-AMP) was at about 3 μV [30]. Using Equations 3.20 and 3.21, the sensitivity of the lock-in amplifier to be used for that particular measurement could be determined.

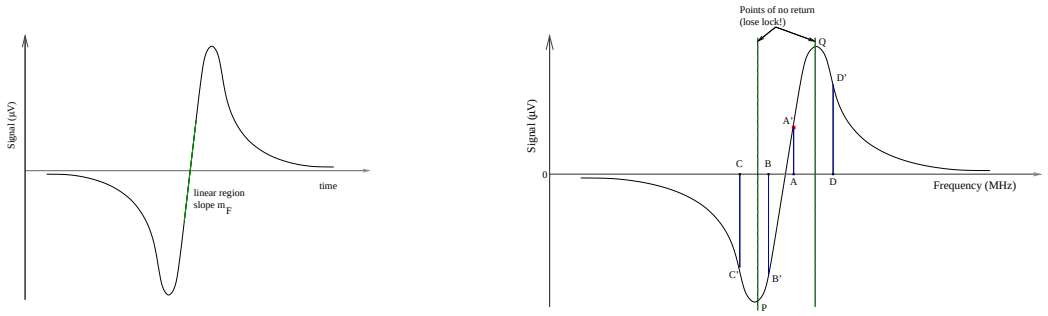

(a) The EPR error signal

(b) EPR lock and flip

Figure 3.18: (a) The EPR *error signal* and (b) various states during an EPR flip. See text for explanation.

Figure 3.18(a) is the derivative of the EPR resonance, or the error signal, which sits at zero. Setting the frequency such that the signal is slightly above or below[31] zero (e.g. ± 50 μV for a signal of a few hundred microvolts), the PI feedback box is now connected and turned on. The system is now locked and sits at position A on the frequency axis

Now we flip the ^{3}He spins using AFP by sweeping the RF through resonance. In the particular example above, the spins now are aligned parallel to the holding field thus reducing the Zeeman energy level difference by an amount proportional to the helium polarization. The EPR frequency thus jumps to point B, and the lock follows. Once we have enough points in the flipped state, we flip back to the original state and the lock jumps back to point A. If, after the flip, the system jumps to point C (that is, the change in the Zeeman

multimeter was used and the output measured gave us the correct number of turns. This process can be eliminated by using a graduated potentiometer know and calibrating it before hand.

[30] This was way better than the JLab box which had about 9-10 turns (not high gain) and the ground was at about 3.5 mV. Also, the gain was not very linear. Hence the decision to use the Kentucky box.

[31] Ideally, we set the frequency before the lock to positive if the ^{3}He spins are anti-parallel to the magnetic holding field, and negative if they are parallel. For example, if the ^{3}He spins are parallel, the Zeeman splitting is lower than it will be after the ^{3}He spin-flip (anti-parallel) and thus the locked-on frequency will jump to a higher value. This measure makes losing lock less likely. This corresponds to a "hat" shaped EPR.

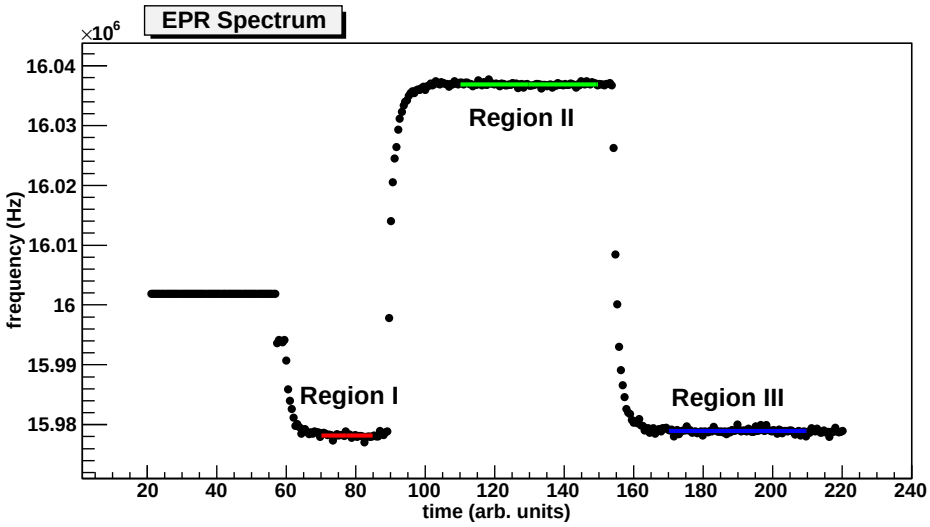

Figure 3.19: (color) EPR spectrum during G_E^n. Region I is before the ^{3}He spin flip, Region II, after and Region III brings the system back to its original configuration.

splitting is larger than the frequency range of the error signal) then the lock is lost, and the ^{3}He spins stay in the flipped state, unable to come back to their initial state. They now need to be flipped back manually and quickly else the system gets depolarized. This was the case in this experiment where the shift in frequency after spin-flip was larger than the frequency range of the error signal. Almost all the EPRs were done manually. The EPR software allowed for this by switching to the manual mode or by extending the time the system was in the flipped state so that sufficient time is available for finding the resonance and locking it. Some ^{3}He polarization values as measured by EPR are shown in Figure 3.20.

A concern about a change in the EPR frequency was noted by previous experiments due to the AFP RF signal. When the AFP RF signal - used to flip the ^{3}He spins - was switched off, a change in the EPR frequency was registered [Singh, 2007, Solvignon, 2006]. No such effect was observed in this experiment. The EPR frequency remained the same whether the AFP RF signal was on or off in either of the states - flipped or unflipped, hat or well. Also, no masing was observed unlike in the previous experiments [Singh, 2007, Sulkosky, 2007].

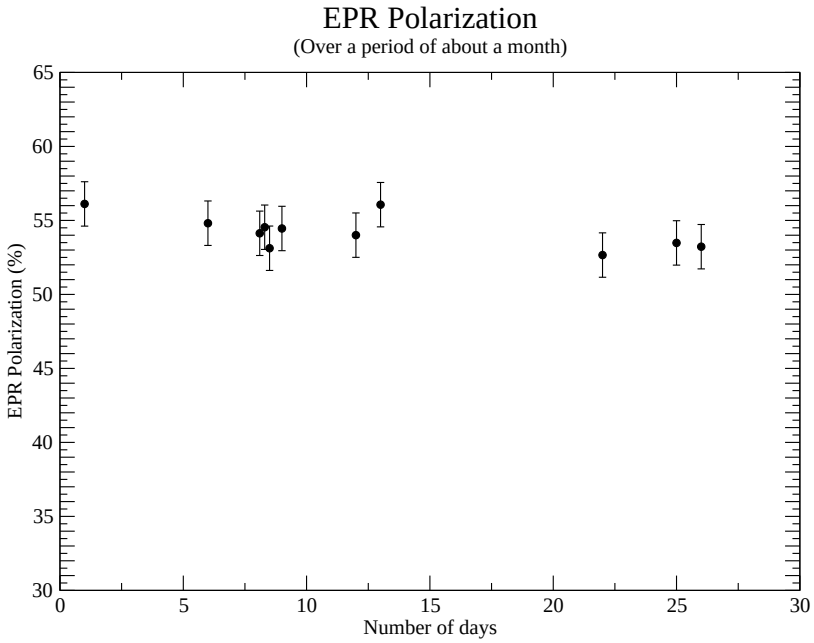

Figure 3.20: ^{3}He polarization measured with EPR in the pumping chamber. This plot shows select EPR numbers over a period of a month from mid-March to mid-April. EPR was done about once a day during this period. (The three values between days 8 and 9 indicate three EPRs were done on that day.)

3.8 Polarization Analysis and Results

3.8.1 NMR-EPR Calibration

The general procedure for NMR-EPR calibrations is to do an NMR measurement first followed by an EPR and then by another NMR. A schematic of the procedure is shown in Figure 3.21. The down sweep of the first NMR measurement is divided by the frequency change during the first EPR flip ($c1$) and the 2nd EPR flip is compared with the up sweep of the second NMR measurement ($c2$). There were a few correction factors involved since the EPR measurement is done at the pumping chamber and the NMR at the target chamber. These included the diffusion constant, temperature corrections in the pumping chamber due to the lasers, and the second NMR coil near the pumping chamber. The calibration constant for the experiment was generally around 0.41%/mV.

3.8.2 Temperature of the Pumping Chamber

The real temperature of the gas in the pumping chamber under running conditions was higher than what the RTDs showed since the lasers heated up the gas inside. This differ-

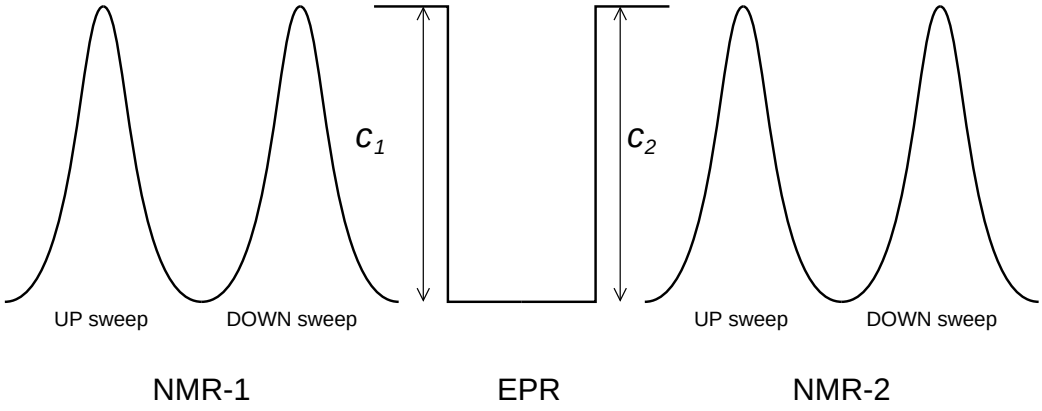

Figure 3.21: A cartoon representation of the NMR-EPR calibration procedure.

ence was calculated using the so-called temperature tests. NMR was performed alternatingly with the lasers on and off. About 15 minutes were given for the temperature to stabilize between measurements and the turning on/off of the lasers. There was a significant difference in the two types of measurements. Knowing the AFP loss per sweep for the NMR measurements, the difference between the real and read-out temperatures was calculated. The real temperature in the pumping chamber for Edna was calculated to be higher than the readout temperature by about 40 C° [Kelleher *et al.*, 2007].

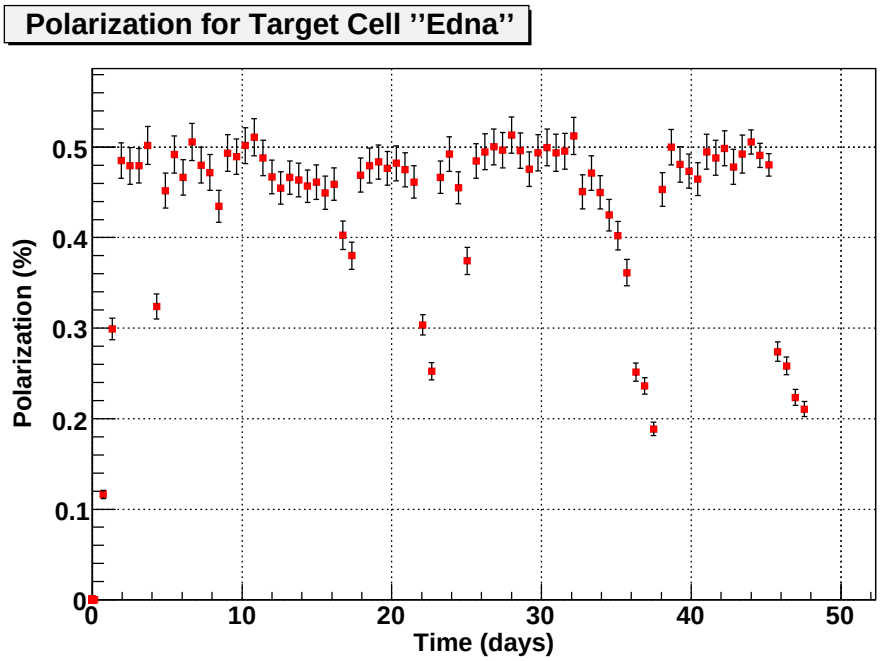

Figure 3.22: (color) Polarization results for target cell Edna. The drops in polarization indicate periods of change in kinematics during which target tests were done.

3.9 Holding Field Direction Measurements

As mentioned in Sec. 2.5.1, the longitudinal asymmetry contributes to the total asymmetry at target polarization direction different than $\theta^* = 90°$and due to finite detector acceptances. To determine how much longitudinal contribution we have in our system, we needed to precisely measure the direction the target spins are pointing in, which meant measuring the direction of the target magnetic holding field direction. To this effect, a precise magnetic compass was developed at Kentucky, and subsequently modified at JLab. The compass had a resolution of about 0.1°. For a ∼2.4° deviation away from 90° results in a correction to the total asymmetry of[32]

$$A'_{\text{long}} = (0.041 \pm 0.002) \cdot A_{\parallel} \,, \tag{3.22}$$

where $A_{parallel}$ is as defined in Equation (2.12).

The compass was an air-floated device as shown in Figure 3.23. It consisted essentially of a magnetic cylinder mounted on a floating disk. The compass when placed in the target region pointed in the direction of the target holding field. The angle made by the compass with respect to the electron beam direction was measured by reflecting laser beams off mirrors and by the Jefferson Lab Alignment group.

3.9.1 Testing and Systematics

The construction of the magnetic compass is shown in Figure 3.24. Compressed air caused the disk (marked with a circled 4 in the figure) to float without friction. On this disk a cylindrical magnet was positioned in a V-shaped groove. The groove helped to ensure positioning repeatability. The cylindrical magnet had a mirror mounted on one end for the laser beam to reflect off, and a disk marked with a circular scale on the other end. The scale had markings every 30° and was used to place the cylinder in the same angular position for every reading. This eliminated the systematic error due to the mismatch of the geometric and magnetic axes of the cylinder.

The geometric and magnetic axes of the cylindrical magnet did not coincide. To determine this angle and correct for it, laser light was reflected off the mirror attached to an end of the cylindrical magnet as described earlier and the position of the reflected spot was noted for various angular positions of the magnet (as seen in Figure 3.25(a)). This

[32]From the second part of Equation (2.10), since we have $\theta^* = 87.63°$, $\theta^{*\circ} \approx 0.041$. $A_{\parallel}$ depends on kinematic variables only and needs to be calculated for each kinematic point.

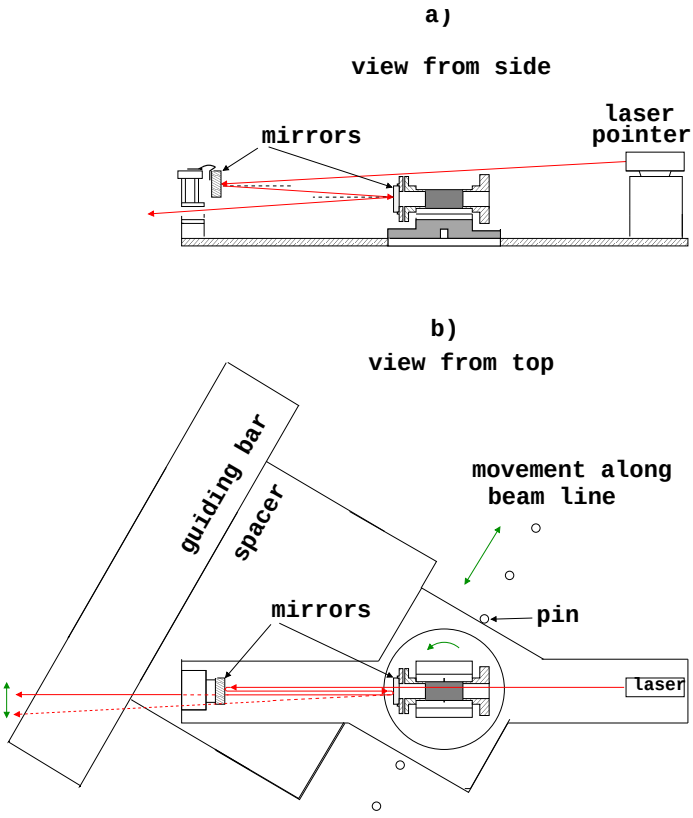

Figure 3.23: (color) The G_E^n compass. The guiding bar and spacer are not shown in a).

spot inscribed an ellipse the minor axis of which was minimized by fine tuning the angle of the mirror mounted on the cylindrical magnet as shown in Figure 3.25(b). The (axis of the) mirror was thus made parallel to the magnetic axis of the cylindrical magnet and the horizontal offset - and thus the error - due to the different angular positions of the magnet was kept at a minimum.

A tiny amount of torque acted on the floating disk due to the air holes not being exactly normal to its lower surface. This torque was calculated by measuring the time period of rotation of the floating disk in a field-free region. This method could also estimate the deviation from horizontality of the disk. The oscillation of the disk about a *preferred* direction would indicate that the disk was not entirely horizontal.

The torque was measured at various air-flows (16, 32, 48 ℓ/min[33]) and no change was seen in the compass readings between the different air-flow rates. Also, no preferred direction was identified indicating good horizontal alignment.

The compass was initially used to study the effects of the opening of the magnet box

[33] ℓ/min = liters per minute.

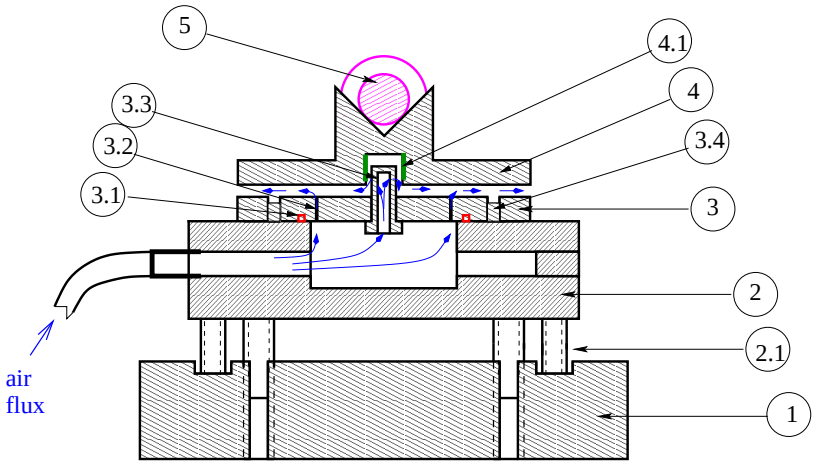

Figure 3.24: Construction of the G_E^n compass. (Sectional view through center.)

door on the direction of the field. When one or both doors were opened, the field direction changed, but was back to the initial value once the doors were closed. There was no change in direction within the resolution of the compass (about 0.1°). A fact noticed at this time was that when the field was swept during an NMR measurement, the direction also changed with the change in field magnitude A crucial test done in the Hall with the BigBite magnet revealed an interesting characteristic. When the BigBite magnet was turned off and back on, the target magnetic holding field direction was different. At least five NMR cycles were required to get the direction back to the nominal value. This *seasoning* of the magnet box would be required for every change in the surrounding magnetic environment close to the target region. During the experiment, the BigBite was turned off only twice and a lot of NMRs were done after the BigBite was turned on as part of the target tests. Thus, the possibility of the field being at a different direction was minimal.

3.9.2 Compass Measurements

We needed to map the magnetic field direction in the region around the target cell length and position relative to the electron beam direction. Ideally, the angle $\phi^* = 0$ and $\theta^* = 90°$ to the direction of momentum transfer. Our compass was not sensitive to the ϕ^*-direction but only to the *transverse* θ^*-direction[34]. Since our target box was at an angle of about 30° with respect to the beamline, the angle of the target holding field with respect to the beamline would ideally be $\theta_{tgt} \approx 120°$.

[34]Another compass, dubbed *the vertical compass* has been developed which is designed to measure the vertical angle, but is sensitive to any general angle in 3-space.

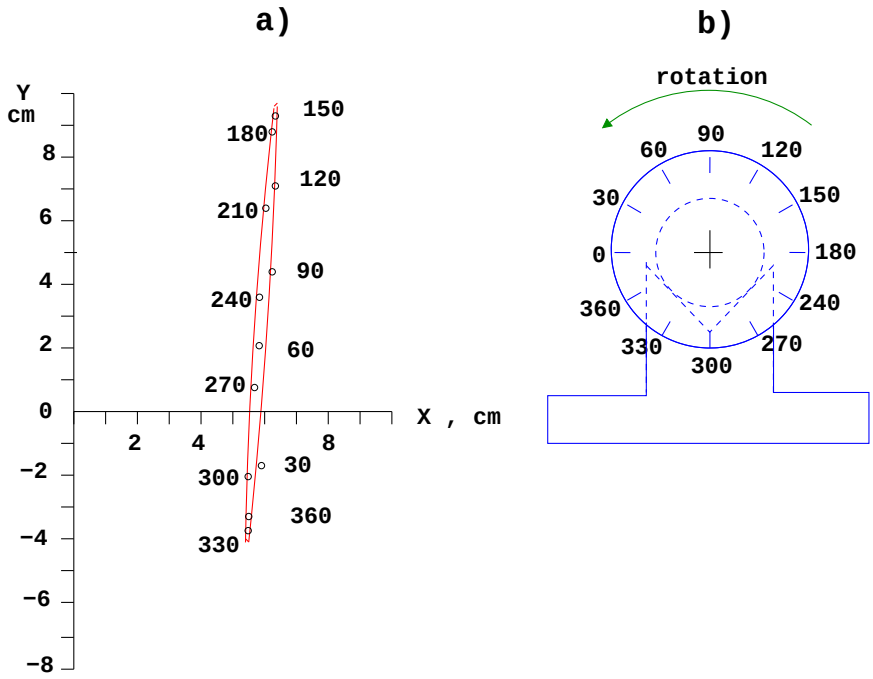

Figure 3.25: (color) The determination of angle between the magnetic axis and mirror. The ellipse is a result of the 360°scan of the cylinder (as shown on the right).

Absolute Measurement

For the compass measurements to correspond to actual angles in the laboratory (Hall A) frame, an *absolute* measurement was necessary to give us the angle relative to the beamline for a fixed compass position in the target region. All other compass measurements would then be with respect to this angle, termed *relative* measurements. The absolute measurement was done with the help of the Jefferson Lab Alignment (or Survey) Group whereas the relative measurements were performed by ourselves.

Following is the procedure employed for the absolute measurement of the field direction [Beck *et al.*, 2007]. A solid aluminum bar was mounted on the frame of the target magnet box (Figure 3.26). A *reference* mirror was mounted at the center of this aluminum bar (called the *reference* bar) . The aluminum bar was about 2 m long and $2'' \times 2''$ in cross-section. The compass was positioned inside the target box at the center of the target region (corresponding to the center of the target cell, marked as hole number 7 in Figure 3.27). A small laser was mounted outside the target box on a tripod at a distance of about two meters from the reference mirror. This laser was positioned such that the laser, the reference mirror

and the compass mirror were collinear[35]. A transparent sheet (an overhead transparency) was placed between the laser and the reference mirror, closer to the laser.

With the reference bar installed, the small laser was turned on. The laser beam passed through the transparency to be incident on the reference mirror and reflected off the mirror to pass through the transparency again. The positions of these laser spots on the transparent screen were marked. The reference bar was then removed. Now the laser light, after passing through the transparency at the same position as before, was incident upon the compass mirror. After reflecting off the compass mirror, the laser beam went through the transparency at a different point. Again, the positions of the spots were marked on the transparent screen. The unknown angle was easily calculated by measuring distances of the mirrors from the transparent screen and between the various spots on the screen.

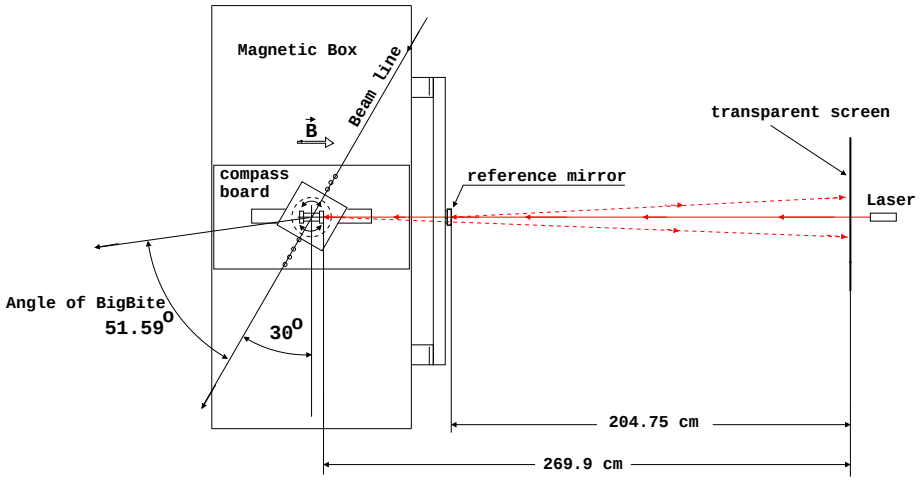

Figure 3.26: The absolute measurement setting. Note that for reflection off the compass mirror, the reference mirror bar was removed. The compass position along the beamline in this figure corresponds to hole #7 shown in Figure 3.27.

The angle of the reference mirror on the aluminum bar was also measured by the Jefferson Lab Alignment Group for the same setting as above. This gave us the angle of the reference mirror with respect to the beamline in the Hall coordinate system, say, $\theta_{\rm Hall}$. Thus, using $\theta_{\rm Hall}$ and the procedure described above the holding field direction was calculated at the center of the target region relative to the beamline.

[35]Note that the axes of the mirrors need not have been aligned to each other or the laser beam direction, and they were not. The only requirement here was that the laser beam be incident on the reflecting surface of the mirror.

Relative Measurements

Once the absolute measurement was done, the transparent screen was removed and a large cardboard screen with a fine scale (of 1 mm divisions) was put in its place. The compass laser was now turned on and the position of the laser spot on the scale was read off. The reference position (corresponding to the center of the target cell) was hole # 7 as shown in Figure 3.27. The compass was then moved along the length of the target in one inch steps and the positions of the laser spot on the cardboard scale for each compass position were read off. The compass edge was kept flush with a fixed *guiding* bar on the compass bench to enable movement along the beamline direction. A $4''$ aluminum spacer was placed between the fixed bar and the compass edge. The measurements were repeated with $3''$ and $5''$ spacers . The complete set of readings with all the horizontal spacers was repeated with a $1''$ vertical spacer. So the entire region around the target cell position was scanned as seen in Figure 3.28.

3.9.3 Friction Torque

Friction, although small, causes a torque to act on the floating disk affecting the compass readings. An estimate of this torque needs to be made to account for systematic errors [Beck, 2006]. Modeling the disk movement using a damped oscillator, we can write the displacement θ as

$$\theta = \theta_{max} \cos(\omega t) e^{-\alpha t} \tag{3.23}$$

where ω is the frequency of angular oscillation of the disk and magnet system and α is the damping rate. In our almost frictionless case, $\alpha \ll \omega$. Timing the oscillations, it was seen that the amplitude dropped from $2''$ to $1''$ in 15 seconds implying

$$\frac{\theta_1}{\theta_2} = e^{-\alpha(t_1 - t_2)} \tag{3.24}$$

$$\text{or} \qquad \alpha = \frac{\ln(2)}{15} \approx 0.06 \text{ s}^{-1} \tag{3.25}$$

The period of oscillation was measured (by a stopwatch) to be about 0.7 s whence the angular velocity can be calculated to be 9 rad/s, thus justifying the $\alpha \ll \omega$ condition above.

When placed in a magnetic field, the compass would have a magnetic potential energy given by

$$U = \vec{m} \cdot \vec{B} = mB \cos\theta \approx mB \left(1 - \frac{\theta^2}{2}\right) \tag{3.26}$$

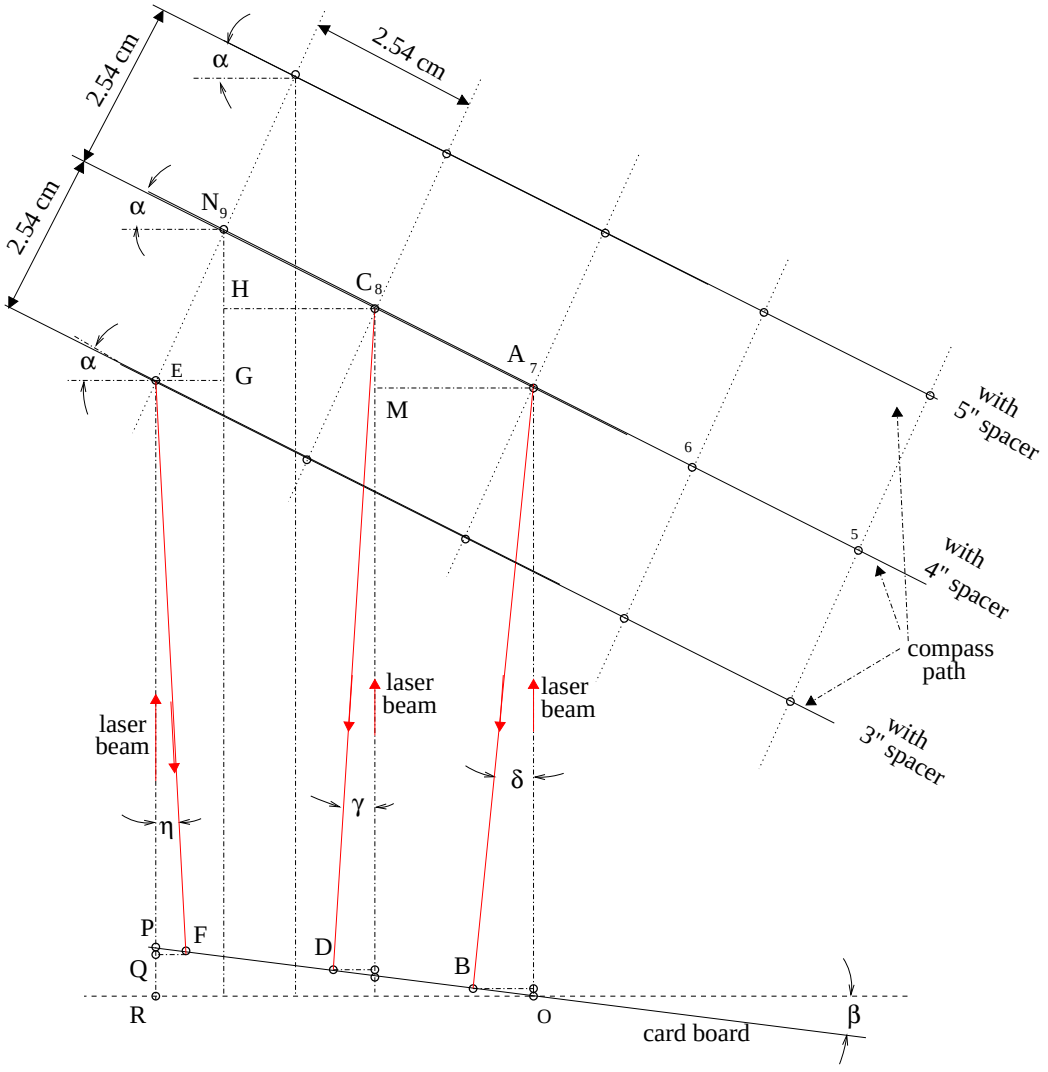

Figure 3.27: The positions of the compass and the corresponding laser spots during scanning. See text for explanation. The $4''$ spacer position corresponded to the beamline.

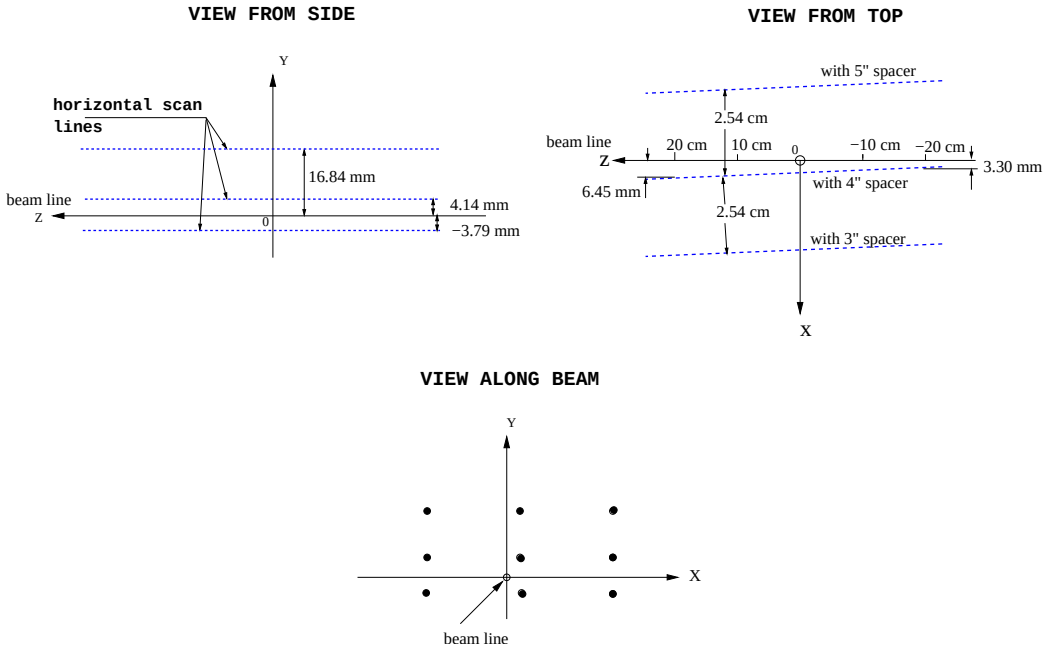

Figure 3.28: The target region scanned by the compass. The result of the scan as shown in Figure 3.29 corresponds to the middle point in the lower figure. Figure from [Beck *et al.*, 2007].

where we have used the small angle approximation for the final equation. Here $\vec{m}$ is the magnetic moment of the compass magnet and $\vec{B}$ is the magnetic holding field, θ being the angle between the two quantities. The torque on the magnet is given by

$$\tau = -\frac{\partial U}{\partial \theta} = mB\delta\theta\,. \tag{3.27}$$

At equilibrium position, this torque equals the frictional torque

$$\tau_{fric} = mH\delta\theta\,. \tag{3.28}$$

Equating the energy dissipated which is the work done by the frictional torque to the change in magnetic energy during the first oscillation cycle[36]

$$E_{diss} = 4\theta_{max}\tau_{fric} = 4\theta_{max}mH\delta\theta = mH\theta_{max}\left(\frac{\dot{\theta}_{max}2\pi}{\omega}\right) \tag{3.29}$$

whence

$$\delta\theta = \frac{\pi}{2\omega}\dot{\theta}_{max} = -\frac{\pi}{2\omega}\alpha\theta_{max}\,, \tag{3.30}$$

[36]The change in the magnetic energy with time

$$\Delta E_{mag} = -\frac{\partial U}{\partial t}\Delta t = -mH\theta_{max}\dot{\theta}_{max}\Delta t\,.$$

For one cycle, $\Delta t = T$.

where the relation $\dot{\theta}_{max} = -\alpha\theta_{max}$ has been used. The measured value of $\theta_{max} = 0.02$ rad yields $\delta\theta = 0.2$ mrad.

3.9.4 Self Effects

Since the compass consisted of a strong magnet (about 6 kG at the ends) and was placed in an iron box, there could be *self effects* due to the compass magnet magnetizing the iron box which in turn could modify the holding field thus compromising measurements. These effects were calculated and found to be negligible.

3.9.5 Direction Measurement Results

Compass measurements - absolute and relative - were done before the experiment, once during the experiment, and after the experiment. The reference bar could be installed in the same position with high accuracy (better than 0.01 mrad). The holding field angle remained stable over the entire period. The result of the compass scan is shown in Figure 3.29. The field angle at the target center was 117.63° and the angle varied by about 10 mrad over the length of the target[37]. The error in measurement was less than 2 mrad or about 0.1°. The fit was used to calculate the angular dependence on the asymmetry (due to the longitudinal contribution) and to correct for it.

Our compass was not sensitive to angles in the vertical plane. This angle was determined to be negligible based on estimates made from the box geometry and symmetry, implying a much more negligible effect on the asymmetry.

3.10 Nitrogen in the Target Cell

The Polarized ^{3}He target cell had about 1.5% nitrogen to effect radiationless quenching of Rb/K so as to prevent depolarization of the target. The G_E^n cells contained about 90 Torr of nitrogen gas which is a little higher than in the earlier experiments ($\sim 60 - 65$ Torr). This was primarily due to a bigger pumping chamber of the G_E^n cells [Singh, 2007]. As such, a few of our detected neutrons come from this nitrogen which we need to identify and correct for our asymmetries. Nitrogen dilution analysis is detailed in Sec. 5.3.1.

[37]The actual length considered during data analysis was ±17 cm so as to cut out the glass end windows. The field angle change in this region was about 10 mrad as seen in the figure.

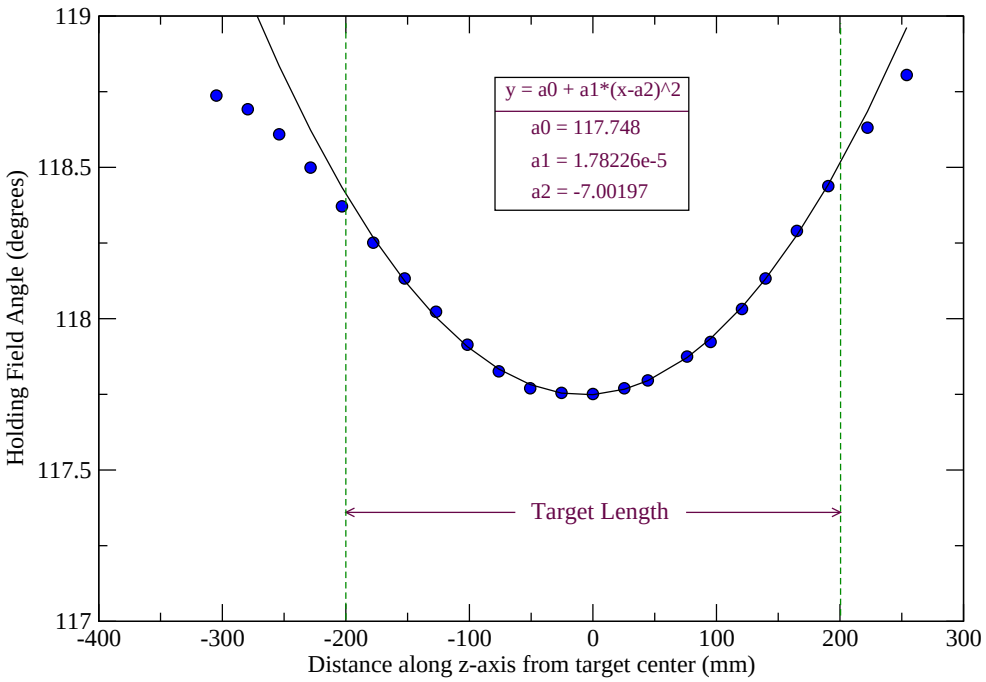

Figure 3.29: The compass results indicating the deviation of the target holding field along the length of the target. The angle at 0 is relative to the beam direction. The fit is performed only over the range of the target length. The scans at other positions (in both the horizontal and vertical planes as seen in Figure 3.28) had the same structure and the readings were within 1 mrad of these values. The deviation of the field in the same direction on both sides of the target center is explained in Figure 3.30.

Copyright © Ameya Suresh Kolarkar 2008

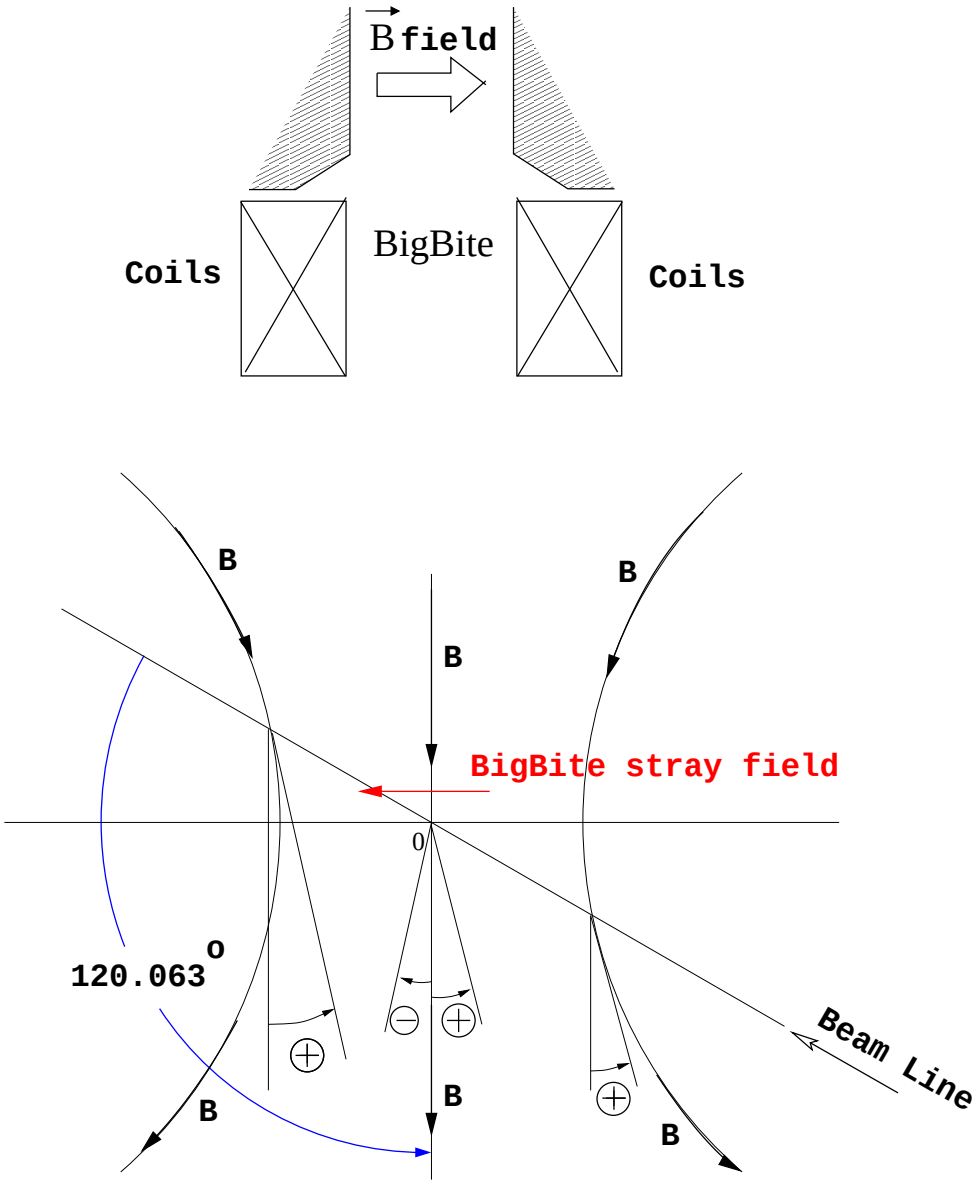

Figure 3.30: The angle the target cell made with the holding field causes the angle to change in the same direction on either side of the target center.

CHAPTER 4: DETECTORS AND ELECTRONICS

The two detectors used in this experiment were the Neutron Detector (ND) and the BigBite Spectrometer (BB) that matched in solid-angle acceptance. The Hall A standard High Resolution Spectrometers (HRSs) were not used. Some of the electronic modules and hardware from the unused left HRS were used in the trigger system. In this chapter we shall describe the detectors and the Data Acquisition (DAQ) hardware and electronics.

4.1 The Neutron Detector

Scintillators are used for timing measurements. Since we detected neutrons in coincidence with electrons using Time-of-Flight (TOF), we used a huge array of scintillators - called the Neutron Detector (ND) or the BigHAND (Big Hall A Neutron Detector) - to detect the neutrons and establish good timing resolution of detected events. Other detectors like the gaseous ionization chambers or liquid scintillators do not have this timing advantage.

The scintillation detectors were made up of organic plastic material. They work by emitting light when charged particles such as protons deposit energy as they pass through them [Leo, 1987]. Neutrons, being neutral, cause the scintillators to emit light only when they hit a nucleus in the shielding or the scintillator itself causing charged particles such as protons to be ejected. The construction and shielding used in the ND is described in the following sections.

4.1.1 Construction

Four different types of scintillator bars were used for the ND. These were the UVa bars (from the University of Virginia), CMU bars (from Carnegie Mellon University), Glasgow bars (from the University of Glasgow, Scotland) and veto bars. The UVa bars were were taken from an older experiment so they had to be taken apart and reassembled[1].

The bars were polished using polishing wax and a felt cylinder mounted on a drill. The bars were then wrapped in aluminized Mylar sheets to prevent photons (incident at angles greater than the critical angle for total internal reflection) from escaping the bars. They were finally wrapped in black plastic sheets for protection (both mechanical and from

[1]While disassembling the PMTs and the light guides, the PMTs come off easily while the light guides are detached from the scintillators using 50% isopropyl alcohol and cutting with a blade or knife.

outside light) and easy handling. Light guides were glued to the ends of the bars (the glue was dried using UV light) and Photo-Multiplier Tubes (PMTs) were attached to the light guides. The PMTs were mounted in homemade casings that were tested for gas leaks using a U-tube manometer (as certain gases, like helium, can damage the PMTs). These bars were then tested with cosmic rays.

The size of the ND as a whole was $4.2 \times 2.0 \times 6.2$ m^3 , and was comprised of 340 scintillator bars, each connected to two PMTs [Proposal, 2002, Ngo and Shahinyan, 2007]. The solid angle on the NA was approximately 100 msr at a distance of 8 meters. It had an aspect ratio of 1:2.5 (horizontal to vertical) and was well-matched with BigBite's acceptance. The timing resolution was about 0.3 ns at a distance of 8 meters which, for a a neutron momentum of 2.58 GeV/c, corresponded to a momentum resolution of 250 MeV/c. The momenta of the detected neutrons can thus be obtained from their time of flight from the target.

The signals from the PMTs were then fed into Analog-to-Digital Converters (ADCs) that give us the amplitude of the signal, and into Time-to-Digital Converters (TDCs) that give us the time when the particles pass through the detectors. The amplitude of the signal correlates to the energy deposited by the particle passing through the scintillator. The segmentation of the neutron detector planes permitted a coarse determination of the neutron's vertical position. The ADCs integrated the pulses over a $\sim$150 ns time window. The time of the pulses were recorded in multi-hit TDCs: the veto detectors with LeCroy 1877 TDCs run in common-stop mode at 0.5 ns/channel, and the neutron detectors bars with F1 TDCs set to 0.1183 ns/channel.

4.1.2 Planes of the Neutron Arm

The NA contained overall ten planes of detectors: two veto counter planes, one marker counter plane, and the rest neutron detectors planes. The individual planes of the NA were created with the use of modular cassettes, which allowed for easy installation into the NA frame.

In front of the NA is a 5.04 cm thick lead wall. The sole purpose of this wall is to reduce the rate at which the veto detectors will fire due to background and spurious events. Although this does decrease our overall statistics, the wall makes it possible to use the veto detectors to identify charged particles. Without the wall the rate in the veto plane would

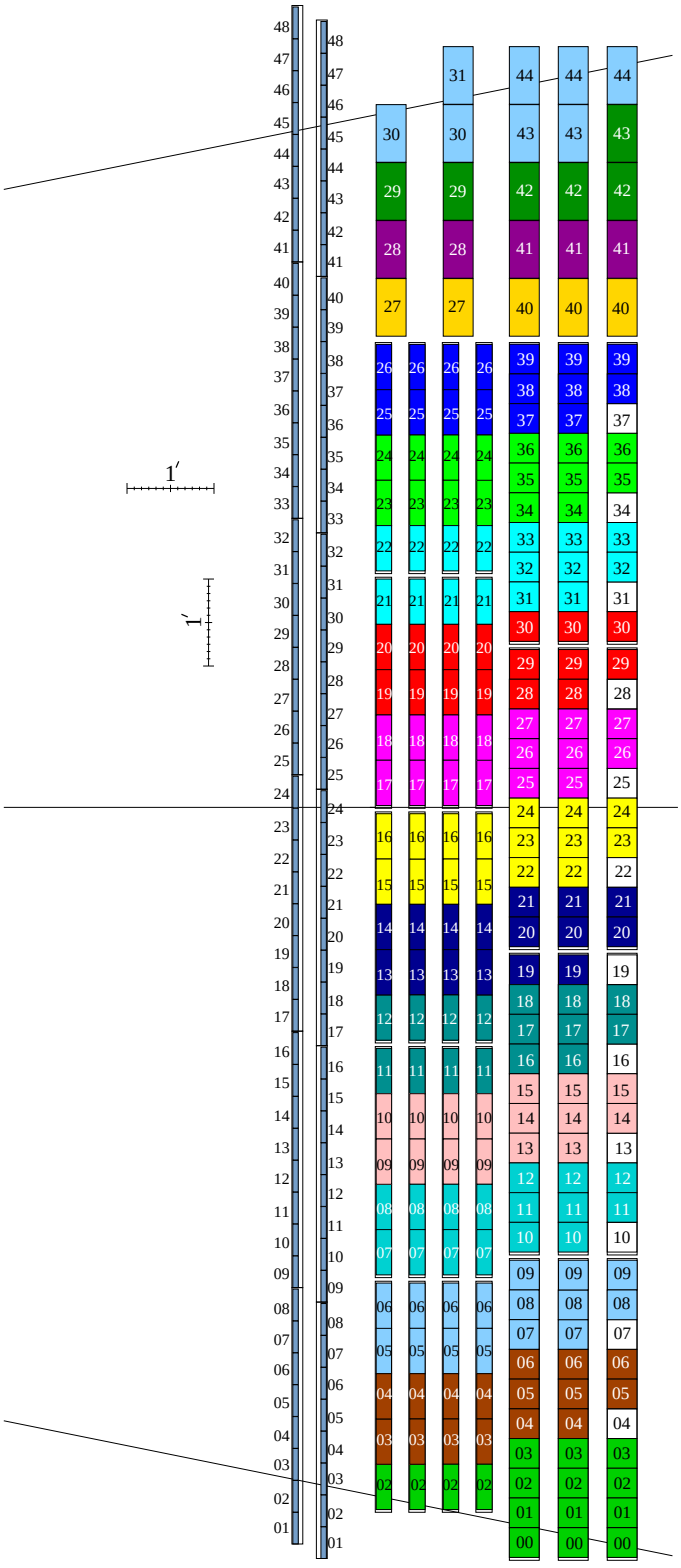

Figure 4.1: The Neutron Detector. (Figure is to scale and does not show the lead or iron shielding.) The neutrons come in from the left in the figure. (Figure taken from the collaboration's technical drawings.)

be much higher, causing an increased dead time in each of the bars.

The next two planes were the veto planes described as the V1 and V2 plane of the NA. Each of these planes contain six cassettes, which each contain eight veto scintillator bars. After the veto planes were the marker counters which were used mainly to calibrate the $y-$position inside the NA, and to obtain the speed of light propagation through the scintillator bars in the neutron planes. In between the Marker Counters and the N1 plane of the NA is a $1''$ thick lead wall the purpose of which is to increase the rate at which neutrons "convert" to protons so that they can be tracked through the NA. In front of the lead wall is a $1/2''$ thick iron wall used to support the lead wall. (Figure 4.1.)

The next seven planes are considered the main neutron detector planes of the NA. The planes N1 through N4 were the CMU scintillator bars. Planes N1 and N3 had a Glasgow cassette placed at the very top, which contained Glasgow scintillator bars. The last three planes of the NA, N5 through N7, each contained UVA cassettes each of which contain ten UVa bars. At the top of each of these planes sat a Glasgow cassette that was the same as the ones that sat on top of the N3 plane.

At the back of the NA there was another $1''$ thick lead wall supported by a $1/2''$ thick iron wall to reduce the noise and background events that could come from behind the NA.

4.1.3 Neutron Arm Position

During the experiment the NA was placed on rails so that it could be moved to different positions for different kinematics. Fiducial and foil markers were used by the survey team in order to keep track of the location of the NA. Two survey reports were written for the experiment, one before experiment and the other after. A plumb bob was attached to the front of the NA casing and used by the surveyors as a point of reference for the position determination. Knowing the coordinates of the plumb bob allowed us to understand where the different planes of the NA were with respect to the target. Also obtained from using the fiducial and foil marker data is the angle of the NA with respect to the beam line. This angle was about $30°$. Table 4.1 lists the coordinates of the plumb bob for each of the kinematic runs and its distance from the target.

Table 4.1: The Neutron Arm Position and Angles at all the kinematics.

Beam Energy(GeV)	Distance from Target(m)	Theta (degrees)	Distance to Rail (m)
N/A	6.51	35.1	3.070
1.519	12.00	35.1	3.303
2.641	12.00	28.3	2.109
3.290	12.00	30.3	1.266
2.079	9.26	35.1	3.303

4.1.4 ND performance

The ND performed well during the experiment. Other than a few detectors giving trouble and a few PMTs going bad, there were no major issues with the ND. The mounting of the ND on rails proved very useful while moving it at different positions and angles for different kinematics. These position changes were done within hours.

4.2 The BigBite detector

The electrons were detected in the BigBite (BB) spectrometer, which is a large momentum and angular acceptance, non-focusing spectrometer. It consists of a large dipole magnet and detector set. The original spectrometer was acquired by Jefferson Lab from NIKHEF and the detector package was replaced for this experiment. The dipole magnet reached a maximum field strength of 1.2 Tesla. The detector set consisted of three multi-wire drift chambers, a scintillator plane, and two lead glass calorimeters. Figure 4.2 shows the BB construction and detector stack. In the configuration used for the experiment, the BB had a solid angle acceptance of 76 msr averaged over the extended (40 cm) target. Its acceptance for a *point target* approaches 95 msr. This was one of the main reasons BB was chosen over the High Resolution Spectrometer (HRS), which is standard Hall A equipment, as such high resolution was not required.

4.2.1 Construction

First, let us define our coordinate system. There were three different coordinate systems used in the tracking code [Craver, 2007b, Riordan, 2007]. The standard LAB coordinate system, the target coordinate system, and the detector coordinate system. These systems are defined in Figure 4.3.

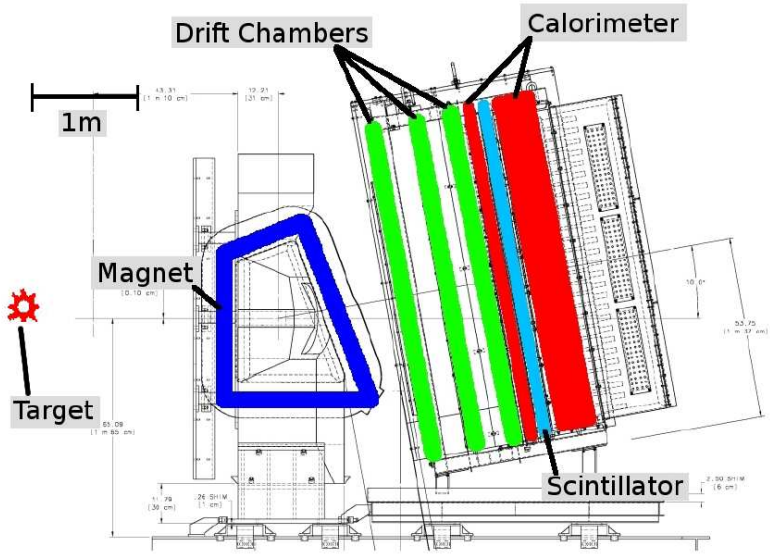

Figure 4.2: BigBite spectrometer stack.

The LAB, or HALL, coordinate system is where y points up (against gravity), z is in the nominal direction of the beam, and x is to the left when looking in the direction of the beam. The target coordinate system has the origin at the center of the target, x goes with gravity, z is parallel to the ground in the direction of the central angle of the BigBite spectrometer, and y is to the left looking down z.

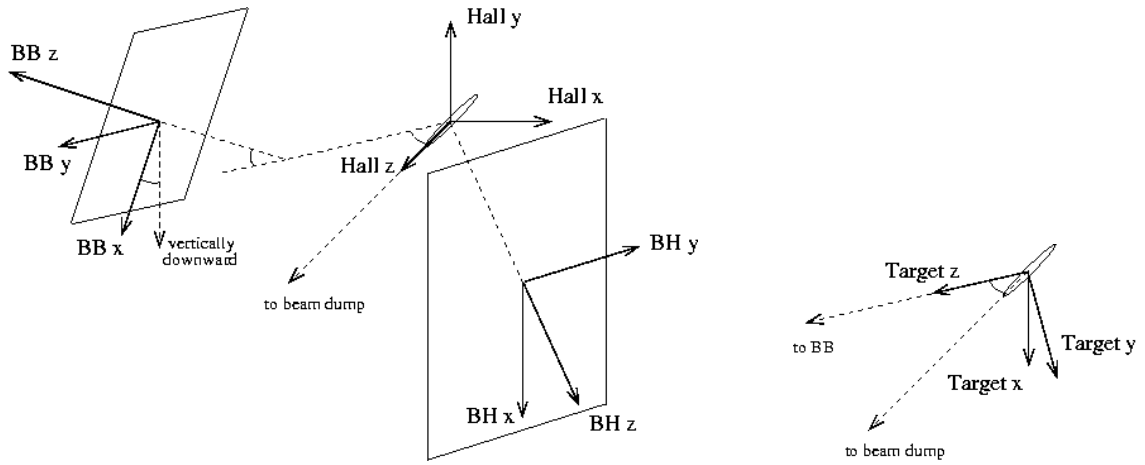

(a) Hall and detectors coordinate systems.

(b) Target coordinate system.

Figure 4.3: The three coordinate systems used in the experiment. Figures from [Craver, 2007b].

The detector coordinate system origin is specified by center of the first plane of the drift chambers. The x-axis is "down" in the dispersion direction (the direction of increasing

Table 4.2: BigBite configuration during the experiment for all the kinematic points. Table taken from [RIORDAN, 2007]

Distance from Target to Magnet face	1.09m
Distance z_{targ} from Target to Drift Chamber 1 Center	2.25m
Height difference (y_{LAB}) from Target to Drift Chamber 1 Center	0.17m
Detector Stack Pitch	10°

scattered electron momentum), the z-axis is in the nominal direction of particles such that $z = 0$ is defined by the first plane of the chamber, and the y-axis is defined so we have a right handed coordinate system. This can be seen in Figure 4.3 where we are looking along the z-axis.

Multi-Wire Drift Chambers

The drift chambers of the spectrometer consisted of three separate horizontal drift chambers spaced approximately 35 cm apart [CRAVER, 2007a]. The drift chambers were the first set of detectors after the magnet and were the highest spacial resolution detectors in the whole set. To achieve the ability to resolve points in three dimensions, three different types of planes were used, which were called U, X and V planes. All chambers had signal wires 20 μm in diameter separated by 1 cm. Field wires 90 μm in diameter were placed midway between the sense wires to shape the field. The wire planes were surrounded by cathode planes. The distance between planes was 6 mm (3 mm from the wire to either cathode.) The three wire orientations referred to as X/U/V were horizontal and $\pm 30°$ to the horizontal. This allowed for increased resolution in the vertical (dispersion) direction. Cathodes and field wires were held at a voltage of about 1800 V. Chamber 1 (closest to the target) was 35 cm (horizontal) $\times$ 140 cm (vertical) and contained six wire planes. Chambers 2 and 3 were 50 cm $\times$ 200 cm and chamber 2 contained only three wire planes, while chamber 3 (nearest to the shower detector) had all the six wire planes. The chambers were filled with a gas mixture containing equal proportions of argon and ethane gases kept at slightly above atmospheric pressure.

The signal wires were triggered when a charged particle ionized the gas when it passed through the chamber. The wires were put at some potential difference due to which the free floating charges drifted towards the wires and generated an electrical signal which was then read out by a TDC. The amount of time it took to drift from the track to the wire

was then converted into a distance. The purpose of the tracking code is to take these times, convert them to a distance, and then use these distances to fit a straight line across several planes to determine the track of a detected particle.

Preshower and Shower Detectors

The shower detectors, also called calorimeters, absorb particles incident on them and measure the amount of heat deposited which corresponds to the energy of the detected particle (whence the name *calori*meter, from the Latin word *calor* meaning heat). Two such calorimeters were used in the experiment called the preshower and shower detectors. The shower and preshower detectors were located behind the drift chambers at approximately z_{det}=1.0 m and z_{det}=0.85 m, respectively. The preshower detector consisted of 54 35 cm×8.5 cm blocks set in two columns and 27 rows. The shower detector consisted of 189 8.5 cm×8.5 cm blocks set in 7 columns and 27 rows. These detectors consisted of lead-glass blocks which, when a charged particle passed through, produced a shower of electrons. The amplitude generated in these tubes was roughly linearly dependent upon the energy of the particle. The combination of the shower and pre-shower gave an energy resolution of $\approx 10\%$ of the total energy. The purpose of the shower and pre-shower system was to help in particle identification. In Figure 4.4 we see clearly separated regions that correspond to (negative) pions and electrons. We could, thus, select events where electrons had caused the trigger and filter out the (negative) pions[2]. Furthermore, x- and y-position information was also obtained from the block that had a signal in the shower. Even though this position resolution was quite poor (8.5 cm in both directions) it could be used to fix a point of our track which allowed identification of a path for the scattered electron [Riordan, 2007].

Scintillator

A set of 13 scintillator paddles resides between the pre-shower and shower providing timing information. This timing, with a resolution of about 300 ps, when associated with a track can then be used to provide timing corrections. Since the scintillator plane resides about 1 m from the nearest drift chamber plane, timing corrections to the drift times can be up to a few nanoseconds, which can be significant in tracking. The timing calibration procedure

[2]The positive pions were deflected in the opposite direction as the negatively charged particles by the BigBite magnet.

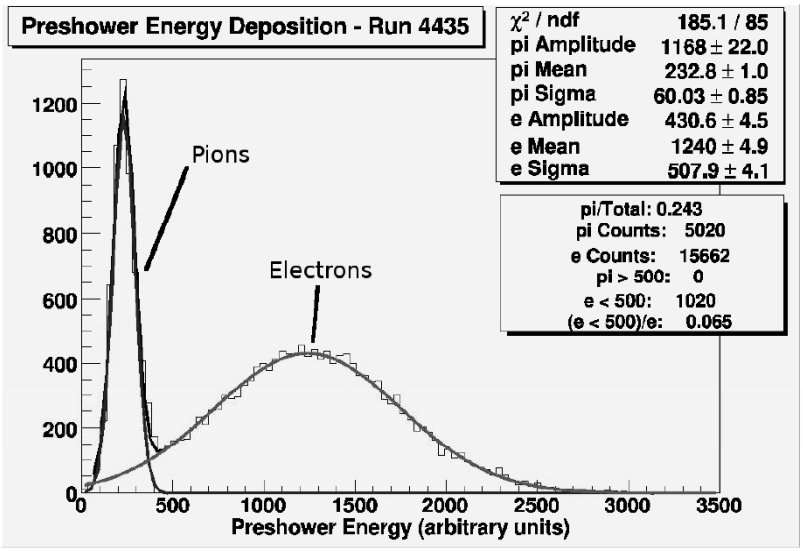

Figure 4.4: Pre-shower detector separating out pions and electrons. [RIORDAN, 2007]

is described in Section 5.1.1.

4.2.2 BB performance

During the experiment commissioning period and the earlier part of the first kinematic point ($Q^2 = 1.3$ (GeV/c)^2), with 15 μA current, very high background rates were observed in the wire chambers causing them to trip. It was then decided to run the experiment with 8 μA current. Though this reduced the luminosity, the high target polarization ($\sim$50%) later on in the experiment somewhat compensated for the loss of luminosity, since the Figure-of-Merit is proportional to the square of the target polarization times the luminosity.

Finding Tracks

A tracking code was developed to find straight line "tracks" of the particles (electrons) by using signals from the BigBite detector stack [RIORDAN, 2007]. These signals primarily come from the drift chambers, but information from the shower, pre-shower, scintillator and the change in electron trajectories due to the BB magnetic field is also used. The spatial resolution achieved at the wire chambers was around hundreds of microns. The tracking code had to accomplish the following tasks:

1. Identify the subset of hits that represent our signal, eliminating noise as best as possible.

2. Identify the combination of hits which represents our true track.

3. Identify which left/right configuration of hits is the true configuration.

4. Develop a method to handle multiple tracks.

Once a track is found, using the knowledge that it originated from the electron beam and how it travels through the magnetic field, we can then measure the momentum of the electron to an accuracy of about 1% of the momentum.

The tracking algorithm worked in general as follows. In the decoding stage, hits in the drift chamber were identified and hits outside a particular time window were removed.

In the coarse tracking process, a cluster in the shower was identified along with all valid combinations of wires across all active planes. Using a minimum χ^2 fit with only the wire positions for each combination, a subset of the tracks is saved; these are potentially real tracks. Tracks that are sufficiently similar were identified and poor χ^2 combinations were removed. Also, hits that were outside a path between the magnetic target image and the shower were not considered.

Finally, in the fine tracking process, the drift time from the associated paddle hit from the coarse tracking was corrected. The drift distance from each wire for the coarse tracks was found from the drift time. Then proper left/right differentiation of the tracks was identified from the best combinations sorted by χ^2. Again, sufficiently similar tracks were identified as the same track and poor χ^2 combinations were removed.

Timing Cuts

A set of timing window cuts are performed immediately after decoding the hits recorded in the TDCs and after the TDC offsets have been applied. The purpose of these cuts is to remove hits that are not associated with the trigger. The width of the time window is defined by the maximum drift time, about 200 ns. This window is roughly constant between all planes. The hits that do not pass these cuts are not written to any output after replaying.

This type of cut reduces the number of hits to consider by about a factor of ten. However, placing too tight cuts greatly reduces the ability to perform tracking on hits that may have come out of time and not caused the trigger. This limits the chances of the tracking process to finding only one real track per event. Further cuts on these hits can be applied to

remove effects such as crosstalk. This is currently not done in the code, but is discussed in the second paragraph below.

Shower Cuts

The shower cuts define regions in each plane where hits for tracking are considered. The regions are based upon the reconstructed position of the target image and the position of the cluster in the shower. The effect of these cuts was to put very coarse momentum cut on the data. After the shower clusters were determined, a window around the cluster center and the target image was used to define two ends of a volume. If any portion of a wire with a recorded hit entered in this volume, it was considered valid and available for tracking.

Wire Crosstalk

Crosstalk between wires occurs when a sense wire acquires a signal and a signal is induced in the adjacent wire. Fortunately, the signal appeared to be induced about (7 ± 2) ns after the original signal and could, in theory, be removed from the data, though this was not implemented in the code. The first chamber appeared to be more sensitive to this effect (due to different amplifier/discriminator cards). Roughly 12% of the hits in the first chamber were a crosstalk signal compared to 5% of the other two chambers. For more details about the BigBite tracking and optics see [Riordan, 2007].

4.3 Pulsed Beam Analysis

In the pulsed beam mode, the electron bunches arrived at 31 MHz instead of the CEBAF standard 499 MHz. It provided a much cleaner environment to allow for the study of detector resolution. The pulsed beam data served the following purposes:

1. With a hydrogen target, it was a measure of the detector timing resolution for time-of-flight analysis.

2. With a nitrogen target, it was indicative of the effect of the nuclear medium (Fermi momentum of the nucleons) on the timing resolution of the detectors.

3. It also helped in matching the detector timing to the beam RF phase.

When the Hall was in the pulsed beam mode, a *liquid scintillator* detector (LSD) was placed close to the target area outside the box opposite to the BigBite side. The LSD was placed inside a metal box (the *brown box*[3]). Figures 4.5, 4.6 and 4.7 show the results of the pulsed beam analysis [KOLARKAR, 2006b].

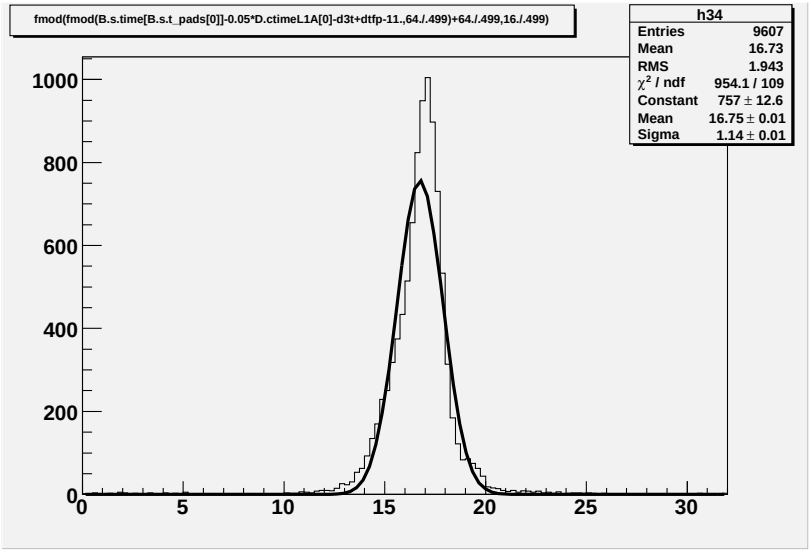

Figure 4.5: Pulsed beam scattering off a hydrogen target: Matching of the BigBite scintillator timing to the pulsed beam phase.

4.4 Data Acquisition System

For data acquisition (DAQ), the experiment used custon-made hardware and software components collectively known as the CODA (CEBAF Online Data Acquisition) [GROUP, 1995]. The outputs from all the components of the experiments are fed into electronic modules (ADCs, TDCs, scalers) and read out into buffers forming the Read-Out Controllers (ROCs). The buffers transmit data over to the Event Builder via intranet where they are organized with respect to the CODA data structure. Another homebuilt module, the Trigger Supervisor (TS) records each event associated with the ROCs and synchronizes the data coming into the ROCs. The TS was programmed to use prescalers which determined how often data was read out into the datastream via CODA. It was also used to synchronize both the detectors.

[3]The "brown box" was magnetic and caused some changes in the target region: The NMR gave polarization values of 60% and the EPR frequency had changed. These effects were identified and corrected for.

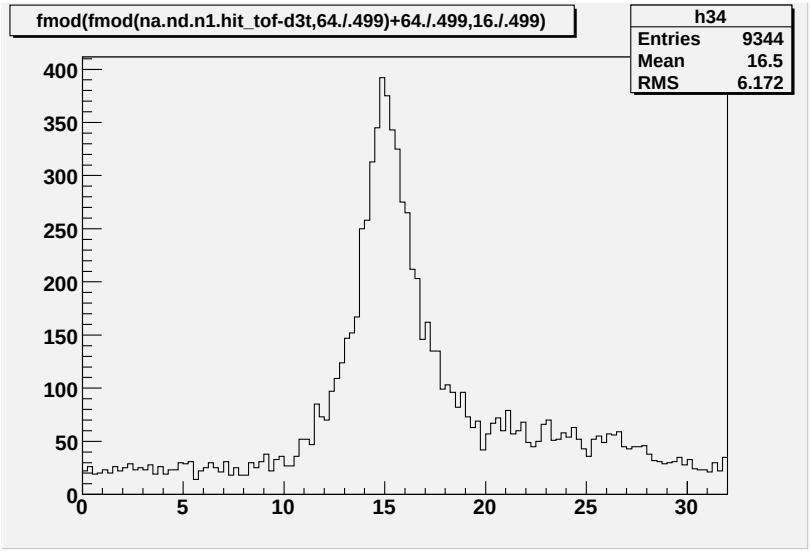

Figure 4.6: Pulsed beam scattering off a hydrogen target: Matching of the Neutron Detector plane N1 timing to the pulsed beam phase.

Also, a slow controls software system called EPICS (Experimental Physics and Industrial Control System) [Group, 2004] was used to read out information about the beam, magnets, energy spread, half waveplates and other accelerator instruments. This information was also fed into the datastream.

4.5 Helicity

As this experiment ran along with the G^0 experiment in Hall C, we had to use the G^0 helicity structure. G^0 is a parity experiment and as such needs to have good control over the electron beam parameters thus giving it priority over other Halls regarding beam parameters. We were not very sensitive to the G^0 helicity structure - as will be shown later in the section - so we could run in parallel with Hall C without any helicity problems. G^0 had their own helicity-predicting algorithm which pseudo-randomly decided the next helicity state of the electron beam. The detailed G^0 helicity structure is described below [Pitt, 2001].

The G^0 helicity structure differs from the usual helicity structure in the following ways:

1. It generates a fixed integration period ($\frac{1}{30}$ s) with continuous phase slip relative to the power line cycle instead of the present *line-locked* scheme;

2. It generates a *quartet* of helicity states instead of the present *pairs* of helicity states.

If $T_{line} = \frac{1}{60}s$ is the period of the power line cycle, then the pulse period is $2T_{line}$. This

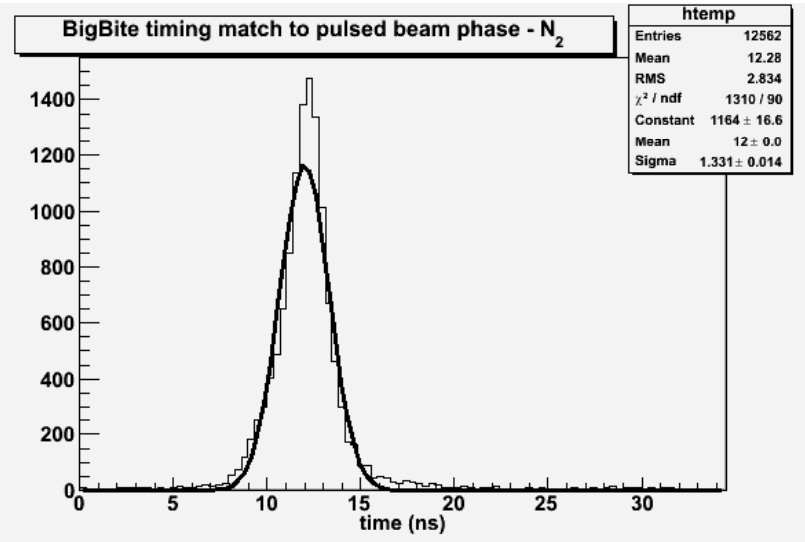

Figure 4.7: Pulsed beam scattering off a nitrogen target: Matching of the BigBite scintillator timing to the pulsed beam phase.

pulse period usually equals $T_{settle} + T_{stable}$, where T_{settle} is the time required for the Pockels cell (that switches the electron helicity) to stabilize (after switching) and T_{stable} is the time interval where the Pockel cells are stable and is our actual data taking interval (integration). For the G^0 helicity mode, $T_{stable} = 2T_{line} = \frac{1}{30}$ s. This slips the integration phase with respect to the power line cycle enabling all phases of the 60Hz line to be sampled and nearly perfectly cancels the 60 Hz power line noise over the actual data-taking interval, which is not possible in the usual scheme.

The helicity signal sequence in the G^0 mode was a quartet structure instead of the usual "pairs" structure, as shown in Figure 4.8. Earlier (*pairs* scheme), the first member of the sequence was pseudo-randomly chosen and the next member was its complement, i.e. either $+-$ or $-+$. In the G^0 scheme, the sequence came in as $+--+$ or $-++-$. The first member of the quartet was pseudo-randomly chosen with a helicity predicting algorithm and the others followed according to the above scheme. The advantage of this scheme is that it provides exact cancellation of linear drifts over the timescale of the sequence. In the *pairs* scheme, averaging over multiple pairs is necessary to cancel such linear drifts. For G_E^n, we could still use this scheme in the *pairs* mode since the first two members of the quartet sequence are complementary to the next two.

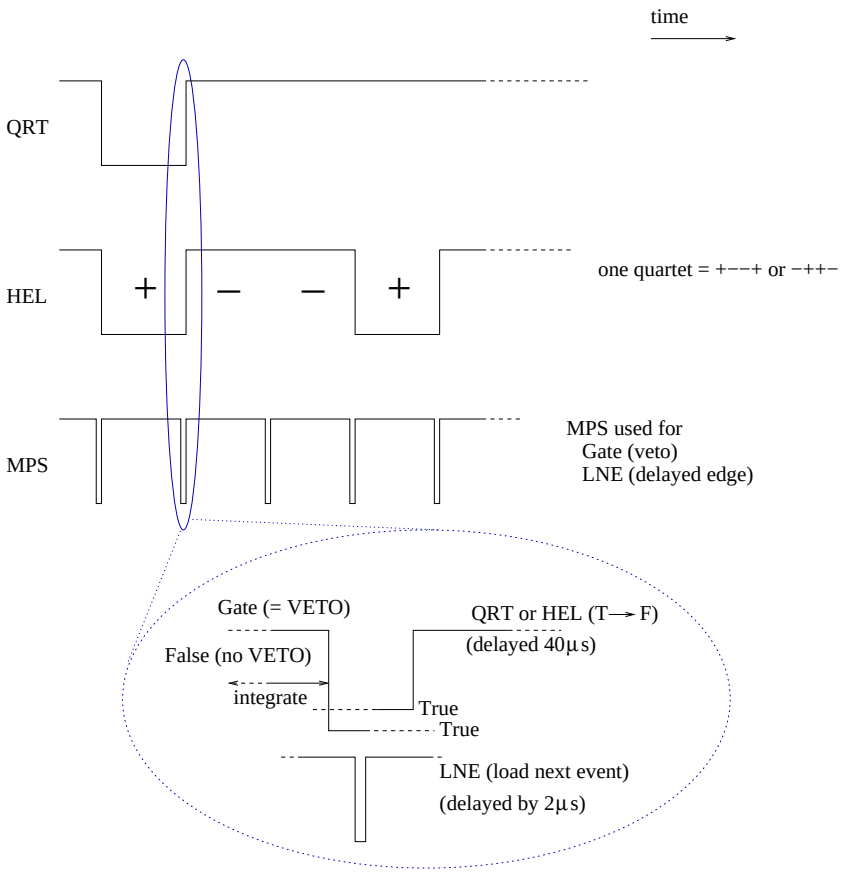

Figure 4.8: Oscilloscope view of the G^0 helicity structure used during the G_E^n experiment. MPS is the master pulse which acts as the gate and, with a 2 μs delay, as the LNE signal. The LNE loads data into the helicity scaler. QRT is the quartet signal which denotes the beginning of the HEL (= helicity) signal. The first state of the helicity quartet signal is chosen pseudo-randomly using software. [Michaels, 2006]

4.6 Scalers

Scalers count triggers as the particles are detected in the detectors and the PMTs fire at a high rate. They give us raw counts and/or rates and are especially helpful in high rate situations such as ours where signals or pulses or events arrive too rapidly to be recorded individually ("deadtimeless" scaler readout[4]). Usually scalers are synchronized to an external clock which is common to all the triggers. In our case, this clock[5] was 105 kHz. A scaler display was used for real time monitoring of quantities like rates in the ND, BB and coincidence events as well as BPMs, BCMs and helicity signal readouts. Scalers were

[4]From the Struck SIS GmbH manual. http://www.struck.de

[5]The clock normally used for the HRSs in Hall A is 1024 Hz. Ours was a very high rate experiment thus making it useful to have a high frequency clock.

also used to determine livetimes and accumulated charge. These signals could be displayed as counts or rates determined from the 105 kHz clock.

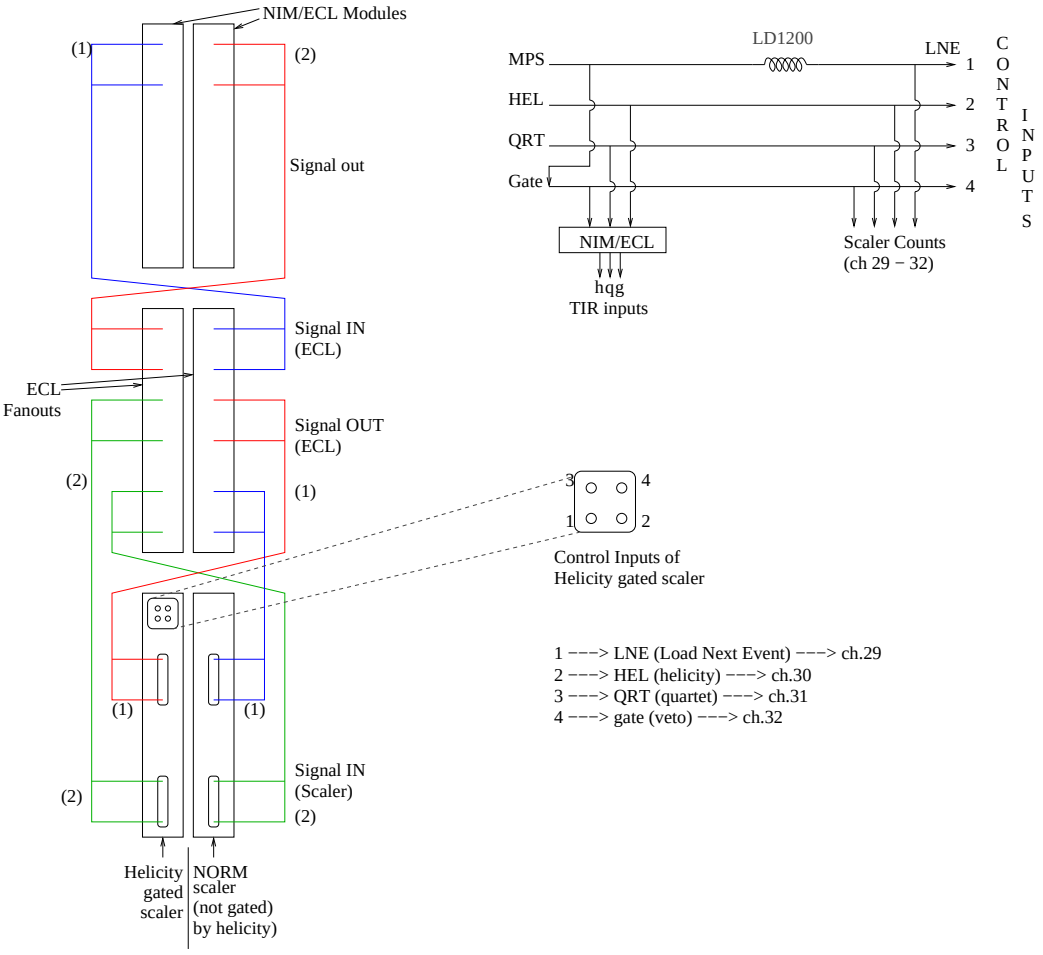

Figure 4.9: Scaler circuit diagram and channels. (1) and (2) are two example signals fed into the scalers. NORM is the normalization scaler and TIR is the Trigger Interrupt Register. The scaler counts are displayed in real-time and can be converted into rates using the 105kHz clock on board the scaler modules.

The scalers used were the SIS3800 and SIS3801 VME modules from SIS GmbH. A few of these were borrowed from the left HRS which was not used for this experiment. The difference between these two modules was that the 3801 was a multi-channel scaler (or *multiscaler*), whereas the 3800 only had inputs (though version 2 of the 3800 module had four outputs also like the 3801.) The 3801 module was configured to behave like the 3800 which was the desired behavior for the scaler modules.

The scaler modules were mounted on the `bbvme1` VME crate. Eight physical scalers were mounted on the crate. The first physical scaler was gated by helicity (meaning the events

it recorded were sorted into positive or negative helicity states); it, thus, acted like two (virtual) scalers giving us a total of nine scalers in the crate. Each scaler had 32 channels numbered from 1 to 32. A `scaler.map` file contained the information about scaler maps required to identify the channels and display them onto Graphical User Interfaces (GUIs) and read them into the DAQ. The information from the scalers could be displayed within a terminal console or on a graphical window. Appendix D shows the scaler map for this experiment.

In addition to these scalers, a separate scaler readout was used for the ND which read the F1 TDC rates for the scintillator PMTs in real time.

4.7 Beam Position and Raster Calibration

A calibration of the Beam Position Monitors (BPMs) using the HARPs results in a precise knowledge of the position of the raster spot. There is, however, a significant delay between the time of an event and the readouts of the BPMs. For this reason, the vertex of each event cannot be precisely determined from the BPM readout directly. Therefore the much faster readouts of the raster currents were used for this purpose. The observed raster current distributions and the relation between raster current and BPM position is seen in Figure 4.10 [Craver, 2007b]. Additionally, the BPMs have a finite bandwidth and cannot reproduce the true position distribution created by the raster, which is driven with a triangular wave pattern. The method used to calibrate the BPMs as well as that used to extract a refined position from the raster current are detailed in [Craver, 2007b].

The position of the raster spot with respect to the nominal beam position after the calibration was known to the level of precision of the agreement between the two position measurement methods. This task was completed using HARP scan data collected in April 2006 and its results are valid for all the data sets. For details on the BPM/raster calibrations, see [Craver, 2007b].

Copyright © Ameya Suresh Kolarkar 2008

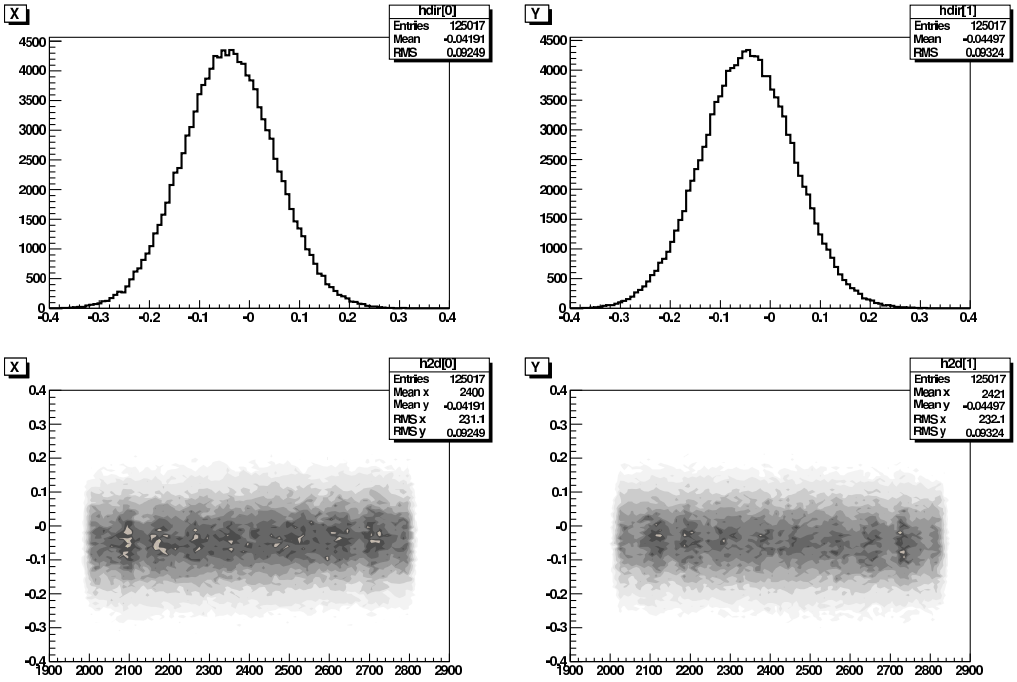

Figure 4.10: BPM calibration. For the lower plots, the $x-$ and $y-$axes represent corresponding raster sizes. The upper plots show the projections on the respective axes separately.

CHAPTER 5: ANALYSIS AND RESULTS

This chapter presents the analysis and results for one of the four kinematic regimes at which the current experiment took data. G_E^n was a (double) coincidence experiment[1] in which electrons and the corresponding neutrons were detected with dedicated detectors. The coincidence was based on Time-of-Flight (TOF).

5.1 Detector Calibrations

To get the TOF for the coincidence events, the scintillators in both the detectors had to be calibrated with reference to a standard trigger. The scintillator bars themselves had to be calibrated first so that the mean recorded timings of the bars were aligned to each other and the timing resolution was of the order of 250-300 ps. The following sections describe the scintillator calibrations for both of our detectors.

5.1.1 BigBite Scintillator Calibration

There are thirteen scintillator paddles in the BigBite detector. The scintillator plane is located between the pre-shower and shower detectors. They are numbered 0 through 12 beginning at the bottom. The x-axis points downwards (i.e. in the direction of increasing electron momentum) and the y-axis leftwards as seen from the target (as given by a right handed coordinate system); see Figure 4.3. The TDC values determined the timing of the hits on these 13 paddles. There are two PMTs on the two ends of the scintillators. The timing offsets on these are given in TDC units where 1 TDC unit = 0.035 ns. Presented below is the procedure for the determination of these timing offsets [Kolarkar, 2006a].

$$t'_l = t_0 + \frac{l}{2c_n} - \frac{y}{c_n} + t_l^{tw} \tag{5.1}$$

$$t'_r = t_0 + \frac{l}{2c_n} + \frac{y}{c_n} + t_r^{tw} \tag{5.2}$$

where we have deduced the $y-$dependence on x by looking at the plot of the time difference between adjacent bars versus pedestal-subtracted ADC values; subscripts l and r indicate

[1] There are also triple coincidence experiments in which three particles are detected in coincidence. Here, we detect only two, and generally, the term "double" can be dropped.

left and right, c_n is the speed of light in the scintillators and t^{tw} is the *time-walk* correction factor.

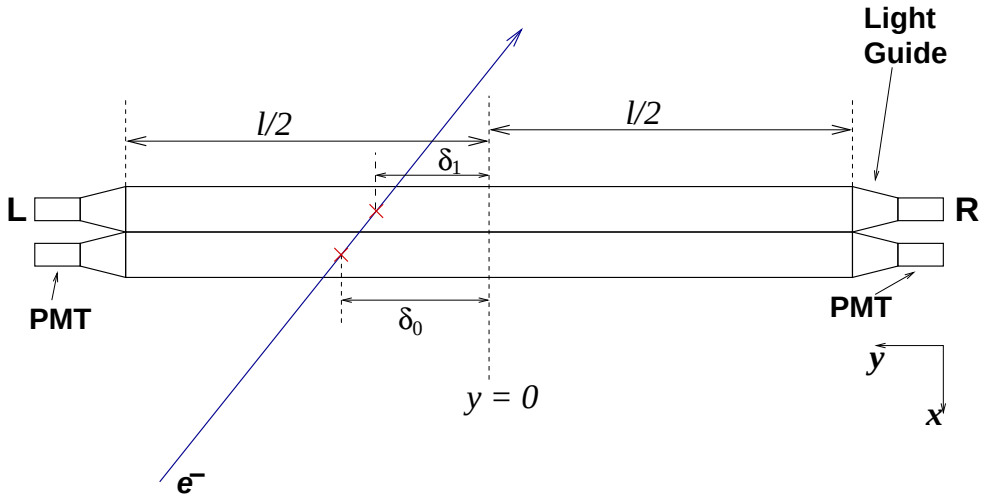

Figure 5.1: Schematic representation of a particle traversing two consecutive scintillator paddles.

First, all the left photo-multiplier tubes (PMTs) are aligned. This is done by plotting the difference of the left PMT corrected times for adjacent paddles, and changing the TDC time offsets in the BB scintillator database (`db_B.s.dat`; henceforth Bsdb). Then the right PMTs are aligned similarly. The run is replayed again with this new database and alignment is checked again. This is repeated if necessary. For these alignments, paddle # 6 (i.e. the seventh, or middle, paddle) was taken as the reference.

Once the left and right times are independently aligned, the difference between the left and right time average ((L+R)/2 or the `B.s.time` variable) is plotted, and so is the left and right time difference ([L-R] or the $y-$position) for adjacent paddles. Note that this does not necessarily align the time differences to zero, but some arbitrary value (which can be made zero if required). Given the resolution of these TDCs to be 35 ps, an alignment of the scintillators to within ± 50 ps was deemed good enough.

Time-walk effects arise since, depending on the type of trigger, the TDCs would trigger at a later time for lower amplitudes even though the times of the peaks are the same [Leo, 1987]. The correction factor t^{tw} is proportional to some fractional power of $1/A$, i.e. $t^{tw} \propto 1/A^p$; $0.5 \leq p \leq 1$, where A is the ADC signal. The scintillation light as it reaches

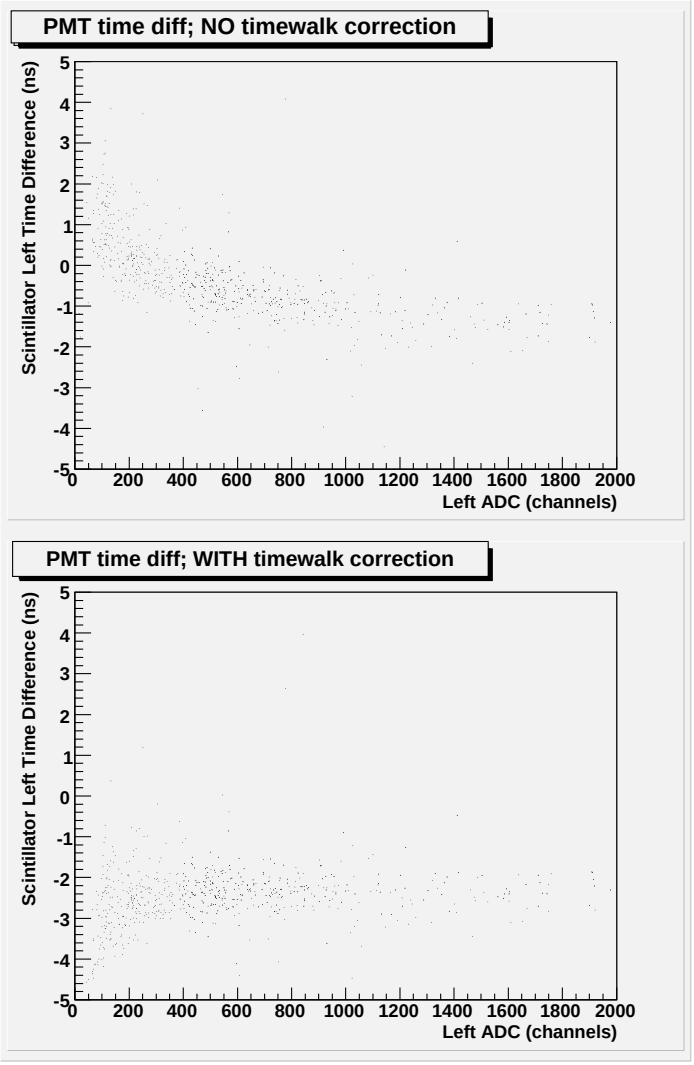

Figure 5.2: Time-walk effect and correction. The scintillator left time differences in the lower plot are linear (constant) after the correction.

the photomultiplier tubes is attenuated (assuming $p = 1/2$ in this case)

$$A_l = A_0 \exp\Big(\frac{-(l/2 - y)}{\Gamma}\Big) = c_0 \exp\left(+y/\Gamma\right) \tag{5.3}$$

$$A_r = A_0 \exp\Big(\frac{-(l/2 + y)}{\Gamma}\Big) = c_0 \exp\left(-y/\Gamma\right) \tag{5.4}$$

$$t'_l = t_0 + \frac{l}{2c_n} - \frac{y}{c_n} + \frac{c_1}{\sqrt{A_0}} \exp\left(\frac{-y}{2\Gamma}\right) \tag{5.5}$$

$$t'_r = t_0 + \frac{l}{2c_n} + \frac{y}{c_n} + \frac{c_1}{\sqrt{A_0}} \exp\left(\frac{+y}{2\Gamma}\right) \ , \tag{5.6}$$

where Γ is the characteristic decay length for the signal in the scintillator in which the signal amplitude drops by a factor e.

Typical results for kinematic #4 ($Q^2 = 1.7$ (GeV/c)^2) are shown in Figures 5.3 and 5.4.

More iterations result in better alignment for the run that was used for the calibration but worsens it for other runs. This was mainly a binning factor and also due to the fact that the intrinsic resolution of the BB scintillator TDCs was about 35 ps.

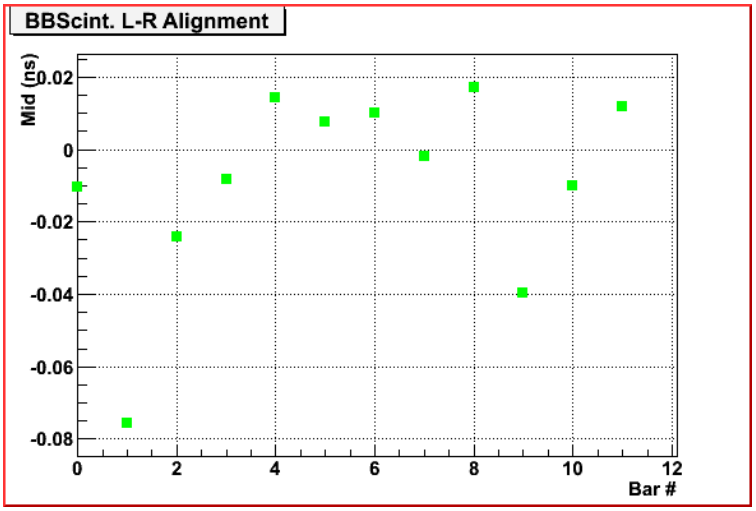

Figure 5.3: The average-time alignment for two consecutive BB scintillator paddles.

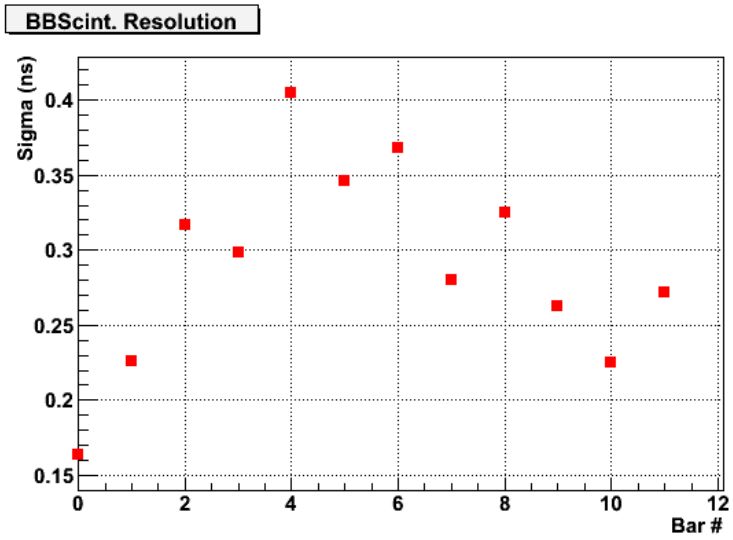

Figure 5.4: Resolution for comparison of timing of two adjacent paddles. Note that this resolution is for two paddles; the resolutions for single paddles are better than seen in the figure by a factor of $\sqrt{2}$.

BigBite Optics: The Magnetic Midplane Model

BigBite optics calibration was done using a very simple model called the "magnetic midplane model" [Riordan, 2007]. All interactions were treated at a single point on the midplane of

the BigBite magnet. No change in the non-dispersive direction was assumed. With these assumptions, one could trace a track to a unique point on the BB midplane and along the beam. This fully described the electron track after it left the target.

5.1.2 Neutron Detector Scintillator Calibration

Since the ND had 7 planes each with a number of scintillator bars (Section 4.1), we use the notation N*p*-*bb*, where N stands for the Neutron arm, *p* denotes the plane number and *bb* denotes the bar number in plane *p*. The principle behind the ND calibration was similar in concept to the BB scintillator calibration. The time-of-flight (TOF) spectrum of a detected "event" in a bar in a plane, say N1-14, was compared with the TOF spectrum of an adjacent bar in the same plane, N1-15 (vertical matching), for the same "event". The difference in these timings was put to a constant (taken, without loss of generality, to be zero) relative to a single detector, which in this case was the bar N1-10[2]. This process was done iteratively till all bars in a plane were aligned.

Then, detectors in planes N2 through N4 had offsets calculated relative to the detector bar N1-10. For example, to get the offset for detector N3-11, the timing spectra (N3-11 - N2-11), (N2-11 - N1-11), and (N1-11 - N1-10) were used. Thus, all bars in planes N1 - N4 (excluding the Glasgow detectors) were aligned with N1-10. To align bars from planes N5 through N7, bars N4-10 and N5-14 were first aligned (since these line up in the horizontal plane, see Figure 4.1), and then all bars of planes N5 through N7 were aligned relative to N5-14. Thus all bars of al planes were aligned relative to bar N1-10. A similar process was done for the Glasgow detectors, but a database with detector status per run had to be constructed since detectors in the Glasgow plane were removed and added on a run by run basis.

5.1.3 Neutron Detection Analysis

The geometry, channel map, calibration constants, etc. of each plane were specified in a database. Each plane contained an array of scintillator bars. In the case of the neutron detector planes both sides of a single bar were read out and combined, while for the veto bars each left- and right-paddle was read out independently.

[2]There was nothing sacrosanct about bar N1-10, and in fact could have been any bar conveniently located with respect to the other planes and that which recorded a relatively large number of events.

The analysis of the neutron detector was done in the following steps:

1. Decoding
2. Plane-by-plane reconstruction
3. Cluster-building
4. Cluster-to-Veto matching
5. Track construction for easier comparison to BB calculations

1. **Decoding**

   The first step was to take the raw data from a CODA file and write out the ADC and TDC values to ROOT-files. Since the TDCs are multi-hit, the general storage of the ADC and TDC readout as a set of parallel arrays. This allows for tight-packing of the data. These sets have an array for the bar number, the raw readout value, and then the values after some corrections have been applied.

2. **Intra-plane Reconstruction**

   At the coarse processing stage, the hits[3] in the correlations between the ADCs and TDCs for a given bar were constructed; this was not performed at the decoding stage so the multi-hit capabilities of the TDCs could be used.

   First the TDC and ADC hits were sorted by bar number and value. To speed up the search for matching hits, temporary index arrays were used to hold the location of the hits. The corrected times from the TDC, were selected to use only those entries within a 300 ns time window as given in the database.

   The "hits" on each bar were then constructed: for the neutron detector planes both PMTs on a bar were required to have ADC and TDC information while for the veto planes only the single attached PMT had to have the complete information. The left and right times for each bar were corrected for timewalk effects using the ADC readout of the same bar like in the BB case (Section 5.1.1).

   With the corrected times the time of the hit on the bar, its position along the bar, and energy deposition was calculated and the complete hit was constructed. The hits

[3] A "hit" is when the PMT fires due to a particle being detected in the scintillator bar.

were sorted in ascending order by bar number. For the veto detectors the same steps were followed, except that only one side PMT was used, such that a mean-time could not be formed.

3. **Cluster finding**

   The individual hits in seven neutron detector planes had to be matched together to construct a small number of "clusters" per event. This is performed at the "FineProcess" level by the analysis software. Refer to Figure 5.5 for the following explanation. First, all the "hits" in the neutron detector planes constructed in the previous step were sorted through, and those which lied within the dimensions of the bar were put

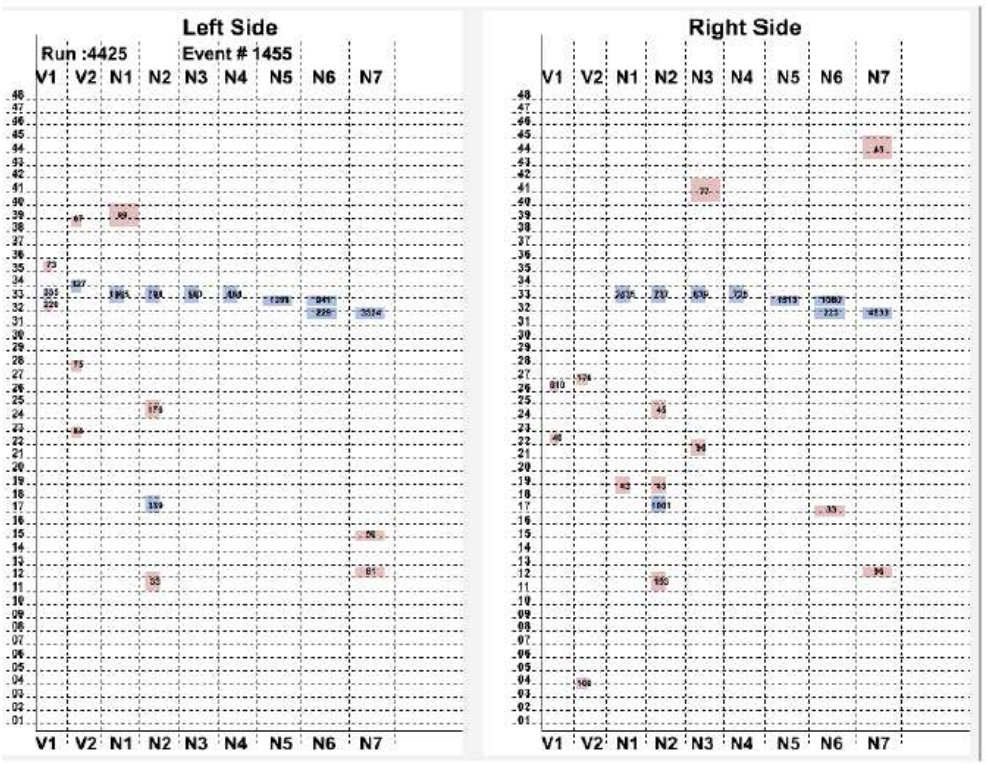

Figure 5.5: The Neutron Detector showing a neutron event. The blue "hits" show the path of a neutron cluster through the detector scintillators.

into an array of good "single hits". The "single hits" were then iterated over, and those which were either neighbors vertically (i.e. in adjacent bars in the same plane) or in neighboring planes and at roughly the same vertical position, and have times matching to within a short window (set to 10 ns) were joined together into a cluster. The cluster continued to grow to collect all "hits" with the given criteria. The next unused "single hit" was then used as the beginning of the next cluster, and so on, until

all the "single hits" were members of a cluster, even if that cluster contained only one hit bar. The geometric correlation between bars was generated at initialization and stored. The clusters are sorted in order of descending deposited energy.

4. **Veto to Cluster matching**

   To look for a matching hit in the veto counters, a ray from the front of the cluster towards the target center was used to match to the veto bars and get the matching bar, VetoInt. The index of the veto hit and the corresponding veto bar for each veto plane that best matched the time of the cluster within ± 1 bar of VetoInt was stored with the cluster. If no match was found the veto bar was listed as VetoInt and the index was set to -1. The time of the veto-hit was just from the temporary time arrays mentioned above, and thus not corrected for the position along the veto bar.

5. **ND to BB matching**

   "Tracks" were then generated from the clusters, where rays from the target center to the primary hit were generated and put into the Hall Coordinate System (HCS). The path-length from the target to the hit was calculated, as well as the direction of the momentum 3-vector. However, the β $(= v/c)$ and magnitude of the momentum vector are arbitrary at this point since the BigBite arm was not used (whence the time-of-flight is not fully calculated). The location of the tracks' intersections at $Z = 0$ of the ND are calculated and reported, as well as their equivalent target θ and ϕ variables. To get the proper "time-of-flight" of the candidate nucleon track, the time relative to the electron in BigBite was calculated.

5.2 RF Analysis

The CEBAF electron beam ran - in continuous mode - at a frequency of 499 MHz meaning the electron bunches came about every 2.004 ns [Kolarkar, 2006b]. The RF analysis looked at the correlation between the particles detected by the detectors and the RF phase of the electron beam. For both the detectors (BB and ND), the time-walk and path-length corrected RF phase correlation is as shown in Fig. 5.6. The sharper the spike is, the better the timing synchronization between the pulse of electrons and the particles detected by the detectors. If there were no correlation, the plot would be flat (constant).

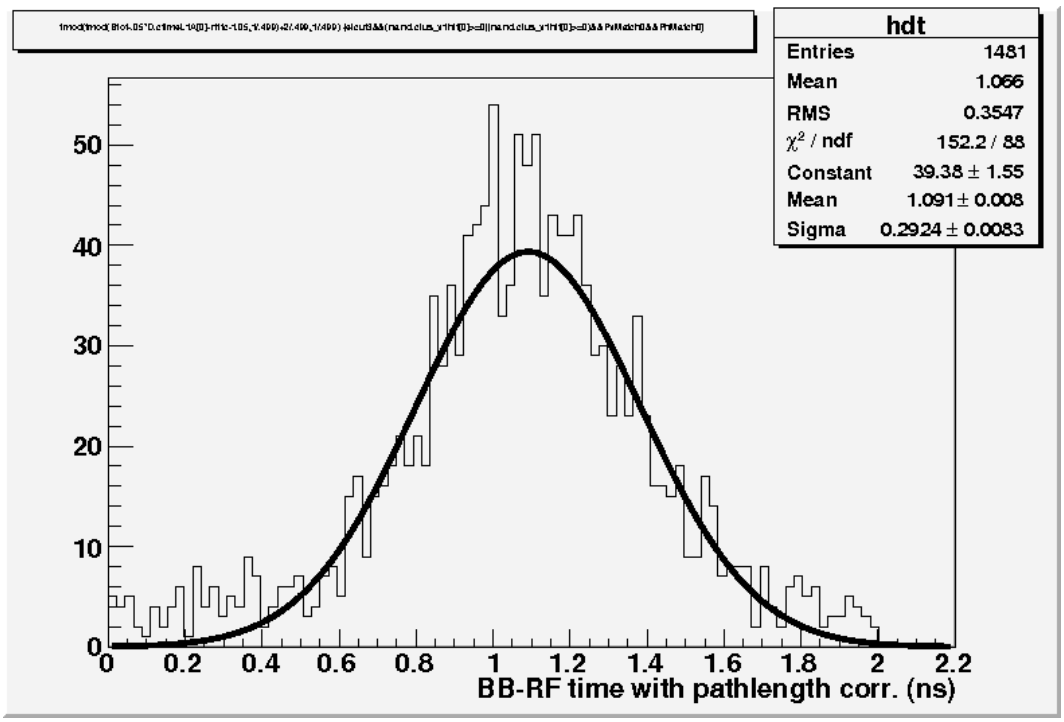

Figure 5.6: BigBite scintillator correlation with the beam RF phase for all planes. (This plot is for production run 4364.)

5.3 Dilution Factors

5.3.1 Nitrogen Dilution

To get the nitrogen dilution factor, D_{N_2}, we took data with a reference cell filled with nitrogen at 135 psig (about 10 atm). The physical characteristics of the reference cell were identical to that of the target cell. During analysis, similar cuts were made to production runs and the nitrogen runs to determine the dilution from nitrogen.

The dilution factor can be calculated from the following [Kolarkar, 2007b]. The yield Y_e is the number of good[4] events normalized with charge, livetime, detector efficiencies and *one-track-only* correction factor.

$$Y_e = \frac{N_{cuts}}{Q \cdot \mathrm{LT} \cdot \epsilon \cdot \kappa} \tag{5.7}$$

$$D = 1 - R\frac{Y_e^{(N_2)}}{Y_e^{(^3He+N_2)}} \tag{5.8}$$

[4]Good meaning the ones left after all appropriate cuts have been made.

where $R \equiv \frac{\rho_{targ}(N_2)}{\rho_{ref}(N_2)}$ is the ratio of density of nitrogen in the target cell to the that in the reference cell, N_{cuts} is the total number of events after all cuts have been made, Q is the total charge during the run, LT is the livetime, ϵ represents the efficiencies of various detectors and κ is the one-track-only correction factor (see below). Since this was a coincidence experiment, both BigBite and the Neutron Detector parameters had to be included in the analysis. The Neutron Detector detected all the tracks from multi-track events whereas the BB discarded all but the one-track events. This fact was taken into account through the κ factor. The one-track correction factor on the BigBite side is given as

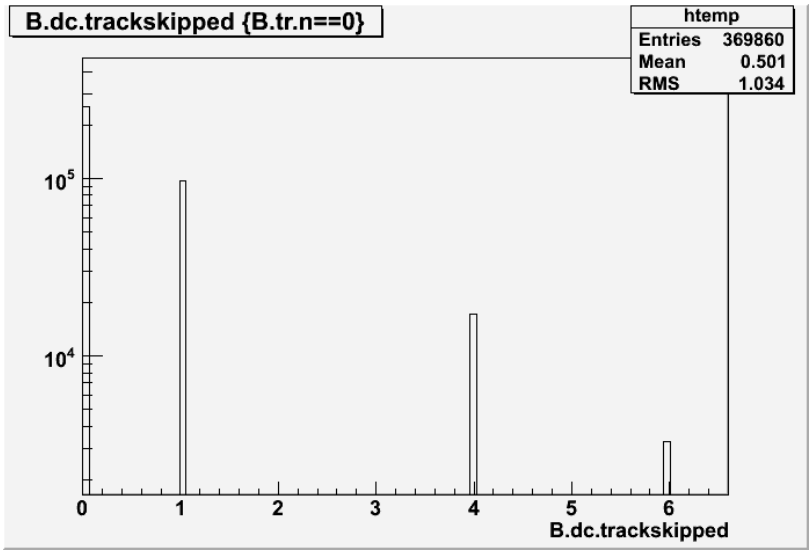

Figure 5.7: The number of tracks discarded by the BigBite tracking algorithm. There were upto six tracks present for some events.

$$\kappa = \frac{\text{number of one track events accepted}}{\text{total number of events for all tracks}} \tag{5.9}$$

From Figure 5.7, we see that for the BigBite detector, $\kappa = 0.498 \pm 0.002$ for production data and 0.542 ± 0.002 for the nitrogen runs. The number of one-track events skipped by the tracking algorithm was 13.32% for production data and 12.34% for nitrogen data. The skipped one-track events were disregarded. On the ND side, all tracks were accepted, so we did not need to compute the one-track correction factor for the Neutron Detector.

The dilution factor (Equation (5.8)) depends on specific momentum cuts. Different cuts on the parallel and perpendicular missing momenta, p_{mpar} and p_{mperp}, respectively, give different values for the dilution factor, D. In particular, for cuts defined in Section 5.6.1, $D_{N_2} = 0.955 \pm 0.02$.

For our kinematic, run number 4585 was the nitrogen reference run, and was used to get the nitrogen dilution for runs at that kinematic. The detector efficiencies, ϵ, were assumed to be the same for all the runs of the same kinematic point [KOLARKAR, 2007b].

5.3.2 Proton-to-Neutron Conversion

When we scattered off the electrons from a hydrogen target, we detected neutrons in our Neutron Detector. This was due to the protons "converting" into neutrons in the shielding and other material (lead, iron, glass) in their path. Similarly, a neutron could, in the presence of a nucleus, convert into a proton (and a negative pion) and be detected as a charged particle in the ND. The effect due to this was substantial as is clear from the analysis below.

Let us denote the observed number of neutrons and protons by $N^{(n)}$ and $N^{(p)}$, respectively [FEUERBACH, 2007]. Then

$$N^{(n)} = N_n^{(n)} + N_p^{(n)} \tag{5.10}$$

$$N^{(p)} = N_n^{(p)} + N_p^{(p)} \tag{5.11}$$

where the subscript indicates the nucleon that the detected particle started out as from the target. Since neutron and proton detection efficiencies and scattering cross-sections are different, we have

$$N_n^{(n)} \propto (A - Z)\sigma_n \mathcal{P}_n^{(n)} \tag{5.12}$$

$$N_p^{(p)} \propto Z\sigma_p \mathcal{P}_p^{(p)} \tag{5.13}$$

where $\mathcal{P}$ denotes the probability of detecting particle a as particle b and σ_a is the cross-section for quasi-elastic scattering off particle a, and $A(Z)$ is the atomic mass number (atomic number) of the target nucleus. The ratio of the above equations yields

$$R_{(A-Z)/Z} := \frac{N^{(n)}}{N^{(p)}} = \frac{\frac{(A-Z)}{Z}\frac{\sigma_n}{\sigma_p}\frac{\mathcal{P}_n^{(n)}}{\mathcal{P}_p^{(p)}} + \frac{\mathcal{P}_p^{(n)}}{\mathcal{P}_p^{(p)}}}{\frac{(A-Z)}{Z}\frac{\sigma_n}{\sigma_p}\frac{\mathcal{P}_n^{(p)}}{\mathcal{P}_p^{(p)}} + 1} \,. \tag{5.14}$$

We now define the dilution factors as the fraction of observed neutrons or protons that

are correctly identified as coincidence events:

$$D_n = \frac{N_n^{(n)}}{N_n^{(n)} + N_p^{(n)}} = \frac{\frac{\sigma_n}{\sigma_p}\frac{\mathcal{P}_n^{(n)}}{\mathcal{P}_p^{(p)}}}{\frac{\sigma_n}{\sigma_p}\frac{\mathcal{P}_n^{(n)}}{\mathcal{P}_p^{(p)}} + 2\frac{\mathcal{P}_p^{(n)}}{\mathcal{P}_p^{(p)}}} \tag{5.15}$$

$$D_p = \frac{N_p^{(p)}}{N_n^{(p)} + N_p^{(p)}} = \frac{2}{\frac{\sigma_n}{\sigma_p}\frac{\mathcal{P}_n^{(n)}}{\mathcal{P}_p^{(p)}} + 2}\ . \tag{5.16}$$

The dilution factors can be determined by comparing the neutron and proton events from targets with different neutron-to-proton (n/p) ratios. We compared events from ^3He, N_2 and H_2 targets which have a n/p ratio of 1:2, 1:1 and 0:1 respectively. Thus

$$R_{H_2} = \frac{\mathcal{P}_p^{(n)}}{\mathcal{P}_p^{(p)}} \tag{5.17}$$

$$R_{N_2} = \frac{\frac{\sigma_n}{\sigma_p}\frac{\mathcal{P}_n^{(n)}}{\mathcal{P}_p^{(p)}} + \frac{\mathcal{P}_p^{(n)}}{\mathcal{P}_p^{(p)}}}{\frac{\sigma_n}{\sigma_p}\frac{\mathcal{P}_n^{(n)}}{\mathcal{P}_p^{(p)}} + 1} \tag{5.18}$$

$$R_{^3\mathrm{He}} = \frac{\frac{\sigma_n}{\sigma_p}\frac{\mathcal{P}_n^{(n)}}{\mathcal{P}_p^{(p)}} + 2\frac{\mathcal{P}_p^{(n)}}{\mathcal{P}_p^{(p)}}}{\frac{\sigma_n}{\sigma_p}\frac{\mathcal{P}_n^{(n)}}{\mathcal{P}_p^{(p)}} + 2} \tag{5.19}$$

which yields for the ^{3}He dilution factors

$$D_n = \frac{R_{^3\mathrm{He}}(R_{N_2} + R_{H_2}) - 2R_{N_2}R_{H_2}}{R_{^3\mathrm{He}}(R_{N_2} - R_{H_2})} \tag{5.20}$$

$$D_p = 2\frac{R_{N_2} - R_{^3\mathrm{He}}}{R_{N_2} - R_{H_2}} \tag{5.21}$$

About 64-67% of detected neutrons for kinematic #4 actually started out as neutrons, and hence our raw asymmetry needs to be corrected by this dilution factor.

5.4 ND Acceptance Studies with Monte Carlo

We have seen in Section 1.2.3 that the nucleons inside a nucleus can possess momenta up to about 200 MeV/c for light nuclei[5]. This is the Fermi momentum of the nucleons. The missing perpendicular and parallel momentum cuts that we apply on our data essentially give us the range of this missing momentum distribution. During the experiment, we had limited acceptance for our deterctors in the direction transverse to the outgoing neutron momentum direction. This directly relates to the transverse components of the initial

[5]The spin-dependent distribution of the nucleons in ^{3}He are described in [Milner *et al.*, 1996].

neutron momenta (given by the perpendicular missing momentum, p_{mperp}). The main objective of these Monte Carlo acceptance studies was to determine what fraction of the transverse momenta of the outgoing neutrons are we accepting through our ND, or, to determine the maximum initial momenta the nucleons can posses so that they can be detected in quasi-elastic kinematics by our limited acceptance ND. Thus, we attempted to determine the phase-space acceptance of the ND for a particular momentum transfer value.

In the case of a hydrogen target, there is no Fermi momentum present and hence the spread in the outgoing proton spectrum is due only to the spread in the momentum transfer vector, $\vec{q}$. For other nuclei, for every $\vec{q}$, there is a further spread due to the Fermi momenta of the nucleons in the target.

5.4.1 A brief introduction to MCEEP

MCEEP is the Monte Carlo simulation package for $(e, e'p)$ experiments [Ulmer, 1991]. It was later extended to the neutrons, too. The version used for this study (version 3.9) contains information about the Jefferson Lab detector packages and various targets [Kolarkar, 2007a]. Since our detectors were custom-made for the experiment, their geometry and positions were specified in the MCEEP input data[6]. For our acceptance studies, the detectors geometries were put in the program with the proper dimensions, positions and angles. The input files are described in Appendix F.

5.4.2 Results and Future Prospects

A number of studies were performed: (i) phase-space of neutrons to determine what fraction of target neutrons we are capable of detecting, (ii) acceptance effects on the longitudinal asymmetry, (iii) effects of nitrogen in the target on the asymmetry, (iv) radiative corrections (internal too but mostly external). More studies are planned in the near future.

Figure 5.8 shows an "infinite" (meaning a lot larger than the actual size) Neutron Detector which accepts all the neutrons from our target. The black box frames within (in the upper figures) depict the real size and position of the ND. From these plots, we see that the size of the ND was indeed good enough. In Figure 5.10, the size of the ND was varied from about five times larger to one-fifth as large, and the number of accepted events as a fraction of total available neutrons is plotted. The figure indicates that with our

[6]BigBite will be part of the standard Hall A equipment in the future.

real ND, we indeed accept about 87% of all available neutrons up to a given perpendicular missing momentum value ($P_{\mathrm{mperp}} < 150$ MeV/c). Figure 5.9 is also the same with absolute (horizontal and vertical) dimensions.

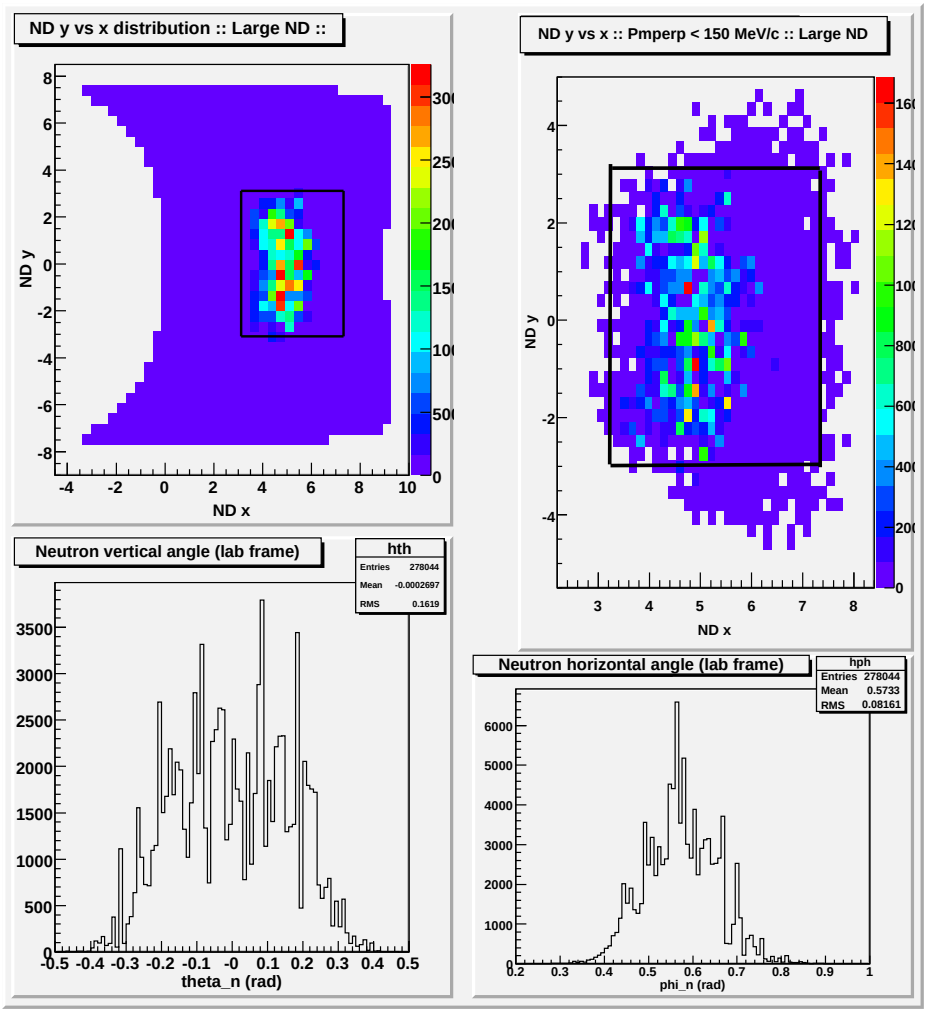

Figure 5.8: MCEEP: An "infinite" ND is considered (much larger than the real ND dimensions). The top left plot has no perpendicular missing momentum cuts whereas the one on the top right has $P_{mperp} < 150$ MeV/c. The black outline is the position and size of the real Neutron Detector. The lower two plots show the horizontal and vertical angular spread of the neutrons. All variables are defined within the laboratory coordinate system.

Figure 5.11 shows the distribution of the nitrogen P_{mperp} events compared to O_2 in the MCEEP program (since MCEEP does not simulate processes with N_2 target and oxygen is close enough in atomic mass and number). Considering the nuclear shell structure of nitrogen and oxygen, the nitrogen data was actually compared to oxygen's $s_{\frac{1}{2}}$ distribution.

We note that the plots in this section use the two-body-break-up (2bbu) as opposed to

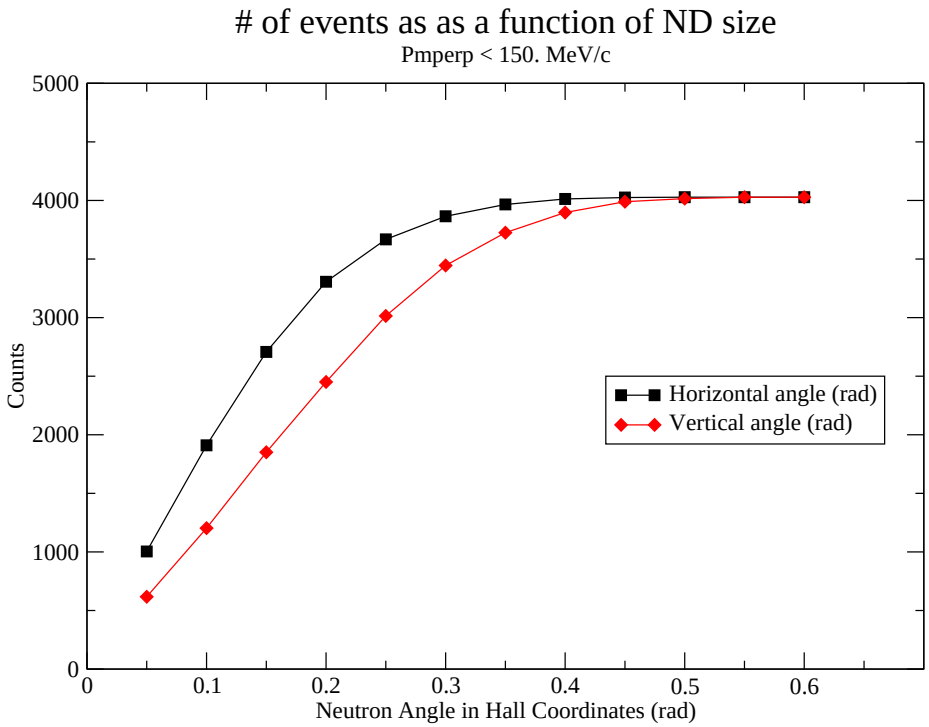

Figure 5.9: MCEEP: Number of events with different ND sizes - horizontal and vertical independently - with $P_{mperp} < 150$ MeV/c cut.

three-body-break-up (3bbu) functions which should be used in the case of a neutron knock-out from ^{3}He[7]. This configuration did not exist in the MCEEP code and is being input in the local version. We note that, from [Jans *et al.*, 1982], the 3bbu spectrum is about eight times smaller than the 3bbu spectrum at the peak and falls off more slowly than the 2bbu spectrum, which is also seen in our comparison of data versus 2bbu simulations. Some more analysis appears in [Kolarkar, 2007a].

5.5 Radiative Effects and Corrections

Radiative corrections can be classified into internal and external. External radiation comprises of photons given off due to scattering off the glass walls of the target cell and other things along the way. Internal effects arise due to two photon exchange and other such effects shown in Figure 2.13. Both effects result in energy loss thus apparently *increasing* the momentum transfer value for a given kinematic point.

[7]Since the two *left-over* protons cannot form a bound system.

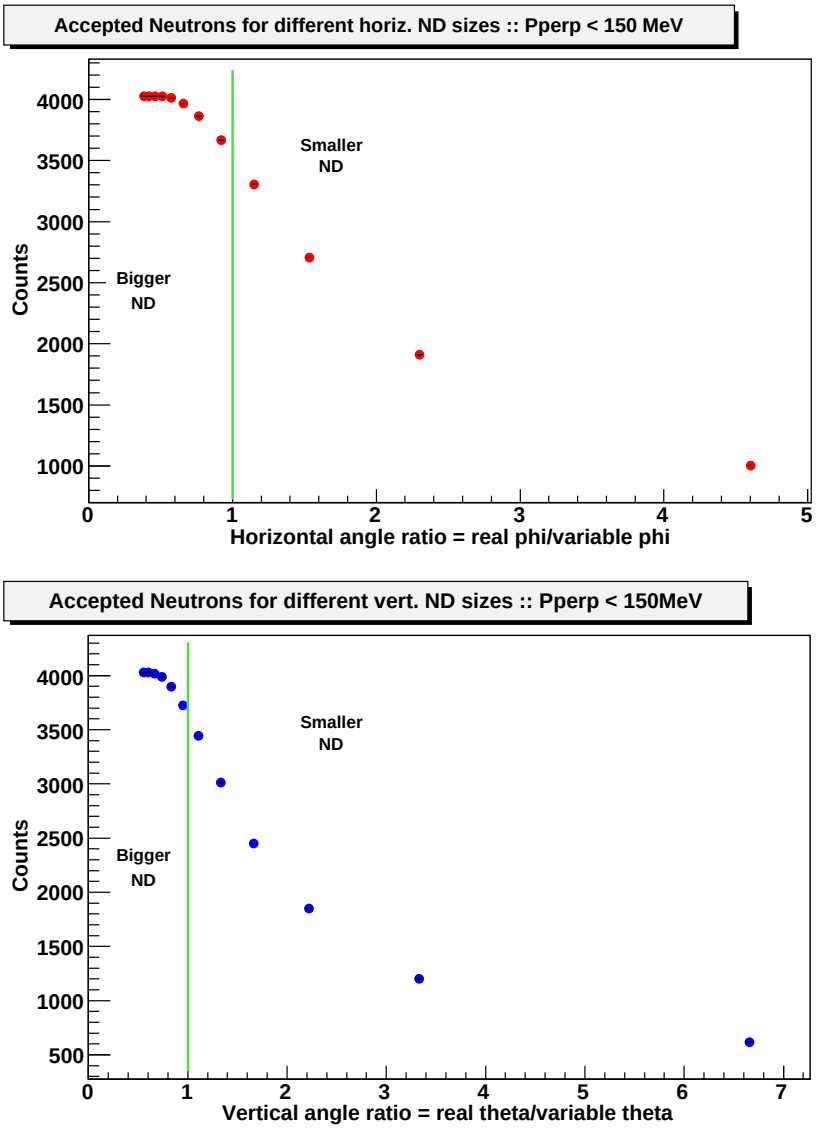

Figure 5.10: MCEEP: Number of neutrons accepted as a function of the horizontal and vertical size of the ND. The vertical line in both plots indicates the size (along the corresponding axis) of the real ND. These plots show that the real ND accepts about 87% of neutrons scattered from the target.

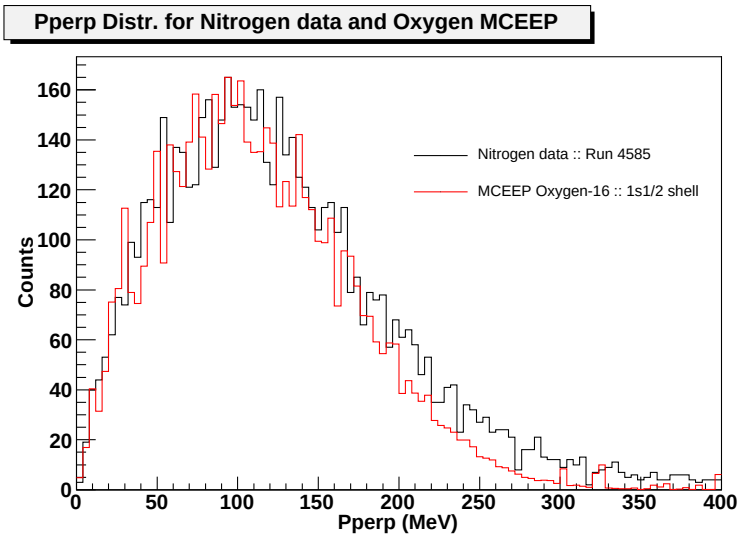

Figure 5.11: MCEEP: Comparing nitrogen reference cell data with oxygen $1s_{\frac{1}{2}}$ from MCEEP. This was mainly to check the efficiencies and spatial acceptances as a function of perpendicular missing momentum (phase space).

5.5.1 Internal Effects

The measured cross-section found to be related to the lowest-order (Born) cross-section by a factor $(1+\delta)$ [Schwinger, 1949, Mo and Tsai, 1969]:

$$\left.\frac{\mathrm{d}\sigma}{\mathrm{d}\Omega}\right|_{\mathrm{meas}} = (1+\delta)\left(\frac{\mathrm{d}\sigma}{\mathrm{d}\Omega}\right)\Bigg|_{\mathrm{Born}} \tag{5.22}$$

where

$$\delta = \frac{-2\alpha}{\pi}\left[\left(\ln\frac{E}{\Delta E} - \frac{13}{12}\right)\left(\ln\frac{-q^2}{m^2} - 1\right) + \frac{17}{36} + \frac{1}{2}f(\theta)\right] , \tag{5.23}$$

$$f(\theta) = \ln(\sin^2\tfrac{1}{2}\theta)\ln(\cos^2\tfrac{1}{2}\theta) + \Phi(-\sin^2\tfrac{1}{2}\theta) . \tag{5.24}$$

Here E is the energy of the incident of scattered electrons and ΔE is the maximum energy loss of the electron or the maximum kinematically allowed energy of the photon. In *potential scattering* [Mo and Tsai, 1969], the energy of the incident and scattered electron is the same and so is the maximum energy loss of the electron and the maximum energy of the radiated photon. For multiple photon emissions, the $(1+\delta)$ would be replaced by e^{δ} to take into account higher-order corrections[8]. Internal radiative corrections need to be applied to both electrons and hadrons.

[8]For other forms of δ for higher-order corrections, see Reference [Mo and Tsai, 1969].

5.5.2 External Effects

The basic mechanism of collision loss for electrons is the same as that for heavy charged particles, as given by the well known Bethe-Bloch formula. However, this formula takes a different form to account for the indistinguishability of the final electrons and the fact that the maximum energy transfer $W_{max} = T_e/2$, where T_e is the kinematic energy of the incident electron. The formula in this case reads

$$-\frac{\mathrm{d}E}{\mathrm{d}x} = 2\pi N_a r_e^2 m_e c^2 \rho \frac{Z}{A}\frac{1}{\beta^2}\left[\ln\left(\frac{\tau^2(\tau+2)}{2(I/m_e c^2)^2}\right) + F(\tau) - \delta - 2\frac{C}{Z}\right] \tag{5.25}$$

where

$\mathrm{d}E/\mathrm{d}x$:	mean energy loss per unit path length
r_e:	classical electron radius (2.818 fm)
$m_e c^2$:	electron rest energy (0.511 MeV)
N_a:	Avogadro's number (6.022×10^{23} mol^{-1})
I:	mean excitation potential of the material
Z:	atomic number of absorbing material (target)
A:	atomic mass number of absorbing material
ρ:	density of absorbing material
z:	charge of incident particle in units of e
β:	v/c of the incident particle
γ:	$1/\sqrt{1-\beta^2}$
δ:	density correction
C:	shell correction
W_{max}:	maximum energy transfer in a single collision
τ:	kinetic energy of the electron; and
$F(\tau)$	$= 1 - \beta^2 + \frac{\tau^2/8 - (2\tau+1)\ln 2}{(\tau+1)^2}$.

Furthermore, the above formula represents the mean energy loss for charged particles while passing through matter. In general, an initially monoenergetic beam after passing through matter of a certain thickness, will show a certain energy distribution which, on average, is reduced by an amount given by the Bethe-Bloch formula. These distributions were also calculated by the MCEEP program.

5.5.3 Simulation and Results

For our kinematic range (1.8 through 3.4 $(\mathrm{GeV}/c)^2$), the internal radiative corrections were expected to be small ($\lesssim 1\%$) [Afanasev *et al.*, 2001, Plaster, 2004]. Studies for radiative corrections due to the electron were performed using the Monte Carlo code MASCARAD [Afanasev *et al.*, 2001] and MCEEP. The effects from the hadrons were much smaller compared to those from the electron.

The input file for the MASCARAD code is given in Appendix E.1. The MASCARAD results indicate a 0.931% correction to the transverse asymmetry due to internal radiative effects at $Q^2 = 1.7$ (GeV/c)^2. Results for all four kinematic points are tabulated in Table 5.1. The energy of the radiated photon was restricted by the detector range. The maximum energy the radiated (real) photon can have would be equal to the maximum energy a scattered electron could lose and still be detected in the detector. The BB detector energy range was quite high ($\gtrsim$ 200 MeV for our lowest momentum transfer point) and so the maximum radiated photon energy was taken to be of the order of the pion mass ($\sim$ 135 MeV) so as to stay below the single-pion production threshold.

Other than MASCARAD, MCEEP was used to get internal radiative correction estimates. MCEEP also does not calculate the numbers for neutral particles, but since the difference between the neutrons and protons at our kinematics is negligible [Afanasev, 2007], we could use MCEEP for proton calculations and extend them to the neutron. The single and multi-photon radiative tail as calculated by MCEEP is shown in Figure 5.12. For external radiative correction numbers, the energy lost by the scattered electron while passing through the target region (due to ionization) and through the target cell glass as calculated by MCEEP are presented in Table 5.2.

Table 5.1: Radiative corrections Δ_i (internal) to the transverse asymmetry from MASCARAD for polarized scattering (transverse asymmetry).

kine-matic	Q^2 (GeV/c)^2	Δ_i (%)
1	1.3	0.948
2	2.5	0.914
3	3.4	0.901
4	1.7	0.931

Table 5.2: Energy loss from other than target material from MCEEP for kinematic 4.

Energy loss from other than target material		
Beam		0.0744 MeV
Scatt. Electron	(sidewall):	1.5550 MeV
Hadron	(sidewall):	1.6879 MeV
Scatt. Electron	(endcap):	0.6690 MeV
Hadron	(endcap):	0.5539 MeV

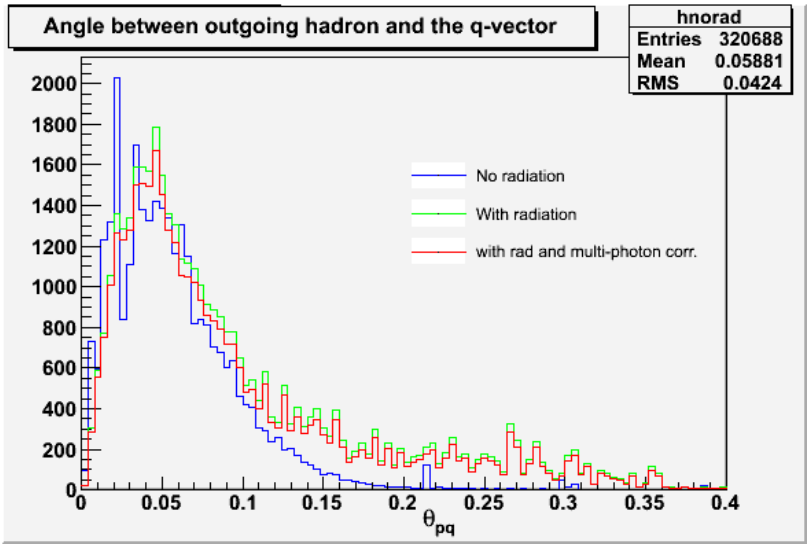

Figure 5.12: Internal radiative correction plots by MCEEP. The plot show the angle between the outgoing hadron and $\vec{q}$.

5.6 Asymmetries and G_E^n

5.6.1 Quasielastic Events Selection

The following initial cuts were made for kinematic #4 ($Q^2 = 1.7$ (GeV/c)^2). On the BB side, a cut on the pre-shower detector ADC of greater than 450 channels filtered out the pions so that mostly electrons went through the scintillators for timing purposes. A cut on the target vertex of ± 17 cm left events from the target glass endcaps out thus ensuring that our events came from only the gaseous target in the cell. The energy-to-momentum matching was $|1 - \frac{p}{E}| \leq 0.4$, or 40%. The scattered electron momentum as obtained from tracking was kept between 0 and 1.4 GeV/c i.e. $0. < p_e < 1.4$ GeV/c. The angular spread of the outgoing neutrons was kept within 40 mrad of the virtual photon direction in both x and y directions. Then cuts on the invariant mass $0.8 < W < 1.15$, and the perpendicular and parallel missing momenta, $P_{\rm mperp} < 150$ MeV/c and $|P_{\rm mpar}| \equiv |P_{\rm par} - q| < 250$ MeV/c were placed, where the three quantities above are defined as follows:

$$W \equiv (p+q) = \sqrt{M^2 + 2M\nu - Q^2} \tag{5.26}$$

$$P_{\rm mperp} = |\vec{p}|\sin(\theta_{nq}) \tag{5.27}$$

$$P_{\rm par} = |\vec{p}|\cos(\theta_{nq}) \tag{5.28}$$

where θ_{nq} is the angle between the outgoing neutron and the momentum transfer 3-vector, $\vec{q}$, and $\vec{p}$ is the neutron 3-momentum. $\nu = E - E'$ is the energy transfered. These cuts are shown in Figure 5.13.

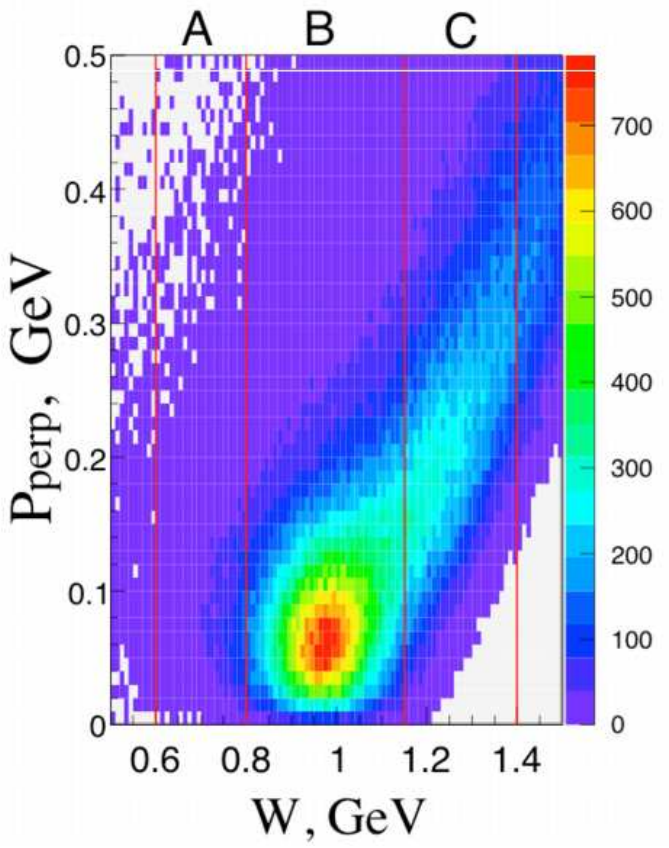

Figure 5.13: W vs. perpendicular missing momentum for kinematic #4.

5.6.2 Asymmetries

Now the observed asymmetry has to be corrected for the "false" asymmetries arising from instrumental effects like the helicity-dependent livetimes (DAQ and electronic) and accumulated charge [Feuerbach, 2007]. To first order, these effects are small and we can write

$$A_{obs} = A - \left(1 - \frac{Q_-}{Q_+}\right) - \left(1 - \frac{\eta_-}{\eta_+}\right) \tag{5.29}$$

where $Q_\pm$ and $\eta_\pm$ are the accumulated charge and livetimes for positive and negative helicity states, A is the raw asymmetry obtained from the quasi-elastic yields.

Furthermore, this A_{obs} needs to be corrected for background coincidence events like protons misidentified as neutrons and accidentals (both neutrons and misidentified protons).

After all corrections to the observed asymmetry have been made, we have, for the physics asymmetry

$$A_{phys} = \frac{A_{obs}}{P_e P_t P_n D_{N_2} D_n} \ , \tag{5.30}$$

where P_e is the electron beam polarization, P_t is the target polarization, P_n is the contribution of the neutrons to the target polarization, D_{N_2} is the nitrogen dilution factor and D_n is the proton-to-neutron conversion factor (Table 5.3).

5.6.3 Extracting G_E^n

Now we use Equation 1.14 to get the ratio $\Lambda = G_E^n/G_M^n$ [Franklin, 2006]. Knowing the value of G_M^n from a recent Hall B experiment, we then extract the value of G_E^n. The preliminary result is shown in Figure 5.14.

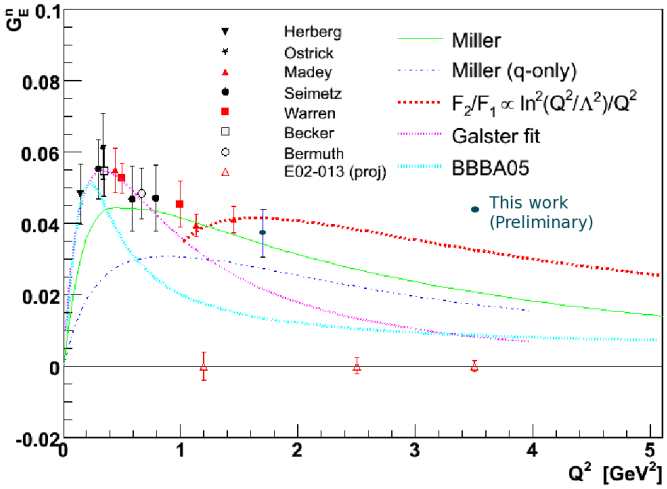

Figure 5.14: G_E^n at $Q^2 = 1.7$ (GeV/c)^2. $G_E^n = 0.03457 \pm 0.007239\%$. (Preliminary result.)

5.6.4 Errors: Statistical

The statistical error bars were calculated as

$$\Delta A = \sqrt{\left(\frac{\partial A}{\partial N_-}\right)^2 (\Delta N_-)^2 + \left(\frac{\partial A}{\partial N_+}\right)^2 (\Delta N_+)^2} \tag{5.31}$$

with

$$\frac{\partial A}{\partial N_\mp} = \mp \frac{2N_\pm}{N^2} \ , \qquad \text{where } N = N_+ + N_- \ . \tag{5.32}$$

Here $N_{+(-)}$ is the number of positive (negative) helicity events and $\Delta N_\pm = \sqrt{N_\pm}$.

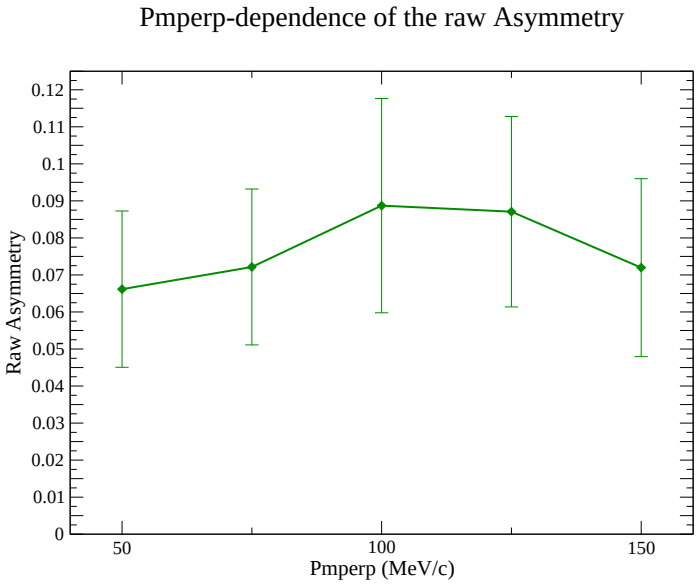

Figure 5.15: The variation of the raw asymmetry as a function of the perpendicular missing momentum cut, P_{mperp}. We see that, within errors, the asymmetry does not change, implying that the electrons at these momenta do indeed scatter off the neutrons. This plot is for one run only.

5.6.5 Errors: Systematic

The nuclear medium influences the way we see the structure of a bound nucleon. One of the effects is the nuclear EMC effect (see, for example, the review [Geesaman *et al.*, 1995]), which shows that the structure function of the nucleus is suppressed at large x_{Bj} relative to that of the deuteron. In our case, the restriction to small values of missing momenta will substantially suppress the onset of the EMC effect ([Proposal, 2002]). Also, the measured asymmetry is less sensitive to nucleon structure modifications since the bulk of the EMC effect will be less revealed in the form factor ratios. Color Transparency (CT) is another effect which could hinder the extraction of G_E^n at high Q^2. This effect has been investigated in quasielastic proton knock-out by electrons from nuclei for Q^2 from 1 to 8 $(\mathrm{GeV}/c)^2$ [Proposal, 2002]. The experiment observed no signature for CT up to Q^2=8 $(\mathrm{GeV}/c)^2$ in the kinematics of restricted missing momentum and energy. Moreover, the comparison with theoretical calculations demonstrated that the Glauber approximation adequately describes the data for a wide range of nuclei (ranging from the Deuteron to Iron) [Proposal, 2002]. Thus for the Q^2 of this experiment, we expect that the Glauber approximation will reliably describe the final state interactions in the ^{3}He(e, e′n) reaction.

The key to the experiment is that it is possible to select small momenta in the ^{3}He wave

function by requiring $P_{mperp} < 30$ MeV/c. Additionally, these cuts ensure the suppression of the proton polarization, which is already a small factor ($< 3\%$), and suppress small non-nucleonic admixtures in the wave function. Furthermore, they signicantly suppress the final state interactions, since the struck nucleon is rather far from other nucleons. Besides, most of the rescattering in these kinematics actually removes nucleons to larger transverse missing momenta, and hence they do not affect asymmetries calculated in the PWIA in order to extract $R = G_E^n/G_M^n$.

The choice of high Q^2 causes a significant suppression of meson exchange effects in the extraction of R [Proposal, 2002]. At $Q^2 > 1$ (GeV/c)^2 the overall additional Q^2 dependence of the MEC amplitude as compared to the PWIA amplitude will be $(1 + Q^2/\Lambda^2)^2$, where $\Lambda^2 = 0.81$ (GeV/c)^2. Additionally, the MEC contribution will be suppressed due to the restriction of small P_{mperp} and E_m. Usually MEC effects start to contribute at rather large nucleon momenta of the order of 300 MeV/c.

Corrections to the impulse approximation seem significantly less than 10% (expected at the level of 2-5%), and most of these effects will be possible to correct for.

Table 5.3 summarizes the systematic errors for the $Q^2 = 1.7$ (GeV/c)^2 data. Contributions from the final state interactions are not included in it as that is work in progress.

Table 5.3: Systematic errors for $Q^2 = 1.7$ (GeV/c)^2 data. The *Nuclear Effects* include FSI and other effects due to the neutron being in a nuclear medium (Section 2.6.1). Total systematic error is about 6% - 9%.

Quantity	Value	Syst. Error
P_e	0.85	2-3%
P_t	0.482	$\sim 4\%$
P_n	0.86	2-3%
D_{N_2}	0.955	$\sim 2\%$
Nuclear effects	0.85 to 1	$\sim 2 - 5\%$

Copyright © Ameya Suresh Kolarkar 2008

CHAPTER 6: CONCLUSION AND OUTLOOK

6.1 Conclusions

We see from Figure 5.14 that the one preliminary result - along with results from [Plaster *et al.*, 2006] - suggests a departure from the Galster parametrization, and lie more in line with the Miller curve. Of course, these results are preliminary and the FSI calculations and other corrections due to nuclear effects may move the point around (by less than about one sigma), but still would remain at least three sigma away from the Galster fit[1]. So we can say that the Galster parametrization does not work at higher Q^2. Although, a refit with different values for the parameters A_τ and B_τ might provide a better fit for the new data (Equation 1.49).

As for the theory models, the results definitely lay to rest some of them. The strongest theory contender is the full Miller calculation based on the *cloudy bag* model described in Section 1.3.3 [Miller, 2002, Miller, 2003]. The results will give us more insight into the sign of the charge distribution of the neutron core. Also, an as yet unpublished paper by [Miller *et al.*, 2007] on the ratio of the proton form factors reveals that the magnetization density of the proton extends out further than the charge distribution, also contrary to the common belief to far. A similar analysis for the neutron should also be very interesting.

The pQCD curve, too, seems to fit the higher Q^2 points. The difference between the Miller curve and the pQCD prediction curve is quite large around this Q^2 region and beyond. Higher Q^2 results will either decide between these two curves, or open up the arena for other contestants.

Various other ongoing efforts to devise parametrization fits will have better data to play with. For example, Kelly's parametrization for G_E^n (Equation 1.50) used the Galster parametrization mainly due to lack of high quality data at high Q^2. Now the parametrization can be extended to G_E^n as well. The BBBA form factor fits [Bradford *et al.*, 2006] borrow Kelly's parametrization and use additional conditions from duality to constrain G_E^n, again because of a lack of high quality data at high Q^2. Our results will set them on track for obtaining a good fit to G_E^n too, hopefully without the additional duality conditions. It will also be interesting to see how the GPD limits will be affected by the results. Better phase-space pictures of the neutron will become available.

[1] The error bars will decrease once all the systematic corrections are properly incorporated.

Interpreting the G_E^n versus Q^2 data in terms of a physical charge density distribution, however, remains the arena of theory models. Whether we look at the neutron in physical space[2] in the Breit frame, the infinite momentum frame, or any other (physically or mathematically) convenient frame that can be come up with, its Fourier transform into momentum space will have to agree with the data in Figure 5.14.

6.2 Future

There are quite a few experiments that are aleady approved at Jefferson Lab for measuring nucleon form factors at higher Q^2 and more precisely. These are mostly after the 12 GeV upgrade. A higher Q^2 experiment for G_E^n is due to run in Hall C at Jefferson Lab. In small and steady steps, we inch towards better understanding of the neutron structure and a better understanding of our (visible matter) Universe.

Copyright © Ameya Suresh Kolarkar 2008

[2]To get a static distribution, the time component in coordinate 4-space should disappear. In 4-momentum space, this corresponds to zero energy transfer to the nucleon.

Appendix A: FERMI GAS MODEL

The polarized ^{3}He target used in the experiment at about 245° possesses quite a lot of thermal energy[1]. The distribution of momenta of the nucleons within the enclosed space (the so-called Fermi momentum distribution) lies between 200 and 250 MeV/c. Both the nucleonic momentum distribution encountered in quasi-elastic electron-nucleus scattering and the nucleon binding energies can be understood in terms of the Fermi gas model. This appendix describes the Fermi Gas Model for the ^{3}He gas.

The nucleus can be described as a Fermi gas in which the nucleons move around as quasi-free particles [Povh *et al.*, 1999]. The Fermi momentum P_F is related to the mean square momentum by

$$P_F^2 = \frac{5}{3}\langle P^2 \rangle. \tag{A.1}$$

An analysis of quasi-elastic scattering off different nuclei can thus determine the Fermi momentum P_F and the effective average nuclear potential strength, S, of the nucleons. Apart from the lightest nuclei, the Fermi momentum is nearly independent of the atomic mass number A of the nuclei, and is approximately 250 MeV/c.

A.1 The Fermi Gas Model

The protons and neutrons that build up the nucleus are viewed in the Fermi gas model as comprising two independent system of nucleons [Povh *et al.*, 1999]. The nucleons being fermions, obey Fermi-Dirac statistics. It is assumed that that the nucleons can move freely inside the entire volume of the nucleus within the constraints imposed by the Pauli principle.

We assume that the potential felt by every nucleon, which is a superposition of the potentials of all other nucleons, has the shape of a well. The number of possible states available to a nucleon in a volume V and momentum range dp is given by

$$\mathrm{d}n = \frac{4\pi p^2 \mathrm{d}p}{2\pi\hbar} V. \tag{A.2}$$

In the nuclear ground state, i.e. at absolute zero temperature, the lowest states will all be occupied up to some maxumum momentum which we call the *Fermi momentum* p_F. The number of such states can by found by integrating Equation A.2 as

$$n = \frac{V p_\mathrm{F}^3}{6\pi^2\hbar^3}. \tag{A.3}$$

[1] Thermal nucleons at room temperature - $\sim 25^\circ$C - move at around 34 m/s.

Since every state can contain two fermions of the same species, we can have

$$N = \frac{V(p_{\mathrm{F}}^{\mathrm{n}})^3}{3\pi^2\hbar^3} \qquad \text{and} \qquad Z = \frac{V(p_{\mathrm{F}}^{\mathrm{p}})^3}{3\pi^2\hbar^3} \tag{A.4}$$

neutrons and protons, respectively. The superscripts n and p denote neutrons and protons, respectively. With a nuclear volume

$$V = \frac{4}{3}\pi R^3 = \frac{4}{3}\pi R_0^3 A, \tag{A.5}$$

a value for $R_0 = 1.21$ fm and assuming the same radius for the neutron and proton potential wells, we find for a nucleus with $Z = N = A/2$ the Fermi momentum

$$p_{\mathrm{F}} = p_{\mathrm{F}}^{\mathrm{n}} = p_{\mathrm{F}}^{\mathrm{p}} = \frac{\hbar}{R_0}\left(\frac{9\pi}{8}\right)^{1/3} \approx 250 \ \ \mathrm{MeV}/c. \tag{A.6}$$

For lighter nuclei, p_{F} tends to be somewhat smaller and the Fermi gas model does not werk very well in such cases. For example, in our case, for the ^{3}He nucleus, $A = 3$, $N = 1$ and $Z = 2$ and so

$$p_{\mathrm{F}}^{\mathrm{n}} \approx 217.2 \ \ \mathrm{MeV}/c \qquad \text{and} \qquad p_{\mathrm{F}}^{\mathrm{p}} = 273.6 \ \ \mathrm{MeV}/c. \tag{A.7}$$

which are higher than experimental values [Moniz *et al.*, 1971, Whitney *et al.*, 1974].

Appendix B: FREQUENCY SWEEP NMR

Nuclear Magnetic Resonance or NMR as described in Section 3.6 is symmetric with respect to the two factors inside the radical in the denominator. Thus NMR can be performed using the Field Sweep method wherein the RF frequency is kept constant and the holding field is swept through resonance, or the Frequency Sweep method in which the holding field is kept constant and the rf is swept through resonance. The Frequency Sweep (FS) method can be effectively used in situations where changing the magnetic field is not preferable. Such situations arise when, for example, hysteresis effects are prominent or NMR and EPR are to be performed together. In this appendix we shall develop the formalism for Adiabatic Fast Passage using Frequency Sweep NMR (FS-NMR).

B.1 Frequency Sweep Fundamentals

According to the classical theory of electromagnetism, a magnetic moment $\vec{M}$ in a field $\vec{H}$ experiences a torque $\vec{T} = \vec{M} \times \vec{H}$, equal to the rate of change of angular momentum of the magnetic moment, $\hbar(\mathrm{d}\vec{I}/\mathrm{d}t)$. Since $\vec{M} = \gamma\hbar\vec{I}$, we get

$$\frac{\mathrm{d}\vec{M}}{\mathrm{d}t} = \gamma\vec{M} \times \vec{H} \tag{B.1}$$

Now, let us consider a frame S' rotating with respect to the laboratory frame with an angular velocity $\vec{\omega}$. From the general law of relative motion, we can relate the time derivatives of $\vec{M}$ in the two reference frames as

$$\frac{\mathrm{d}\vec{M}}{\mathrm{d}t} = \frac{\partial\vec{M}}{\partial t} + \vec{\omega} \times \vec{M} \tag{B.2}$$

Combining (1) and (2), the motion of the magnetic moment in the rotating frame is given by

$$\frac{\partial\vec{M}}{\partial t} = \gamma\vec{M} \times (\vec{H} + \frac{\vec{\omega}}{\gamma}) \tag{B.3}$$

This euqation has the same form as Equation B.1 provided we replace the magnetic field $\vec{H}$ by an effective field $\vec{H_e} = \vec{H} + (\vec{\omega}/\gamma)$, the sum of the laboratory field $\vec{H}$ and a fictitious field $\vec{H_f} = +(\vec{\omega}/\gamma)$.

Let $\vec{H} = \vec{H_0}$, the holding field in the laboratory frame directed along the z-axis. By choosing a rotating frame with $\vec{\omega} = -\gamma\vec{H_0}$, the effective field $\vec{H_e}$ vanishes. This is the

Larmor frequency, $\omega_0 = \gamma H_0$, with which the magnetic moment precesses in the laboratory frame. Now suppose we turn on a field $\vec{H}_1$ perpendicular to $\vec{H}_0$ and rotating about it with angular velocity $\vec{\omega}$. The unit vector $\hat{\imath}$ of the x-axis in the rotating frame S' being taken along the field $\vec{H}_1$, the effective field $\vec{H}_e$ is static in S' and is given by

$$\vec{H}_e = (H_0 + \frac{\omega}{\gamma})\hat{k} + H_1\hat{\imath} \tag{B.4}$$

B.2 The Adiabatic Condition

Here, we derive the adiabatic fast passage condition for the RF Sweep rate. From the equation of motion (1), we can deduce that

$$\frac{\mathrm{d}}{\mathrm{d}t}(M^2) = 2\vec{M} \cdot \frac{\mathrm{d}\vec{M}}{\mathrm{d}t} = 0 \tag{B.5}$$

that is, the magnitude of the magnetization M is a constant of the motion, whatever the variation of H with time. If this variation is sufficiently slow, the angle of the magnetization with the instantaneous direction of the field is also a constant of the motion, as we shall now show.

The variation of the vector $\vec{H}$ with time can be described generally by

$$\frac{\mathrm{d}\vec{H}}{\mathrm{d}t} = \vec{\Omega} \times \vec{H} + \Omega_1\vec{H} \tag{B.6}$$

where the vector $\vec{\Omega}$ and the scalar Ω_1 have the dimensions of frequency.

Consider a frame S' where the z-axis is continuously aligned along the instantaneous direction of the field $\vec{H}$. According to Equation B.6 the relative motion of S' with respect to the laboratory will be a rotation about the instantaneous axis $\vec{\Omega}$. In that frame the magnetization will change in time according to

$$\frac{\partial\vec{M}}{\partial t} = \gamma\vec{M} \times (\vec{H} + \frac{\vec{\Omega}}{\gamma}) \tag{B.7}$$

By definition, in this frame $H_x = H_y = 0$ and

$$\frac{\partial M_z}{\partial t} = M_x\Omega_y - M_y\Omega_x \tag{B.8}$$

If $|\Omega| \ll |\gamma H|$ then, approximately,

$$\frac{\partial M_x}{\partial t} \cong \gamma H M_y, \qquad \frac{\partial M_y}{\partial t} \cong -\gamma H M_x.$$

M_x and M_y are approximately sinusoidal functions with instantaneous frequency $\omega_0(t) = -\gamma H(t)$.

After a long time t, the change in M_z would be

$$\Delta M_z = M_z(t) - M_z(0) = \int_0^t [M_x(t')\Omega_y(t') - M_y(t')\Omega_x(t')]\,\mathrm{d}t.$$

If the variation of $\vec{\Omega}$ with time is sufficiently slow, or to be precise, if its Fourier expansion has negligible components at frequencies of the order of $|\gamma H(t)|$, then, for any t,

$$|\Delta M_z| \sim \left|\frac{M\Omega}{\gamma H}\right| \ll M$$

and M_z, that is, the component of $\vec{M}$ along the field, will remain constant. This is the adiabatic theorem.

We apply this result to our system of magnetic moments. For the RF sweep, we have,

$$\frac{\mathrm{d}\vec{H}_e}{\mathrm{d}t} = \frac{\dot{\omega}}{\gamma}\hat{k} + \dot{H}_1\hat{i} \tag{B.9}$$

where the dot represents the derivative with respect to time. Substituting for $\hat{k}$ and $\hat{\imath}$ to transform into a frame defined by $\vec{H}_e$ and $\hat{n} \times \vec{H}_e$, we get

$$\frac{\mathrm{d}\vec{H}_e}{\mathrm{d}t} = (\cos\theta\frac{\dot{\omega}}{\gamma} + \sin\theta\,\dot{H}_1)\hat{H}_e + (\sin\theta\frac{\dot{\omega}}{\gamma} - \cos\theta\,\dot{H}_1)(\hat{n} \times \hat{H}_e) \tag{B.10}$$

where $\hat{H}_e = \vec{H}_e/|\vec{H}_e|$, and $\hat{n}$ is a unit vector orthogonal to $\vec{H}_0$ and $\vec{H}_1$. Comparing this with Equation B.6 gives

$$\Omega = \sin\theta\frac{\dot{\omega}}{\gamma H_e} - \cos\theta\,\frac{\dot{H}_1}{H_e} = \frac{H_1}{\gamma H_e^2}\dot{\omega} - \frac{H_0}{H_e^2}\dot{H}_1 \tag{B.11}$$

The quantity Ω is the smaller the farther from resonance. We assume that the variation of H_1 with respect to time (due the different frequency response of the electronics at different frequencies), over the range of frequency swept, is small comp ared to the sweep rate. It is observed that H_1 changes about 2 to 5% over the entire range. Now, applying the adiabatic condition $|\Omega| \ll |\gamma H_e|$, we get

$$\dot{\omega} \ll \frac{\gamma^2 H_e^2}{\sin\theta} \tag{B.12}$$

This condition is strongest at resonance ($\theta = 90°$) and gives

$$\dot{\omega} \ll \gamma^2 H_1^2 \tag{B.13}$$

Note that, at resonance, $H_e = H_1$ and that the $\cos\theta$ term in Equation B.11 vanishes. To this condition we can add that the effects of relaxation must be negligible during the time of passage τ through resonance

$$\tau \cong \frac{H_1}{\dot{\omega}/\gamma} \ll T_1, T_2 \tag{B.14}$$

or, since in our case $T_2 \ll T_1$, we can write the AFP condition for frequency sweep NMR, with $H_1 = \omega_1/\gamma$, as

$$\frac{|\gamma H_1|}{T_2} \ll |\dot{\omega}| \ll \gamma^2 H_1^2. \tag{B.15}$$

Appendix C: EPR INSTRUMENT DETAILS

Below is a list of the instrument and their nominal settings during EPR:

1. RF generator: HP E4400B

   - Amplitude -1dB to 5dB depending on the strength of the D_2 light;
   - $\Delta\nu_{depth} = 20 - 40$kHz, depends on the jump in frequency when ^{3}He spins are flipped.

2. RF amplifier: KY58

   - The amplifier knob was at the 1 o'clock position[1].
   - The amplifier had an upper limit of 20 MHz, so we could not use it efficiently for the potassium de-excitation.
   - The amplifier had to be placed in the Hall, close to the target region for good signal fidelity. The signal in the EPR RF coil when the amplifier was in the Counting House was very noisy. It was also placed in the same lead brick housing as the photodiode.

3. Lock-in Amplifier: EG&G 7265

   - Time constant $\tau = 100$ ms - since the time scale of our feedback loop based on the integration time constant of the KY NU-112 PI box was about 100 ms.
   - Sensitivity S=2 mV for FM sweep; for spin-flip, this depends on the slope m_{FM}, see Section 3.7.2.
   - Phase was chosen to make the FM sweep line shape in the lock-in X channel to look symmetric sitting at zero (See Figure 3.18(a)).
   - AC gain was set to the highest possible value without overloading the amplifier. This is generally one step below the value at which the AC gain readout LED starts flashing.
   - Filter slope - 6 dB/octave for a feedback circuit. Otherwise, in general, for digital lockins, the slope is ≥ 12 dB/octave.

[1]The output of the E4400B was not sufficient to de-excite the Rb/K atoms so an amplifier had to be used.

4. Counter - SR620

    - This reads off the frequency corresponding to the Zeeman splitting. Once the PI circuit is locked, this follows the EPR frequency.

5. Modulator - SR560

    - Modulated the frequency of the D_2 light at ν_{mod} and formed the external reference input for the lock-in amplifier.
    - $\nu_{mod} = 200$ Hz.
    - $A_{mod} = 0.6$ to 1.5 V (depending on the polarization of the target).

Appendix D: SCALER MAP

```
# This file:  scaler.map
# Author:  Robert Michaels, Jlab
# Contains time-dependent text-based mapping of Hall A scaler channels
# which permits getting data from THaScaler by names like "bcm_u3".
# Also contains "directives" that control xscaler and simplify
# the map, e.g.  tying helicity scaler map to non-helicity scaler
# For documentation about this file, see
# http://hallaweb.jlab.org/equipment/daq/THaScaler.html (scroll to "scaler.map"
# near the end of that web page).
#
# ------- Jan 1 2006
DATE 1 1 2006
# directives
xscaler-tabs gen 0:norm 1:nplus 2:nminus 3:gen3 4:gen4 5:gen5 6:gen6 7:gen7 8:gen8
xscaler-layout gen 0:8x4 1:8x4 2:8x4 3:8x4 4:8x4 5:8x4 6:8x4 7:8x4 8:8x4
xscaler-pageslot gen 0:slot2 1:slot0 2:slot1 3:slot3 4:slot4 5:slot5 6:slot6 7:slot7
8:slot8
xscaler-pagename gen 0:'GeN Normalization Scaler (NOT gated by helicity)'
xscaler-pagename gen 1:'GeN Normalization Scaler ++ gated by helicity PLUS'
xscaler-pagename gen 2:'GeN Normalization Scaler -- gated by helicity MINUS'
xscaler-pagename gen 3:'GeN scaler in 3rd slot (first non-norm scalers)'
xscaler-pagename gen 4:'GeN scaler in 4th slot'
xscaler-pagename gen 5:'GeN scaler in 5th slot'
xscaler-pagename gen 6:'GeN scaler in 6th slot'
xscaler-pagename gen 7:'GeN scaler in 7th slot'
xscaler-pagename gen 8:'GeN scaler in 8th slot'
xscaler-server gen IP:129.57.192.5 port:5022
# careful, normslot is also defined in THaScaler::InitData()
xscaler-clock gen slot:2 chan:11 rate:105000
```

```
#
slot-offset gen -1:-1 1:-2
#
# ok, this is confusing.  The slot numbers in 4th column are the virtual slot,
# which is 1 more than the physical slot because the helicity scaler appears
# as two banks(slots) of data.  So slot 0=hel+, 1=hel- but it is one physical
# slot (which at the moment is off to the far left).
gen3 0 9 3 0 32 GeN Data in 1st non-norm scaler (3rd phy.  slot)
gen4 0 9 4 0 32 GeN Data in 1st non-norm scaler (4th phy.  slot)
gen5 0 9 5 0 32 GeN Data in 1st non-norm scaler (5th phy.  slot)
gen6 0 9 6 0 32 GeN Data in 1st non-norm scaler (6th phy.  slot)
gen7 0 9 7 0 32 GeN Data in 1st non-norm scaler (7th phy.  slot)
gen8 0 9 8 0 32 GeN Data in 1st non-norm scaler (8th phy.  slot)
# Normalization scaler:  triggers and charge
# hel cr sl ch #ch
trigger-1 0 9 2 0 1 trigger 1 = electron arm
trigger-2 0 9 2 1 1 trigger 2 = neutron arm
trigger-3 0 9 2 2 1 trigger 3 = e-N coinc
trigger-4 0 9 2 3 1 trigger 4
trigger-5 0 9 2 4 1 trigger 5
trigger-6 0 9 2 5 1 trigger 6
trigger-7 0 9 2 6 1 trigger 7
trigger-8 0 9 2 7 1 trigger 8
clock 0 9 2 11 1 105 kHz clock
TS-accept 0 9 2 12 1 Trigger Supervisor accepted triggers
bcm_u1 0 9 2 16 1 Beam current, upstream cavity, gain = 1
bcm_u3 0 9 2 17 1 Beam current, upstream cavity, gain = 3
bcm_u10 0 9 2 18 1 Beam current, upstream cavity, gain = 10
bcm_d1 0 9 2 19 1 Beam current, downstream cavity, gain = 1
bcm_d3 0 9 2 20 1 Beam current, downstream cavity, gain = 3
bcm_d10 0 9 2 21 1 Beam current, downstream cavity, gain = 10
#
```

```
#
# ------- Jan 10 2005
DATE 10 1 2005
```

Appendix E: MASCARAD DETAILS

MASCARAD is the model-independent radiative corrections simulation program that gives out a number for radiative corrections to the transverse asymmetry (in our case). The program is based on a paper by [Afanasev *et al.*, 2001]. This appendix aims to provide details of results presented in Section 5.5.3 and Table 5.1. Below is an example MASCARAD input file followed by an explanation of the input variables/parameters and then the output file.

E.1 MASCARAD Input File

```
2.64        !  bmom - lepton momentum
0.0         !  tmom - proton momentum
1           !  lepton - 1 electron, 2 muon
1d5 1d5 1d5 ! numbers of events
1 3 0 0
3           !  nev - number of samples for each poin
11333522    !  random seed
1
0.28
-2.5
-2.5
```

E.2 Run Options

In the above input file for, the lepton momentum was 2.64 GeV/c and $Q^2 = 2.5$ (GeV/c)^2. This is for the transverse asymmetry case where the target polarization is perpendicular to the momentum transfer vector. The number 0.28 corresponds to the *inelasticity* cut, or the missing mass for the single-pion production threshold.

The energy of the radiated photon is limited by the detector acceptance, that is, it can be equal to the maximum energy a scattered electron can lose and still be detected in the detector. This energy in our case was higher that the single-pion production threshold, and hence, was cut-off to this value ($\sim$ 135 MeV).

E.3 Output File

```
 bmom =   2.640
 tmom =   0.000
 lepton  1
 cutv =   0.000
  nev =    3
 iy :  11333522
 npoi =  1
 0.7467E-06  0.913  0.003  0.915  0.915  0.000
-0.1642E-06  0.913  0.001  0.913  0.914  0.000
```

The output file above first outputs the input parameters and then the results. The first results line (second to last line of the file) is for unpolarized scattering while the last line is for polarized scattering. The number of interest to us is the second to last column of the last row, which is the total radiative correction to the transverse asymmetry, the last column being the error associated with it. Thus, $\Delta_i = 0.914\%$ at $Q^2 = 2.5$ (GeV/c)^2.

Appendix F: MCEEP INPUT AND OPTIONS

This appendix describes some details of the MCEEP simulation for ND acceptance studies. The correct position, angles and distances have been used for both the BB and the ND. Also, the ND pointing angle (see Section F.2) has been incorporated. The luminosities are at 8 μA beam current and the normal target density as described in Chapter 3. More on this study can be found in [Kolarkar, 2007a].

F.1 Input File and Parameters

```
1000000                                  # tries
4,4,4,4,4,4                              for default ranges
939.5656,0,2.6                           m_eject,z_eject,em_bound
2079.,0.,0.,1500.,-52.0,0.,1500.,35.74,0.   kinematics
50.0,-50.0,25.0,-50.0                    momentum acceptances
'R','R',229.4,871.6,225.,625.              nominal solid angles
0.3322,1.,1.                             luminosity,time,spec_fac
250.,2.6,2.6                              for singles only
3.,2.,0.001432,4,1                       targ: a,z,dens,targ_mod,eloss_mod
-0.2,0.2                                 targ: cell start/end
1.09,8.965                                drift to aperture - nom. sld. ang.
0.85,0.,0.,0.,0.                         beam: pol, vert, disp, df, tof_win
0.,0.,0.,0.,0.                           beam: FWHM   in cm,cm,mr,mr,%
0.,0.,0.,0.,0.                           beam: offset in cm,cm,mr,mr,%
'R',0.002,0.002                          beam: raster shape, X size, Y size
'E',F,2,-90.,0.,0.,0.                    ELECTRON ARM
'NTU',1,0.,'ngen_electron.ntu'
'DFT',109.0                                drift to front face of coll.
'P',F,2,-90.,0.,0.,-173.4                 HADRON ARM
'NTU',1,0.,'ngen_hadron.ntu'
'DFT',896.5                                drift to front face of veto 1.
0                                        # global cuts
0                                        # specific cuts
1                                        # plots
'NTU',1,33,1,2,3,4,5,6,7,8,9,10,11,12,13,14,15,16,17,18,22,23,24,25,26,28,30,
31,34,39,40,41,45,46,47,'n_3He.ntu'
Comments:  3He(e,e'n) with JLAB Hall A BB and ND
           ~8 uA on 40 cm pol. 3He
           Only acceptance
```

The simulation worked as follows. Polarized electrons are incident on the polarized ^{3}He target. The particles drift through air towards the detectors. The electrons are accepted into a region the size of the BB solid angle acceptance and the neutrons go through a box of roughly the size of the real ND. The detector packages of neither the BB nor the ND are built into MCEEP so we only looked at the acceptance. The spatial acceptance as a

function of the perpendicular missing momentum enabled us to construct a phase-space for the accepted neutrons.

The target was modeled using the Meier-Hajduk (M-H) wavefunction. There were other models in MCEEP but only two of the five wavefunctions - the M-H and Salmè - had spectral functions for two-body *and* three-body break-ups (2bbu and 3bbu, respectively). Since our main intent is to study knock-out of a neutron from a ^{3}He nucleus, the recoil "particle" cannot be in a bound state since two protons do not form a bound system. So a neutron-knockout by default becomes a 3bbu problem. [Kievsky *et al.*, 1997], [Schulze and Sauer, 1993], [Meier-Hajduk *et al.*, 1983].

F.2 ND Pointing Coordinates

The normal to the front face of the ND did not point at the target center but a little upstream. This distance was calculated using the angles as measured by the survey group, and shown in Figure F.1. The survey results are very well documented in [Ngo and Shahinyan, 2007].

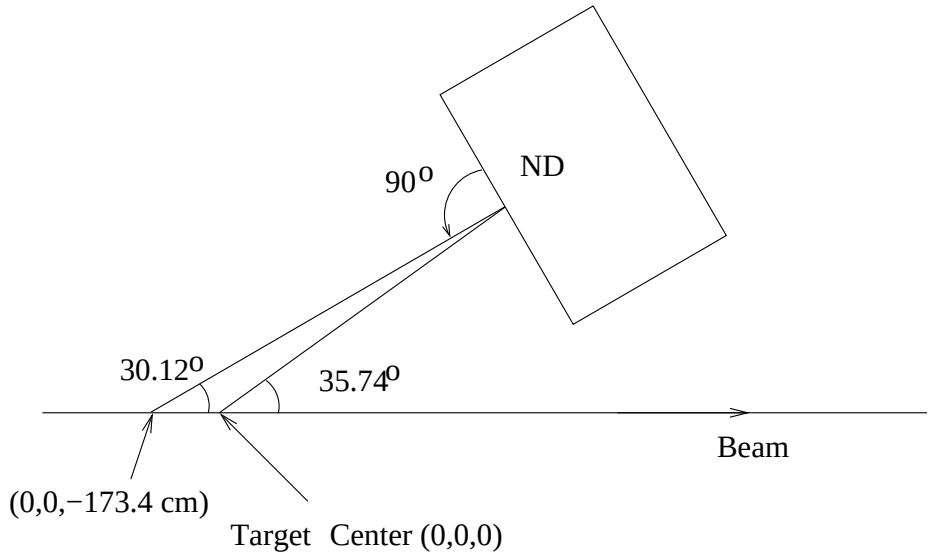

Figure F.1: The distance upstream where the normal to the front face of the ND was pointing during kinematic #4.

F.3 Running MCEEP

While running MCEEP, the following options were used:

- Continuum for 3bbu, Bound for 2bbu;
- (e,e′n) for neutron, (e,e′p) for proton;
- option 200 for polarized scattering;
- option 20 for ^{3}He spectral funstion (Meier-Hajduk); option 40, 42 to compare with nitrogen;
- no radiation, or single photon radiation;
- no enforcement of acceptance or singles.

The single-photon radiation option was chosen to get the energy losses for external radiative corrections (Section 5.5.2). Options 40 and 42 were chosen to compare with the nitrogen data. The output for option 40 ($s_{1/2}$ shell for oxygen) and option 42 ($p_{1/2}$ shell for oxygen) were weighted by a factor of 1/2.5 before comparing with the nitrogen data. The output of the simulation was converted into ROOT format for analysis.

BIBLIOGRAPHY

[Abragam, 1996] Abragam, A. (1996). *Principles in nuclear magnetism.* Oxford University Press Inc., New York, USA.

[Afanasev, 2007] Afanasev, A. (2007). Private Communication.

[Afanasev *et al.*, 2001] Afanasev, A., Akushevich, I., and Merenkov, N. (2001). *Phys. Rev. D* **64**, 113009.

[Akhiezer and Rekalo, 1968] Akhiezer, A. I. and Rekalo, M. P. (1968). *Sov. Phys. Dokl.* **13**, 572.

[Arnold *et al.*, 1981] Arnold, R. G., Carlson, C. E., and Gross, F. (1981). *Phys. Rev. C* **23**, 363.

[Arrington *et al.*, 2007] Arrington, J., Melnitchouk, W., and Tjon, J. A. (2007). *Phys. Rev. C* **76**, 035205.

[Arrington *et al.*, 2006] Arrington, J., Roberts, C. D., and Zanotti, J. M. (2006). *arXiv:hep-ph/nucl-th/0611050 v1* **1**.

[Babcock *et al.*, 2003] Babcock, E., Nelson, I., Kadlecek, S., Driehuys, B., Anderson, L. W., Hersman, F. W., and Walker, T. G. (2003). *Phys. Rev. A* **91**.

[Babcock *et al.*, 2005] Babcock, E., Nelson, I. A., Kadlecek, S., and Walker, T. G. (2005). *Phys. Rev. A* **71**, 013414.

[Beck, 2006] Beck, A. (2006). Private Communication.

[Beck *et al.*, 2007] Beck, A., Kolarkar, A., Korsch, W., Nelyubin, V., Nikolenko, D., and Wojtsekhowski, B. (2007). Magnetic Field Direction of the Target Holding Field for the G_E^n experiment. Technical report, Jefferson Lab.

[Belitsky *et al.*, 2003] Belitsky, A. V., Ji, X., and Yuan, F. (2003). *Phys. Rev. Lett.* **91**, 092003.

[Berestetskii *et al.*, 1982] Berestetskii, V. B., Lifshitz, E. M., and Pitaevskii, L. P. (1982). *Quantum Electrodynamics*, volume 4 of *Landau and Lifshitz Course of Theoretical Physics*. Butterworth Heinemann, 2 edition.

[Bhagwat *et al.*, 2006] Bhagwat, M. S., Höll, A., Krassnigg, A., and Roberts, C. D. (2006). *nucl-th/0610080* .

[Bijker and Iachello, 2004] Bijker, R. and Iachello, F. (2004). *Phys. Rev. C* **69**, 068201.

[Bradford *et al.*, 2006] Bradford, R., Bodek, A., Budd, H., and Arrington, J. (2006). *Nucl.Phys.Proc.Suppl.* , 127–132.

[Brodsky and Farrar, 1975] Brodsky, S. J. and Farrar, G. R. (1975). *Phys. Rev. D* **11**, 1309.

[Brodsky *et al.*, 2004] Brodsky, S. J., Hiller, J. R., Hwang, D. S., and Karmanov, V. A. (2004). *Phys. Rev. D* **69**, 076001.

[Burkardt, 2004] Burkardt, M. (2004). *Phys. Lett. B* **595**, 245.

[Chann *et al.*, 2002] Chann, B., Babcock, E., Anderson, L. W., and Walker, T. G. (2002). *Phys. Rev. A* **66**, 032703.

[Craver, 2007a] Craver, B. (2007a). Private Communication.

[Craver, 2007b] Craver, B. (2007b). Beam Position Calibration for G_E^n. Technical report, Jefferson Lab.

[Diehl, 2003] Diehl, M. (2003). *arXiv:hep-ph/0205208 v2* **2**.

[Dombey, 1969] Dombey, N. (1969). *Rev. Mod. Phys.* **41**, 236.

[Donnelly and Raskin, 1986] Donnelly, T. W. and Raskin, A. S. (1986). *Ann. Phys.* **169**, 247.

[Ernst *et al.*, 1960] Ernst, F. J., Sachs, R. G., and Wali, K. C. (1960). *Phys. Rev.* **119**, 1105.

[Feuerbach, 2007] Feuerbach, R. J. (2007). Determining the QE Neutron Asymmetry. Technical report, College of William and Mary.

[Feynman, 1969] Feynman, R. P. (1969). *Phys. Rev. Lett.* **23**, 1415.

[Franklin, 2006] Franklin, G. B. (2006). Gen asymmetry corrections for finite angular acceptance. Technical report, Jefferson Lab.

[Friar, 1991] Friar, J. L. (1991). Few-nucleon systems. In *Modern topics in electron scattering*, page 104. World Scientific.

[Friar *et al.*, 1990] Friar, J. L., Gibson, B. F., Payne, G. L., Bernstein, A. M., and Chupp, T. E. (1990). *Phys. Rev. C* **42**, 2310.

[Friedrich and Walcher, 2003] Friedrich, J. and Walcher, T. (2003). *arXiv:hep-ph/0303054 v2* **2**.

[Galster, 1971] Galster, S. (1971). *Nucl. Phys.* **B32**, 221.

[Gari and Krümpelmann, 1985] Gari, M. F. and Krümpelmann, W. (1985). *Z. Phys. A* **322**, 689.

[Geesaman *et al.*, 1995] Geesaman, D. F., Saito, K., and Thomas, A. (1995). *Annu. Rev. Nucl. Part. Sci.* **45**, 337.

[Group, 2004] Group, T. C. S. (2004). The EPICS Control System at Jefferson Lab. http://www.jlab.org/accel/documents/epics$_d$oc.html.

[group, 1995] group, T. J. C. (1995). *CODA, CEBAF Online Data Acquisition*. Jefferson Lab, http://coda.jlab.org/manuals.htm.

[Guichon and Vanderhaeghen, 2003] Guichon, P. A. M. and Vanderhaeghen, M. (2003). *Phys. Rev. Lett.* **91**, 142303.

[Happer, 1972] Happer, W. (1972). *Rev. Mod. Phys.* **44**, 169–249.

[Hyde-Wright and de Jager, 2004] Hyde-Wright, C. E. and de Jager, K. (2004). *Annul. Rev. Nucl. Part.Sci.* **54**, 217–267.

[Iachello *et al.*, 1973] Iachello, F., Jackson, A. D., and Landé, A. (1973). *Phys. Lett. B* **43**, 191.

[J. H. Mitchell, 2000] J. H. Mitchell, e. (2000). *Hall A Experimental Equipment Operations Manual*. Jefferson Lab.

[Jans *et al.*, 1982] Jans, E. *et al.* (1982). *Phys. Rev. Lett.* **49**, 974.

[Ji, 2004] Ji, X. (2004). *Annu. Rev. Nucl. Part. Sci.* **54**, 413–50.

[Kelleher *et al.*, 2007] Kelleher, A. M., Averett, T. D., Katich, J., Cates, G., Nelyubin, V., Tobias, W. A., Singh, J., and Kolarkar, A. (2007). Target Report for Target Cell Edna. Technical report, Jefferson Lab.

[Kelly, 2004] Kelly, J. J. (2004). *Phys. Rev. C* **70**, 068202.

[Kievsky *et al.*, 1997] Kievsky, A., Pace, E., Salmè, G., and Viviani, M. (1997). *Phys. Rev. C* **56**, 64.

[Kolarkar, 2006a] Kolarkar, A. (2006a). BigBite Scintillator Timing and RF Timing Calibration. Technical report, University of Kentucky.

[Kolarkar, 2006b] Kolarkar, A. (2006b). Pulsed Beam Analysis for E02-013 Experiment. Technical report, University of Kentucky.

[Kolarkar, 2007a] Kolarkar, A. (2007a). Monte Carlo Neutron Detector Acceptance Studies for E02-013. Technical report, University of Kentucky.

[Kolarkar, 2007b] Kolarkar, A. (2007b). Nitrogen Dilution Analysis. Technical report, University of Kentucky.

[Kramer, 2003] Kramer, K. M. (2003). *A search for higher twist effects in the newton spin structure function* $g_2^2(x, Q^2)$.. PhD thesis, The College of William and Mary.

[Leo, 1987] Leo, W. R. (1987). *Techniques for Nuclear and Particle Physics Experiments, A How-to Approach*. Springer Verlag, Berlin, 1st edition.

[Lu *et al.*, 1999] Lu, D.-H., Tsushima, K., Thomas, A. W., Williams, A. G., and Saito, K. (1999). *Phys. Rev. C* **60**, 068201.

[Madey *et al.*, 2003] Madey, R. *et al.* (2003). *Phys. Rev. Lett.* **91**, 12002.

[Meier-Hajduk *et al.*, 1983] Meier-Hajduk, H., Hajduk, C., Sauer, P. U., and Theis, W. (1983). *Nuclear Physics A* **395**, 332–348.

[Michaels, 2006] Michaels, R. (2006). Hall A in G0 Helicity Mode. Technical report, Jefferson Lab, http://www.jlab.org/ rom/g0helicity.html.

[Miller, 2002] Miller, G. A. (2002). *Phys. Rev. C* **66**, 033201(R).

[Miller, 2003] Miller, G. A. (2003). *Phys. Rev. C* **68**, 022201.

[Miller, 2007] Miller, G. A. (2007). *Phys. Rev. Lett.* **99**, 112001.

[Miller and Frank, 2002] Miller, G. A. and Frank, M. R. (2002). *Phys. Rev. C* , 065205.

[Miller *et al.*, 2007] Miller, G. A., Piasetzky, E., and Ron, G. (2007). *arXiv:0711.0972v1 [nucl-th]* . To be published.

[Milner *et al.*, 1996] Milner, R. G. *et al.* (1996). *Physics Letters B* **379**, 67–72.

[Mo and Tsai, 1969] Mo, L. W. and Tsai, Y. S. (1969). *Rev. Mod. Phys.* **41**, 205.

[Moniz *et al.*, 1971] Moniz, E. J. *et al.* (1971). *Phys. Rev. Lett.* **26**, 445.

[Newbury *et al.*, 1993] Newbury, N. R., Barton, A. S., Cates, G. D., Happer, W., and Middleton, H. (1993). *Phys. Rev. A* **48**, 4411–4420.

[Ngo and Shahinyan, 2007] Ngo, T. and Shahinyan, A. (2007). Neutron arm geometry for the G_E^n Experiment. Technical report, Jefferson Lab and California State university and Yerevan Physics Institute.

[Perdrisat *et al.*, 2006] Perdrisat, C. F., Punjabi, V., and Vanderhaeghen, M. (2006). *arXiv: hep-ph/0612014* **1**.

[Pitt, 2001] Pitt, M. (2001). Helicity control requests from the G^0 experiment. Technical report, Jefferson Lab and Virginia TechJefferson Lab.

[Plaster, 2004] Plaster, B. (2004). *The Neutron Electric Form Factor to* $Q^2 = 1.45$ *(GeV/c)*^{2}. PhD thesis, M.I.T.

[Plaster *et al.*, 2006] Plaster, B. *et al.* (2006). *Phys. Rev. C* **73**.

[Povh *et al.*, 1999] Povh, B., Rith, K., Scholz, C., and Zetsche, F. (1999). *Particles and Nuclei, An Introduction to the Physical Concepts*. Springer-Verlag.

[Proposal, 2002] Proposal, E. (2002). Measurement of the neutron electric form factor G_E^n at high Q^2.

[Raskin and Donnelly, 1989] Raskin, A. S. and Donnelly, T. W. (1989). *Annals of Physics* **191**, 78–142.

[Riordan, 2007] Riordan, S. (2007). BigBite Spectrometer Tracking Code. Technical report, Jefferson Lab.

[Romalis, 1997] Romalis, M. V. (1997). *Laser polarized ^{3}He target used for a precision measurement of the neutron spin structure.* PhD thesis, Princeton University.

[Sachs, 1962] Sachs, R. G. (1962). *Phys. Rev.* **126**, 2256.

[Schulze and Sauer, 1993] Schulze, R.-W. and Sauer, P. U. (1993). *Phys. Rev. C* **48**, 38.

[Schwinger, 1949] Schwinger, J. S. (1949). *Phys. Rev.* , 790.

[Singh, 2007] Singh, J. (2007). Private Communication.

[Slifer, 2004] Slifer, K. (2004). *Spin Structure of ^{3}He and the Neutron at Low Q^2; A Measurement of the Extended GDH Integral and the Burkhardt-Cottingham Sum Rule.* PhD thesis, Temple University.

[Solvignon, 2006] Solvignon, P. (2006). *Measurement of the ^{3}He spin structure functions in the resonance region: A test of quark-hadron duality on the neutron.* PhD thesis, Temple University.

[Sulkosky, 2007] Sulkosky, V. (2007). *The spin structure of ^{3}He and the neutron at low Q^2: A measurement of the generalized GDH integrand.* PhD thesis, College of William and Mary.

[Thomas, 1984] Thomas, A. W. (1984). *Adv. Nucl. Phys.* **13**, 1.

[Ulmer, 1991] Ulmer, P. (1991). MC for electro-nuclear coincidence experiments. CEBAF-TN-91-101.

[Unser, 1981] Unser, K. (1981). *IEEE Transactions on Nuclear Physics, Nuc. Sci.* **28**, 2344–2346.

[UVa, 2006] UVa (2006). E02-013 GEn-style Helium-3 Target Cell Inventory. http://galileo.phys.virginia.edu/research/groups/spinphysics/gen/gencells.html.

[Wagshul and Chupp, 1994] Wagshul, M. E. and Chupp, T. E. (1994). *Phys. Rev. A* **49**, 3854–3869.

[Walker, 1989] Walker, T. G. (1989). *Phys. Rev. A* **40**, 4959.

[Whitney *et al.*, 1974] Whitney, R. R. *et al.* (1974). *Phys. Rev. C* **9**, 2230.

VITA

Ameya Suresh Kolarkar

- **Date and place of birth:**
  — July 28, 1976; Nagpur, India.
- **Educational institutions attended and degrees awarded:**
  — University of Kentucky, Ph.D. 2008 (expected).
- **Professional positions held:**
  — Research Assistant, University of Kentucky, 1999-2001, 2002-2007
  — Teaching Assistant, University of Kentucky, 2001-2002
- **Professional Publications:**

1. M. Mazouz *et al.*, (Jefferson Lab Hall A Collaboration), *Deeply virtual compton scattering off the neutron*, Phys. Rev. Lett. 99:242501, 2007
2. David S. Armstrong *et al.*, (G0 Collaboration), *Transverse Beam Spin Asymmetries in Forward-Angle Elastic Electron-Proton Scattering*, Phys. Rev. Lett. 99:092301, 2007.
3. R. Shneor *et al.*, (Jefferson Lab Hall A Collaboration), *Investigation of proton-proton short-range correlations via the* ^{12}*C(e,e'pp) reaction*, Phys. Rev. Lett. 99:072501, 2007.
4. A. Acha *et al.*, (HAPPEX Collaboration), *Precision Measurements of the Nucleon Strange Form Factors at* $Q^2 \sim 0.1{-}^2$, Phys. Rev. Lett. 98:032301, 2007
5. C. Munoz-Camacho *et al.*, (DVCS, Hall A Collaborations), *Scaling tests of the cross-section for deeply virtual compton scattering*, Phys. Rev. Lett. 97:262002, 2006
6. D. S. Armstrong *et al.*, (G0 Collaboration), *Strange quark contributions to parity-violating asymmetries in the forward G0 electron-proton scattering experiment*, Phys. Rev. Lett. 95:092001, 2005
7. K. A. Aniol *et al.*, (HAPPEX Collaboration), *Constraints on the nucleon strange form-factors at* $Q^2 \sim 0.1{-}^2$, Phys. Lett. B 635:275-279, 2006

8. K. A. Aniol *et al.*, (HAPPEX Collaboration), *Parity-violating electron scattering from He-4 and the strange electric form-factor of the nucleon*, Phys. Rev. Lett. 96:022003, 2006